Chemical and structural stability of proton conducting perovskite ceramic for fuel cells and electrolyzers

Settakorn Upasen

▶ To cite this version:

HAL Id: tel-01242857
https://tel.archives-ouvertes.fr/tel-01242857

Submitted on 14 Dec 2015

Université Pierre et Marie Curie

Ecole doctorale n°388

Chimie Physique et Chimie Analytique de Paris Centre

« De la Molécule aux Nano-objets : Réactivité, Interactions et Spectroscopies, MONARIS »

Thèse

pour obtenir le grade de

DOCTEUR DE L'UNIVERSITÉ PIERRE ET MARIE CURIE
Spécialité : Chimie Physique et Chimie Analytique

présentée par
Settakorn UPASEN
le 10 Septembre 2015

Sujet de la thèse

« Stabilité chimique et structurale de pérovskites céramiques de conductrice protoniques pour piles à combustible et électrolyseurs »

« Chemical and structural stability of proton conducting perovskite ceramic for fuel cells and electrolyzers »

Thèse dirigée par Philippe COLOMBAN

Devant un jury composé de :

Rapporteurs

M. Gilles TAILLADES   Professeur des Universités, ICGM, Montpellier

Mme Maggy COLAS   Chargée de recherches HDR, SPCTS, Limoges

Examinateurs

M. Marc SIMON   Directeur de Recherche, LCPMR, UPMC, Paris

M. Fabrice MAUVY   Professeur des Universités, ICMCB, Bordeaux

M. Mathieu MARRONY   Senior Scientist, EIFER, Germany

M. Philippe COLOMBAN   Directeur de Recherche, MONARIS, UPMC, Paris

Mme Aneta SLODCZYK   Docteur HDR, UPMC, Paris

ACKNOWLEDGMENTS

UPASEN, Settakorn

CONTENTS

INTRODUCTION

Introduction

Renewable energy from intermittent and variable sources such as wind, wave, biomass, and solar is expected to make an increasing contribution to worldwide energy supplies [1]. According to a current report from 2014 [2], global renewable electricity generation rose approximately 240 terawatt hours (TWh) (+5.0% year-on-year) to reach nearly 5070 TWh. Moreover, it is accounted for almost 22% of total power generation [2]. However, renewable energy sources are rather very expensive comparing to the primitive energy sources such as coal, oil/natural gas [3] and nuclear power. Furthermore, intermittency of renewable sources such as the wind and solar (photovoltaic (PV)) presents a major obstacle to their extensive application into the electricity grid [4]. The cost of electricity storage is an additional concern. To date, only the water pumped storage can retain electricity using hydroelectric damp (STEP in French) at low cost but potential convenient locations are rare. Sodium/Sulfur batteries using beta alumina ceramic membrane also provide an attractive solution, and more than hundreds of MW are installed by NGK/TEPCO worldwide. For example, since decades, the batteries are combined with renewable energy sources as in Reunion Island. Biomass energy also exhibits some significant disadvantages i.e. greenhouse gas emission and solid wastes combustion [5,6]. Furthermore, vast quantities of heat energy are being released into the atmosphere as waste on a daily basis. It is estimated that roughly 3×10^{13} kWh of heat energy is being lost as dissipative waste energy each year from US manufacturing alone [7]. A part of the waste heat is generated in a power plant by incomplete recycling of fuel combustion or chemical reaction. The essential quality of heat is not its amount but its value. Such valuable heat wastes can still be reused for some useful and economic purpose. The strategy to recover this heat depends on the waste temperature and the financial implications [8]. For optimal utilization and to ensure safe operation with a renewable resource, technological improvements are required. These include management of heat loss, improvements of the connectivity and increasing the amont of intermittent renewable energy to electricity networks.

Over last two decades, the management of renewable resources by mean of an electrolyzer-based management (EBM) has been established [9]. EBM offers a versatile means for optimizing the process of harnessing energy supplies derived from variable and/or

intermittent renewable resources. The principal components of the EBM system, shown in Fig. 1, are an electrolyzer, a gas storage system, and a fuel cell. A heat engine/generator combination could be also used. Both electrolyzer and fuel cell are high-current, low-voltage DC devices [9]. Consequently, the energy management significantly yields the overall energy conversion efficiency.
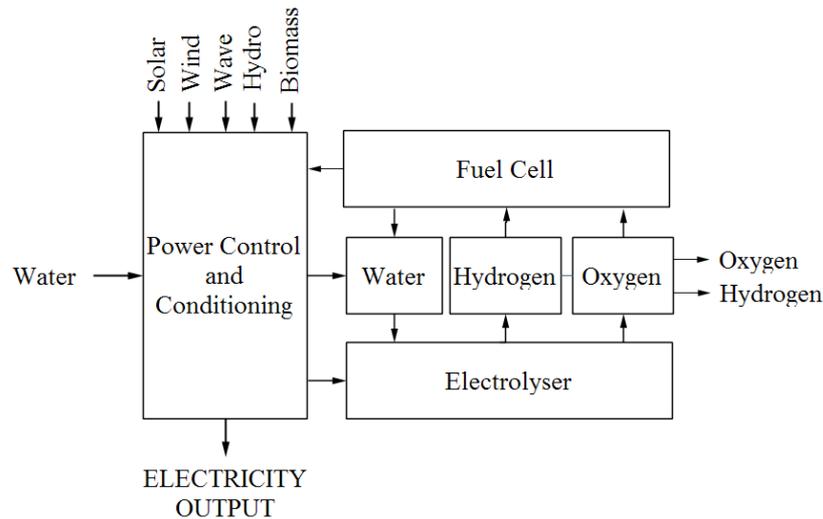
Figure 1: *Schematic diagram of a stand-alone electrolyzer and fuel cell-based management (EBM) system configured for renewable-resource inputs [9].*

Hydrogen can be considered as an essential element in the fuel cell and electrolysis applications (EBM system) in the renewable power plant. Before theavailable of natural gas, hydrogen mixed methane was produced by the action of water on hot coal (coke). Hydrogen can potentially play a significant role in our future energy systems - By 2019, the hydrogen generation market is predicted to reach $138.2 billion [10]. Like electricity, hydrogen is an energy carrier and has one of the highest energy density values per mass, a yield of 122 - 140 kJ/g. Such energy density value is about three times greater than that of hydrocarbon fuel [11]. Moreover, hydrogen is a non-toxic and extremely environment-friendly, since water is the only exhaust product when hydrogen is converted into electricity.

Hydrogen could be produced using excess electricity from the electrical power plant of renewable energy sources, through electrolysis of water as illustrated in Fig. 1. An electric current is used to split water into oxygen and hydrogen. Hydrogen can then be utilized by the

fuel cell to generate power/electricity producing only water and heat as byproducts. Another interesting possibility of hydrogen application is the conversion of CO_2 gas into methane (CH_4) according to the Sabatier reaction:

$$CO_2 + 4H_2 \rightarrow CH_4 + 2H_2O \qquad \text{...(eq. 1)}$$

The CO_2 conversion has already been established. A 250 kW Power-to-Gas plant in Werlte, Germany currently produces 300 m^3 of CH_4 per day [12].

Electrolysis and fuel cell technologies have shown tremendous application potential. However, further intensive studies are necessary to improve their performance and especially their stability for long-term use. The material stability determines the operating cost.

Historical background of electrochemical conversion technology

The benefits of electrochemical energy conversion devices in connection with renewable power plants [13-17] are many as the various types of electrolyzer/fuel cell-based technologies demonstrate. Table 1 shows an operating condition of different electrolyzers/fuel cells over a wide range of temperature, from ambient to over 1000°C, and using diverse materials as electrolytes and electrodes.

The early 1800s, William Nicholson and Anthony Carlisle observed the evolution of gasses during the voltaic pile replication experiments. This allowed them to discover the electrolysis phenomenon leading to water splitting [18]. Water splitting is a general term for a chemical reaction in which water is separated into oxygen and hydrogen. In 1939, the first large-scale water electrolysis plant, with a hydrogen generation capacity of 10,000 m^3 h^{-1}, went into operation. In 1948, the first pressurized industrial electrolyzer was manufactured by Zdansky and Lonza [19], whereas the first solid-oxide water electrolysis unit was developed in 1972 [20].

In 1838, William Robert Grove invented the first fuel cell. He deployed a combination of sheet iron, copper and porcelain plates, and a solution of sulfate of copper and dilute acid. He called such first fuel cell the "gas battery". Later, Johnson Matthey [21] developed the cell with a platinum catalyst, and used hydrogen to generate an electric current. The innovation of the fuel cell was based on reversing chemical reaction to that occurring during electrolysis of

Table 1: *Technical characteristics of different electrolysis and fuel cells [22-24].*

Type	Discovered /Established year	Temperature °C	Fuel	oxidant	Membranes		Efficiency (%)
					Electrode catalyst	Electrolyte	
Water electrolysis technologies							
Alkaline Electrolyzers (AEC)	1902	60-80	Water	O_2/Air	Nickel-based	KOH or NaOH	62-82
Proton Exchange Membrane Electrolyzers (PEMEC)	1966	50-80	Water	O_2/Air	Platinum/Iridium	Humidified polymer membrane	67-82
Solid Oxides Electrolyzers (SOEC)	1972	900-1000	Water/stream	O_2/Air	Nickel cermet	ceramic	81-86
Fuel cell technologies							
Proton Exchange Membrane (PEM)	1960	50-80	hydrogen from hydrocarbons or methanol	O_2/Air	Platinum/Iridium	polymer membrane	40-50
Direct methanol fuel cell (DMFC)	1960s	60-130	methanol	O_2/Air	Platinum/Iridium	polymer membrane	Up to 40
Alkaline Fuel cells (AFC)	1939	150 - 200	pure hydrogen	O_2/Air	Nickel-based	KOH	50-55
Phosphoric acid fuel cell (PAFC)	1970s	150-200	hydrogen from hydrocarbons and alcohol	O_2/Air	Platinum	Phosphoric acid	40-50
Molten Carbonate Fuel Cells (MCFC)	1950s	630-650	Hydrogen, carbon monoxide, natural gas, propane, marine diesel	CO_2/O_2/Air	Metals	Lithium potassium carbonate salt	50-60
Solid Oxide Fuel Cells (SOFC)	1853	900-1000	natural gas or propane	O_2/Air		ceramic as stabilized zirconia and doped perovskite	45-60
Protonic Ceramic Fuel Cell (PCFC)	1970s	500-700	Hydrogen	O_2/Air		the thin membrane of barium cerium oxide	45-60

water. In 1853, solid oxide-based fuel cells (SOFCs) came into existence after the discovery of substantial galvanic electrolyte by J.-M. Gaugain [25]. Wiedemann reported that at the end of the 19th century, the expression "solid electrolyte" was used more frequently [26]. In the 1930s, some changes were made to fuel cells, mostly concerning their design such as shape and size. In the case of 'Bacon Cell', developed by Francis Thomas Bacon [22] in 1932, the modifications, related to the introduction of nickel gauze electrodes and the use of potassium hydroxide as an electrolyte, were carried out. The Bacon Cell was the forerunner of the alkaline fuel cell (AFC). Later in 1939, the first alkaline electrolyte fuel cell was built. Bacon spent almost thirty more years to achieve an operational fuel cell. By 1959, he demonstrated a fuel cell that could generate 5kW of energy. In the late 1950s and early 1960s, NASA in collaboration with industrial partners began the development of fuel cell generators for Gemini manned space missions. The first proton exchange membrane (PEM) fuel cell unit, developed with the help of Willard Thomas Grubb at General Electric (GE), was the result of this collaboration. Furthermore, another GE researcher, Leonard Niedrach improved Grubb's PEMFC by using platinum as a catalyst [24].

From the mid-1960s, Shell was involved in the development of direct methanol fuel cell (DMFC) as the use of liquid fuel was considered to be a great advantage for vehicle applications. More than fifty years of research allowed the PEMFC and DMFC devices to estrabish as commercial products e.g. perfluorinated ionomer (PFI) membranes, Nafion® (Dupont de Nemours), and Dow membrane (Dow Chemical Co.) [27,28]. Very rapidly they have dominated the small market share in the portable, stationary and transport sectors (Balard, Navigant Research, etc.). However, it is well known that several significant problems remain; e.g. high cost due to the use of platinum, liquid water management and durability of the polymer electrolyte.

In the 1970s, because of important fuel shortage and then very high oil prices, the so-called First Oil Crisis, many national governments and large companies initiated research projects to develop more efficient and low cost forms of energy generation. Significant advances in Phosphoric acid fuel cell (PAFC) technology, in particular concerning its stability and performance, appeared as a direct result of these undertakings. For example, large Stationary PAFC units for prime, off-grid power, including a 1 MW unit were developed by International Fuel Cells (IFC, later UTC power).

Furthermore, development of solid oxide fuel cell (SOFC) has become significant. Most of SOFCs research concerns the electrolyte/devices operating at high temperatures (HT-SOFC, > 900-1000°C). W. Nernst in 1899 [29,30] showed that apart from a mixture of metal oxides, 15 mol % Y_2O_3 doped ZrO_2 (15YSZ) exhibits high oxygen conductivity at elevated temperature. He suggested that 15YSZ could be used in lamps as a glowing filament. Schottky in 1935 [31] proposed that 15YSZ could be a potential candidate for the solid electrolyte. Wagner in 1943 [32] showed that solid-oxide solutions permit ionic conduction where oxygen ions hop through vacancies created by acceptor doping in the host lattice. Baur and Presis [33,34] in subsequent years proved this by demonstrating solid ceramic oxide fuel cell working with YSZ at 1000°C. Later, in the 1970s to 2010, the SOFCs research moved towards operating at intermediate temperature (IT-SOFC, 300-600°C) using thin film heterolayer and nanocomposite (~5-10 µm) electrolytes [35,36]. From 2010, the electrolyte free fuel cells with one layer/single component devices were proposed to fulfill low-temperature operation requirement [37,38].

Recent status of solid oxide-based fuel cells and electrolyzers

In spite of continuing research related to the understanding of material requirements/ optimization and their electrochemical behavior, the commercialization of solid oxide-based fuel cells and electrolyzers is still limited to test/niche market. It is mainly because of the significantly high cost of SOFC- and of SOEC-based power systems, in which expensive metal interconnects such as platinum, palladium, and silver are used [39]. Besides, there is no materials stable enough. To make these systems more economically viable, the incorporation of lower cost, stainless steel into the stack design is one of the solutions. However, these steel parts need protection coatings against high-temperature oxidation.

Lowering the operation temperature of SOFC/SOEC to 600-500°C should permit the use of less expensive metallic interconnects and casings, which could facilitate the development of this technology. However, working at such "low" temperature the proton conducting materials appear better adapted. It is due to lower activation energy of proton conduction (about 0.3-0.6 eV) in comparison with that of oxygen-ion conduction (0.7 - 1 eV) [37]. The protonic conductivity is greater than 10^{-4} S.cm^{-1} [40] in intermediate temperature (500-600°C).

Consequently, a recent (2015) review of Bi et al., [41] indicts that a number of published papers concerning proton conducting oxides (indexed in Scopus) has significantly increased in recent years, almost three times over ten years. The authors compared the study percentage between the proton conducting fuel cell and proton conducting electrolyzer. They show that the few studies devoted for electrolyzer application address dilemma in choosing electrolyte materials with proper features of proton conductivity and chemical stability. Hence, the researchers are continuously seeking a "good" material. This means chemically, mechanically and structurally stable proton-conducting oxide showing long lifetime, can be used as an electrolyte and/or as an electrode. Besides, zirconates and nickelates appear as the most promising candidates for proton conducting application, and as an electrolyte and an electrode material, respectively. Consequently, they are the subject of this thesis. A review of their actual "status" is given in chapter 2.

Electrochemistry of fuel cell and electrolyzer: the difference between oxide and proton conduction mechanism

The principal reaction of a fuel cell and water electrolyzer is chemically inverse, given by equation 2.

$$H_2(g) + \frac{1}{2}O_2(g) \Leftrightarrow H_2O(g) \qquad \ldots \text{(eq. 2)}$$
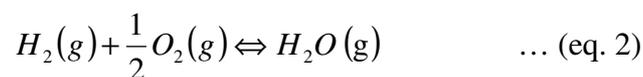
The forward reaction between hydrogen gas and oxygen gas appears in the fuel cell system. Applying thermodynamic potentials to the above equation (eq. 2) at room temperature and atmosphere pressure, the total energy (ΔH, enthalpy) of -285.82 kJ is required. Excess heat ($T\Delta S$, entropy) of the reaction, about 48.7 kJ, can be expelled to the environment. Consequently, the amount of energy ($\Delta G = \Delta H - T\Delta S$, the change of Gibbs free energy) per mole of hydrogen is -237.1 kJ, which can be provided as the electrical energy. In an ideal case, the fuel energy is converted to electrical energy at an efficiency of 83% ($\Delta G/\Delta H$ x 100%) [42].

In contrast, the reverse reaction is visible in the water electrolyzer system. In addition, the system needs energy: first to dissociate the water molecule, and then to expand the produced gasses. Considering the system operating at room temperature and under atmosphere pressure,

the total electrical energy demand (ΔG) and energy from environment ($T\Delta S$) are approximately 237.13 kJ and 48.7 kJ, respectively [42].

Figure 2 presents schematics of an oxygen-conducting SOFC and of a proton-conducting fuel cell and electrolyzer. *Note: Proton Conducting Fuel Cell and Proton Conducting Electrolysis Cell are abbreviated as PCFC and PCEC, respectively.* In keeping with the development of solid oxide-based fuel cell technology, oxygen-ion conducting cell will be discussed first. The solid oxide fuel cell, Fig. 2a consists of two electrodes generally cermets sandwiched around a dense ceramic electrolyte such as the most used zirconium oxide stabilized with yttrium oxide (YSZ). Fuel gas - hydrogen - is fed into the anode of the fuel cell. Oxygen, usually carrying by air, enters the cell via the cathode. The anode disperses the hydrogen gas equally over its whole surface and conducts the electrons that are freed from hydrogen molecule, to be used as power in the external circuit. The cathode contributes the oxygen fed to its surface and conducts the electrons back from the external circuit, where they can recombine with oxygen ions (eq. 3). The oxygen ions pass across the electrolyte and react with hydrogen to form water (eq. 4). The electrolyte determines the operating temperature of the fuel cell, separates two gases and is used to prevent two electrodes from coming into electronic contact blocking electrons. Typically, this system works at high temperature range (HT-SOFC), between 800°C and 1000°C.
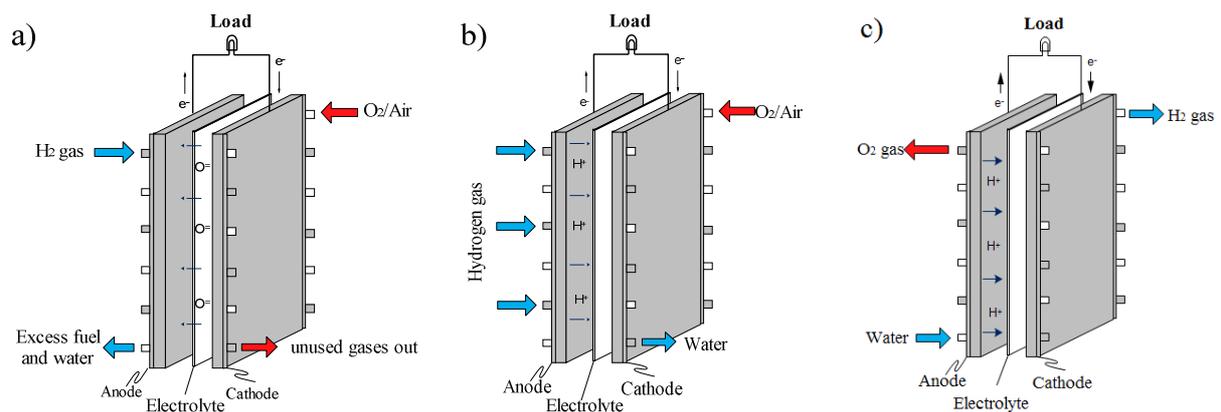
Figure 2: *Schematic diagram of a) solid oxide fuel cell (SOFC), b) proton conducting fuel cell (PCFC) and c) proton-conducting electrolysis cell (PCEC).*

Table 2: *Electrochemical reactions occurring in SOFC, PCFC, and PCEC system.*

	SOFC	PCFC	PCEC
Anode	$H_2 + O^{2-} \rightarrow H_2O + 2e^-$ (eq. 3)	$H_2 \rightarrow 2H^+ + 2e^-$ (eq. 6)	$H_2O \rightarrow 2H^+ + 1/2\,O_2 + 2e^-$ (eq. 9)
Cathode	$1/2\,O_2 + 2e^- \rightarrow O^{2-}$ (eq. 4)	$1/2\,O_2 + 2H^+ + 2e^- \rightarrow H_2O$ (eq. 7)	$2H^+ + 2e^- \rightarrow H_2$ (eq. 10)
Overall	$H_2 + 1/2\,O_2 \rightarrow H_2O$ (eq. 5)	$H_2 + 1/2\,O_2 \rightarrow H_2O$ (eq. 8)	$H_2O \rightarrow H_2 + 1/2\,O_2$ (eq. 11)

The configuration of PCFC (Fig. 2b) and PCEC (Fig. 2c) is similar to oxygen ion conducting fuel cell. However, the principal operating mechanism is different. In the case of PCFC, Fig. 2b, hydrogen fuel gas is fed into the anode side and on oxidation releases the electrons (Eq. 6). The released electrons are transported to the cathode via an external circuit. At the cathode, the oxidant air is reduced and consumes the transported electrons to form water with H_2 supplied by an electrolyte (Eq. 7). The PCFC electrolyte is typically a ceramic material e.g. Ln-doped $BaZrO_3$ perovskite, which shows high proton conductivity in the temperature range of 400-600°. The electrodes are commonly used of cermets.

In the case of PCEC, Fig. 2c, the water (steam) is fed into anode side, where it is electrochemically split into oxygen, and protons (eq. 9). The released electrons are transported to the cathode via an external circuit while the protons migrate through the dense electrolyte layer i.e. remarkable Ln-doped cerates/zirconates [43]. At the cathode side, the protons combine with electrons to form dry H_2 (eq. 10), which is the desired product. The oxygen gas as a byproduct is discharged at the anode side. Note, since the produced hydrogen is very reactive, it can be used to transform the CO_2 into CH_4 or other chemicals in the cathode chambers. The CO_2 stable cathodes are then requested to be used in PCEC/CO_2 converters.

The Lei Bi et al. [44] review describes the complexity of reaction steps occurring at a single-phase anode of proton-conducting electrolyzer (Fig. 3). The single-phase anode model provides both pathways for proton (H^+) and electron (e^-), enabling the electrochemical reactions to occur on the whole electrode surface. Steps 1 - 3 describe the dissociation of H_2O molecule into O^{2-} and H^+. Steps 4 - 7 explain the formation and adsorption of O_2. Steps 8 - 9 describe the proton migration to triple phase boundary (TPB) sites, which are regarded as the

reaction active sites. Note, oxygen-ions do not participate in the reactions at TPB. The proton transfer process, including the proton transfer from decomposed H_2O to TPB (step 8) and the proton migration to the electrolyte from the TPB sites (step 9), is the rate-limiting step. This mechanism is rather different from that of HT-SOFCs (and from that for proton-conducting SOFCs), in which oxygen vacancies also have to diffuse to the TPB area.

Step 1: $H_2O(g) \rightarrow H_2O_{ad}$

Step 2: $H_2O_{ad} \rightarrow OH^- + H^+_{ad}$

Step 3: $OH^- \rightarrow O^{2-}_{ad} + H^+_{ad}$

Step 4: $O^{2-}_{ad} - e \rightarrow O^-_{ad}$

Step 5: $O^-_{ad} - e \rightarrow O_{ad}$

Step 6: $2O_{ad} \rightarrow O_2(ad)$

Step 7: $O_2(ad) \rightarrow O_2$

Step 8: $H^+_{ad} \rightarrow H^+_{TPB}$

Step 9: $H^+_{ad} \rightarrow H^+_{electrolyte}$
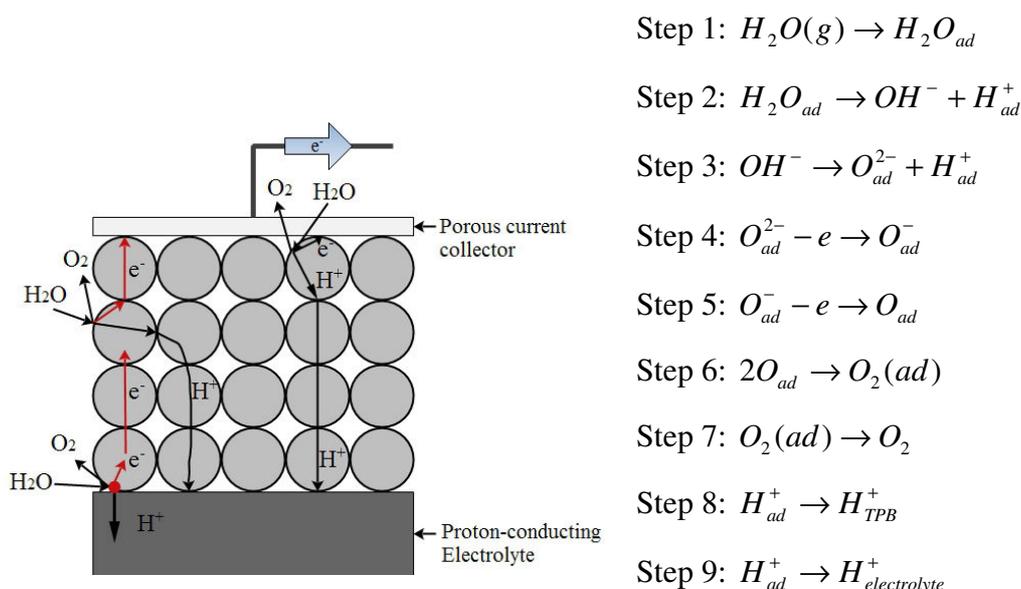
Figure 3: *Schematic reaction steps of single-phase anode material with simultaneous proton and electron conduction for proton-conducting PCECs after [44].*

PCFCs and PCECs under water vapor pressure: advantages and drawbacks

In advanced applications, the proton-conducting *PCFC* and *PCEC* have operated under moderate to high temperature/pressure. Conventional electrolyzers, for example, which are capable to produce the hydrogen under 10-30 bar of H_2O, are available on the market [45]. The management of water/gas pressure is well established in nuclear plant industry: for instance a boiling water (nuclear) reactor (BWR, ancient generation) operates at 70 bar and 285°C, and a pressurized water reactor (PWR, present generation) works at 150 bar and 320°C [46,47]. In the future in advanced nuclear plant, the supercritical water cooled reactor (SCWR) should operate at 450°C and under 250 bar. This could be considered as a high net power cycle efficiency system, providing not only the electricity need but also deliver relatively high-temperature process heat [47].

To understand the advantages and drawbacks of steam applications, the properties of water at elevated temperature and under pressure should be considered. As presented in Fig. 4 the supercritical water (T_c = 373.95°C and P_c = 220.5 bar), has both liquid-like and gas-like characteristics with high diffusivity and good heat-transporting properties. The water behaves as a non-polar solvent according to a significant decrease of dielectric constant [48]. The degree of hydrogen bonding decreases when the temperature increases [49]. As such supercritical water seen as a dense gas offering a medium with excellent transport properties, while possessing complete solvency for most of gases [50,51]. In a recent study, the chemical potential gradient (~3 x 10^{-4} mol.s^{-1}.m^{-2}) of mixed conducting ceramics (BZY) under water pressure at 750°C has been reported by Einar et al. [52].
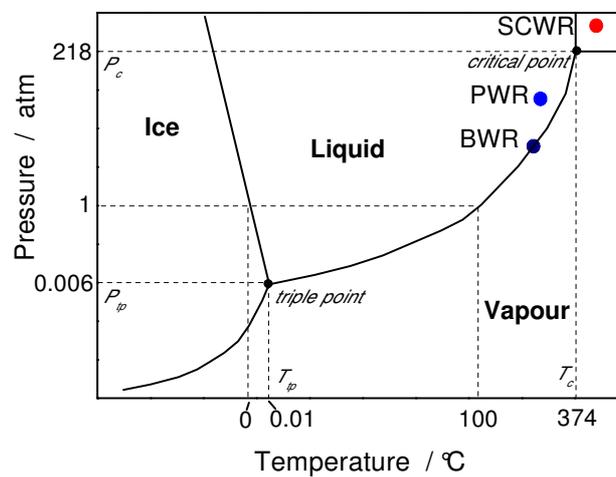
Figure 4: *Phase diagram of the one component H_2O and indication of the working conditions of different reactor types in nuclear power plant detailed in the text (note: the diagram is not to scale and three data points of reactor's working condition in hydrogen production nuclear plant were collected from literature [46]).*

However, the use of high-pressure steam can also have serious drawbacks such as high corrosion potential. In fact, water corrosion has received considerable attention during the past decades and convenient stable Ni/Cr-based steel have been developed [53,54]. The corrosion of stainless steel and nickel-based alloy during the process of supercritical water oxidation (SCWO) and aqueous solutions were discussed by Kritzer et al. [55,56]. They reported that the solubility and dissociation processes of both attacking inorganic ions (e.g.

CO_3^{2-}, OH$^-$, H$^+$, F$^-$, Cl$^-$, Br$^-$) and corrosion products (e.g. Cr_2O_3, CrOOH, $NiCl_2$, $NiBr_2$ etc.) play the most important role in corrosion at high-temperature water. In the other words, with high density and high ionic product of the solvent, significant solubility and dissociation processes were observed. These accelerated electrochemical forms of corrosion. The characteristics of corrosion films were related to the physical and chemical properties of water: corrosion layer was lower by orders of magnitude, at the highest supercritical experimental of 500°C, compared with corrosion at subcritical 300°C [57-61]. The occurrence temperature of a typical corrosion, in the case of both general dissolution and stress corrosion cracking (SCC), was determined as 250-300°C. For pitting corrosion, a localized form of corrosion occurring in the passive state of a metal, the occurrence temperature was 150-200°C with inhibitors of hydroxide and/or carbonates ions. Due to its stochastic and non-predictive nature, pitting is a very dangerous form of corrosion.

In the case of ceramic materials, there are two potential corrosion mechanisms: ion exchange and chemical reactions.

In the case of ion-exchange process, some elements/cations for example K$^+$, Ni$^+$, Li$^+$, Mg^{2+}, Mn^{4+}, etc. (ions with high diffusional mobility) exchanged with proton/protonic species, and were released into a solution. The species size mismatch led to cracks that increased the surface reaction and accelerated the corrosion. For example, the β-spodumene (LAS) matrix composite - a very interesting material because of its low and controlled thermal expansion - was corroded by proton ionic exchange reaction: (Na$^+$)-H$^+$ giving rise to contractions/cracks and then crumbling [53].

External corrosion by chemical reactions, is often observed in the case of highly hydroscopic alkaline/alkaline-earths–based compounds, for example the Ln-doped (Ba/Sr)(Ce/Zr)O$_{3-\delta}$ electrolytes [62-65]. The authors show that treatment of the ceramics exposed to medium/high pressure (10-80 bar) in the middle-temperature range (300-500°C) gives rise to unexpected secondary phases, i.e. CeO_2, Ba/SrO, Ba/Sr(OH)$_2$ and Ba/SrCO$_3$ present mostly on the surface of the anhydrous samples. In fact, such pressure/temperature treatment induces the surface hydroxylation (and carbonation reactions when CO_2 is dissolved in water), as shown in equation 12 and 13, respectively. I may be note that such corrosion layer can be present not only on the surface but also in the bulk. Different electrolytes/

14

electrodes show different degradation/corrosion levels [62-65] that allows dealing with their long-term stability determination.

$$(Ba/Sr)CeO_3 + H_2O \rightarrow (Ba/Sr)(OH)_2 + CeO_2 \qquad \dots \text{(eq. 12)}$$

$$(Ba/Sr)CeO_3 + CO_2 \rightarrow (Ba/Sr)CO_3 + CeO_2 \qquad \dots \text{(eq. 13)}$$

Proton defects and diffusion in solid oxide-based anhydrous materials

Water molecules split at the surface of solid oxide ceramic, they enter or penetrate to the crystal lattice in the dissociated form according to Equation 14 based on the Kröger-Vink notation:

$$H_2O(g) + V_0^{\bullet\bullet} \leftrightarrow OH' + H^{\bullet} \qquad \dots \text{(eq. 14)}$$
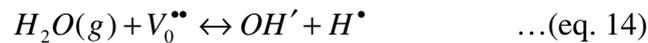
where V is an oxygen vacancy; a positive charge is represented by a dot ($\bullet$) and a negative charge by a prime ($'$).

The concentration and mobility of inserted protons determine the proton conductivity of a material. The hydroxide/proton ion concentration is proportional to the square root of the water partial pressure (or hydrogen partial pressure) in the surrounding atmosphere according to the Sievert's law behavior [66,67]. The proton concentration increases with increase in the water pressure up to a certain value. This varies depending on a material.

Due to the tiny size of a proton - just between that of electron and the smallest ion, Li^+ - the physics and chemistry of a proton [68], in the solid state, are unique. The proton is very reactive with its environment. The most common case is of the proton's penetration of the covalent shell of neighboring acceptor ions, to form the classical XHn moieties (e.g. OH^-, H_3O^+). However, the proton can also interact with two acceptors giving rise to the Hydrogen bonds or even with more acceptors that lead to the presence of the so-called ionic, free proton.

The proton mobility in solid oxides may occur by protons hopping between adjacent oxygen ions at normal lattice sites (the so-called Grotthuss-type mechanism) or by diffusion of the whole XHn species [66]. The very local diffusion of protons between sites occurs mainly by rotational diffusion of a proton around oxygen ions. A proton transfer toward a

neighboring oxide ion permits a long range diffusion [69]. The proton diffusion is characterized by its activation energy, the rotation diffusion being the faster reaction with lower activation energy, for instance, <0.2 eV [70-74]. In addition, the total activation energy of the proton conduction, can also be influenced (induced or not) by distortion of the solid oxide-based structure, depending on the materials.

Proton-conducting anhydrous materials and their properties

During the last two decades, perovskite-type oxides received significant attention due to their important application potential. The general formula of perovskite structure is ABO_3, e.g. cerates ($ACeO_3$) and zirconates ($AZrO_3$), where A is usually a 'big' alkaline earth cation, Ca, Sr or Ba. The presence of proton is not intrinsic. They must be inserted. Proton insertion/incorporation is possible once an oxygen vacancy is present. Taking yttrium (Y) doped $BaCeO_3$ as an example, oxygen vacancies are created due to the partial substitution of the tetravalent Ce at the B site by the trivalent Y, as described by equation 15:

$$Y_2O_3 \rightarrow 2Y'_{Ce} + 3O_o^x + V_O^{\bullet\bullet} \qquad \dots \text{(eq. 15)}$$
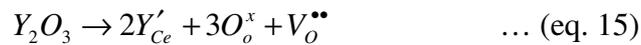
Proton conducting perovskite materials are firstly characterized by the occurrence of protonic conduction at high temperature. The potential of a perovskite ceramic as fuel cell electrolyte membrane was first demonstrated in 1964 by Forrat et al. [75]. Further research was undertaken by Iwahara et al. [76] at the time of the Oil crisis in 1981. They reported that Sc-doped $SrCeO_3$, as an electrolyte, exhibited relatively high proton conduction at 700-1000°C. Furthermore, the current efficiency increased to 50-95 % in the 0.1-0.8 $A.cm^{-2}$ current range, with water vapor supplied at 1 atm. It was obsearved that such high working temperature demands expensive materials for the cell interconnectors, caused thermal stresses, and limited the lifetime of proton conducting materials. Therefore, current researches are attempting to reduce the operating temperature below 700°C or better still to 600°C. The objective is to have operating temperatures sufficiently high to avoid the use of expensive catalyzers as in the case of RT Nafion®-based devices and sufficiently low to permit the use of standard steels for casing and piping. Since the ion transport mechanism in the ceramic electrolyte is a thermally activated process, the increasing electrolyte resistivity becomes another significant problem. To overcome this demerit, the search for electrolyte materials

with high proton conductivity (low resistivity) and/or reducing the electrolyte thickness are necessary.

At LADIR laboratory, (actually MONARIS laboratory since january 2014) [64,77-83], proton-conducting perovskite electrolytes such as Ln-doped BZY and SZY have been investigated in order to better understand the phase stability, and especially to distinguish between the bulk and surface proton contents as well as to determine a true proton nature in perovskite host membrane. The research was focused on lanthanide-modified barium/ strontium zirconate ($BaZr_{0.9}Yb_{0.1}O_{3+\delta}$, $SrZr_{0.9}Yb_{0.1}O_{3+\delta}$, $BaZr_{0.25}In_{0.75}O_{3+\delta}$ and $BaCe_{0.5}Zr_{0.3}Y_{0.16}Zn_{0.04}O_{3+\delta}$) materials. As mentioned above, the partial substitution of the Zr^{4+} by a Ln^{3+} element allows the oxygen vacancy formation, and hence the incorporation of protonic species at moderate temperature (300-600°C) and under water vapor pressure. Note, the insertion of proton species in the perovskite framework is strongly dependent on external parameters such as temperature and water partial pressure. The investigated samples were treated using an autoclave device, which allows the measurements as a function of high temperature (from RT to 620°C) and under high water vapor (up to 100 bar) pressure [63]. The utilized autoclave platform is unique. It was developed in direct relation to the study of water steam electrolyzer prototypes earlier developed, with low cost of hydrogen production, by AREVA NP [45,84]. These results show that protonation and proton conduction processes are in strict competition with hydroxylation. The hydroxylation is detected by the traces of secondary phases i.e. $Ba(OH)_2$, $Sr(OH)_2$ in pristine powder materials and low ceramics density (high active surface area). Testing high dense ceramic pellets (more than 95% of theoretical density) under high temperature and high water vapor pressure conditions enhances enhances the homogenous distribution of bulk protons. The bulk-proton saturated state needs about 100 hours of protonation in the case of 1 mm thick ceramic [78,83,85]. Furthermore, under such conditions, the structural phase transitions were observed. With the insertion of protons, the protonation decreased the distortion of the cubic perovskite unit-cell as well as its volume [64].

Objective of this work

The above description shows clearly that perovskite oxide-based materials are potential proton-conducting membranes, both electrolytes and electrodes, for fuel cell and electrolysis

applications. Prototypes have been tested by different groups [64,77-83]. In order to go further than prototypes, the stable electrolytes and electrodes against vapor pressure (pH_2O) are necessary. The structural and chemical stability of proton-conducting materials against CO_2 is also very important because of the possibility of CO_2 valorization due to its direct reaction with produced hydrogen.

The main purpose of the study presented here is to investigate the structural and chemical stability of perovskite-related oxide ceramics. Such ceramics were provided by different academic and industrial groups - AREVA NP, Imperial College, ICMCB-Université de Bordeaux (Table 3). Two potential perovskite electrolytes of hydrogen economy devices (PCFC/PCEC): were considered: Zn-doped $BaCe_{0.4}Zr_{0.5}Y_{0.1}O_{3-\delta}$ (BCZY:Zn from Imperial College) and $SrZr_{0.9}Er_{0.1}O_{3-\delta}$ (SZE, from AREVA NP). Also, another two perovskite-related oxides apply as cathode materials developed in Mauvy's group at ICMCB, Bordeaux ([86,87]): rare-earth nickelates and lanthanum strontium cobalt ferrite were tested. These ceramics, were investigated in operating conditions : under medium and high water vapor pressure (20 bar and 40 bar) at intermediate temperature (~550°C) [63]. Particular attention was paid to the structural and chemical stability of the ceramics against CO_2-containing water in the view of approaching the 'real' industrial operating conditions, especially a prior to the CO_2 conversion into methane or other chemicals.

Table 3: *Description of investigated perovskite-related oxides.*

Sample name	Composition	Abb.	Application	Collaborators/Providers
Zn,Y-doped barium mixed cerate zirconate	$BaCe_{0.5}Zr_{0.3}Y_{0.16}Zn_{0.04}O_{3-\delta}$	BCZY:Zn	electrolyte	Department of Materials, Imperial College London
Er-doped strontium zirconate	$SrZr_{0.9}Er_{0.1}O_{3-\delta}$	SZE	electrolyte	AREVA NP
Rare-earth nickelate	$La_2NiO_{4+\delta}$	LNO	cathode	ICMCB, Université de Bordeaux
	$Pr_2NiO_{4+\delta}$	PNO	cathode	
	$Nd_2NiO_{4+\delta}$	NNO	cathode	
Lanthanum Strontium Cobalt Ferrite	$La_{0.6}Sr_{0.4}Co_{0.2}Fe_{0.8}O_{3-\delta}$	LSFC6428	cathode	ICMCB, Université de Bordeaux

According to previous studies performed at the laboratory, the protonation process as well as stability/ageing tests, were performed using the autoclave devices [83][1]. Structural and chemical characterization of pristine and protonated samples were investigated using several analysis techniques such as Raman (RS) and infrared (IR) spectroscopy, thermogravimetry (TG), thermal expansion (TE), X-ray and Neutron diffraction.

This manuscript is divided into seven chapters.

Chapter 1 will introduce the fundamentals of protonic species and proton conduction. This chapter will help us to describe the proton bonding and its localization in bulk and surface of solid-state frameworks. Proton content and proton conductivity measurement will be also briefly discussed.

In **Chapter 2**, fundamentals of perovskite-related oxide structure, phase transition and electrochemical properties will be concisely addressed. Raman and IR vibrational signatures of perovskite-based oxides and consequently mode assignments will be also described.

Chapter 3 presents the vibrational characterization of some secondary phases such as oxides, carbonates and hydroxides, expected to be formed in the corroded perovskite layer.

Chapter, 4 to 7 are in the form of published articles, as indicated below:

Chapter 4 "Combined bulk and surface analysis of the $BaCe_{0.5}Zr_{0.3}Y_{0.16}Zn_{0.04}O_{3-\delta}$ (BCZYZ) ceramic proton conducting electrolyte" focuses on the examination/differentiation of bulk and surface structural and chemical modifications of BCZYZ in its non-protonated and protonated forms. The importance of chemical and crystallographic purity as well as the choice of protonation conditions are disscused. The reseach paper was published in *Solid State Ionics* (A. Slodczyk, M.D. Shaop, **S. Upasen**, Ph. Colomban, J. Kilner, [88])

Chapter 5, "Structural stability of anhydrous proton conducting $SrZr_{0.9}Er_{0.1}O_{3-\delta}$ (SZE) perovskite ceramic vs. protonation/deprotonation cycling: Neutron diffraction and Raman studies" is a study of protonation/deprotonation treatment effect on structural and chemical

---

[1] *Treatment procedure and equipment details is described in Appendix A.*

stability of SZE perovskite-oxide ceramic. It was published in the *Journal of Physics and Chemistry of Solids* (A. Slodczyk, Ph. Colomban, **S. Upasen**, F. Grasset, G. André [89])

Chapter 6, "Protonation and structural/chemical stability of $Ln_2NiO_{4+\delta}$ ceramics vs. H_2O/CO_2: High temperature/water pressure ageing tests" – the $Ln_2NiO_{4+\delta}$ ceramics are considered as cathode materials. The protonation treatment under free- and CO_2-saturated water pressure and at 550°C offer accelerating aging tests of these ceramics. Consequently, it allows the choce ot the most pertinent composition of industrial application requiring a selected material with longer lifetime. This research was published in *Journal of Alloys and Compounds* (**S. Upasen**, P. Batocchi, F. Mauvy, A. Slodczyk, Ph. Colomban [90]).

Chapter 7: "Chemical and structural stability of $La_{0.6}Sr_{0.4}Co_{0.2}Fe_{0.8}O_{3-\delta}$ (LSCF6428) ceramic vs. medium/high water vapor pressure" - the LSCF6428 ceramic is another investigated cathode sample. The study allows determining the reactivity rate by comparison with nickelate candidates and search to identify the most stable ceramic for long duration energy application. This research was published in *Ceramics International*, actually in press (**S. Upasen**, P. Batocchi, F. Mauvy, A. Slodczyk, Ph. Colomban).

The **Conclusion** attempts to identify the most important results of the research undertaken and presents some **Perspectives** for future work.

Finally, an **Extended Summary** in the French language is provided.

References

[1]   Deploying renewables: best and future policy practice. International Energy Agency, Paris France, 2011.

[2]   Midium-Term Renewable Energy Marker Report 2014: market analysis and forecasts to 2020. International Energy Agency, Paris France, 2014.

[3]   Y. Krozer, Renewable Energy 50 (2013) 68.

[4]   B. K. Sovacool, Utilities Policy 17 (2009) 288.

[5]   A. Kumar, N. Kumar, P. Baredar, A. Shukla, Renewable and Sustainable Energy Reviews 45 (2015) 530.

[6]   R. García, C. Pizarro, A. Álvarez, A. G. Lavín, J. L. Bueno, Fuel 148 (2015) 152.

[7]   T. Hendricks, W. Choate, Engineering scoping study of thermoelectric generator systems for industrial waste heat recovery. Industrial Technologies Program (ITP), Technical Report. Pacific Northwest National Laboratory (PNNL) and BCS, 2006.

[8]   A. Peer, G. Prabhakar, Journal of Energy Technologies and Policy 2 (2012) 39.

[9]   R. G. M. Crockett, M. Newborough, D. J. Highgate, Solar Energy 61 (1997) 293.

[10]   Rohan, Hydrogen generation market worth $138.2 billion by 2019. Markets and Markets, September 2014.

[11]   I. K. Kapdan, F. Kargi, Enzyme and Microbial Technology 38 (2006) 569.

[12]   ZSW, World's largest Power-to-Gas plant for generating methane enters operation - stage prior to industrial application achieved. ZSW, Stuttgart, Germany, 2012.

[13]   F. Orecchini, A. Santiangeli, International Journal of Hydrogen Energy 36 (2011) 8126.

[14]   B. Zakeri, S. Syri, Renewable and Sustainable Energy Reviews 42 (2015) 569.

[15]   S. A. Mahmoud, B. S. Mohamed, A. S. El-Tabei, M. A. Hegazy, M. A. Betiha, H. M. Killa, E. K. Heikal, S. A. K. Halil, M. Dohium, S. B. Hosney, Energy Procedia 46 (2014) 227.

[16]   Z. Wang, C. J. Liu, Nano Energy 11 (2015) 277.

[17]   J. Cot-Gores, A. Castell, L. F. Cabeza, Renewable and Sustainable Energy Reviews 16 (2012) 5207.

[18]   P. Millet, S. Grigoriev, in: P. M. Diéguez, L. M. Gandía, G. Arzamendi, (Eds.), Renewable Hydrogen Technologies, Elsevier, Amsterdam, 2013, p. 19.

[19]   D. M. F. Santos, C. A. C. Sequeira, J. L. Figueiredo, Química Nova 36 (2013) 1176.

[20]   A. Nechache, M. Cassir, A. Ringuedé, Journal of Power Sources 258 (2014) 164.

[21]   K. A. Adamson, in: K. A. Adamson (Ed.), Stationary Fuel Cells, Elsevier, Oxford, 2007, p. 7.

[22]   A. B. Stambouli, E. Traversa, Renewable and Sustainable Energy Reviews 6 (2002) 433.

[23]   R. Bhandari, C. A. Trudewind, P. Zapp, Journal of Cleaner Production.

[24]   T. Elmer, M. Worall, S. Wu, S. B. Riffat, Renewable and Sustainable Energy Reviews 42 (2015) 913.

[25]   H. H. Mobius, Journal solid state elcectrochemistry 1 (1997) 2.

[26]   N. Mahato, A. Banerjee, A. Gupta, S. Omar, K. Balani, Progress in Materials Science.

[27]   Water Electrolysis and Renewable Energy Systems. Fuel Cell Today, Hertfordshine, UK, 2013.

[28]   S. M. J. Zaidi, in: T. Mastsuura (Ed.), Polymer Membranes for Fuel Cells, Springer Science + Bussiness Media, LLC, 2009, p. 7.

[29]   S. de Souza, S. J. Visco, L. C. De Jonghe, Solid State Ionics 98 (1997) 57.

[30]   N. W., Z electrochemistry 6 (1899) 40.

[31]   S. W., Wiss Veroff Siemens-Werke 14 (1935) 1.

[32]   W. C., Naturwissenschaften 31 (1943) 265.

[33]   E. Baur, H. Preis, Z Elektrochem 44 (1938) 695.

[34]   E. Baur, H. Preis, Z Electrochem 43 (1937) 727.

[35]   B. Zhu, International Journal of Energy Research 33 (2009) 1123.

[36]   X. X. Guo, I. Matei, J. S. Lee, J. Maier, Applied Physics Letters 91 (2007) 13102.

[37]   E. Fabbri, D. Pergolesi, E. Traversa, Chemical Society Reviews 39 (2010) 4355.

[38]   H. Iwahara, Solid State Ionics 86–88, Part 1 (1996) 9.

[39]   A. Q. Pham, B. W. Chung, R. S. Glass, Protective coating for fuel cell interconnects. Google Patents, 2002.

[40]   W. G. Coors, Journal of Power Sources 118 (2003) 150.

[41]   L. Bi, S. Boulfrad, E. Traversa, Solid State Ionics 275 (2015) 101.

[42]   K. W. Harrison, R. Remick, G. D. Marin, A. Hoskin, Hydrogen Production: Fundamentals and case study summaries, the 18th World Hydrogen Energy Conference, Germany, 2010.

22

[43] G. Tsekouras, D. Neagu, J. T. S. Irvine, Energy & Environmental Science 6 (2013) 256.

[44] L. Bi, S. Boulfrad, E. Traversa, Chemical Society Reviews 43 (2014) 8255.

[45] B. Sala, F. Grasset, O. Lacroix, A. Sirat, K. Rahmouni, M. Keddam, H. Takenouti, D. Goeuriot, B. Bendjeriou, Ph. Colomban, Method for generating hydrogen and oxygen by steam electrolysis. Google Patents, 2014.

[46] F.G. Naterer, I. Dincer, C. Zamfirescu, hydrogen production from nuclear energy, Springer-Verlag London, 2013.

[47] Z. Wang, G. F. Naterer, in: P. V. Tsvetkov (Ed.), Nuclear Power - deployment, operation and sustainability, InTech, Rijeka, Croatia, 2011, p. 447.

[48] D. P. Fernandez, A. R. H. Goodwin, E. W. Lemmon, J. Sengers, R. C. Williams, Journal of Physical and Chemical Reference Data 26 (1997) 1125.

[49] T. Yamaguchi, Journal of Molecular Liquids 78 (1998) 43.

[50] T. M. Seward, E. U. Franck, Berichte Der Bunsen-Gesellschaft-Physical Chemistry Chemical Physics 85 (1981) 2.

[51] M. L. Japas, E. U. Franck, Berichte Der Bunsen-Gesellschaft-Physical Chemistry Chemical Physics 89 (1985) 1268.

[52] E. Vollestad, H. Zhu, R. J. Kee, Journal of the Electrochemical Society 161 (2014) F114.

[53] Ph. Colomban, Materials Science Forum 251-254 (1997) 833.

[54] Ph. Colomban, S. Cherifi, G. Despert, Journal of Raman Spectroscopy 39 (2008) 881.

[55] P. Kritzer, The Journal of Supercritical Fluids 29 (2004) 1.

[56] P. Kritzer, N. Boukis, E. Dinjus, The Journal of Supercritical Fluids 15 (1999) 205.

[57] S.P. Huang, K. Daehling, T.E. Carleson, P. Taylor, C. Wai, A. Propp, Acs Symposium Series 406 (1989) 276.

[58] L. B. Kriksunov, D. D. Macdonald, Journal of the Electrochemical Society 142 (1995) 4069.

[59] L. B. Kriksunov, D. D. Macdonald, Corrosion testing and prediction in SCWO environments, American Society of Mechanical Engineers, United States, 1995.

[60] D. M. Harradine, S.J. Buelow, P. C. Dellorco, R. B. Dyer, B. R. Foy, J. M. Robinson, J. A. Sanchez, T. Spontarelli, J. D. Wander, Hazardous Waste & Hazardous Materials 10 (1993) 233.

[61]   W. D. Kevin, H. S. Richard, D. A. Hazlebeck, J. R. Adele, Innovations in Supercritical Fluids, American Chemical Society, 1995, p. 313.

[62]   Ph. Colomban, O. Zaafrani, A. Slodczyk, Membranes 2 (2012) 493.

[63]   A. Slodczyk, O. Zaafrani, M. D. Sharp, J. A. Kilner, B. Dabrowski, O. Lacroix, Ph. Colomban, Membranes 3 (2013) 311.

[64]   A. Slodczyk, M. Limage, Ph. Colomban, O. Zaafrani, F. Grasset, J. Loricourt, B. Sala, Journal of Raman Spectroscopy 42 (2011) 2089.

[65]   Ph. Colomban, C. Tran, O. Zaafrani, A. Slodczyk, Journal of Raman Spectroscopy 44 (2013) 312.

[66]   A. S. Nowick, Y. Du, Solid State Ionics 77 (1995) 137.

[67]   T. Norbya, Solid State Ionics 40–41, Part 2 (1990) 857.

[68]   Ph. Colomban, Proton Conductors: Solid, Membranes and Gels - Materials and Devices, Cambridge University Press, Cambridge, 2011.

[69]   K. D. Kreuer, Solid State Ionics 136–137 (2000) 149.

[70]   W. Münch, G. Seifert, K. D. Kreuer, J. Maier, Solid State Ionics 86–88, Part 1 (1996) 647.

[71]   W. Münch, G. Seifert, K. D. Kreuer, J. Maier, Solid State Ionics 97 (1997) 39.

[72]   W. Münch, K. D. Kreuer, G. Seifertli, J. Majer, Solid State Ionics 125 (1999) 39.

[73]   W. Münch, K. D. Kreuer, G. Seifert, J. Maier, Solid State Ionics 136–137 (2000) 183.

[74]   K. D. Kreuer, S. Adams, W. Münch, A. Fuchs, U. Klock, J. Maier, Solid State Ionics 145 (2001) 295.

[75]   F. Forrat, G. Dauge, P. Trevoux, G. Danner, M. Christan, Acad. Sci. Paris 259 (1964) 2813.

[76]   H. Iwahara, T. Esaka, H. Uchida, N. Maeda, Solid State Ionics 3–4 (1981) 359.

[77]   A. Slodczyk, Ph. Colomban, N. Malikova, O. Zaafrani, S. Longeville, J. M. Zanotti, O. Lacroix, B. Sala, Solid State Ionics 252 (2013) 7.

[78]   A. Slodczyk, Ph. Colomban, S. Willemin, O. Lacroix, B. Sala, Journal of Raman Spectroscopy 40 (2009) 513.

[79]   A. Slodczyk, Ph. Colomban, D. Lamago, G. Andre, O. Zaafrani, O. Lacroix, A. Sirat, F. Grasset, B. Sala, Journal of Materials Research 27 (2012) 1939.

[80]   Ph. Colomban, A. Slodczyk, D. Lamago, G. Andre, O. Zaafrani, O. Lacroix, S. Willemin, B. Sala, Journal of the Physical Society of Japan 79 (2010) 1.

24

[81]   A. Slodczyk, Ph. Colomban, G. Andre, O. Zaafrani, F. Grasset, O. Lacroix, B. Sala, Solid State Ionics 225 (2012) 214.

[82]   Ph. Colomban, Aneta Slodczyk, Oumaya Zaafrani, Olivier Lacroix, Johan Loricourt, Frederic Grasset and Beatrice Sala, MRS proceeding 1309 (2011).

[83]   O. Zaafrani, Dotoral thesis "Protonation, distorsions structurales et espèces protoniques dans des pérovskites lacunaires", Université Pierre et Marie Curie, Paris, France, 2010.

[84]   B. Sala, F. Grasset, O. Lacroix, A. Sirat, K. Rahmouni, M. Keddam, H. Takenouti, D. Goeuriot, B. Bendjeriou, Ph. Colomban, Procédé de génération d'hydrogène et d'oxygène par électrolyse de vapeur d'eau, Google Patents, france, 2013.

[85]   A. Slodczyk, Ph. Colomban, O. Zaafrani, O. Lacroix, J. Loricourt, F. Grasset, B. Sala, MRS proceeding 1309 (2011).

[86]   J. Dailly, S. Fourcade, A. Largeteau, F. Mauvy, J. C. Grenier, M. Marrony, Electrochimica Acta 55 (2010) 5847.

[87]   F. Mauvy, C. Lalanne, J. M. Bassat, J. C. Grenier, H. Zhao, P. Dordor, P. Stevens, Journal of the European Ceramic Society 25 (2005) 2669.

[88]   A. Slodczyk, M. D. Sharp, S. Upasen, Ph. Colomban, J.A. Kilner, Solid State Ionics 262 (2014) 870.

[89]   A. Slodczyk, Ph. Colomban, S. Upasen, F. Grasset, G. André, Journal of Physics and Chemistry of Solids 83 (2015) 85.

[90]   S. Upasen, P. Batocchi, F. Mauvy, A. Slodczyk, Ph. Colomban, Journal of Alloys and Compounds 622 (2015) 1074.

CHAPTER 1

"Protonic species and proton conduction"

Chapter 1

Protonic species and proton conduction

In this chapter, we will first discuss the fundamentals of ionic and protonic conduction, in relation to solid chemistry defects. Then, we will address the protonic species throughout hydrogen bonds and mechanism/model of proton delocalization. Discrimination between bulk and surface protonic species in solid-state frameworks, their impact on thermal stability and phase transitions of perovskite frameworks as well as proton content measurement will also be explained. Finally, we will briefly discuss different types of proton conductors.

1.1 Fundamentals of ionic and proton conductions

Fundamentally, "Ionic conduction" is defined as the long range motion of an ion from one site to another through defects or specific pathway in a solid lattice or in an aqueous/ionic solution [1]. Alternatively, the term of "Proton conduction" is commonly employed when protons are transferred.

For ionic or protonic species with an activated diffusion, the conductivity (σ) is proportional to the product of the self-diffusion coefficient (D) and the concentration (C) of mobile species [2]. Hence, the conductivity (σ) can be expressed through the Nernst-Einstein relation as follows:

$$\sigma = \left(DC \cdot e^2\right)/kT \qquad \qquad \text{... (eq. 1.1)}$$

Since both D and C value are thermally activated, σ can be presented in the following way:

$$\sigma T = \left[\frac{D_0 C_0 \cdot e^2}{k}\right]\left[\exp-\frac{E_f + E_d}{kT}\right] = \sigma_0 \exp\frac{E_a}{kT} \qquad \qquad \text{... (eq. 1.2)}$$

where E_f and E_d are enthalpies of formation and diffusion of charge carriers, respectively, E_a is the activation energy of conduction and σ_0 is the associated pre-exponential factor.

The conductivity of a material is commonly measured at high temperature in isotherms or isobars using direct methods such as AC2. At higher frequency, the conductivity is

determined using microwave relaxation and vibrational spectroscopy (THz range). As the frequency increases, the diffusion length decreases and the mobile species meet the discontinuity of the (periodic) potential. Consequently, the frequency-dependent monotonic behavior will disappear and different relaxations will determine the electric behavior.

In Infrared (IR) spectroscopy, the absorption coefficient $\alpha(\omega)$ is related to $\sigma(\omega)$ by [3]:

$$\alpha(\omega) = \frac{4\pi\sigma(\omega)}{nc} \qquad \text{… (eq. 1.3)}$$

where n is the refractive index and c is the velocity of light. The scattered intensity $I(\omega)$ measured *in* Raman spectroscopy (RS) is also related to frequency dependent conductivity by [4]:

$$\sigma(\omega) \propto \frac{\omega I(\omega)}{n(\omega) + 1} \qquad \text{… (eq. 1.4)}$$

where $n(\omega)$ is the Bose-Einstein population function.

According to their conductivity value, ionic compounds such as halides, sulfides, oxides etc. can be divided into three major groups [5]: i) insulators present the ionic conductivity lower than 10^{-10} $\Omega^{-1}cm^{-1}$ at high temperature (500-1000C). and very large activation energy (>1 eV); ii) ionic conductors (IC) in which the presence of point defects leads to a conductivity up to 10^{-5} $\Omega^{-1}.cm^{-1}$ at similar temperature and activation energy between 0.5 and 1 eV; and iii) superionic conductors (SIC) exhibit high conductivity (>10^{-4} $\Omega^{-1}.cm^{-1}$) and a low activation energy (<0.3eV). Thus, the main difference between IC and SIC groups concerns the activation energy (E_a): lower than 0.3 or even 0.2 eV for SIC group. Consequently temperature increase does not exert a significant effect on conductivity.

1.2 Defect chemistry

As mentioned above, the diffusion or conductivity (diffusion of charged species) in solids takes place because of defects in densely packed framework or because the availability of many empty sites along the 1D, 2D or 3D pathway of poorly packed framework. Indeed, defects determine a number of properties of crystalline solid [6]. The defects present in the

ionic solid can be considered as imperfections or deviations from an ideal structure. In other words, the ideal crystal structure is used as the reference state, and any deviation from this ideal state is termed as a defect. There are different types of structural defects: point defects, line defects, or plane defects. Furthermore, the point defects, especially related to this study, will be described.

Figure 1.1a illustrates point defects such as vacancies and interstitial atoms [7]. In the case of pure material, without any substitution, vacancies may be created by the lack of an atom. When, an atom jumps to a new adjoining position on the surface, it leaves behind a vacancy. A host atom in bulk diffuses to fill the vacancy thereby displacing the vacancy towards the bulk. An interstitial atom occupies the vacancy between the (bigger) host atoms. Vacancies and interstitial atoms appearing in a pure material are defined as "intrinsic". However, the point defects present in a crystal lattice can also be caused by foreign atoms such as subtituent/dopant (intentionally added to a material) and impurities (uncontrolled). These are called "extrinsic" point defects. In both intrinsic and extrinsic defects, the vacancies appear to maintain electro neutrality.
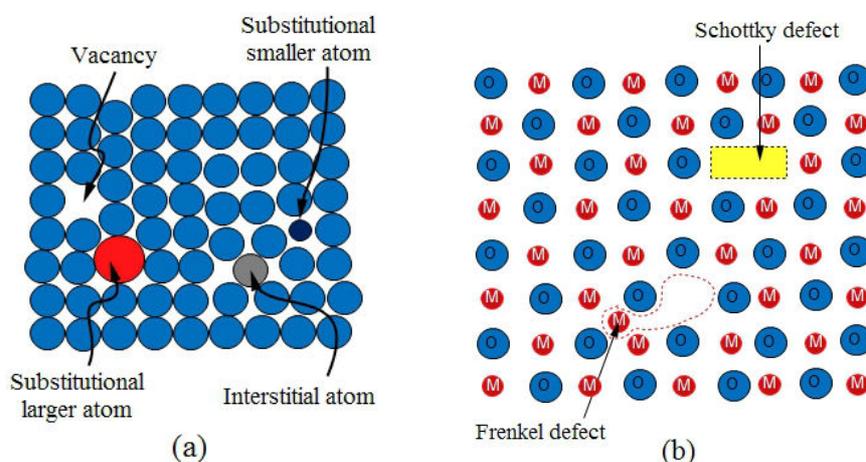
Figure 1.1: *Scheme of (a) Point defects (b) Schottky and Frenkel defect forms in metal oxides solids (MO).*

For example, in the case of metal oxide solid (MO), Fig. 1.1b, the most common defects are the so-called Schottky and Frenkel ones. These two defects can be written using Kröger's notation:

$$M_M + O_O \Leftrightarrow V_M + V_O \left(Schottky\ defect\right) \qquad \dots \text{(eq. 1.5)}$$

$$M_M \Leftrightarrow V_M + M_i \left(Frenkel\ defect\right) \qquad \dots \text{(eq. 1.6)}$$
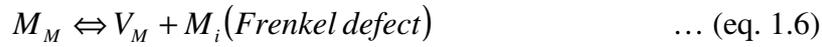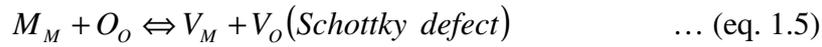
where M_M is atom M on site M, O_O is atom O on site O, V_M is vacant site M, V_O is vacant site O and M_i is atom M on interstitial site. The excess charge associated with an M vacancy is balanced if there is an O vacancy nearby, called a *Schottky* defect. Alternatively, the charge in balance caused by the vacancy can be corrected by adding an interstitial of the same species; an M vacancy is compensated by an M interstitial, called a *Frenkel* defect.

The formation of defects and equilibrium reactions in MO solid can be charged positively (•), negatively, (′) or they can remain neutral (x), giving rise to electronic defects, e.g.

$$V_M{}^x \Leftrightarrow V_M' + h^\bullet \qquad \dots \text{(eq. 1.7)}$$

where h represents an electron hole.

Considering metal hydroxide solids $M(OH)_2$ i.e. $Mg(OH)_2$, $Cd(OH)_2$, the defects of OH^x in such host lattice framework can be predicted: excess protons ($H^\bullet$) and proton vacancies (O').

$$\left[OH\right]^x = H^\bullet + O' \qquad \dots \text{(eq. 1.8)}$$

The defect structures in both MO and $M(OH)_2$ compounds contain equilibrium concentrations of negatively and positively charged point defects. These are a result of internal equilibrium in the crystal and do not involve the surrounding reactions. In addition, if such metal oxide is exposed to a hydrogen-rich atmosphere, oxides may form extrinsic hydrogen defects. For example, in the case of interstitial protons ($H_i^\bullet$) from water vapor which is considered in this thesis, the proton defect reaction can be written [8]:

$$\frac{1}{2} H_2 O \left(gas\right) \Leftrightarrow H_i^\bullet + e' + \frac{1}{4} O_2 \left(gas\right) \qquad \dots \text{(eq. 1.9)}$$
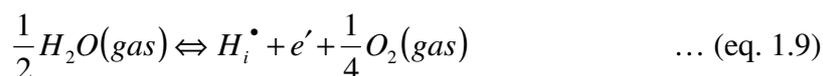
Oxygen vacancies in metal oxides are created when oxygen atom in regular lattice sites depart for the surrounding in gas phase or by substitution of a cation M^{n+} with a cation M^{p+}, p<n, and then occupied by protons. It may be expressed as [9]:

$$H_2O(g) + V_O^{\bullet\bullet} + O_O^x = 2OH_O^{\bullet} \qquad \text{...(eq. 1.10)}$$

The introduction of protonic defects in oxides submitted to water-containing atmosphere has been intensively reviewed by Colomban and Novak [8].

Protonic species

Proton, noted as H^+, without electrons outside the nucleus is a unique species among different ions. As noted previously, it has a very small size, intermediate between the electron and Li^+ ion (radius of the order 10^{-13} cm, as compared with 10^{-8} cm for all other ions) [10]. Because of these particular features proton can exert an enormous polarizing power on any molecule or ion in its neighborhood. In other words, a proton is very reactive with its environment. Generally protons can be distinguish as:

i. The proton that penetrates covalence sphere of acceptor ion. In most caseshydrogen is normally covalently attached to one atom, a proton donor, leading to common ions: hydroxyl group (OH^-) with oxygen atom, oxonium (H_3O^+) with water molecule, ammonium (NH_4^+) with ammoniac, hydrazinium ($N_2H_5^+$) with hydrazine, etc. All these species easily solved themselves. Consequently they give more complex entities to form $[H(H_2O)]_n^+$, or "cationic proton hydrates" [11].

ii. The proton that interacts with two acceptor ions creates the "hydrogen bonds". The hydrogen bonding occurs when two electronegative atoms, such as nitrogen and/or oxygen, interact with the same hydrogen giving rise to following entities: O-H…O or N-H…O. The proton (H^+) maybe centered in the hydrogen bond (Fig. 1.2b) or located closer to one of the acceptors (Fig. 1.2a)

The corresponding potential energy well of hydrogen bonds (Fig. 1.2d) is very anharmonic. Consequently it plays an important role on thermal expansion of a material and its vibrational signature. In the case of Brönsted AH acid, when a molecule is engaged in an A-H…B hydrogen bond, the basic group represents a supplementary attraction potential for the proton and can create a second (II) potential well, as dashed curves in Fig. 1.2d. The potential function of the free AH group is modified by the potential B: the A-H distance increases while the A...B distance decreases with respect to the sum of the Van der Waals

33

radii of A and B atoms. On the other hand, the potential well (I) for AH group becomes broader and the vibrational levels become closer. Consequently, the shift of AH stretching band leads to lower frequencies observed by Infrared (IR) and Raman spectroscopy. Moreover, the AH stretching absorption bands are also characterized by an increase of intensity and band breadth on hydrogen bonding.

iii. In rare cases a proton interacts with more acceptors and becomes the "ionic or free proton" Here the lengthening of the bond gives rise to some ionic character with long distance coulombic interactions. In addition, the hydrogen species free of any covalent bonding may interact with more than 2 acceptors (Fig. 1.2c) [12-14].
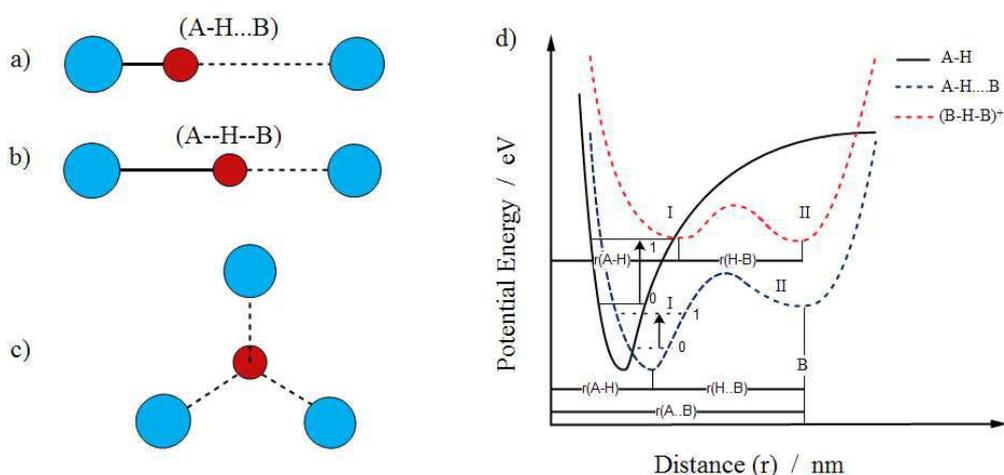
Figure 1.2: *Schematic of a single donor acceptor of hydrogen interaction (**a-b**), of an ionic proton (**c**); and **d** the potential energy well of proton involved in the A-H..B hydrogen bond [12,15], Note: the red ball represents proton.*

Different types of hydrogen bonds may be identified, i.e. weak, moderate and strong, according to the shape of the potential curve of the proton of an A-H…B system or the position of proton [16]. Asymmetric AH…B system, as blue dashed curve in Fig. 1.2d, contains a weak or moderate hydrogen bond. The potential barrier separating two minima is high and the proton is always closer to one atom than to the other (A or B). Red dashed curve (1.2d) is characteristic for the (A…H…B) system containing strong hydrogen bonds. In such a case, potential barrier is small with symmetric double minima. Table 1.1 gives approximate classification of O-H…O hydrogen bond system, the most common in protonic conductors.

Table 1.1: *Approximate classification of O-H…O hydrogen bonds [16].*

Hydrogen bond	R(O..O) distance A°	Wavenumber*/Examples	
Weak	2.70	>3200	H$_2$O (ices, hydrates)
			R-OH (alcohols, phenols)
Moderate	2.70-2.60	3200-2800	RCOOH (acids)
Strong	2.60-2.40	2800-700	MH (RCOO)$_2$ (acid salts)

* The profile and bandwidth are also modified, the bands broaden and exhibit components (so called ABC components) when the H-bond is strengthened.

The distance of O…O (in Table 1.1) shows the distinction of hydrogen bond strength - weak (long) and strong (short). In addition, empirical relationship between O-H stretching frequencies and O…O distances is used to predict the hydrogen bond strength. However the band broadening could make the measurement difficult and no IR or Raman features are recorded for ionic proton. Only incoherent neutron scattering can be used to characterize these protonic features [17]. With respective variation of 10, 60 and 120 cm^{-1}/pm, the hydrogen bond strength changes from weak to medium-strong and strong, respectively [15]. It means that the variation of wavenumber with O..O distance is much higher for strong hydrogen bonds.

1.2.1   Proton transfer

The energy potential barrier determines the proton transfer. The proton can move easily (tunneling) only when the energy barrier between donor and acceptor sites is low [18].

Freund' study of Mg(OH)$_2$ offers a very didactic example [18]. The energy potential curve of hydrogen bond in Mg(OH)$_2$ was ascertained from the optical transition energies E_{0n} of the O-H stretching mode from zero level to the *n*-th excited level using the *Morse potential* equation [17]. The experimental results helped to calculate the dissociation energy (D) of free OH$^-$ (OH$^-$ = O^{2-} + H$^+$), i.e. 4.70 eV, which was similar to that value derived from the thermodynamic data (4.71 eV). Corresponding to the vibrational stretching excitation of the O-H oscillator, the O-H stretching peaks varied as a function of transition energy (E), and the observed overtones were then given by $E_{0n} = E_n - E_0$, with n=1, 2, 3…. In addition, the value

for E_{0n} was obtained from overtones of the O-H stretching mode which occurred at approximately twice, thrice, four times the frequency of the O-H fundamental peak (Fig. 1.3a). Note, the fundamental O-H peak is very narrow, and detected near the high wavenumber, 3700 cm^{-1} for IR and 3655 cm^{-1} for Raman.
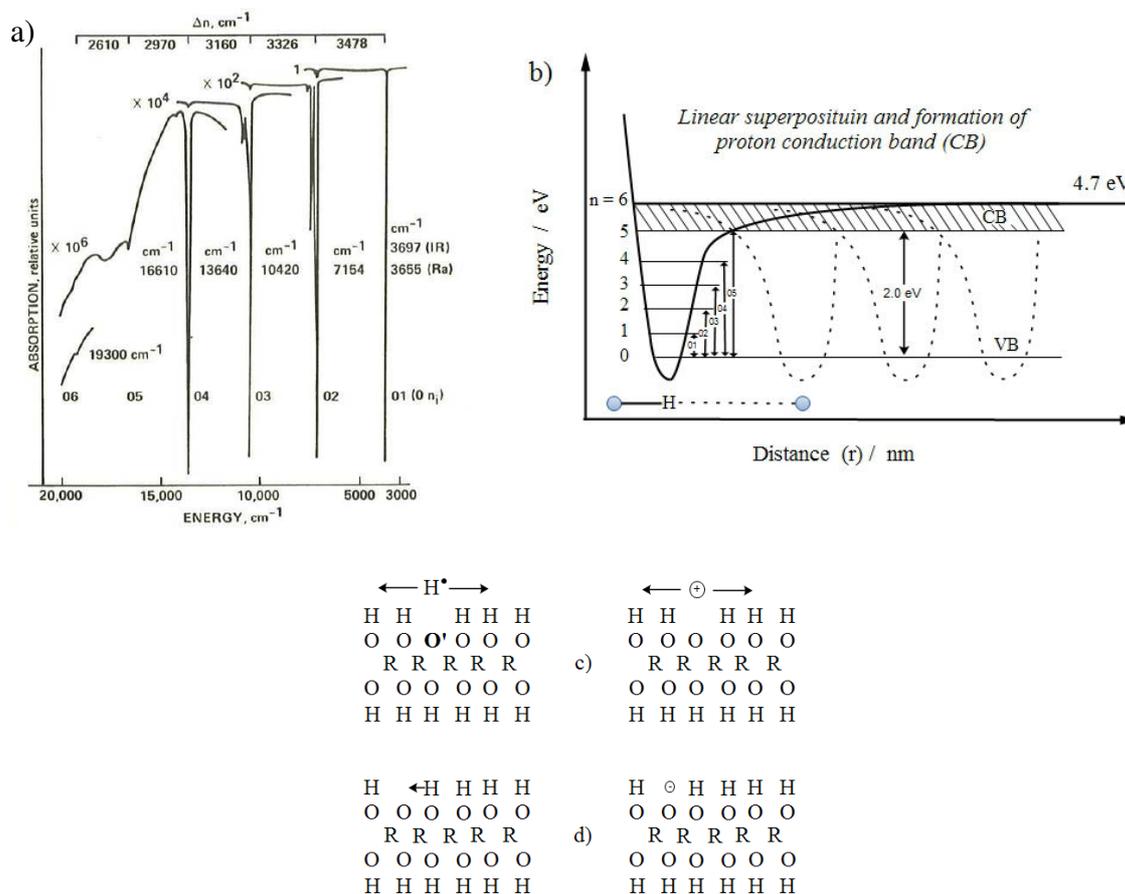
Figure 1.3: *a) overtone series of the stretching mode in Mg(OH)$_2$ b) Morse potential well of Mg(OH)$_2$ and its linear superposition schematically presented the formation of proton conduction band (CB) above the fifth excited level, c) delocalization of proton in CB, d) diffusion of a proton vacancy [18].*

Figure 1.3b shows an interesting feature, namely that the overtone sequence appears to come to an abrupt end above the 5th exited level. It gives a linear array of OH$^-$ ions separated by the same distance as in the Mg(OH)$_2$ structure. In fact, a series of deep wells, where the protons are located on the 0 level, is defined as the valence band (VB). Above the 05th transition with energy of 2.0 eV, the superposition produces a continuum energy region, defined as a proton conduction band (CB).

The existence of CB leads to the possibility of proton (H^+) conductivity measurement. It implies that protons that reach this high-energy state cease to be bound to their parent O^{2-}, and exhibit '*delocalization form/state*', as shown in Fig. 1.3c. The protons in excess ($H^{\bullet}$) are highly mobile charge carriers. Proton vacancy carries a negative charge. Furthermore, the diffusion of proton vacancy from left to right occurs because a proton of neighboring OH^- jumps from right to left as shown in Fig. 1.3e. Note, the proton jump in this $Mg(OH)_2$ case occurs within the four intermediate energy levels and/or energy of 0.4 eV.

1.2.2   Mechanism and model of proton transfer

Fundamentally, a proton is transferred through a solid/liquid framework in one of two distinct ways:

i)   By "vehicle mechanism" ("V-mechanism"), the proton is carried by a molecule such as H_2O and gives rise to H_3O. It is also rides on a carrier molecule of type such as NH_4^+. For example, H_3O^+ is the mobile species in β-alumina like open layered structure [19]. The conduction depends on an excess of available sites. In β-alumina, oxonium ions occupy only Beevers-Ross (BR) sites ($\sigma_{RT} \sim 10^{-11}$ $\Omega^{-1}.cm^{-1}$ and $E_\sigma = 0.8$ eV) while in β"-alumina, oxonium ions can occupy both prismatic and tetrahedral sites ($\sigma_{RT} \sim 10^{-9}$ $\Omega^{-1}.cm^{-1}$ and $E_\sigma = 0.6$ eV).

ii)   By "Grotthuss mechanism" ("G-mechanism"), the proton jumps from a donor to a suitably placed acceptor molecule, for example from H_3O^+ to H_2O or from H_2O to OH^- as in Hydrogen Uranyl Phophate hydrate (HUP) and in water [19,20] This mechanism involves (a) displacement of H^+ along a hydrogen bond, with a transfer energy barrier (E_{bar}) and (b) transport of H^+ from this hydrogen bond to the next, with a bond breaking energy barrier E_{bond}. Diffusion of the water molecule and ions also takes place and the total conductivity is the superimposition of different mechanisms.

Beside the mechanism of proton transfer, the proton conductivity models were discussed by Colomban et al. [21]. Three main types of theoretical description can be made :

i)   *"Liquid-like/Viscous models"* for highly disordered solid electrolytes. These models are applicable when a proton hops through membranes such as glass and polymer. The corollary is that the conductivity increases when the viscosity decreases [21] and more complex laws than Arhenius' law are observed.

ii)   "Hopping models". In these models the proton spends most of its time executing relatively low-amplitude vibrations in equilibrium lattice positions, and spends a very short time in jumping among permitted sites.

iii)   "Lattice gas model". When the temperature is sufficiently high and allows the proton to reach the continuum, the species diffuses without strong interaction with the (low) potential wells. The proton is delocalized over many sites.

In the present study, with a very stable host framework (melting temperature > 1500°C) and a low concentration of proton [2,17], the lattice gas model is considered. As presented in figure 1.4, generally, five different proton motion types are schematized: a) tunneling, b) jumping, c) ballistic or Kramer's regime, d) liquid-like diffusion and e) gas-like motion. The hydrogen normally hops from one site to another by thermal activation. This hopping activity requires sufficient screening between ions that host lattice potential to become dominant. Consequently, it ensures that the two ions do not occupy the same lattice site.
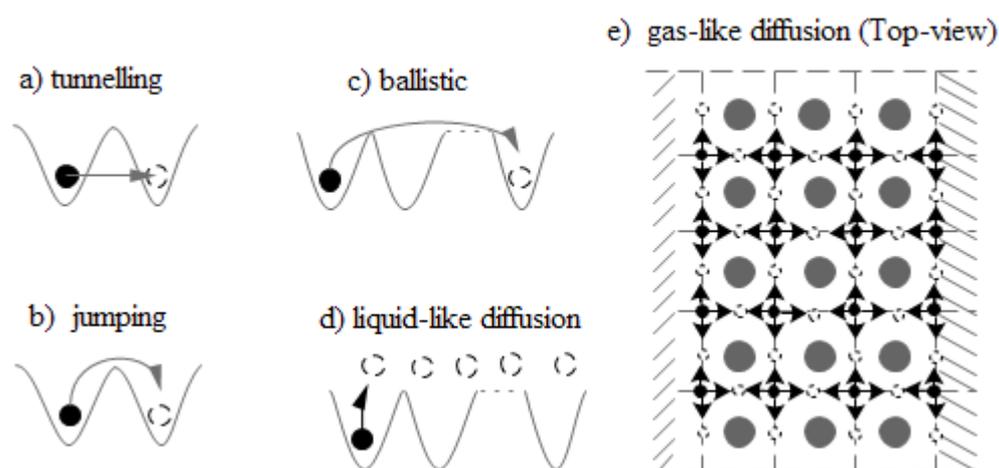
Figure 1.4: *Representation of different behavior of proton delocalization described by lattice gas models (Note: • symbol represents protonic species, H⁺).*

Different assumptions of slow or fast movement of distinct protonic behavior, as presented in Fig. 1.4, are possible. In the case of short timescale, the species oscillates on a given site, while on long timescale, the proton diffuses. In fact, the slow or fast systems, yielding different regimes (hopping and diffusive), depend on two critical parameters: i) temperature versus hopping potential height ($T/\Delta V$) and ii) γ-damping to ω_0-vibrational frequency ratio (γ/ω_0).

The proton conduction mechanism is significantly related to the definition of the local (meV energy range) and long range diffusion (μeV) proton motions [14]. Several studies using elastic and quasi-elastic neutron technique as a function of temperature and momentum transfer have been published for different perovskite-type compounds [22-24]. Hempelmann et al. [25] and Matzke et al. [26] postulate that the proton diffusion in Sr-cerate consists of a sequence of free diffusion and trapping/escape events, according to the common ion jump model. The mean jump length at 0.4 nm, is close to the unit-cell parameter value The mean distance between the traps ~1.7 nm is close to the distance between substituents. Previous studies [27,28] suggested that in the case of highly dense $BaZr_{0.97}Yb_{0.03}O_{3-\delta}H_{0.0001}$ the fastest local motion of bulk proton observed at 500-600°C, is associated with the largest width of the quasi-elastic peak, consequently with subtle structural modifications and energy activation conductivity changes.

1.3 Protons in bulk and surface of solid-state frameworks

As discussed in section 1.2, the defects introduced from a water/hydrogen containing atmosphere, yield interstitial proton ($H_i^\bullet$), eq. 1.10. The interstitial protons can be incorporated with the host lattice defects i.e. oxygen vacancy.

Fig. 1.5 presents the schematic of metal oxides (MO_x) with the hydrogen defects, bonded or not to oxygen ions detected on a material surface and in the bulk. Presumption product is expected to form either as "hydrogen bronzes" (H_xMO_n) i.e. $H_{0.23}VO_{2.5}$, $H_{0.34}MoO_3$, $H_{0.33}UO_{2.67}$, or "oxy-hydroxides" ($MO_{n-x}(OH)_x$) i.e. $Al(OH)_3$, $In(OH)_3$, $VO(OH)_2$ [29].
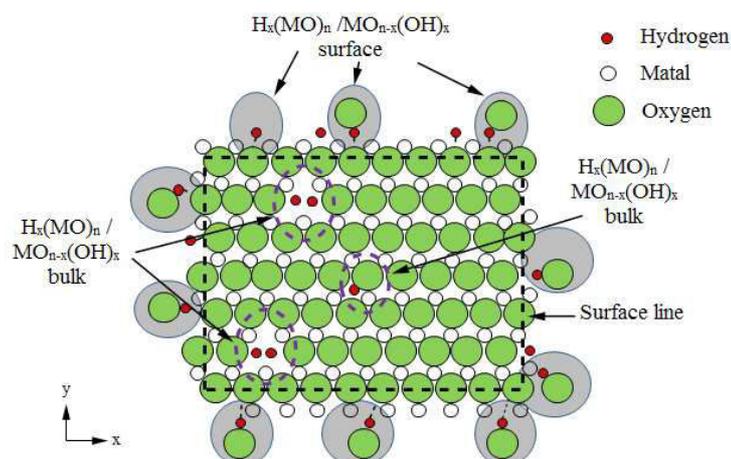
Figure 1.5: *H^+ defect under water vapor pressure interacting on surface and bulk of metal oxide $(MO)_n$ framework [29].*

The water, in gas-phase, dissociates itself at the solid surface into a hydroxide ion (OH^-) and a proton (H^+). Hydroxide ion, or protonic species, interact initially with oxygen defects on ionic-host surface lattice and the proton, forming a covalent bond with the host lattice oxygen, implied as 'surface proton". Although the surface species are usually observed in form of undesirable second phases i.e. hydroxides and/or carbonates, such surface proton materials can also be considered as proton conductors. Since the aim is to enhance proton conduction, an introduction of the bulk protons must be deployed. The presence of bulk defects facilitates the migration of protonic species or vacancies, called "bulk proton". The diffusion is associated with the local perturbation of the bulk structure related to the occurrence of protonic conductivity for example $MnO_{1.78}.nH_2O$ gives $\sigma_{RT} \sim 10^{-5} \; \Omega^{-1}cm^{-1}$ [30].

In order to understand the properties of proton conductor, it is important to differentiate between surface and bulk protonic species. Colomban et al. [14] have suggested a method that compares materials having very different surface to volume ratio (*S/V*). The ultra dense single crystals/ ceramics have very low porosity, and the *S/V* ratio is low. On the contrary, ultra fine powders and highly porous materials can have a higher *S/V* ratio.

Another approach to distinguish between the bulk and the surface species is based on the different energies required for the elimination of proton species located in different lattice sites. The possible proton locations/sites are [14]: (i) species adsorbed at the external surface, (ii) adsorbed at the surface of internal pores, (iii) chemically bonded at the external or pore

surface, and (iv) protons present in the bulk structure. Such varied proton locations formed instable species with difference of bonding energy. Thermal treatments at temperatures above the bonding energy, specifically eliminate the instable species. These are addressed in the next section.

1.4 Thermal stability and phase transition

The thermal stability of proton conducting material is directly related to the nature of the protonic species and to the strength of the H-bond. Table 1.2 summarizes the typical conducting protonic species and their stability range [12]. The variation of the bonding strength between a proton and its environment plays an important role. The proton conducting gels have the weakest H-bond strength and the lowest thermal stability (<80°C). For example, hydrated phosphotungstic ($H_3PW_{12}O_{40}.29H_2O$, PWA) and hydrated phosphomolibdic ($H_3PMo_{12}O_{40}. 30H_2O$) acid, exhibit dehydration level steps at ~21, 12, 6 (>60-80°C) and 0 H_2O molecules (>250°C) [12]. The H_3O^+ ions lose their water at ~200-400°C as a function of the host framework. In the case of "ionic" protons and hydroxyl ions, it remains hosted in oxide frameworks above 500°C, sometime up to 1000°C [12,14]. Oxonium β-aluminas are good examples for the latter case. They are stable up to ~400°C and above 400°C. The evaluating protons destroy the β-aluminas framework, leading to the proton-containing crystalline transition alumina. Note, thermal stability of pristine Na β-aluminas in the lack of protons exceeds 1600°C.

Table 1.2: *Typical conducting protonic species and their stability range [12].*

Protonic species	Typical stability range / °C
H_2O, $H^+(H_2O)_n$ (gels)	<80
H_3O^+, NH_4^+	<400
OH^-	<600
H^+	<900

In order to increase the thermal stability range of a protonated material, one significant factor is the application of water pressure. Two alternative applications of partial water pressure are possible: i) the entire device itself must work under pressure i.e. autoclave, ii) the proton conductor is encapsulated by a host framework that kinetically retains the water and

hence increases the partial water pressure at a very local scale. According to the Jurin's law determining the equilibrium pressure close to a curveted surface [12] together with capillary condensation -- (Kelvin equation: more condensation in a porous medium will occur by increasing the vapor pressure [31]), -- the different size and the geometry (curvature radius) of the pores/ cavities of frameworks are also important factors.

The presence of protons and their diffusion can give rise to phase modifications /transitions as a function of the H-bond strength. For example, $H_3OUO_2PO_4.3H_2O$ (HUP), $CsHSO_4$ and $NH_4H(S/Se)O_4$ have been widely studied [8,20,32]. Hydrogen uranyl phosphase, $H_3OUO_2PO_4.3H_2O$ (HUP), is an interesting case of phase transition [20]. Four phases defined by temperature -- I (-3.15°C), II (-3.15 to -75.15°C), III (-75.15 to -123.1°C) and IV (below –123.1°C) -- were observed. In phase I, a quasi-liquid state of water layer related to the rotational and translation disorder of H_2O and H_3O^+ species was observed with considerable orientational disorder of phosphase tetrahedra. In phase II, the structure became orthorhombic with drastically reduction of the translational disorder. In this phase, the protonic species could also be described in term of $H_5O_2^+$ and H_9O_4. In phase III, the rotation of water molecules hydrogen bonded to PO_4 groups and the structure became uniaxial and long range in the form of HUP sheets. Finally, in phase IV, the last degree of rotational freedom of the water molecules around the intra-square O...O directions was frozen,and the system appeared completely ordered.

$CsHSO_4$, is a good example to illustrate specific defects in protonic materials under partial pressure of water. The structure of room temperature phase I consists of infinite $(HSO_4^-)_n$ chains with the O…O distance of 0.257 nm and protons appear to be disordered between two equilibrium sites creating a statically symmetric hydrogen bond. The transition from phase I to phase II detected at 44.8°C, is interpreted in term of a conversion from infinite chains to cyclic dimmers with a subsequent weakening of the hydrogen bonds and increased orientational disorder HSO_4^- ions. In the case of the transition from phase II to phase III observed at 143°C, the structure exhibits high dynamic disorder. Raman bands, assigned as external mode, collapse into a broad wing near Rayleigh line. This is a characteristic of the plastic phase, and implies a free rotation of HSO_4^- ions on given sites. Phase III, furthermore, can be considered as a spectroscopic manifestation of a quasi-liquid state of the proton, the

superionic phase. Under high partial pressure of water conditions, finally, the enthalpy of the transformation of chains (2-17 Cal.g^{-1} for phase I to phase II) into dimmers (15-33 Cal.g^{-1} for phase II to phase III) increase by more than a factor of 10 [8,20]. The phase transitions and local structural modifications are also observed for perovskites proton conduction. This problem will be discussed in Chapter 2.

1.5 Bulk proton (H$^+$) contents

Because of the absence of electron clouds and presence of rather high incoherent background, the location from X-ray/neutron diffraction refinements of protons in a disordered structure at room temperature and *a fortiori* at higher temperature is a difficult task. The thermal motion and the distribution of mobile protons across different sites for fast proton conductors or superionic conductors makes the proton location impossible. Consequently, to detect hydrogen and protonic species in solids, it is mandatory to couple different methods to ensure a complete view of all hydrogen-containing species, and, further, to establish the relationship between the measured signal and H-species content.

Intensive studies related to the determination of protonic species content have been performed by Colomban et al. [14,28]. The H$^+$ measurement techniques could be classified as i) direct methods and ii) indirect methods:

Table 1.3: *Direct and indirect measurement methods of H-content in solids.*

Direct methods	Indirect methods
H-NMR, microwave relaxation, neutron scattering, IR spectroscopy, TGA	DTA/DSC, TE, Raman spectroscopy

The direct methods probing hydrogen atom and H-bonds commonly employ, (Table 1.3, H-NMR), microwave relaxation, neutron scattering, IR spectroscopy and TGA techniques. The first–three techniques have been mostly used to study the proton location and dynamics and not to measure precisely the proton content [14]. For example, NMR study of $(NH_4)_4Fe(CN)_6.1.5H_2O$ (AFC) [33] showed that one of two non-equivalent NH_4 groups, together with the water protons, may be expected from the presence of three different,

narrowed NMR signals. In addition, the narrowing ^{1}H NMR signals resulted from complete isotope local motion with partial average of the intermolecular dipolar interaction by translational motion. Work on this subject is rare. Hellmut et al [34] have conducted experiments to precisely measure the proton content using H-NMR technique i.e. "water traces" in various silicate glasses $Ca_2Mg_5Si_8O_{22}$, $Al_2Si_4O_{10}$ $NaAlSi_2O_6$, $CaSO_4$. The concept of quantitative NMR application is based on direct proportionality of the area under an NMR peak to the number of nuclear spins contributing to that peak.

The Infrared (IR) spectroscopy is the most used direct technique to measure the hydroxyl ion and water content in solids. In IR technique, the huge anharmonicity of the X-H bond enhances the intensity of overtones and combination bands that can be detected by transmission measurements through matter. Owing to the low proton mass, its stretching vibrational signatures take place at high wavenumber: 1000-3800 cm^{-1} and combination/overtones are detected up to 10.000 cm^{-1}. For example, OH groups in $H_6V_6O_{13}$ presents bending modes in the range of 800-1100 cm^{-1} [34]. The H atom of hydroxyl groups is an independent oscillator that gives rise to very narrow IR stretching band. This shows a great ability of IR technique to detect weak narrow signatures of protonic species at low concentrations. The band width increases with electrical/mechanical coupling. The H-bond strength also increases and detection becomes difficult, even impossible. As such inelastic neutron spectroscopy should be preferred.

In the case of Raman technique, as indirect method, the low polarisability of the X-H bond leads to a poor Raman intensity of the protonic species signature. However, the narrow bandwidth of the stretching mode promotes their detection even when their intensity is very small [14]. The exact wavenumbers of the Raman modes depend on both the atomic masses and the bonding of the individual atoms. For example, Raman bands of lithium β-alumina hydrated with water at 3622, 3871, 3472 and 3409 cm^{-1} , were identified as OH^- species from two different origins; (i) OH^- species from the bonding of a proton to one of the bridging oxygen in conduction plane (ii) OH^- species from dissociation of an H_2O molecules [35].

Methods such as diffraction and vibrational spectroscopy give direct information if the H-content is sufficient to give a reliable signature. However, in many cases the low content combined with high static and dynamic disorder of the conduction protons hinder a reliable

analysis of the protonic species. Indirect measurement methods such as differential thermal/scanning calorimeter analysis (DTA/DSC), and thermal expansion (TE) give relative events (jumps, kinks) when matter including proton-containing species evolves, and the hosting framework is heated. Very small events can be detected. For example, thermal expansion (TE) measures the anharmonicity of the chemical bonds [14]. It is very sensitive to any phase transition of first order (thermal expansion jump), second order (kink or rate change) or even O'Keefee type (plot anomaly) [36]. The area delimited by the heating and cooling lines measures the stability of the material: For a stable material, the overlapping is nearly perfect. On the contrary, a significant area indicates a material evolution.

Here, we will further discuss a useful example of neutron scattering and thermal gravimetric analysis, which were employed to estimate the proton contents in previous study on similar compounds [14,37].

Due to the huge incoherent cross-section of hydrogen element ($^{H}\sigma_{inc}$ = 80.26 barns, [38,39]) neutron scattering techniques are among the best methods to study the proton containing materials. They allow firstly, to determine the proton content (elastic scattering), and secondly, to determine the local (rotation and translational jumps) and long range diffusive proton dynamics (quasi-elastic scattering from μeV to tenth of meV range). The ratio of incoherent neutron cross-sections (σ_{incoh}) calculated for protonated and deprotonated (or non-protonated) compounds is proportional to the ratio of elastic peak intensity (I) recorded for protonated and deprotonated (non-protonated) materials [38,39]).

For example, elastic neutron scattering has been used to determine the content of bulk protons in Sr- or Ba-based high dense zirconate ceramics as a function of temperatures [27,28]. Figure 1.6a shows the elastic peak intensity variation in the expected working temperature range in the case of $SrZr_{0.9}Ln_{0.1}O_{3-\delta}$ measured under dynamic high vacuum on dense ceramic pellets. The highest intensity at room temperature reveals the presence of the bulk and surface protonic species. At 400°C, the ceramic is cleaned out from the protonic surface species, while above 600°C, the departure of bulk protons appears. The intensity comparison allows a precise determination of the H content after calibration with reference materials i.e. non-absorbing vanadium and high-absorbing cadmium metals). Comparison must be made at about the same temperature with the same instrument/resolution/energy

window because the intensity of the elastic peak strongly depends on the H motion. Diffusing hydrogen contribute to the peak broadening if their energy is close to the resolution, or to the background if their energy is larger (long-range diffusion) [14,37]. Different instruments are necessary to study the different motions.
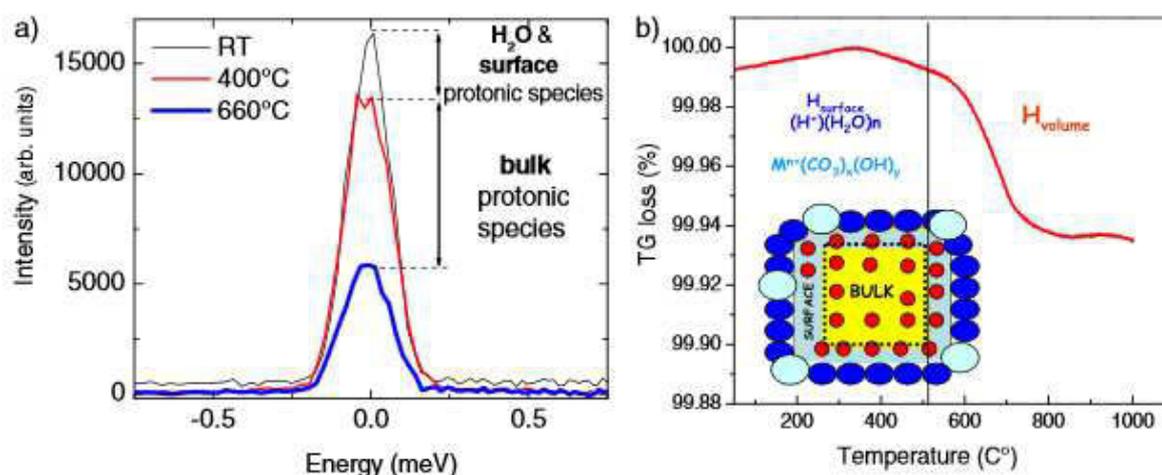
Figure 1.6: *Determination of protonic species content : (a) elastic peak intensity variation as a function of temperature and (b) mass loss detected by TG analysis in the case of SrZrLnO$_{3-\delta}$ [14,37], Note: schema draw in (b) illustrates the distinction of bulk and surface protons.*

The TGA results, (fig. 1.6b), show an agreement with the neutron elastic scattering result. The authors concluded that bulk proton amount depended on the surface area, i.e. the densification of ceramic. Very low H$^+$ content (0.001-0.005 mole H/mole perovskite) was observed in the case of high dense ceramic (>97%). Colomban et al. [14,37] showed that in the case of highly dense ceramic, the content of protonic moieties adsorbed at the surface was lower than that at the "bulk". On the other hand, the lower the ceramic density (higher porosity, higher active surface), the higher the content of surface protonic species. Studies by Hempelmann et al. [40] regarding cerate-based perovskite (SrCe$_{0.95}$Yb$_{0.05}$O$_{0.29}$), showed that the proton content in cerate ceramic (~95% theoretical density) remained low, about ~0.02, ten times higher than that of zirconate [37]). But no differentiation was noticedbetween surface and bulk H-content. The conductivity of cerates being higher than of zirconate, a higher bulk H content was expected. In order to measure the accuracy of the H-contents, it is necessary to combine different, direct and indirect, measurement techniques.

1.6 Proton conductors

Proton conductors can be classified according to the preparation method, structural dimensionality and conductivity mechanism [2].

The preparation method based classification can be divided into two: i) direct synthesis and ii) ion exchange. The direct synthesis is usually used for hydrates materials i.e. $Sb_2O_2.5.4H_2O$, $SnO_2.2H_2O$, $ZrO_2.1.75H_2O$. The ion exchange is a substitution of conducting ions i.e. Na^+ in β-alumina.

Second criterion practically concerns the nature of the mobile ion and the dimensionality of the potentially mobile ion sub-lattice. For example, polycrystalline materials (i.e. phase I of $CsHSO_4$) with a structure containing 1D conduction pathways, will have a very low overall conductivity due to an blocking effect at the grain boundaries. In other words, each grain boundary encountered along microscopic diffusion pathway is a wall, and creates a barrier to long-range diffusion.

The last classification criterion, the value of proton conductivity, allows distinguishing conductors and superionic conductors. The correlation between two parameters of proton conductivity (σ and E_a value) is employed according to the proton conductivity mechanism. The $σ_0$ term (eq. 1.2) is directly related to the concentration of the conducting protonic species. Indeed, there are three ranges of σ value: high value for loosely packed structures ($>10^{-3}$ $Ω^{-1}.cm^{-1}$), intermediate value for quasi-liquid like or gels (10^{-7}-10^{-3} $Ω^{-1}.cm^{-1}$), and low value in case of extrinsic defect materials ($<10^{-7}$ $Ω^{-1}.cm^{-1}$) [2]. Therefore, three types of proton conductors could be classified as:

i) *Anhydrous protonic conductors.* – their activation energy is rather high and the proton conduction is related to the presence of defects. The conducting species are proton or proton vacancies. Typical examples for this protonic conductor type are KH_2PO_4 ($σ_{RT}$ ~10^{-8} $Ω^{-1}.cm^{-1}$ and E_a ~0.55 eV [41]) and ice ($σ_{RT}$ ~10^{-7}/10^{-8} $Ω^{-1}.cm^{-1}$ and E_a ~0.55 eV [42])

ii) *Ionic conductors containing a loosely packed lattice with high concentration of potentially mobile species.* These materials have high σ and high activation energy at

low temperature. The proton conducting species ride on a carrier molecule such as H_3O^+ or NH^+ (*V-mechanism*). In addition, good illustration materials for this proton conductor are oxonium or ammonium in β–alumina. For example β-$Al_{11}O_{16}1.25O.(NH_4^+)$ yield σ_{RT} $1.5x10^{-7}$ $\Omega^{-1}.cm^{-1}$ and E_a ~0.5 eV, β-$Al_{11}O_{16}1.25O.(H_3O^+)$ yield σ_{RT} ~10^{-10} $\Omega^{-1}.cm^{-1}$ and E_a ~0.8 eV [2].

iii) *Compounds containing protonic species in quasi-liquid state.* This protonic conductor type is considered either inside the structure (intrinsic or bulk conductors) or at the surface (gels or particle hydrates). Protonic species may jump from one acceptor to the other (*G-mechanism*). One good material for intrinsic or bulk protonic is, for example, $CsHSO_4$ [2] owing to σ_{RT} ~10^{-2} $\Omega^{-1}.cm^{-1}$ and E_a ~0.33 eV. For surface protonic conductors, gels or particle hydrates such as $V_2O_5.1.6H_2O$ yield conductivity of ~10^{-3} $\Omega^{-1}.cm^{-1}$ at room temperature with activation energy (E_a) of ~0.35 eV [2].

Perovskite-based oxide solid solution exhibits protonic conduction in an atmospheric containing hydrogen or steam from moderate to high temperature. For example, pure $SrCeO_3$ or $BaCeO_3$ ceramics owned the conductivities of which at least 10^{-2} S cm^{-1} at 1000°C and at least 10^{-3} S cm^{-1} at 600°C exposed to pure hydrogen gas [43]. However, the conduction in $BaCeO_3$-based ceramics may be partly protonic and partly oxide ionic as a function of temperature range and water partial pressure [44]. Below 600°C, the oxygen vacancy conductivity remains very small with respect to the protonic conductivity [27]. Characterization of perovskite-based oxide structure as well as its electrical properties will be further discussed in next chapter.

References

[1]   A. R. West, in: P. G. Bruce (Ed.), Solid State Electrochemistry, University Press Cambridge, United Kingdom, 1995, p. 7.

[2]   Ph. Colomban, A. Novak, in: Ph. Colomban (Ed.), Proton conductors: Solids, membranes and gels - materials and devices, Cambridge University Press, New York, 2008, p. 38.

[3]   W. Hayes, G. F. Hopper, F. L. Pratt, Journal of Physics C: Solid State Physics 15 (1982) L675.

[4]   M. J. Delaney, S. Ushioda, Solid State Communications 19 (1976) 297.

[5]   A. Potier, in: Ph. Colomban (Ed.), Proton conductors: solids, membranes and gels - materials and devices, Cambridge University Press, the United States of America, 2008, p. 1.

[6]   P. K. A. T. Norby, Defects and Transport in Crystalline Solids, University of Oslo, University of Oslo, 2007.

[7]   S. O. Kasap, Principles of Electronic Materials and Devices, McGraw-Hill, 2002.

[8]   Ph. Colomban, A. Novak, in: Ph. Colomban (Ed.), Proton conductors: solids, membrane and gels - materials and devices, Cambridge University Press, the United States of America, 2008, p. 61.

[9]   P. J. Gellings, H. J. M. Bouwmeester, Solid State Electrochemistry, CRC Press. Inc., the United States of America, 1996.

[10]   R. P. Bell, The Proton in Chemistry, Chapman & Hall, 1973.

[11]   D. J. Jones, J. Roziere, in: Ph. Colomban (Ed.), Proton conductors: Solids, membrane and gels -materials and devices, University Cambridge Press, United States of America, 2008, p. 18.

[12]   Ph. Colomban, in: M. Aparicio, A. Jitianu, L. C. Klein (Eds.), Sol-Gel Processing for Conventional and Alternative Energy, Springer US, 2012, p. 59.

[13]   F. Fillaux, H. Ouboumour, J. Tomkinson, L. T. Yu, Chemical Physics 149 (1991) 459.

[14]   Ph. Colomban, Fuel Cells 13 (2013) 6.

[15]   Ph. Colomban, A. Novak, in: Ph. Colomban (Ed.), Proton conductors: Solids, membranes and gels - materials and devices, Cambridge University Press, the United States of America, 2008, p. 367.

[16]   A. Novak, Large Molecules, Springer Berlin Heidelberg, 1974, p. 177.

[17]   Ph. Colomban, Proton Conductors: Solid, Membranes and Gels - Materials and Devices, Cambridge University Press, Cambridge, 2011.

[18]   F. Freund, in: Ph. Colomban (Ed.), Proton Conductors: Solids, membranes and gels - materials and devices, Cambridge University Press, the United States of America, 2008, p. 138.

[19]   A. Potier, in: Ph. Colomban (Ed.), Proton Conductors: Solids, membranes and gels - materials and devices, Cambridge University Press, the United States of America, 2008, p. 1.

[20]   Ph. Colomban, A. Novak, in: Ph. Colomban (Ed.), Proton conductors: solids, membranes and gels - materials and devices, Cambridge University Press, the United States of America, 2008, p. 254.

[21]   Ph. Colomban, A. Novak, in: Ph. Colomban (Ed.), Proton conductors: Solids, membranes and gels - materials and devices, Cambridge University Press, New York, USA, 2008, p. 457.

[22]   W. Münch, G. Seifert, K. D. Kreuer, J. Maier, Solid State Ionics 86–88, Part 1 (1996) 647.

[23]   K. Kreuer, Annual Review of Materials Research 33 (2003) 333.

[24]   W. Münch, K. D. Kreuer, G. Seifertli, J. Majer, Solid State Ionics 125 (1999) 39.

[25]   R. Hempelmann, Physica B: Condensed Matter 226 (1996) 72.

[26]   T. Matzke, U. Stimming, C. Karmonik, M. Soetratmo, R. Hempelmann, F. Güthoff, Solid State Ionics 86–88, Part 1 (1996) 621.

[27]   Ph. Colomban, A. Slodczyk, D. Lamago, G. Andre, O. Zaafrani, O. Lacroix, S. Willemin, B. Sala, Journal of the Physical Society of Japan 79 (2010) 1.

[28]   A. Slodczyk, Ph. Colomban, O. Zaafrani, O. Lacroix, J. Loricourt, F. Grasset, B. Sala, MRS proceeding 1309 (2011).

[29]   P. G. Dickens, A. M. Chippindale, in: P. Colomban (Ed.), Proton conductors: Solids, membranes and gels - materials and devices, Cambridge University Press, New York, USA, 2008, p. 101.

[30]   J. C. Charenton, P. Strobel, Solid State Ionics 24 (1987) 333.

[31]   R. J. Hunter, Foundations of Colloid Science, Oxford University Press, 2001.

[32] Ph. Colomban, A. Novak, in: Ph. Colomban (Ed.), Proton conductors: solids, membranes and gels - materials and devices, Cambridge University Press, the United States of America, 2008, p. 165.

[33] M. S. Whittingham, P. S. Connell, R. A. Huggins, Journal of Solid State Chemistry 5 (1972) 321.

[34] P. G. Dickens, A. M. Chippindale, S. J. Hibble, P. Lancaster, Materials Research Bulletin 19 (1984) 319.

[35] R. Frech, in: Ph. Colomban (Ed.), Proton conductors: Solids, Membranes and Gels - materials and devices, Cambridge University Press, New York, USA, 2008, p. 377.

[36] U. B. Mioč, R. Ž. Dimitrijević, M. Davidović, Z. P. Nedić, M. M. Mitrović, Ph. Colomban, Journal of Materials Science 29 (1994) 3705.

[37] Ph. Colomban, A. Slodczyk, European Physical Journal-Special Topics 213 (2012) 171.

[38] A. J. Dianoux, G. Lander, Neutron data booklet, Old City Publishing, Philadelphia, USA, 2003.

[39] A. J. Dianoux, G. Lander (Ed), Neutron data booklet. Old City Publishing, Philadelphia, USA, 2003.

[40] R. Hempehnann, C. Karmonik, T. Matzke, M. Cappadonia, U. Stimming, T. Springer, M.A. Adams, Solid State Ionics 77 (1995) 152.

[41] R. S. Bradley, D. C. Munro, S. I. Ali, Journal of Inorganic and Nuclear Chemistry 32 (1970) 2513.

[42] Ph. Colomban, A. Novak, Journal of Molecular Structure 177 (1988) 277.

[43] H. Iwahara, in: Ph. Colomban (Ed.), Proton Conductors: Solids, membranes and gels - materials and devices, Cambridge University Press, New York, USA, 2008, p. 122.

[44] H. Iwahara, H. Uchida, K. Morimoto, Journal of the Electrochemical Society 137 (1990) 462.

CHAPTER 2

"Perovskite-Related Oxides"

Chapter 2

Perovskite-Related Oxides

In this Chapter, we will summarize the fundamentals of perovskite-related oxides structures, their phase transitions and electrochemical properties. This will assist in understanding the research undertaken by this author, subsequently. We will focus on the Raman and IR spectra, and consequently vibrational mode assignments, of perovskite-based oxides. All descriptions in this - Chapter - correspond- to our investigated samples, listed in Table 3 of the "Introduction".

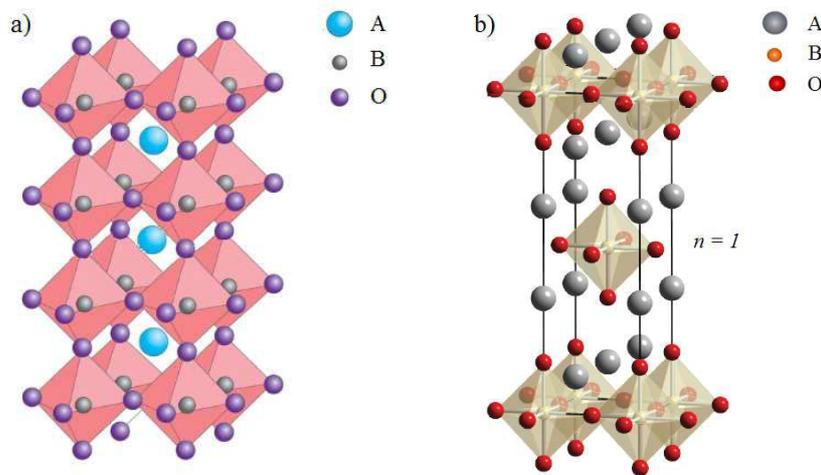## 2.1 Structure of perovskite-related oxides

The so-called *perovskite* name comprises large families of compound, including oxide compounds. The typical chemical formula of perovskite structure is ABO_3, illustrated in Figure 2.1a, where A is a large cation (e.g. akali, alkaline earth, rare earth ions) and B is a small or medium sized metal ion often a transition metal ion. The name corresponds to natural mineral $CaTiO_3$. The ideal cubic structure (Pm-3m) is made of two sub-lattices:

(i)   large-sized 12-coordinated cations at the A site where Coulombian interactions are important

(ii)   small-sized 6-corordinated cations at the B site formed of BO_6 octahedral with covalent bond.

Typical perovskite compounds such as $SrTiO_3$ [1] and $BaZrO_3$ [2] have a cubic lattice with $Pm\overline{3}m$ space group at/close to room temperature. However, many perovskite-oxides are slightly distorted variants showing lower symmetry i.e. hexagonal, orthorhombic, etc. The structural variants result from the competition between the degree of freedom of each sub-lattice, which are strongly related to their properties, particularly piezo- or ferro-electric properties.

Perovskite compounds with different combinations of charged cations in A and B sites for example, $Na^{1+}Nb^{5+}O_3$, $Ba^{2+}Ti^{4+}O_3$, and $La^{3+}Al^{3+}O_3$ have been discovered. According to the simple ternary perovskite, the perovskite structure can also allow complex charge

compensated compositions formula such as A'A''B'B''O$_3$, - called *perovskite solid-solution*. A case study related to our research shows that because the presence of protons is not intrinsic to the ideal structure, they must be modified by substitution of trivalent cations e.g. lanthanides elements at B sites to form oxygen vacancies. The presence of oxygen vacancies promotes oxygen vacancy/ion diffusion and conductivity at high temperature [3,4]. Hence, this complex perovskite oxides can be formed as AB'B''O$_{3-\delta}$ i.e. SrZr$_{0.9}$Yb$_{0.1}$O$_{3-\delta}$, SrZr$_{0.9}$Yb$_{0.1}$O$_{3-\delta}$ [3] .

Figure 2.1: *a) Ideal perovskite structure (ABO$_3$) b) a perovskite-related structure in Ruddelsden-Popper phase, (A$_2$BO$_4$) [3].*

A further factor affecting the perovskite structure is large non-stoichiometry and substitutions. A number of perovskite-related structures, with perovskite building blocks, are formed when excesses, deficiencies, or substitutions beyond the solubility limits, create ordered defects and - new phases. - These comprise oxygen deficiency (**Brownmillerite**, A$_2$B$_2$O$_5$) and A atom access (**Ruddelsden-Popper**, A$_2$BO$_4$).

In this project, Ruddelsden-Popper (RP) type structures were investigated. These are a series of structure having the general formula A$_{n+1}$B$_n$O$_{3n+1}$ or AO(ABO$_3$)$_n$. In addition, the RP type structure presented in Figure 2.1b consists of two units: the ABO$_3$ perovskite unit and AO rock salt unit, which are connected in series along the *c*-axis.

To understand the deviation from the ideal cubic structure, the ABO$_3$ oxides are first regarded as purely ionic crystals [3]. In the case of the ideal structure, the following relationship between the radii (r) of A, B, and O^{2-} ions may be proposed:

$$r_A + r_O = \sqrt{2}\left(r_B + r_O\right) \qquad \text{…(eq. 2.1)}$$

Therefore, the deviation from the ideal structure in perovskite oxides can be expressed through the following - "tolerance factor", t:

$$t = \frac{\left(r_A + r_O\right)}{\sqrt{2}\left(r_B + r_O\right)} \qquad \text{…(eq. 2.2)}$$

In perovskite-type compounds, the value of t usually lies between 0.80 and 1.10. In the case of the ideal cubic structure, the value of t is close to 1 or at least grater than 0.89 [3]. In the case of some perovskite oxides with lower t values, the crystalline is in the illmenite structure - a polymorph of the perovskite structure where A and B have approximately the same size.

Figure 2.2 shows the crystal symmetries detected in the case of $A^{2+}B^{4+}O_3$ and $A^{3+}B^{3+}O_3$ perovskite combinations. As the tolerance factor decreases, the unit lattice structure is shifted from cubic to triclinic because of increased distortions. The tolerance factor suggests that the stability and crystal group are mainly determined by the ratio of the ionic radii of the A and B cations. However, the structure is not dependent only on the size, but also on the nature of the A and B atoms.
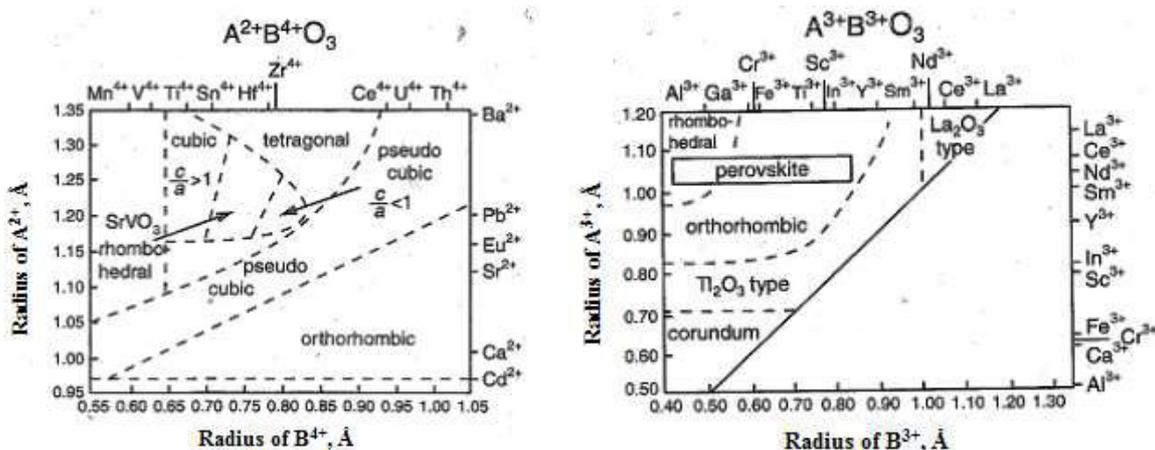
Figure 2.2: *The effect of ionic size of A- and B-site cations on the observed distortions of the perovskite structure [3].*

In the case of Ruddelsden-Popper structure (A_2BO_4), the tolerance factor is the measure of misfit between the ionic rock salt (A_2O_2) and the covalent perovskite (BO_2) layers. For

example La_2NiO_4, the ideal tolerance factor is $0.866 < t < 1.0$ [5,6]. Furthermore, the t value increases with increasing Ni^{3+} content [5].

2.2 Structural phase transitions

Structural phase transition on perovskite-related oxides can be driven by many parameters such as chemical composition, oxygen stoichiometry (δ), temperature, pressure/stress, magnetic or electric fields etc. We recall that XRD and neutron diffraction 'see' the mean structure whereas Raman spectroscopy 'see' the superimposition of the contribution of the nanodomains [7-12].

2.2.1 Zirconate- and Cerate-based perovskite oxides

First, the structure phase transition of undoped zirconates and cerates oxides as a function of temperature would be discussed. Figure 2.3 illustrates the phase diagram of undoped $BaZrO_3$, $SrZrO_3$, $BaCeO_3$ and $SrCeO_3$. (Note: the data were gathered and summarized from previously published literature [13-21]). The phase transitions in such perovskite-based oxides were performed in temperature range of 25 to 1200°C using X-ray diffraction (XRD) and/or high-resolution neutron powder diffraction.
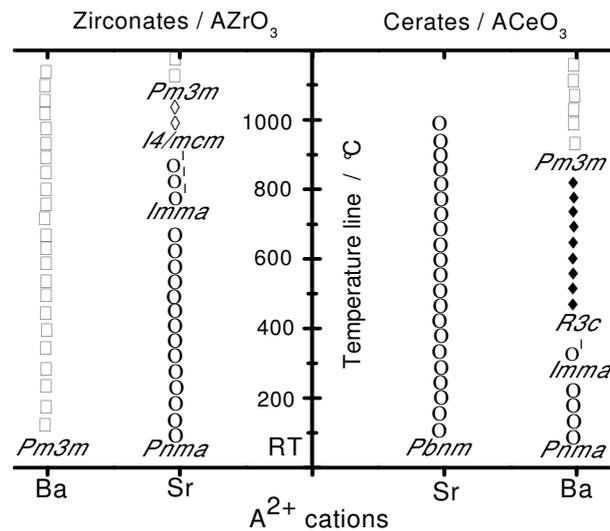
Figure 2.3: *The structural forms of undoped barium/strontium zirconates and cerates gathering data from literatures [13-21], each symbol represents the crystal phase: O - orthorhombic, O' – pseudo tetragonal, ♦ - tetragonal, - cubic.*

Figure 2.3 clearly shows that $BaZrO_3$ and $SrCeO_3$ undergo more phase transitions than $SrZrO_3$ and $BaCeO_3$. Sugimoto et al. [19] report that the structure of $BaZrO_3$ - remained in cubic lattice phase with *Pm-3m* space group. Similar to strontium cerate ($SrCeO_3$), the structure shows orthorhombic with *Pbnm* space group throughout the temperature range of 25-900°C [15].

In contrast, the $SrZrO_3$ and $BaCeO_3$ oxides undergo three steps of structural phase transitions. For $SrZrO_3$, Howard et al. [18] report that the crystal structure varies from primitive orthorhombic (*Pbnm*) to pseudo-tetragonal (*Imma*)/body-centered orthorhombic (*Ibnm*) at 750°C, then to tetragonal phase (*I4/mcm*) at 840°C and finally to cubic phase (*Pm-3m*) at1070°C. More or less temperature value of each step in structural modification of such $SrZrO_3$ was observed by others [16,19,20]. In the case of $BaCeO_3$, the structure undergoes from the orthorhombic (*Pnma*) to the pseudo-tetragonal (*Immm*) configuration at ~300°C, then to the rhombohedral phase (*R-3c*) at ~400°C, and the cubic (*Pm-3m*) at 900°C [13,14].

In Table 2.1, room temperature symmetry of substituted barium/strontium zirconate ($AZrO_{3+\delta}$) and cerate ($ACeO_{3+\delta}$) are summarized according to the cited literature [20,22-24]. As reported by Giannici et al. [22], the structural modification of $BaZrO_{3+\delta,}$ from cubic to tetragonal occurs when yttrium (Y^{3+}) in amount of 6 %mole is substituted. Similarly, Kreuer et al. [25] concluded that such phase transition appears when the minimum amount of Y-content of ~5 %mole, is substituted with 10 %mole of either gadolimium (Gd) or indium (In) in $BaZrO_{3+\delta.}$ The structure also exhibits the tetragonal phase. Such different trivalent substituent at B-site leads to a significant reduction of the mobility of protonic defects. However, the authors concluded that the Y^{3+} is found to be the most optimal as acceptor for $BaZrO_3$ due to its significantly higher proton conductivities.

In the case of doped $SrZrO_{3+\delta}$, Koto et al. [23] studied the characterization of 5 and 10 %mole of Ytterbium (Yb) in $SrZrO_{3+\delta}$ using X-ray diffraction (XRD). The authors found that 10 % mole Yb- $SrZrO_3$ had orthorhombic symmetry with space group Pnma from room temperature to 900°C, which similar to that of 5 %mole Yb-doped. In addition, the unit-cell volume of the 10 %mole Yb-doped increases linearly with increasing temperature. However, a slightly bent of the unit-cell volume vs. temperature curve, between 500 and 600°C, was observed due to the loss of oxygen.

Table 2.1: *Symmetry and Unit-Cell parameters of barium and strontium zirconate- and cerate-based oxides at room temperature (25°C).*

Compound	Notation	Symmetry	Space Group	Lattice parameters / Å			Ref.
				a	b	c	
Zirconate-based oxides							
$BaZrO_{3-\delta}$	BZ	Cubic	*Pm-3m*	4.1931	4.1931	4.1931	[22]
$BaZr_{0.94}Y_{0.06}O_{3-\delta}$	BZY6	Tetragonal	*P4/mbm*	5.9438	5.9438	4.1991	[22]
$BaZr_{0.90}Y_{0.10}O_{3-\delta}$	BZY10	tetragonal	*P4mm*	4.2151	4.2151	4.2047	[25]
$BaZr_{0.90}In_{0.10}O_{3-\delta}$	BZIn10	tetragonal	*P4mm*	4.1989	4.1989	4.2022	[25]
$BaZr_{0.90}Gd_{0.10}O_{3-\delta}$	BZGd10	tetragonal	*P4mm*	4.2205	4.2205	4.2069	[25]
$SrZrO_{3-\delta}$	SZ	Orthorhombic	*Pnma*	5.816	8.225	5.813	[20,23,24]
$SrZr_{0.9}Yb_{0.1}O_{3-\delta}$	SZYb	Orthorhombic	*Pnma*	5.8321	8.2221	5.8079	[23]
Cerate-based oxides							
$SrCeO_3$	SC	Orthorhombic	*Pbnm*	6.0117	6.1538	8.5886	[17]
$BaCeO_{3-\delta}$	BC	Orthorhombic	*Pmcn*	8.791	6.252	6.227	[26]
$BaCe_{0.9-x}Zr_xY_{0.1}O_{3-\delta}$	BCY : Zr ≤0.2	Orthorhombic	*n/a*	8.712	6.134	6.18	[27]
	BCZY Zr>0.2	Cubic	*n/a*	4.209	4.209	4.209	[27]
$BaCe_{0.4}Zr_{0.5}Y_{0.1}Zr_{0.04}O_{3-\delta}$	BCZY :Zn	Cubic	*Pm-3m*	4.295	4.295	4.295	[28]
$BaCe_{0.6}Zr_{0.3}Y_{0.1}Zr_{0.04}O_{3-\delta}$	BCZY :Zn	Orthorhombic	*Pnma*	8.663	6.137	81.237	[28]
$BaCe_{0.5}Zr_{0.35}Sc_{0.1}Zr_{0.05}O_{3-\delta}$	BCZS :Zn	Orthorhombic	*Pbnm*	6.085	6.073	8.596	[29]

For the doped cerate-based oxide, many authors [28,30-36] have published that $BaCe_{(1-y)-x}Zr_xY_yO_{3-\delta,}$ (BCZY) material allows obtaining electrolyte with both high proton conductivity and good chemical stability. Structural study of barium cerate was first performed by Jacobson in 1972 [37]. Subsequently in 1992, Knight et al. [38] determined the structure of $BaCe_{0.9}Y_{0.1}O_{0.29}$ using a pulsed neutron source and time of light diffraction. The room temperature structure is orthorhombic with *Pmcn* space group. In the last decades, several studies focused on synthesis, characterization and chemical stability test of partially substituted BC by Zr and Y formed as $BaCe_{(1-y)-x}Zr_xY_yO_{3-\delta}$ [28,39-42].

For example, the structure of $BaCe_{0.8-x}Zr_xY_{0.2}O_{3-\delta,}$ with $0.2 \leq Zr \leq 0.6$ [42] is cubic. Chien et al. [39] reported that the $BaCe_{0.7}Zr_{0.1}Y_{0.2}O_{3-\delta}$ (BZCY712) ceramic also shows cubic structure. The studies show that the first impact of zirconium substitution is the stabilization

of the cubic phase of barium zirconate and secondly, a decrease in unit-cell parameters with increasing content of zirconium doping. Ricote et al. [40] and Koji et al. [27] studied the crystallographic phases of $BaCe_{0.9-x}Zr_xY_{0.1}O_{3-\delta}$ ($0 < Zr < 0.9$) ceramics at room temperature. They reported that the compounds with the Zr substitution between $0.3 \leq Zr \leq 0.9$ show a pseudo cubic structure. The increasing of Zr concentration leads to a decrease of the lattice parameters, which reflects the substitution of small Zr^{4+} for Ce^{4+}-site. (0.72 and 0.87 Å, respectively) . Furthermore, a statistically distribution of Ce and Zr in $BaCe_{0.9-x}Zr_xY_{0.1}O_{3-\delta}$ ($0 \leq x \leq 0.9$) was well observed.

Tao et al. [32] pointed out that zinc addition decreases the firing temperature and thus makes possible co-firing of both electrodes and electrolyte. 1 %mole of ZnO addition in barium cerium zirconate (BCZY) allows firing at 1325°C. The zinc compound is an unlikely B-site substituent because of its low charge (Zn^{2+}) and small size (radii 0.72 Å), which could reduce ionic conductivity. It may be noted that oxide additives with metal ions, having a stable oxidation state of 2 and an ionic radius similar to Zr^{4+}, result in the best sinterability [43]. This synthesis method, extremely beneficial to sintering, yielded 97% dense sample. The effect of Zn addition on the structure of $BaCe_{0.9-x}Zr_xY_{0.1}O_{3-\delta}$ ceramic has been intensively studied by Amsif et al [28]. The powders of $BaCe_{0.9-x}Zr_xY_{0.1}O_{3-\delta}$ (x = 0.1, 0.3, 0.5, 0.7 and 0.9) were prepared by the freeze-drying precursor method. Then, a polycrystalline Zn powder was added to precursor powders and they were pressed into disks and sintered at 1200 and 1300°C for 10h. They observed that the $BaCe_{0.9-x}Zr_xY_{0.1}O_{3-\delta}$ (x = 0.1, 0.3) samples with Zn addition exhibited an orthorhombic structure with *Pnma* space group. However, the Zn-doped BCZY samples in case of x > 0.3 showed a cubic structure with *Pm-3m* space group. The addition of 4 mol.% Zn into this phase permits reduction of the unit-cell volume. In fact, the Zn^{2+} with radii of 0.74 Å replaces the Zr^{4+} (radii 0.72 Å) than Ce^{4+}, which results in smaller lattice distortion.

The phase transition behavior of $Sr_{1-x}Ba_xZrO_3$ were studied by Takayuki et al [19]. The results show that three phase transitions were observed with Ba-doped amount; a phase boundary from primitive orthorhombic (Pbnm) to body-centered orthorhombic (*Ibmm*) for x = 0.4 - 0.5, from body-centered orthorhombic (*Ibmm*) to bode-centered tetragonal (*I4/mcm*) for x = 0.5 - 0.6, and from the body-centered tetragonal (I4/mcm) to cubic phase (*Pm3m*) for x =

0.8 - 0.9. According to the temperature impact $Sr_{0.5}Ba_{0.5}ZrO_3$ exhibits a phase transition from *Ibmm* to *I4mcm* between 100–200°C, and from *I4mcm* to *Pm3m* between 400-500°C. For $Sr_{0.4}Ba_{0.6}ZrO_3$, the structural phase transition from *I4mcm* to *Pmcm* was between 300-400°C.

Nieto et al. [44] studied the phase transitions and proton transport in $BaCe_{0.95}Yb_{0.05}O_{3-\delta}$ perovskite. They reported that three phenomena of phase transitions appeared at RT-800°C temperature range: orthorhombic (*Pnma*) to tetragonal (*Imma*) at ~320°C, tetragonal (*Imma*) to rhombohedral (*R3c*) at ~450°C, and rhobohedral (*R3c*) to cubic (*Pm3m*) at 800°C.

Protonic-conducting $BaCe_{0.8-x}Zr_xY_{0.2}O_{2.9}$ ceramic powders fabricated by using glycine-nitrate (G/N) combustion method was investigated in terms of structural properties by Cien et al. [39]. They observed that calcined BZCY (x = 0.0-0.8) powders fabricated with G/N = ½ exhibited a single cubic structure and a structural transformation from cubic to rhombohedral for Zr/Ce < 2/6. Katahira et al. [27] showed that $BaCe_{0.9-x}Zr_xY_{0.1}O_{3-\alpha}$ exhibited a single phase over the whole range $0 \leq x \leq 0.9$. Symmetry of lattice was either orthorhombic (x ≤ 0.2) or cubic (0.3 ≤ x ≤ 0.9). The chemical stability test of sintered specimens was in CO_2 atmosphere (pH_2O ~0.017 bar) at 900°C for 2h. It showed that Zr-substituted $BaCeO_3$ stability against CO_2 increased with increasing Zr-content. Similar to Pooja et al. [42], chemical stability of $BaCe_{0.9-x}Zr_xY_{0.2}O_{3-\alpha}$ (x = 0.4) in CO_2 atmosphere and in boiling water for several days were studied. The structural characterization was performed using powder XRD pattern. The result showed that doping Zr in lower amount than 0.2, exhibited low tolerance (<0.8659), which resulted in low chemical stability of the perovskite oxide samples under both H_2O and CO_2 atmosphere.

Grimaud et al. [45] studied *in-situ* Raman spectroscopy of $BaCe_{0.9}Y_{0.1}O_{3-\delta}$ water partial pressure of 0.03 bar. They reported that the structural transition from tetragonal (*Imcm*) to rhombohedral (*R-3c*) occurred between 400-500°C. According to previous works at MONARIS/LADIR [8,10,12,46-52] [27], the *in-situ* Raman spectroscopy equipped with autoclave device was employed to investigate structural phase transition of perovskite oxide ceramics under vapor pressure and at intermediate temperature (550-650°C). The protonic conducting Ln-doped strontium zirconates ($SrZr_{0.9}Ln_{0.1}O_{3-\delta}$) [10,52] ceramics exposed under 20 bar H_2O exhibited a structural modifications sequence at ~350°C, ~450°C and ~550°C. In

case of Yb-doped with barium zirconates (BZ) and with strontium zirconates (SZ), structure of both materials remained as pristine phase (cubic for BZ:Yb and orthorhombic for SZ:Yb) after treating the samples under 15 bar H_2O at 200°C for 23 days [12]. However, *in-situ* Raman of $SrZr_{0.93}Yb_{0.07}O_{2.965}$ and $SrZr_{0.93}Yb_{0.07}O_{2.965}H_{0.03}$ [49], as a function of hydrostatic helium pressure (0.5 to 40 GPa), showed a sequence of structural modification at 10, 20 and 35 GPa. This result was similar to phase transition sequence as a function of temperature; orthorhombic (*Pnma*) 750°C to pseudo-tetragonal (*Immm*) 840°C to tetragonal (*I4/mcm*) to cubic (*Pm3m*). Change due to protonation was subtle but clear. For $BaCe_{0.5}Zr_{0.3}Y_{0.16}Zn_{0.04}O_{3-\delta}$ ceramic [12], a phase transformation from distorted rhombohedral to cubic was observed at 500°C under 10 bar H_2O for 10h.

2.2.2 Nickelate-based oxides

$Ln_2NiO_{4+\delta}$ (Ln = La, Pr, Nd) ceramic samples, namely nickelate oxides, exhibited a significant range of oxygen non-stoichiometric composition ($\delta > 0$). An excess of oxygen and charge compensating Ni^{3+} ions (holes) stabilized the Ruddlesden-Poper phase by reducing the instrinsic charge separation between the electropositive La_2O_2 and NiO_2 layers and the structural strain due to the misfit between the La_2O_2 and NiO_2 layers.

Table 2.2 shows the comparison of our XRD analysis, of the three-lanthanide nickelate-based oxides (lattice parameters, space groups), with the literature data [6,53-59]. The most common feature is the orthorhombic distortion at room temperature. However, some materials have the tetragonal structure [6,54]. Several such symmetries of $Ln_2NiO_{4+\delta}$ ceramics were variously observed for the lanthanide elements, oxygen stoichiometry (δ), synthesis route and temperature. For example, the $La_2NiO_{4+\delta}$ ($\delta = 0.18$) were refined in orthorhombic *Fmmm* space group, whereas stoichiometric $La_2NiO_{4+\delta}$ ($\delta = 0$) was in *Bmab* symmetry [55]. In addition, the tetragonal distortion with *I4/mm* space group was obtained by solid state reaction at 1200°C calcination temperature for 12h [6], while the orthorhombic phase (*Bamb* space group) was synthesized by Pechini-method at 1000°C [56].

Table 2.2 : *Symmetry and Unit-Cell parameters of $Ln_2NiO_{4+\delta}$ materials at room temperature (25°C).*

Compound	Notation	Symmetry	Space Group	Lattice parameters / Å			Ref.
				a	b	c	
$La_2NiO_{4+\delta}$	LNO	Orthorhombic	*Fmmm*	5.467	5.462	12.693	[53]
		Tetragonal	*I4/mmm*	3.864	3.864	12.699	[54]
		Orthorhombic	*Fmmm*	5.461	5.472	12.714	[55]
		Orthorhombic	*Fmmm*	5.460	5.474	12.688	[57]
		Orthorhombic	*Fmmm*	5.456	5.462	12.691	[56]
		Orthorhombic	*Fmmm*	5.449	5.457	12.672	[58]
$Pr_2NiO_{4+\delta}$	PNO	Orthorhombic	*Fmmm*	5.462	5.385	12.479	[53]
		Orthorhombic	*Fmmm*	5.391	5.452	12.439	[54]
		Orthorhombic	*Bmab*	5.392	5.545	12.446	[56]
		Orthorhombic	*Bmab*	5.389	5.454	12.443	[58]
$Nd_2NiO_{4+\delta}$	NNO	Orthorhombic	*Fmmm*	5.378	5.457	12.379	[53]
		Orthorhombic	*Fmmm*	5.379	5.442	12.351	[54]
		Orthorhombic	*Bmab*	5.374	5.458	12.376	[56]
		Orthorhombic	*Bmab*	5.384	5.445	12.339	[59]
		Orthorhombic	*Fmmm*	5.459	5.374	12.380	[6]
		Tetragonal	*I4/mmm*	3.866	3.866	12.197	[6]

Note: *cell parameters indicated here are characteristic of non-stoichiometry compounds ($\delta >0$).*

Low and high temperature phase transformation of nickelate-based oxides ($Ln_2NiO_{4+\delta}$, Ln = La, Pr, Nd) have been intensively studied [6,55,57-69]. The structure of ternary oxides $Ln_2NiO_{4+\delta}$ is described as a successive of NiO_2 layers alternating with Ln_2O_2 bi-layers. At high temperature (e.g. >700°C for $La_2NiO_{4+\delta}$ in Fig. 2.4), the structure of nickelates is tetragonal (High Temperature Tetragonal phase, nominated as HTT-phase). Here the Ni^{2+} ions are octahedrally coordinated with six oxygen atoms. As temperature goes down, the in-plane cell parameters for both kinds of layers become different (a.p. NiO_2 > a.p. La_2O_2). In absence of oxidizing atmosphere the resulting stress is relieved by the rotation of the NiO_6 octahedral. The system transforms to an orthorhombic symmetry (Low Temperature Octahedral phase, nominated as LTO-phase). The critical threshold of this phase transition is about 426.5°C for La_2NiO_4, 1226.5°C for Pr_2NiO_4, and 1626.5°C for Nd_2NiO_4 [60].
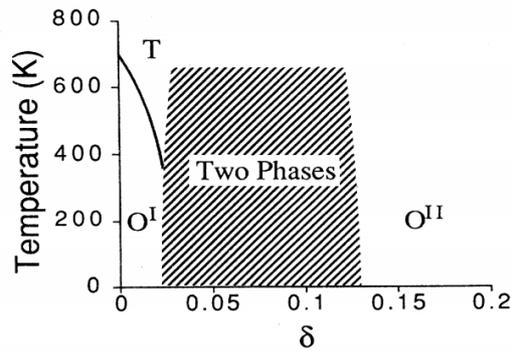
Figure 2.4: *Approximate structural phase diagram for La$_2$NiO$_{4+\delta}$ [55].*

An approximate phase transition diagram for La$_2$NiO$_{4+\delta}$ given by Jorgensen et al. (1989) [55], is shown in Fig.2.4. The estimates are based on the neutron powder diffraction data at low temperature (-263.5°C – 25°C), and data collected from the works of Rodrigues-Cravajal et al [70]. Figure 2.4 illustrates that at least three phases are presented: the orthorhombic (O^I) *Bmab* space group, the tetragonal (T) with *I4/mmm* space group and the orthorhombic (O^{II}) with *Fmmm* space group. The stoichiometric La$_2$NiO$_{4.0}$ with tetragonal *I4/mmm* (T) structure at high temperature undergoes a second order phase transition to orthorhombic *Bmab* (O^I) at 426.5°C. Biphasic phases are expected in the region of 0.02 < δ < 0.13. The *Fmmm* phase (O^{II}) has been proposed as being stable above the δ > 0.13. Unfortunately, no data was taken for temperatures above room level.

After the study of Jorgensen et al. [55], numerous researchers focused on high temperature La$_2$NiO$_{4+\delta}$ phase modification. Fernandez-Diaz et al. (1993) [60], reported that the unstrained tetragonal structure (*I4/mmm*) of La$_2$NiO$_{4+\delta}$ remained in the measured temperature range of 25°C to 826.5°C. In contrast, Stephan [71] reported that non-stoichiometry La$_2$NiO$_{4+\delta}$ (δ~0.18) exhibited *Fmmm* orthorhombic phase (at room temperature) and was transformed to I4/mm tetragonal phase at 150°C.

In the case of praseodymium nickelates, Buttrey et al. [67] show that the Pr$_2$NiO$_{4+\delta}$ sample (δ = 0.06) was tetragonal (*P4$_2$/ncm*) symmetry at low temperature (-268°C to 27°C). Biphasic phase (*P4$_2$/cnm* tetragonal phase and *Pccn* orthorhombic phase) were proposed for Pr$_2$NiO$_{4+\delta}$ sample (δ = 0.02) at above -156°C. For high temperature, Fernandez-Diaz et al. [60] found that the orthorhombic (*Fmmm*) to tetragonal (*F4/mnm*) phase transformation of Pr$_2$NiO$_{4+\delta}$ (δ = 0.2) takes place at a temperature of ~420°C. Similar results to Allançon et al.

[68], they observed an orthorhombic (*Bmab*) to tetragonal (*P42/cnm*) transition at about 447°C for oxidized $Pr_2NiO_{4+\delta}$ ($\delta = 0.28$).
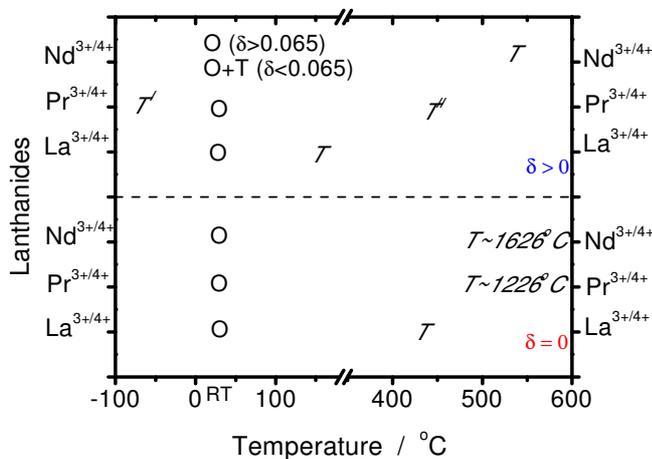
Figure 2.5: *Summary of phase modification of the three lanthanides (La, Pr, Nd) nickelates.*

Figure 2.5 illustrates structural transition of the lanthanides (La, Pr, Nd) nickelate materials over low- and high- temperature range. Concerning non-stoichiometric $Nd_2NiO_{4+\delta}$ oxide, at room temperature, the structure was heavily dependent on oxygen excess [6]. The polycrystalline compounds exhibited biphasic phase between orthorhombic and tetragonal with small amount of excess oxygen ($\delta < 0.065$). At high oxygen excess, the structure became orthorhombic phase. According to Fernandez–Diaz et al. [60], the presence of a distribution of unit-cell parameters in octahedral phase has been shown by neutron powder diffraction study. The orthorhombic strain defined as $S = 25(a-b)/(a+b)$ decreased with increasing temperature. Consequently, the phase transformation for $\delta < 0.28$ took place at a temperature of 516°C and tetragonal F4/mmm phase -occurred.

2.2.3 $La_{1-x}Sr_xCo_{1-y}Fe_yO_{3-\delta}$ materials

Lanthanum Strontium Cobalt Ferrite ($La_{1-x}Sr_xCo_{1-y}Fe_yO_{3-\delta}$; LSFC) can be considered as a solid solution between $La_{1-x}Sr_xCoO_{3-\delta}$ (LSC) and $La_{1-x}Sr_xFeO_{3-\delta}$ (LSF). The LSFC compound mostly resulted in rhombohedral structure with *R-3c* space group, in Table 2.3. Variation of Sr^{2+} and Fe^{3+} ions substitute in A and B cations respectively were factors which caused-symmetry change. Synthesis and characterization of compositions in the system of $La_{0.8}Sr_{0.2}Co_{1-y}Fe_yO_{3-\delta}$ and $La_{1-x}Sr_xCo_{0.2}Fe_{0.8}O_{3-\delta}$ were reported [72,73]. At room temperature,

66

the rhombohedral phase was observed in the as-calcined powder with y ≤ 0.7. Otherwise it exhibited orthorhombic symmetry. Traces of CoO were detected in the sample with y ≤ 0.2 [72,73]. In case of Sr variation (*x*) with y = 0.8, the as-calcined sample was in orthorhombic phase with x < 0.3. The rhombohedral structure was observed with 0.3 ≤ x ≤ 0.4. In addition, the crystal structure of $La_{1-x}Sr_xCo_{0.2}Fe_{0.8}O_{3-\delta}$ with x > 0.8 exhibited coexisting phases of the cubic and the rhobohedral. The single phase of the cubic with *Pm-3m* space group was observed for LSCF6428 ceramic by Dailly et al. [56].

Table 2.3: *Symmetry and Unit-Cell parameters of $La_{1-x}Sr_xCo_{1-y}Fe_yO_{3-\delta}$ materials at room temperature (25°C).*

Compound	Notation	Symmetry	Space Group	Lattice parameters / Å			Ref.
				a	b	c	
$La_{1-x}Sr_xCo_{1-y}Fe_yO_{3-\delta}$	LSCF6428	Rhombohedral	*R-3c*	5.498	5.498	13.378	[53]
	LSCF6428	Cubic	*Pm-3m*	5.484	5.484	5.484	[56]
	LSCF7382	Rhombohedral	*R-3c*	5.447	5.447	13.224	[74]
	LSCF7355	Rhombohedral	*R-3c*	5.459	5.459	13.368	[74]
	LSCF7355	Rhombohedral	*R-3c*	5.481	5.481	13.270	[75]

Note: *cell parameters indicated here are characteristic of non-stoichiometry compounds ($\delta > 0$).*

Tai et al. [72,73] studied crystal structure and thermal properties of $La_{1-x}Sr_xCo_{1-y}Fe_yO_{3-\delta}$ powders. The authors observed a weight change in TG measurement (in air above 500°C. up to 1100°C) resulting from both the loss of lattice oxygen (reduction) and the uptake of oxygen (oxidation). On increasing the Sr content for $La_{1-x}Sr_xCo_{0.2}Fe_{0.8}O_{3-\delta}$ compound, the temperature at which TG weight loss became significant decreased, and the magnitude of oxygen loss increased. Orthorhombic to rhombohedral phase transition was detected for Sr amount of ~ 0.1, at 170 - 250°C.

Thermal and chemical analysis of $La_{0.5}Sr_{0.5}Fe_{1-x}Co_xO_{3-\delta}$ (x = 0, 0.5, 1) materials were reported by Lein et al. [76]. The samples were treated up to 1000°C under N_2 or Air atmosphere. They observed that the sintered materials exhibited the rhombohedral symmetry with *R-3c* space group at room temperature. The second order rhombohedral - cubic phase transition of $La_{0.5}Sr_{0.5}Fe_{0.5}Co_{0.5}O_{3-\delta}$ was located approximately at ~350°C.

Soldati et al. [77] investigated reduction and oxidation cycle of the nanocrystalline $La_{0.6}Sr_{0.4}Fe_{0.2}Co_{0.8}O_{3-\delta}$ oxides by X-ray absorption Near Edge Spectroscopy (XANES) and X-ray powder diffraction (XPD). They confirmed that this material reacted differently under reductive or oxidative atmosphere. Structural modification was observed when treated for 24 hours under Ar atmosphere at 500°C. This resulted in the co-existence of Rhombohedral symmetry with another oxygen vacancy ordered phase. The reduction cycle explained the change in formal valance of the transition metal atoms to lower oxidation state (i.e. $Fe^{4.25+}$ to $Fe^{4.02+}$ and $Co^{3.36+}$ to $Co^{3.07+}$), together with the formation of oxygen vacancies.

Emmerlich et al. [78], studied the effect of the ratio of A-site cations (La+Sr) to B-site cations (Co+Fe) enhancement on the defective structure of the $La_{1-x}Sr_xCo_{1-y}Fe_yO_{3-\delta}$ The use of magnetron sputtering from a designed target allowed the authors to control the chemical composition via synthesis temperature variations. The study showed - the formation of LSCF phases from the rhombohedral to the cubic at 450°C. The extension of cubic stability range to such low temperature was attributed to an increase in the ratio of A-site (La + Sr) to B-site (Co + Fe) cations, which resulted in A-site deficiency observed at higher temperature. The A-site deficiency extended not only the stability range of cubic structure, but also influenced transport properties: 2.5% A-site deficient induced a decrease in electrical conductivity of 33% and increased the formation of oxygen vacancies by 2%.

2.3 Conductivity properties

The aim of this thesis is not the characterization of the charge in proton conductivity. However, data about conductivity observed under similar working conditions was consulted. This was done in order to ascertain a global view of investigated ceramics. Hereafter it is summarized, based on anode/cathode/electrolyte reaction roles of perovskite-based oxides materials.

2.3.1 Electrolytes

Proton conductivities of various solid oxide-based materials were calculated from the data available on proton concentrations and mobilities for a wide range temperature, shown in Figure 2.6. This data clearly illustrated that perovskite-type oxides had the highest proton

conductivities [79,80]. Furthermore, $BaCeO_3$-based materials were among the best proton-conducting oxides.
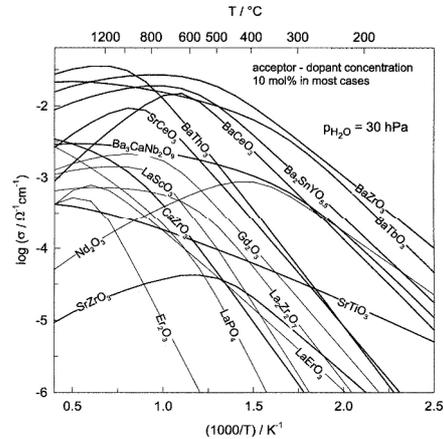
Figure 2.6: *Proton conductivities of oxide systems vs reduced inverse temperature [80].*

Iwahara et al. [81-83] applied Yb-doped $SrCeO_3$ as the proton-conducting electrolyte in steam electrolyzer working at 700-1000°C temperature to produce hydrogen gas. The efficiencies for hydrogen production were 50-95% in the range of 0.1-0.8 A/cm^2. $BaCeO_3$-based ceramic were also developed [84] for similar application. The $BaCeO_3$ was found to be responsive in the presence of oxygen conduction when it exceeded 900°C. The protonic conductivity of alkaline earth zirconates such as $CaZr_{0.9}In_{0.1}O_3$, $SrZr_{0.95}Y_{0.05}O_3$ and $BaCe_{0.95}Y_{0.05}O_3$ was successfully investigated [85-87]. These studies showed that barium and strontium zirconate ceramics exhibited higher conductivities than calcium zirconates.

The cerate ($ACeO_3$) and zirconate ($AZrO_3$) based-oxides have become well-established proton conducting electrolyte [27,86-90]. The pure cerates and zirconates exhibit only low proton incorporation unless doped with subvalent cations [91]. The tetravalent cerium or zirconium ion is substituted by a lower-valent cation, thus constituting defects of effective negative charge. These defects may be charge compensated by oxygen vacancies ($V_O^{\bullet\bullet}$) or interstitial proton ($H_i^{\bullet}$), as discussed in section 1.2.

In the literature consulted [92-100], most of the lanthanide elements were investigated as the substituents. Table 2.4 shows proton conductivity values of some potential Ln (Nd, Sc, Er, Y, and Yb) -doped cerate and zirconate perovskites.

Table 2.4 : *Conductivity of potential proton-conducting electrolytes.*

| Material	Working temperature °C	Activation energy eV	Proton conductivity S.cm^{-1}	Ref.
Cerate-base oxides				
$SrCe_{0.95}Yb_{0.05}O_3$	200	0.63	1.4×10^{-6}	[101]
$BaCe_{0.9}Y_{0.1}O_{3-\alpha}$ (BC: Y)	500-900	n/a	1.8×10^{-2} to 7×10^{-2}	[27]
	400	n/a	$< 10^{-3}$	[102]
$BaCe_{0.9-x}Zr_xY_{0.1}O_{3-\alpha}$ (BCZY)	600-900	0.35	n/a	
$BaCe_{0.95}Nd_{0.05}O_3$	25-200	0.56	1.8×10^{-6} at 112°C	[103]
Zirconate-based oxides				
$SrZr_{0.95}Yb_{0.05}O_3$	100-900	0.4-0.6	$\sim 5 \times 10^{-3}$	[86,104]
$SrZr_{0.95}Er_{0.05}O_3$	100-900	~ 0.55 at 100°C	$\sim 7 \times 10^{-3}$ at 400°C	[104]
$SrZr_{0.95}Sc_{0.05}O_3$	100-900	0.63 at 100°C	$\sim 2.5 \times 10^{-3}$ at 400°C	[104]
$SrZr_{0.95}Y_{0.05}O_3$	100-900	0.57 at 100°C	$\sim 9 \times 10^{-3}$ at 400°C	[104]
$Sr(Ce_{1-x} Zr_x)_{0.95}Yb_{0.05}O_3$	800°C	0.6	4.5×10^{-6}	[105]
$BaZr_{0.9}Y_{0.1}O_{2.95}$	>300	0.3-0.5	n/a	[106]
$BaZr_{0.9}Y_{0.1}O_{3-\alpha}$	500-900	n/a	1.6×10^{-3} to 6×10^{-3}	[27]

Typical values of the activation energy of proton conductivity determined at intermediate temperature was around 0.6eV in Yb-doped $SrCeO_3$ [101], 0.3 to 0.5 eV in Y-doped $BaZrO_3$, [106] and ~0.6 eV in Nd-doped $BaCeO_3$-based electrolytes [103]. Accordingly, the proton-conducting perovskite oxides had advantages in intermediate to low temperature usage (400-700 °C). For example, $BaCe_{0.9}Y_{0.1}O_{3-\alpha}$ reached conductivity of $\sim 10^{-3}$ S.cm^{-1} at 400°C [102].

At intermediate SOCF/SOEC operating temperature (<700°C) -- which allows the electrolyte highly conductive protons -- the main obstacles were related to the increasing electrolyte resistivity. In order to reduce the electrolyte resistance, decreasing electrolyte's thickness was one of the solutions. In fact, the thinner electrolyte film reduced ohmic losses, and consequently allowed the electrolysis cells to operate at lower temperatures [107-109]. For example, relatively low applied voltages of 1.08 V at 0.4 A.cm^{-2} and 1.32 V at 0.6 A.cm^{-2} were required for $SrCe_{0.9}Sc_{0.1}O_{3-\delta}$ electrolyte PCEC with a thickness of 10 mm. [110]. In

70

addition, to achieve the same current densities under the same working conditions voltages of 7.2 V and 8.8 V were required for the cell with a 500µm. thick $SrCe_{0.9}Sc_{0.1}O_{3-\delta}$ electrolyte. Actually, thickness of 100 to 20 µm could be achieved in real devices.

2.3.2 Electrode materials for PCFCs and PCECs

Fundamentally, the electrolysis cell system (PCEC) is a reverse mode of fuel cell system (PCFC). To explain a function of electrodes of these two distinct systems, the cathode side of PCFC (Fig. 2.7a) exhibits oxygen dissociative adsorption, diffusion, reduction, and the formation and evaporation of water by-product. In a PCEC system the mode is reversed and the anode side (Fig. 2.7b) exhibits dissociation of water, oxidation, diffusion and the formation oxygen gas. In addition, the anode side of PCFC (Fig. 2.7a) exhibits oxidation of hydrogen gas, yielding hydrogen ions, which travel throughout the anode side in the direction to meet the electrolyte. The reverse mode occurs at the cathode side of PCEC (Fig. 2.7b). Here the hydrogen ions leave the electrolyte and travel towards the cathode side and produce hydrogen gas. In some cases introduction of water on the dry side improved the device efficiency.
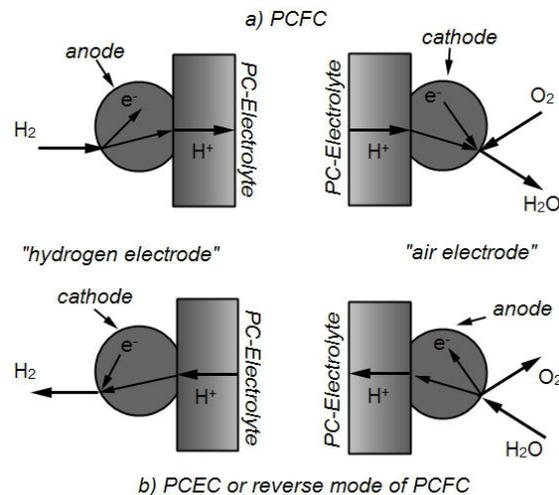
Figure 2.7: *Working diagram of anode and cathode of PCFC (a) and PCEC – reverse mode of PCFC (b) Note: a part involve with fuel may call 'hydrogen electrode' and one involve with oxygen/air call 'air electrode'.*

In fact, some perovskite solid oxide materials used as cathode for PCFC system, could be used as cathode for PCEC. For example, the $La_{0.6}Sr_{0.4}Co_{0.2}Fe_{0.8}O_{3-\delta}$ (LSCF) has been

studied as a cathode for PCFC by Fabbri et al [111]. This materials has also been mentioned for use as anode for PCEC [112]. Similarly, the materials used as cathode for PCFC system were used as anode of PCEC. In some studies [111,113,114], Ni was researched as cathode for PCFC system and as anode of PCEC. Hence, for clearer comprehension, we will refer to "air electrodes" for the PCEC anodes and PCFC cathode, and "hydrogen (or fuel) electrodes" for the PCEC cathodes and PCFC anodes.

As mentioned earlier, most of the protonic SOFCs and SOECs prototypes utilized Pt and Ni. However, Pt was not preferred due to its high cost. Ni was alternatively proposed as hydrogen electrode material, to reduce costs. Although both Pt and Ni performed well with $BaCeO_3$- and $SrCeO_3$-based proton-conducting electrolytes, their performance became poorer with increasing of Zr in the electrolyte composition. Large polarization losses such as $SrZrO_3$ and $BaZrO_3$ [115,116], were noticed. Sakai et al. [117] suggested that the poor performance of these electrodes was attributed to the limited interface area. They also proposed fabrication of plated electrodes, instead of the conventional pasted electrodes, to decrease the electrode particle size. As a matter of this fact, Ni-based composite materials have been investigated the most as hydrogen materials for PCFCs and PCECs.

Table 2.5 summarizes electrical characteristics of Ni-based cermets for hydrogen electrodes applications. The electronic conductivity (S cm^{-1}) is typically measured by the 4 probes method, and the polarization resistance (R_{pol}, Ω cm^2) obtained using EIS on symmetrical cells. The Ni-BZY and Ni-BCY demonstrated excellent catalytic properties and good current collection. Ni-based cermets tended to agglomerate after prolonged operation which led to a reduced three-phase boundary and increased cell resistance. Lei Bi et al. [113] suggested that the area specific resistance (ARS) of Ni-BZY was within the suitable range below 1.5 Ω cm^2. Mather et al. [118], have studied Ni-$CaZr_{0.95}Y_{0.05}O_{2.975}$ (Ni-CZY) and Ni-$SrZr_{0.95}Y_{0.05}O_{2.975}$ (Ni-SZY) cermet anodes for PCFCs prepared by similar mathod. They suggested that the overall polarization resistance was sensitive to the level of proton conductivity in the ceramic-oxide phase. The Ni-CZY electrode was known to produce a polarization resistance higher than Ni-SZY electrode. Comparing chemical stability between Ni-BCY and Ni-BZY [119], the Ni-BCY cermet electrode showed instability in H_2O and CO_2 containing atmosphere, which was unsuitable for practical operation in alternative

carbonaceous fuels. On the contrary, Ni-BZY showed better chemical stability in such carbon dioxide atmosphere.

Table 2.5: *Electrical properties of Ni-based cermet for hydrogen electrode applications.*

Materials	Temp. °C	Testing system	Electrochemical Properties			Ref.
			E_a eV	R_p $\Omega.cm^2$	EIS $S.cm^{-1}$	
Ni-BaSr$_{0.90}$Y$_{0.10}$O$_{3-\delta}$	600	PCFC	n/a	~13	n/a	[120]
Ni-SrCe$_{0.90}$Yb$_{0.10}$O$_{3-\delta}$	700	PCFC	~0.4	5	n/a	[121]
Ni-SrZr$_{0.95}$Y$_{0.05}$O$_{2.975}$	700	PCFC	n/a	~1	n/a	[118]
NiO-BaZr$_{0.8}$Y$_{0.2}$O$_{3-\delta}$	600	PCFC	0.44-0.65	0.37	n/a	[113]
NiO-BaCe$_{0.9}$Y$_{0.1}$O$_{3-\delta}$	600-750	PCFC	~0.7	n/a	>40	[122]

In case of air electrode applications, it is necessary to emphasize again that the two distinct systems involved different reactions; oxygen reduction for PCFC and water oxidation. However, air electrodes for both systems played similar roles. They possessed a larger area of triple phases boundary (TPB, a meeting point of electrode, electrolyte and oxygen ion transfer into the electrolyte) to maximize electrochemical reactions [107,114,119] and to achieve a high electrochemical performance. In addition, Fabbri et al. [111] and He et al. [109] have investigated the air-electrode working mechanism. They indicated that both proton and oxygen ion transport to TPB were rate limiting. Only proton reactions at TPB were limiting in the electrolysis mode. Therefore, the ideal air electrode material for proton conducting electrolytes should also posses both protonic and electronic conduction.

In recent years, only a few materials having both protonic and electronic conductivities have been reported. Table 2.6 summarizes potential perovskite-based oxides for air electrode applications. There are two categories of the electrode: single materials and composite materials. The composite electrodes are generally a mixture component of electrode and electrolyte compound. This material is supposed to increase the ability of protonic transportation. The electrical performances of air electrodes depend on a compatible

electrolyte as well as a cell assembly design. The $Ba_{1-x}Sr_xCo_{1-y}Fe_yO_{3-\delta}$ (BSCF) and $Pr_2NiO_{4+\delta}$ (PNO) in single air electrode was reported by F. Muavy et al. [123], indicating very low polarization resistance (<0.8 $\Omega.cm^2$) in the PCFC system. Furthermore, the authors found that the used of composite electrodes allow an important decrease of polarization resistance for instance 0.23 $\Omega.cm^2$ and 0.19 $\Omega.cm^2$ for PNO-BCY10 and BSCF-BCY10, respectively. The results led many researchers to improve the performance of BSCF by adding silver as the current collectors.

Table 2.6: *Summary of electrical properties of perovskite-based oxide as air electrodes applications.*

Cathode	Electrolyte	Testing system	Temperature °C	R_p $\Omega\ cm^2$	Ref.
Single air electrode					
$Ba_{0.5}Sr_{0.5}Co_{0.8}Fe_{0.2}O_{3-\delta}$	BCY10	PCFC	600	<0.8	[123]
$Pr_2NiO_{4+\delta}$	BCY10	PCFC	600	<0.8	
$La_{0.6}Sr_{0.4}Co_{0.2}Fe_{0.8}O_{3-\delta}$	BCY10	PCFC	600	~6	[56]
$La_{0.58}Sr_{0.4}Co_{0.2}Fe_{0.8}O_{3-\delta}$	BCZY	PCFC	600	0.89	[124]
Composite air electrode					
BCY10-BSCF	BCY10	PCFC	600	0.19	[123]
BCY10-PNO	BCY10	PCFC	600	0.23	
BZCYYb-NNO	BZCYYb	PCFC	750	0.43	[125]

Another example of mixed protonic and electronic conducting materials is $Ln_2NiO_{4+\delta}$ (Ln = La, Pr, Nd) ceramics. They have attracted much attention as alternate air electrode materials for lower-temperature operations. These materials, also gave diffusivity of interstitial oxide-ions at intermediate temperatures. In addition, the thermal expansion coefficient (TEC) values of such $Ln_2NiO_{4+\delta}$ cathodes exhibited a rather good mechanical compatibility with usual electrolytes (12.7×10^{-6} K^{-1}, 13×10^{-6} K^{-1}, 13.6×10^{-6} K^{-1} for $Nd_2NiO_{4+\delta}$, $La_2NiO_{4+\delta}$ and $Pr_2NiO_{4+\delta}$ respectively) [58]. These materials showed intense electrocatalytic activity for oxygen reduction reaction due to their high MIEC properties [56]. The polarization resistance (R_{pol}) of $Ln_2NiO_{4+\delta}$ (Ln = La, Pr, Nd) compounds, obtained from impedance spectroscopy

measurements on symmetrical cell, is shown in Fig. 2.8 [126]. The Pr phases show good electrode materials according to their lowest polarization resistance values.
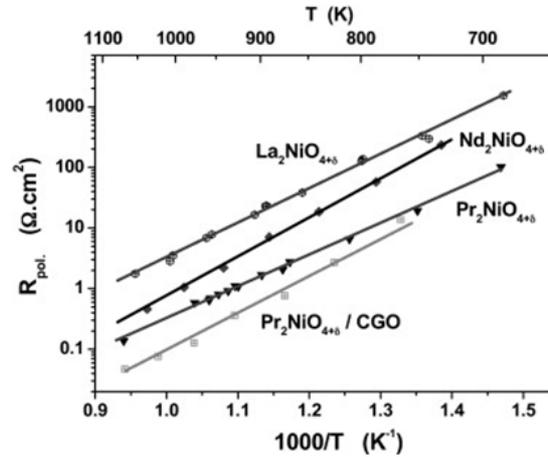
Figure 2.8: *Arrhenius plots of the polarization resistance (R_{pol}) of $Ln_2NiO_{4+\delta}$ (Ln = La, Nd, Pr) [126].*

The iron substitution for cobalt to give $La_{1-x}Sr_xCo_{1-y}Fe_yO_{3-\delta}$ (LSCF) resulted in a compound with fast ion transport, lower TEC and acceptable electronic conduction. Several composite materials based on mixed ionic and electrical conductivity (MIEC) elaborated (i.e. $Ln_2NiO_{4+\delta}$, $La_{1-x}Sr_xCo_{1-y}Fe_yO_{3-\delta}$, $Ba_{1-x}Sr_xCo_{1-y}Fe_yO_{3-\delta}$) with electrolyte compounds (i.e. BCY, GDC) were also studied for protonic-conducting fuel cells. They exhibited a mixed proton and electron conductivity with a good electrocatalytic activity toward the oxygen reduction reaction. However, - there are only a few accessible reports of these composite conductors. In the case of combined $Pr_2NiO_{4+\delta}$ - $BaCe_{0.9}Y_{0.1}O_{3-\delta}$ electrodes, a significant decrease of the polarization resistance with 0.23 $\Omega.cm^2$ under 0.20 bar of pH_2O at 600°C [123], was observed. This implied that the high potential of proton conductivity should also be observed. A $BaZr_{0.1}Ce_{0.7}Y_{0.1}Yb_{0.1}O_{3-\delta}$-$Nd_{1.95}NiO_{4+\delta}$ composite cathode with 60 wt.% of NNO showed 0.43 $\Omega.cm^2$ under water partial pressure at 750°C [125]. Other examples of composite cathodes are LSCF [127,128] and BSCF [123] oxide-based ceramics. The architectured-electrode of BSFC-BCY10 gave lower polarization resistance of 0.19 $\Omega.cm^2$, while the LSCF with BZCY and LCC showed 0.19 $\Omega.cm^2$ and 0.076 $\Omega.cm^2$, respectively. These complex perovskite materials are likely to be potential cathode materials for protonic ceramic fuel cell (PCFC) in the future.

2.4 Vibrational analysis of perovskite-related oxides

The analysis of atom/ion motions using the group theory is a standard procedure used by IR and Raman spectroscopists. It is known as factor group analysis. The symmetry properties of the crystal were determined by studying the effect of each symmetry operation in the factor group on each type of atom in the unit cell. Several symmetry operators were applied to the same vibrational unit. These constituted a "point group". At least one point (the center of gravity) remained unmoved, when the symmetry operations were carried out. Results of factor group analysis, showing the IR and Raman active modes in the case of various expected point symmetry groups of perovskite-liked oxides, are summarized in Table 2.7.

Table 2.7: *Symmetry species and vibrational modes expected for the orthorhombic, tetragonal, rhombohedral and cubic symmetries.*

Factor group	Space group	Known Sample	Irreducible representations			Ref.
			Raman active modes	*IR active modes*	*Inactive modes*	
Orthorhombic structure						
D_{2h}	Pbnm	(Ba,Sr)CeO$_3$	$7A_g + 5B_{1g}$ $+ 7B_{2g}+5B_{3g}$	$9B_{1u}+7B_{2u}+$ $9B_{3u}$	$8A_u + B_{1u}$ $+ B_{2u} + B_{3u}$	[129-134]
	Pnma	SrZrO$_3$	$7A_g + 5B_{1g}$ $+ 7B_{2g}+5B_{3g}$	$9B_{1u}+7B_{2u}+$ $9B_{3u}$	$8A_u + B_{1u}$ $+ B_{2u} + B_{3u}$	[135]
D_{2h}	Bmab	Ln$_2$NiO$_4$ (low-T)	$5A_g + 3B_{1g}$ $+ 4B_{2g} + 6B_{3g}$	$6B_{1u}+7B_{2u}$ $+ 4B_{3u}$	$B_{1u}+B_{2u}+B_{3u}+4A_u$	[136]
Tetragonal structure						
D_{2h}	I4/mmm	Ln$_2$NiO$_4$ (high T)	$2A_{1g} + 2E_g$	$3A_{2u} + 4E_u$	B_{2u}	[136-139]
Rhombohedral structure						
D_{3d}^6	R-3c	LSCF7382	$A_{1g}+4E_g$	$3A_{2u}+5E_u$	$2A_{1u}+3A_{2g}$	[74]
Cubic structure						
O_h	Pm-3m	SrTiO$_3$	none	$3F_{1u}$	$3F_{1u} + F_{2u}$	[140]

The present group theory and vibrational modes were selected from the literature studied [74,129,130,136-140]. The characters of the different irreducible representations were predicted from character table. The highest symmetry (Pm-3m) such as cubic structure had none of Raman active modes. Indeed, there was only one formula unit per unit cell and an

infrared active $3F_{1u}$ phonon. In contrast, in the lower symmetry both Raman and IR modes were active.

This very important point underlined the fact that Raman scattering intensity would be very sensitive to any distortion of the cubic mean structure. Furthermore, because of the very local character of the Raman probe and the Polarisability of the chemical bond(s) involved in the vibrational mode, nanodomains could contribute independently to the spectrum [11,46,52].

2.4.1   Cerate and zirconate materials

For an ideal ABO_3 perovskite-like structure, a low wavenumber range (below ~200 cm^{-1}) revealed the vibrations of the A ion network which coupled themselves with librations modes (T', R') of BO_6 ion-covalent entities leading to the lattice modes. The bending (δ) and stretching (υ) modes of BO_6 octahedra were expected in the 300-500 cm^{-1} and 600-900 cm^{-1} wavenumber range, respectively [141].

According to the orthorhombic phase with Pbnm space group for cerate perovskites, the irreducible representations yielded 24 Raman active modes and 25 IR active modes (Table 2.8) [13,129-135]. For undoped $BaCeO_3$ at -196.15°C, Genet et al. [133] described the motions of each Raman mode below 400 cm^{-1}. They identified that there were 11 number of stretching coordinates; 3 number for Ce-O bonds and 8 number for Ba-O bonds. In addition, the authors considered 6 O-Ce-O and 36 O-Ba-O modes. In the higher wavenumber range, broad and weak bands were at about 520, 630 and 720 cm^{-1}. The authors suggested that this was due to the first- and/or second-order scattering induced by defects such as oxygen vacancies.

In the case of zirconates perovskites at room temperature, undoped $SrZrO_3$ presented an orthorhombic structure with a ZrO_6 octahedra tilted in the unit cell [135]. The $SrZrO_3$ presented 24 Raman active modes as indicated in Table 2.7. In the case of undoped $BaZrO_3$, Ph. Colomban et al. [7] presented that this material had cubic symmetry and the *Pm3m* space group. It may be noted that such cubic symmetry in the first-order Raman activity was forbidden [7]. Yet the authors observed the presence of Raman spectra for such undoped $BaZrO_3$ with significant absolute intensity values induced by the short-range disorder. The

intensity increased after the partial substitution of Zr by lanthanide (Ln-doped $BaZrO_3$), due to the local distorstion induced by oxygen vacancies and Zr substitution. Table 2.8 presents the Raman and IR signatures characteristic of undoped zirconates perovskites studied by our group [12,52,142]. The observed Raman wavenumbers (100-900 cm^{-1}) of both pure barium zirconates and strontium zirconates could be distinguished in three ranges as discussed earlier.

Table 2.8: *Raman and IR signatures and mode assignment of undoped $BaZrO_3$ and $SrZrO_3$ [142].*

Sample	BaZrO₃		SrZrO₃		Assignments
	IR	Raman	IR	Raman	
Observed wavenumber / cm⁻¹			103	114	External modes (lattice modes, T', R')
	136				
		141	140	143	
				166	
		185			
			231		Bending modes of ZrO₆ (δ_ZrO6)
	287	270	279	276	
			302		
				312	
		345			
	376				
			397	391	
		402		410	
		453		439	
		505			
	535				Stretching modes of ZrO₆ (υ_ZrO6)
			542	550	
			660		
	627				
		636		641	
		710			
		737			
				750	
				780	
	820	839	820		

Ph. Colomban et al. [46,47] had also studied Raman scattering of pristine Ln-doped (Yb, Y and In) barium zirconate and barium cerate, Figure 2.9a. A part of their work was

conducted at room temperature. The results showed that the broadening of the Zr-O stretching mode in the case of pristine SZ:Yb was located at ~730 cm^{-1}, and was assigned to the octahedron modes perturbed by oxygen vacancies. Figure 2.9b shows Raman spectra of Y- and Zn-doped BaCeZrO$_{3-\delta}$ observed by Slodczyk et al. [12]. The author observed seven Raman broad lines, This spectrum could not be assigned to the monoclinic symmetry. In other words, the authors suggested that it was in a multiphasic, disordered material. Moreover, the presence of such nanodomains gave rise to the Raman activity depending on the B-site cation octahedra (BO$_6$) polarization. For instance, the contribution modes involving Ce-O and Zr-O bonds were much higher than those of Zn-O bond.
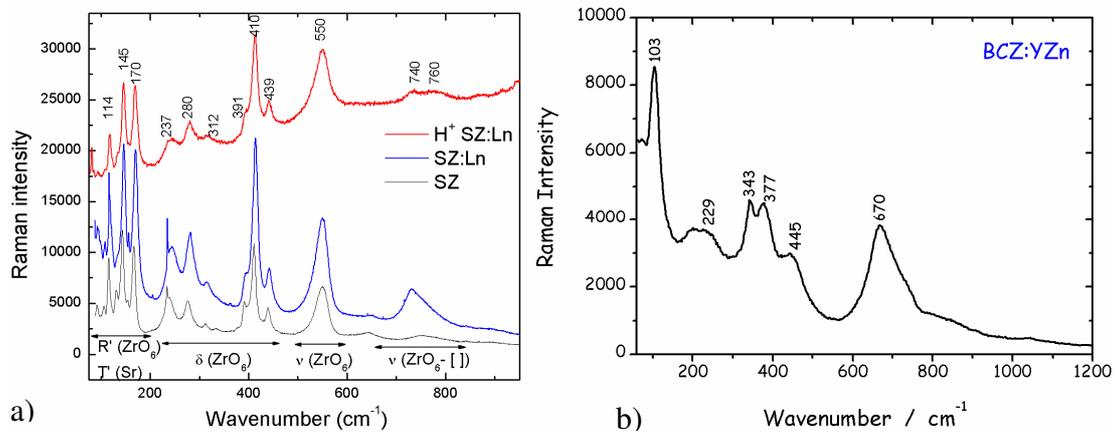
Figure 2.9: *Raman spectra characteristic of SZ, SZ:Ln, and protonated SZ:Ln (a) and BCZ:Y,Zn (b) (Note: reference data from our previous works, Slodczyk et al. [12,49]).*

2.4.2 Nickelate-based oxides

The lattice vibrational modes of stoichiometric and oxidized Ln$_2$NiO$_{4+\delta}$ have been reported by Andres et al. [136]. In the case of stoichiometric Ln$_2$NiO$_4$ (centrosymmetric D$_{2h}$ point group and the primitive cell of the orthorhombic phase (*Bmab*)), 42 normal modes were expected (Table 2.7); 18 Raman active modes, 17 IR active modes and 7 modes were silent. The Ni ions are surrounded by distorted oxygen octahedra but the structure could also be seen as a stacking of alternating planes of Ni-O(1) and planes of Ln-O(2).
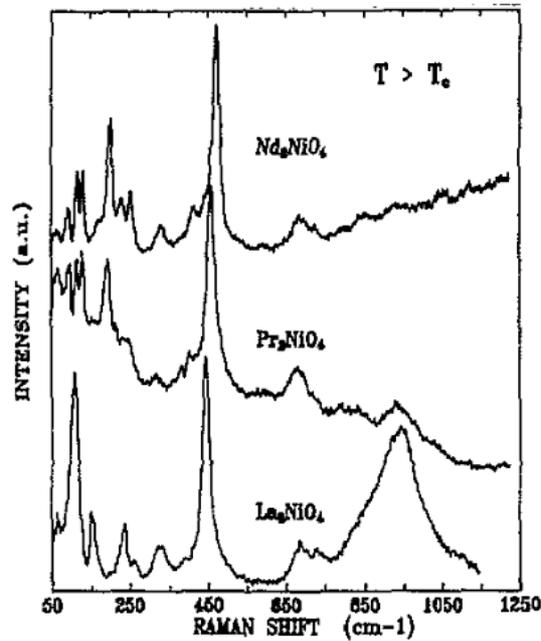
Figure 2.10: *Raman spectra of the stoichiometric Ln$_2$NiO$_4$ compounds at temperature above low-temperature structural phase transition [136].*

Figure 2.10 shows Raman spectra of the stoichiometric Ln$_2$NiO$_4$ compounds studied by Andres et al. [136]. The most intense peak at around 450 cm^{-1} is related to the O(2) stretching modes. The corresponding wavenumber was observed at 443 cm^{-1} for La$_2$NiO$_4$, 457 cm^{-1} for Pr$_2$NiO$_4$, and 470 cm^{-1} for Nd$_2$NiO$_4$. This was not due to a change in the Ni-O(2) distance which was nearly constant for Bmab symmetry compounds (La, ~2.235Å; Pr, ~2.23 Å; Nd, 2.25 Å). It was due to the shortening of the Ln-O(2) distance induced by decreasing the lanthanide ionic radius combined with the mass effect. The same phonon, but associated with the Ln motions, would be shifted in a similar way but at a lower wavenumber at around $\omega_{Ln} = \omega_{O(2)}\sqrt{m_O/m_{Ln}}$. The square root mass ratio was about 3 for the three materials. So the frequency would lie at around 150 – 200 cm^{-1} region to the Ln stretching modes.

Two Raman peaks, detected at the 220-275cm^{-1} region, were assigned to the bending modes of the O(2) and Ln ions. They were separated into motions along the x and y directions. Those parallel to the y-axis corresponded to the tetragonal-to-orthorhombic deformation and maintained a lower energy than the others. Moreover, the stretching and bending motions of the same ions in a vibrational unit were frequently related by the empiric relation, $\omega_s = 2\omega_b$.

80

The equivalent Ln bending mode to stretching mode was attributed to the 100-130 cm^{-1}. The highest-energy one-phonon peak was observed at around 680 cm^{-1} and was due to the Ni—O(1) stretching vibration. Small size of the rare-earth ions induced a more distorted structure with space for interstitial oxygen ions. This finally led to the presence of the tetragonal phase with many defects such as interstitial oxygen ions, or perhaps even to an orthorhombic *Fmmm* or even lower symmetry phase with extra oxygen ions. Table 2.9 indicates the observed IR and Raman characteristic phonon frequencies of tetragonal (I4/mmm) Ln$_2$NiO$_4$ compounds and the mode assignments.

Table 2.9: *Observed phonon frequencies of lanthanide (La, Pr, Nd) nickelate samples.*

Samples	Observed phonon peak position / cm^{-1}							Ref.
				Infrared (IR)				
La$_2$NiO$_{4+\delta}$	109	220	225	343	348	495	685	[136-138]
Pr$_2$NiO$_{4+\delta}$	112	213			320		679	[136,143]
Nd$_2$NiO$_{4+\delta}$	115	228			317		686	[136]
Mode	E$_u$	E$_u$	A$_{2u}$	A$_{2u}$	E$_u$	A$_{2u}$	E$_u$	
Motion	δ Ln-O(II)	δ Ln-O(II)-Ni	υ La-O(II)	υ Ni-O(I)	δ Ni-O(I)	υ La-O(II)-Ni	δ Ni-O(I)	
				Raman (RS)				
La$_2$NiO$_{4+\delta}$	87	151	263	335		443	685	[136-138]
Pr$_2$NiO$_{4+\delta}$	94	160	240	320		457	679	[136]
Nd$_2$NiO$_{4+\delta}$	93	170	254	317		470	686	[136,144]
Mode	E$_g$	A$_{1g}$	E$_g$	E$_g$		A$_{1g}$	E$_u$	
Motion	δ Ln-O(II)	υ La-O(II)	δ La-O(II)-Ni	δ La-O(I)-Ni		υ La-O(II)-Ni	υ La-O(I)-Ni	

The oxidized Ln$_2$NiO$_{4+\delta}$ samples and/or high temperature phase had the tetragonal I4/mmm (D$_{4h}$) symmetry with two formulas in the unit cell and one in the primitive cell. Group theory predicted 2A$_{1g}$+2E$_g$ Raman active modes at the Γ point. However, there were 7 observed IR active modes and 6 observed Raman active modes mentioned in the literature consulted [136-139,143,144].

2.4.3   *La$_{1-x}$Sr$_x$Co$_{1-y}$Fe$_y$O$_{3-\delta}$ materials*

As we discussed in section 2.2.3, the LSC, LSF and LSCF compounds at room temperature, exhibited rhombohedral phase with the R-3c space group. Studies of these complex doubled perovskite are limited. Abrashev et al. [145] reported a case of LaMO$_3$

(M=Al, Mn) perovskite with R-3c space group [145]. In R-3c lattice, the La atoms occupied the 2a ($\frac{1}{4}, \frac{1}{4}, \frac{1}{4}$) positions and gave rise to four modes ($A_{2g} + A_{2u} + E_g + E_u$). The M atoms occupied the 2b ($0,0,0$) positions and participated in four modes ($A_{2u} + A_{2u} + 2E_u$). The oxygen atoms occupied the 6e ($x, \overline{x}+\frac{1}{2}, \frac{1}{4}$) positions and took part in twelve modes ($A_{1g} + A_{1u} + 2A_{2g} + 2A_{2u} + 3E_g + 3E_u$). Within these total 20 Γ-point modes, 18 corresponded to optical phonons. The $A_{1g}+4E_g$ modes were Raman active, the $3A_{2u}+5E_u$ were IR active and the remaining $2A_{1u}+3A_{2g}$ were inactive. Ishikawa et al. [146] studied Raman spectra of the Orbital-Phonon coupling in LaCoO$_3$ with R-3c rhombohedral phase. The geometry of crystal structure was the same as that described by Abrashev et al. [145]. The Raman modes were located at 86, 172, 261, 432, and 584 cm^{-1} at -268.5°C. Their assignments are presented in Table 2.10.

Table 2.10: *Observed Raman frequencies of LSCF compounds [74,128,146,147].*

Samples	Raman (RS) peak position / cm^{-1}					
LaCoO$_3$	86	172	261	432	584	
La$_{0.7}$Sr$_{0.3}$CoO$_3$			298	416	540	646
LaCo$_{0.8}$Fe$_{0.2}$CoO$_3$				485	545	692
La$_{0.7}$Sr$_{0.3}$Co$_{0.8}$Fe$_{0.2}$O$_3$			298	417	550	650
Mode	E$_g$	E$_g$	A$_{1g}$	E$_g$	A$_{2g}$	A$_{2g}$

Very recently, the LSC, LSF, and LSCF materials have been investigated using Raman spectroscopy by Rousseau et al. [74]. Figure 2.11 shows representative Raman spectra of LSCF sample containing the Co amount (5%). A typical Raman spectrum of LSCF consisted of two broad peaks centered at ~546 cm^{-1} and ~632 cm^{-1}, and one broad band at ~420 cm^{-1}, (Fig. 2.11g). Intensity of Raman spectrum increased remarkably at high temperature (>400°C). This indicated the presence of oxygen reduction of LSCF. Namely, the existence of two overlapping bands near 546 and 632 cm^{-1} on the spectrum was observed. Similarly, such overlapping bands result were observed by Siebert et al. [147].

At high temperature together with Jahn-Teller effect, the LSCF E$_g$ vibrational Raman mode at ~432 cm^{-1}, showed strong intensity decrease. Additionally, the broad band of existing

two components was located at 540 cm^{-1}. An observation of a band near 650 cm^{-1} assigned to A$_{2g}$ revealed structural distortion due to the Jahn-Teller effect.
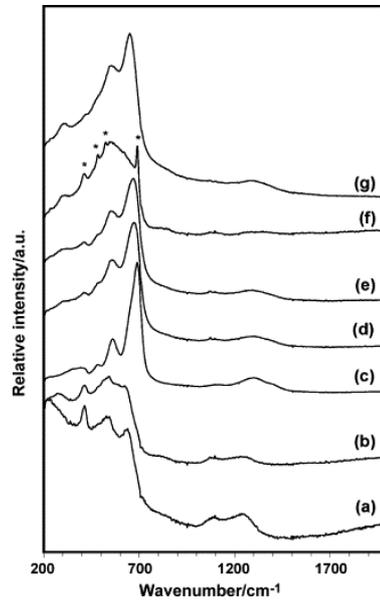
Figure 2.11: *Characteristics of Raman signature at room temperature of (a) LaCoO$_3$, (b) La$_{0.7}$Sr$_{0.3}$CoO$_3$, (c) LaCo$_{0.8}$Fe$_{0.2}$O$_3$, (d) La$_{0.7}$Sr$_{0.3}$Co$_{0.8}$Fe$_{0.2}$O$_3$ (−5% Co), (e) La$_{0.7}$Sr$_{0.3}$Co$_{0.8}$Fe$_{0.2}$O$_3$, (f) La$_{0.7}$Sr$_{0.3}$Co$_{0.8}$Fe$_{0.2}$O$_3$ (+5% Co) and (g) La$_{0.7}$Sr$_{0.3}$Co$_{0.5}$Fe$_{0.5}$O$_3$ samples. *Bands assigned to Co$_3$O$_4$ particles [74].*

References

[1]   W. G. Nilsen, J. G. Skinner, Journal of Chemical Physics 48 (1968) 2240.

[2]   D. Minichelli, F. Ricciardiello, O. Sbaizero, Materials Chemistry and Physics 13 (1985) 153.

[3]   T. Ishihara, Perovskite Oxide for Solid Oxide Fuel Cells, 2009.

[4]   H. Matsumoto, in: T. Ishihara (Ed.), Perovskite oxide for solid oxide fuel cells, Springer Science, New York, USA, 2009, p. 243.

[5]   M. Greenblatt, Current Opinion in Solid State and Materials Science 2 (1997) 174.

[6]   M. Zaghrioui, F. Giovannelli, N. Poirot, D. Brouri, I. Laffez, Journal of Solid State Chemistry 177 (2004) 3351.

[7]   Ph. Colomban, A. Slodczyk, Optical Materials 31 (2009) 1759.

[8]   A. Slodczyk, Ph. Colomban, N. Malikova, O. Zaafrani, S. Longeville, J. M. Zanotti, O. Lacroix, B. Sala, Solid State Ionics 252 (2013) 7.

[9]   A. Slodczyk, M. D. Sharp, S. Upasen, Ph. Colomban, J. A. Kilner, Solid State Ionics 262 (2014) 870.

[10]   Ph. Colomban, A. Slodczyk, D. Lamago, G. Andre, O. Zaafrani, O. Lacroix, S. Willemin, B. Sala, Journal of the Physical Society of Japan 79 (2010) 1.

[11]   A. Slodczyk, Ph. Colomban, O. Zaafrani, O. Lacroix, J. Loricourt, F. Grasset, B. Sala, MRS proceeding 1309 (2011).

[12]   A. Slodczyk, O. Zaafrani, M.D. Sharp, J.A. Kilner, B. Dabrowski, O. Lacroix, Ph. Colomban, Membranes 3 (2013) 311.

[13]   F. Genet, S. Loridant, C. Ritter, G. Lucazeau, Journal of Physics and Chemistry of Solids 60 (1999) 2009.

[14]   K.S. Knight, Solid State Ionics 74 (1994) 109.

[15]   M. Sahu, K. Krishnan, B. K. Nagar, M. K. Saxena, S. Dash, Thermochimica Acta 525 (2011) 167.

[16]   Q. J. Liu, Z. T. Liu, Y. F. Liu, L. P. Feng, H. Tian, J. G. Ding, Solid State Communications 150 (2010) 2032.

[17]   J. Ranlov, K. Nielsen, Journal of Materials Chemistry 4 (1994) 867.

[18]   C. J. Howard, K. S. Knight, B. J. Kennedy, E. H. Kisi, Journal of Physics-Condensed Matter 12 (2000) L677.

[19]   T. Sugimoto, S. Hasegawa, T. Hashimoto, Thermochimica Acta 530 (2012) 58.

[20]   T. Matsuda, S. Yamanaka, K. Kurosaki, S. I. Kobayashi, Journal of Alloys and Compounds 351 (2003) 43.

[21]   K. S. Knight, Journal of Electroceramics 27 (2011) 143.

[22]   F. Giannici, M. Shirpour, A. Longo, A. Martorana, R. Merkle, J. Maier, Chemistry of Materials 23 (2011) 2994.

[23]   K. Koto, M. Itai, C. Numako, Solid State Ionics 154–155 (2002) 741.

[24]   S. K. Gupta, N. Pathak, R. Gupta, S. K. Thulasidas, V. Natarajan, Journal of Molecular Structure 1068 (2014) 204.

[25]   K. D. Kreuer, S. Adams, W. Münch, A. Fuchs, U. Klock, J. Maier, Solid State Ionics 145 (2001) 295.

[26]   D. Medvedev, A. Murashkina, E. Pikalova, A. Demin, A. Podias, P. Tsiakaras, Progress in Materials Science 60 (2014) 72.

[27]   K. Katahira, Y. Kohchi, T. Shimura, H. Iwahara, Solid State Ionics 138 (2000) 91.

[28]   M. Amsif, D. Marrero-López, J. C. Ruiz-Morales, S. N. Savvin, P. Núñez, Journal of the European Ceramic Society 34 (2014) 1553.

[29]   A. K. Azad, J. T. S. Irvine, Solid State Ionics 179 (2008) 678.

[30]   J. Xu, X. Lu, Y. Ding, Y. Chen, Journal of Alloys and Compounds 488 (2009) 208.

[31]   Y. Liu, Y. Guo, R. Ran, Z. Shao, Journal of Membrane Science 437 (2013) 189.

[32]   S. W. Tao, J. T. S. Irvine, Advanced Materials 18 (2006) 1581.

[33]   E. Ruiz-Trejo, Y. Zhou, N. P. Brandon, International Journal of Hydrogen Energy.

[34]   S. Klinsrisuk, J. T. S. Irvine, Solid State Ionics 181 (2010) 168.

[35]   Y. Li, R. Guo, C. Wang, Y. Liu, Z. Shao, J. An, C. Liu, Electrochimica Acta 95 (2013) 95.

[36]   S. Zhang, L. Bi, L. Zhang, Z. Tao, W. Sun, H. Wang, W. Liu, Journal of Power Sources 188 (2009) 343.

[37]   A. J. Jacobson, B. C. Tofield, B. E. F. Fender, Acta Crystallographica Section B 28 (1972) 956.

[38]   K. S. Knight, M. Soar, N. Bonanos, Journal of Materials Chemistry 2 (1992) 709.

[39]   R. R. Chien, C. S. Tu, V. H. Schmidt, S. C. Lee, C. C. Huang, Solid State Ionics 181 (2010) 1251.

[40]   S. Ricote, N. Bonanos, G. Caboche, Solid State Ionics 180 (2009) 990.

[41]   Z. Zhong, Solid State Ionics 178 (2007) 213.

[42]   P. Sawant, S. Varma, B. N. Wani, S. R. Bharadwaj, International Journal of Hydrogen Energy 37 (2012) 3848.

[43]   S. Nikodemski, J. Tong, R. O'Hayre, Solid State Ionics 253 (2013) 201.

[44]   S. Nieto, R. Roque-Malherbe, R. Polanco, L. Fuentes-Cobas, R. S. Katiyar, Ceramics International 40 (2014) 11359.

[45]   A. Grimaud, J. M. Bassat, F. Mauvy, P. Simon, A. Canizares, B. Rousseau, M. Marrony, J. C. Grenier, Solid State Ionics 191 (2011) 24.

[46]   A. Slodczyk, Ph. Colomban, S. Willemin, O. Lacroix, B. Sala, Journal of Raman Spectroscopy 40 (2009) 513.

[47]   A. Slodczyk, Ph. Colomban, D. Lamago, G. Andre, O. Zaafrani, O. Lacroix, A. Sirat, F. Grasset, B. Sala, Journal of Materials Research 27 (2012) 1939.

[48]   A. Slodczyk, Ph. Colomban, G. Andre, O. Zaafrani, F. Grasset, O. Lacroix, B. Sala, Solid State Ionics 225 (2012) 214.

[49]   A. Slodczyk, M. Limage, Ph. Colomban, O. Zaafrani, F. Grasset, J. Loricourt, B. Sala, Journal of Raman Spectroscopy 42 (2011) 2089.

[50]   Ph. Colomban, A. Slodczyk, O. Zaafrani, O. Lacroix, J. Loricourt, F. Grasset, B. Sala, MRS proceeding 1309 (2011).

[51]   Ph. Colomban, C. Tran, O. Zaafrani, A. Slodczyk, Journal of Raman Spectroscopy 44 (2013) 312.

[52]   A. Slodczyk, O. Zaafrani, Ph. Colomban, High water pressure - high temperature autoclave for in situ Raman study of fuel cell/electrolyser materials, Materials Research Society, 2012.

[53]   B. Philippeau, F. Mauvy, C. Mazataud, S. Fourcade, J. C. Grenier, Solid State Ionics 249–250 (2013) 17.

[54]   A. Montenegro-Hernández, J. Vega-Castillo, L. Mogni, A. Caneiro, International Journal of Hydrogen Energy 36 (2011) 15704.

[55]   J. D. Jorgensen, B. Dabrowski, S. Pei, D. R. Richards, D. G. Hinks, Physical Review B 40 (1989) 2187.

[56]   J. Dailly, S. Fourcade, A. Largeteau, F. Mauvy, J. C. Grenier, M. Marrony, Electrochimica Acta 55 (2010) 5847.

[57]   R. Sayers, S. J. Skinner, Journal of Materials Chemistry 21 (2011) 414.

[58]   E. Boehm, J. M. Bassat, P. Dordor, F. Mauvy, J. C. Grenier, P. Stevens, Solid State Ionics 176 (2005) 2717.

[59]   G. Liu, T. T. Chen, J. Wang, X. Q. Liu, X. M. Chen, Journal of Alloys and Compounds 579 (2013) 502.

[60]   M. T. Fernández-Díaz, J. L. Martínez, J. Rodríguez-Carvajal, Solid State Ionics 63–65 (1993) 902.

[61]   M. Zinkevich, F. Aldinger, Journal of Alloys and Compounds 375 (2004) 147.

[62]   P. Odier, Y. Nigara, J. Coutures, M. Sayer, Journal of Solid State Chemistry 56 (1985) 32.

[63]   E. Niwa, T. Nakamura, J. Mizusaki, T. Hashimoto, Thermochimica Acta 523 (2011) 46.

[64]   K. Ishikawa, K. Metoki, H. Miyamoto, Journal of Solid State Chemistry 182 (2009) 2096.

[65]   Y. Toyosumi, H. Ishikawa, K. Ishikawa, Journal of Alloys and Compounds 408–412 (2006) 1200.

[66]   A. V. Kovalevsky, V. V. Kharton, A. A. Yaremchenko, Y. V. Pivak, E. N. Naumovich, J. R. Frade, Journal of the European Ceramic Society 27 (2007) 4269.

[67]   D. J. Buttrey, J. D. Sullivan, G. Shirane, K. Yamada, Physical Review B 42 (1990) 3944.

[68]   C. Allançon, A. Gonthier-Vassal, J. M. Bascat, J. P. Loup, P. Odier, Solid State Ionics 74 (1994) 239.

[69]   E. Niwa, K. Wakai, T. Hori, K. Yashiro, J. Mizusaki, T. Hashimoto, Thermochimica Acta 575 (2014) 129.

[70]   J. Rodríguez-Carvajal, J. L. Martínez, J. Pannetier, R. Saez-Puche, Physical Review B 38 (1988) 7148.

[71]   S. J. Skinner, Solid State Sciences 5 (2003) 419.

[72]   L. W. Tai, M. M. Nasrallah, H. U. Anderson, D. M. Sparlin, S. R. Sehlin, Solid State Ionics 76 (1995) 273.

[73]   L. W. Tai, M. M. Nasrallah, H. U. Anderson, D. M. Sparlin, S. R. Sehlin, Solid State Ionics 76 (1995) 259.

[74]   S. Rousseau, S. Loridant, P. Delichere, A. Boreave, J. P. Deloume, P. Vernoux, Applied Catalysis B: Environmental 88 (2009) 438.

[75] L. da Conceicao, A. M. Silva, N. F. P. Ribeiro, M. Souza, Materials Research Bulletin 46 (2011) 308.

[76] H. L. Lein, K. Wiik, T. Grande, Solid State Ionics 177 (2006) 1795.

[77] A. L. Soldati, L. Baqué, F. Napolitano, A. Serquis, Journal of Solid State Chemistry 198 (2013) 253.

[78] J. Emmerlich, B. M. Linke, D. Music, J. M. Schneider, Solid State Ionics 255 (2014) 108.

[79] K. Kreuer, Annual Review of Materials Research 33 (2003) 333.

[80] T. Norby, Solid State Ionics 125 (1999) 1.

[81] H. Iwahara, T. Esaka, H. Uchida, N. Maeda, Solid State Ionics 3–4 (1981) 359.

[82] H. Iwahara, Solid State Ionics 28–30, Part 1 (1988) 573.

[83] H. Uchida, H. Yoshikawa, H. Iwahara, Solid State Ionics 35 (1989) 229.

[84] T. Yajima, H. Iwahara, H. Uchida, Solid State Ionics 47 (1991) 117.

[85] T. Hibino, K. Mizutani, T. Yajima, H. Iwahara, Solid State Ionics 57 (1992) 303.

[86] T. Yajima, H. Suzuki, T. Yogo, H. Iwahara, Solid State Ionics 51 (1992) 101.

[87] H. Iwahara, T. Yajima, T. Hibino, K. Ozaki, H. Suzuki, Solid State Ionics 61 (1993) 65.

[88] T. Yajima, H. Kazeoka, T. Yogo, H. Iwahara, Solid State Ionics 47 (1991) 271.

[89] H. Iwahara, Solid State Ionics 52 (1992) 99.

[90] H. Iwahara, Solid State Ionics 86–88, Part 1 (1996) 9.

[91] L. Malavasi, C. Fisher, M. Islam, Chemical Society Reviews 39 (2010) 4370.

[92] A. Magrasó, C. Kjølseth, R. Haugsrud, T. Norby, International Journal of Hydrogen Energy 37 (2012) 7962.

[93] Y. Liu, Y. Guo, R. Ran, Z. Shao, Journal of Membrane Science 415–416 (2012) 391.

[94] F. L. Chen, O. T. Sørensen, G. Y. Meng, D. K. Peng, Journal of the European Ceramic Society 18 (1998) 1389.

[95] M. Hakim, C. Y. Yoo, J. H. Joo, J. H. Yu, Journal of Power Sources 278 (2015) 320.

[96] B. Singh, J. H. Kim, J. Y. Park, S. J. Song, Ceramics International 41 (2015) 4814.

[97] N. Maffei, L. Pelletier, J. P. Charland, A. McFarlan, Journal of Power Sources 162 (2006) 165.

[98] C. Chen, G. Ma, Journal of Alloys and Compounds 485 (2009) 69.

[99] N. I. Matskevich, T. A. Wolf, The Journal of Chemical Thermodynamics 42 (2010) 225.

[100] W. B. Wang, J. W. Liu, Y. D. Li, H. T. Wang, F. Zhang, G. L. Ma, Solid State Ionics 181 (2010) 667.

[101] T. Scherban, A. S. Nowick, Solid State Ionics 35 (1989) 189.

[102] H. Matsumoto, Y. Kawasaki, N. Ito, M. Enoki, T. Ishihara, Electrochemical and Solid-State Letters 10 (2007) B77.

[103] J. F. Liu, A. S. Nowick, Solid State Ionics 50 (1992) 131.

[104] T. Higuchi, T. Tsukamoto, N. Sata, K. Hiramoto, M. Ishigame, S. Shin, Japanese Journal of Applied Physics Part 1-Regular Papers Short Notes & Review Papers 40 (2001) 4162.

[105] T. Higuchi, T. Tsukamoto, N. Sata, S. Yamaguchi, S. Shin, T. Hattori, Solid State Ionics 176 (2005) 2963.

[106] H. G. Bohn, T. Schober, Journal of the American Ceramic Society 83 (2000) 768.

[107] L. Bi, S. Boulfrad, E. Traversa, Chemical Society Reviews 43 (2014) 8255.

[108] P. Ranran, W. Yan, Y. Lizhai, M. Zongqiang, Solid State Ionics 177 (2006) 389.

[109] F. He, D. Song, R. Peng, G. Meng, S. Yang, Journal of Power Sources 195 (2010) 3359.

[110] H. Iwahara, H. Uchida, N. Maeda, Journal of Power Sources 7 (1982) 293.

[111] E. Fabbri, L. Bi, D. Pergolesi, E. Traversa, Energy & Environmental Science 4 (2011) 4984.

[112] S. Li, K. Xie, Journal of the Electrochemical Society 160 (2013) F224.

[113] L. Bi, E. Fabbri, Z. Sun, E. Traversa, Journal of the Electrochemical Society 158 (2011) B797.

[114] L. Bi, S. Boulfrad, E. Traversa, Solid State Ionics 275 (2015) 101.

[115] T. Sakai, S. Matsushita, H. Matsumoto, S. Okada, S. Hashimoto, T. Ishihara, International Journal of Hydrogen Energy 34 (2009) 56.

[116] E. Fabbri, A. D'Epifanio, E. Di Bartolomeo, S. Licoccia, E. Traversa, Solid State Ionics 179 (2008) 558.

[117] T. Sakai, H. Matsumoto, T. Kudo, R. Yamamoto, E. Niwa, S. Okada, S. Hashimoto, K. Sasaki, T. Ishihara, Electrochimica Acta 53 (2008) 8172.

[118] G. C. Mather, F. M. Figueiredo, J. R. Jurado, J. R. Frade, Solid State Ionics 162–163 (2003) 115.

[119] N. Nasani, Z. J. Wang, M. G. Willinger, A. A. Yaremchenko, D. P. Fagg, International Journal of Hydrogen Energy 39 (2014) 19780.

[120] N. Nasani, D. Ramasamy, A. D. Brandão, A. A. Yaremchenko, D. P. Fagg, International Journal of Hydrogen Energy 39 (2014) 21231.

[121] G. C. Mather, F. M. Figueiredo, D. P. Fagg, T. Norby, J. R. Jurado, J. R. Frade, Solid State Ionics 158 (2003) 333.

[122] M. Zunic, L. Chevallier, A. Radojkovic, G. Brankovic, Z. Brankovic, E. Di Bartolomeo, Journal of Alloys and Compounds 509 (2011) 1157.

[123] P. Batocchi, F. Mauvy, S. Fourcade, M. Parco, Electrochimica Acta 145 (2014) 1.

[124] S. Ricote, N. Bonanos, P. M. Rørvik, C. Haavik, Journal of Power Sources 209 (2012) 172.

[125] C. Yang, X. Zhang, H. Zhao, Y. Shen, Z. Du, C. Zhang, International Journal of Hydrogen Energy 40 (2015) 2800.

[126] C. Ferchaud, J. C. Grenier, Y. Zhang-Steenwinkel, M. M. A. van Tuel, F. P. F. van Berkel, J. M. Bassat, Journal of Power Sources 196 (2011) 1872.

[127] L. Yang, Z. Liu, S. Wang, Y. Choi, C. Zuo, M. Liu, Journal of Power Sources 195 (2010) 471.

[128] M. Liu, D. Ding, K. Blinn, X. Li, L. Nie, M. Liu, International Journal of Hydrogen Energy 37 (2012) 8613.

[129] T. Scherban, R. Villeneuve, L. Abello, G. Lucazeau, Solid State Communications 84 (1992) 341.

[130] T. Scherban, R. Villeneuve, L. Abello, G. Lucazeau, Solid State Ionics 61 (1993) 93.

[131] S. Loridant, G. Lucazeau, T. Le Bihan, Journal of Physics and Chemistry of Solids 63 (2002) 1983.

[132] S. Loridant, L. Abello, G. Lucazeau, Journal of Raman Spectroscopy 28 (1997) 283.

[133] F. Genet, S. Loridant, G. Lucazeau, Journal of Raman Spectroscopy 28 (1997) 255.

[134] S. Loridant, G. Lucazeau, Journal of Raman Spectroscopy 30 (1999) 485.

[135] L. S. Cavalcante, A. Z. Simões, J. C. Sczancoski, V. M. Longo, R. Erlo, M. T. Escote, E. Longo, J. A. Varela, Solid State Sciences 9 (2007) 1020.

[136] A. de Andres, M. T. Fernandez-Diaz, J. L. Martinez, J. Rodriguez-Carvajal, R. Saez-Puche, F. Fernandez, Journal of Physics: Condensed Matter 3 (1991) 3813.

[137] F. E. Bates, J. E. Eldridge, Solid State Communications 72 (1989) 187.

[138] N. Ogita, M. Udagawa, K. Kojima, K. Ohbayashi, Journal of the Physical Society of Japan 57 (1988) 3932.

[139] B. Rousseau, J. M. Bassat, A. Blin, M. S. de Oliveira, P. Odier, C. Marin, P. Simon, Solid State Sciences 6 (2004) 1131.

[140] M. A. Islam, J. M. Rondinelli, J. E. Spanier, Journal of Physics-Condensed Matter 25 (2013).

[141] O. Zaafrani, Dotoral thesis "Protonation, distorsions structurales et espèces protoniques dans des pérovskites lacunaires", Université Pierre et Marie Curie, Paris, France, 2010.

[142] O. Zaafrani, Protonation, distorsions structurales et espéces protoniques dans des perovskites lacunaires, PhD thesis, Université Pierre et Marie Curie - Paris, 2010.

[143] R. P. S. M. Lobo, C. Allançon, K. Dembinski, P. Odier, F. Gervais, Solid State Communications 88 (1993) 349.

[144] C. Prieto, A. de Andrés, M. Medarde, J. L. Martinez, M. T. Fernández-Díaz, J. Rodríguez-Carvajal, R. Sáez-Puche, F. Fernández, Solid State Communications 80 (1991) 975.

[145] M. V. Abrashev, A.P. Litvinchuk, M. N. Iliev, R. L. Meng, V. N. Popov, V. G. Ivanov, R. A. Chakalov, C. Thomsen, Physical Review B 59 (1999) 4146.

[146] A. Ishikawa, J. Nohara, S. Sugai, Physical Review Letters 93 (2004) 136401.

[147] E. Siebert, A. Boréave, F. Gaillard, T. Pagnier, Solid State Ionics 247–248 (2013) 30

CHAPTER 3

"Potential secondary and corrosion phases"

In this Chapter, the potential secondary and corrosion phases characterized by vibrational spectroscopy will be addressed.

Chapter 3

Potential secondary and corrosion phases

3.1 Potential secondary phases

Alkaline earth metals are basic components that react easily with CO_2 [1-4]. A carbonation reaction for the perovskite-related oxides may be represented as:

$$ABO_3 + CO_2 \rightarrow ACO_3 + BO_2 \qquad \text{…(eq. 3.1)}$$
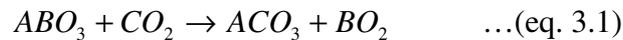
where A, B are generally Ba, Sr, Ce, or Zr cations, respectively. Matsumoto [5] explained that this reaction occurs with 1 bars CO_2 at temperature less than a critical temperature - around 1025°C for Barium cerates and 575 – 628°C for that of zirconates. Therefore, whenever hydrocarbon is used as fuel with barium cerate-based electrolyte, the cell should be operated at higher temperature than the critical temperature in order to avoid deterioration by the reaction with CO_2.

Several studies suggest that cerate zirconate solid solutions are stable in CO_2 (~0.017 bar) [6-8]. For example, sintered perovskite $SrCe_{0.95}Yb_{0.05}O_{3-\delta}$, $SrZr_{0.9}Y_{0.1}O_{3-\delta}$ and $BaCe_{0.6}Zr_{0.3}Nd_{0.1}O_{3-\delta}$ ceramics were exposed to 800°C for 3 h in 100% CO_2 and the H_2-CO-CO_2 mixture. In the case of $SrCe_{0.95}Yb_{0.05}O_{3-\delta}$, CeO_2 and $SrCO_3$ were formed on exposure to both CO_2 and H_2-CO-CO_2 mixture gases. The electrolyte reacted with CO_2, as shown in Eq. 3.2-3.3, to form $SrCO_3$, $BaCo_3$ and CeO_2 [5].

$$SrCeO_3 + CO_2 \rightarrow SrCO_3 + CeO_2 \qquad \text{…(eq. 3.2)}$$

$$BaCeO_3 + CO_2 \rightarrow BaCO_3 + CeO_2 \qquad \text{…(eq. 3.3)}$$
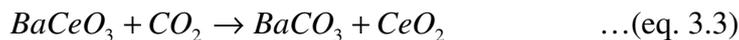
3.1.1 Raman/IR vibrational modes of carbonates

Fundamentally, for CO_3^{2-} ion in the free state, the molecule exhibits four normal modes [9]; υ_1 symmetric stretching mode (A_1', Raman active), υ_2 symmetric bending mode

(A_1'', IR active), υ_3 asymmetric stretching mode (E', IR and Raman active) and υ_4 asymmetric bending mode (E'', IR and Raman active). The normal modes of these four vibrations are shown in Fig. 3.1.
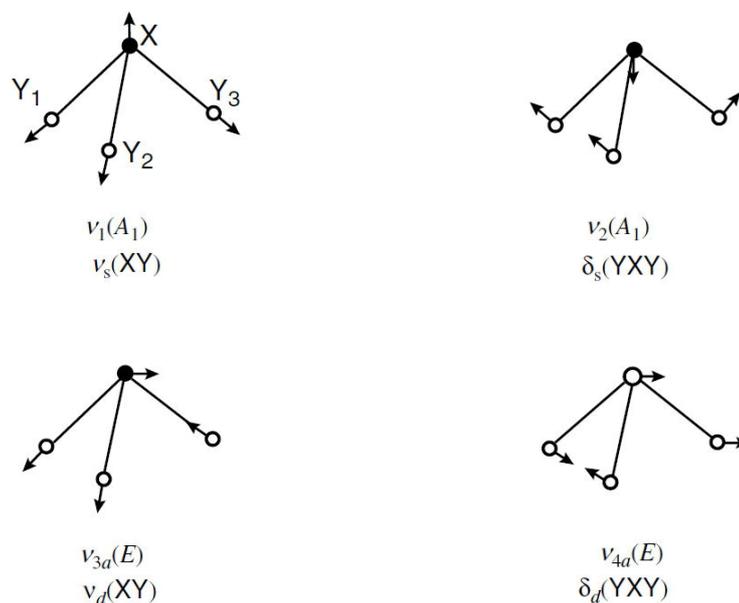
Figure 3.1: *Normal modes of vibration of pyramidal XY$_3$ molecules [9,10].*

Because of the covalent character of CO$_3$ vibrational unit, the stretching mode is well defined and narrow and thus easily detected, even at very low intensity. Although only oxygen atoms move in the symmetric stretching mode, the coupling with the cation is sufficiently strong to induce mass dependent shift and thus the carbonate composition can be identified. Librational and lattice modes are also rather strong and characteristic of each carbonate.

Table 3.1 summarizes the f Raman signature of carbonate compounds.. The Raman study of second phase occuring on surface electrolyte samples was verified by many authors [11-14]. Several type of electrolyte perovskite-oxide ceramics were exposed at intermediate temperature under low to high vapor pressure. In case of SrZr$_{0.9}$Yb$_{0.1}$O$_{3-\delta}$ ceramic, the Raman peak at ~1070 cm^{-1} was observed and assigned as traces of SrCO$_3$. For different Ln-doped barium zirconates, Raman signature of BaCO$_3$ compounds was observed at 1060 cm^{-1}.

Table 3.1: *Raman signature of potential carbonate compounds (Note: the bold characters are strong bands).*

Formula	Raman wavenumber / cm^{-1}	Ref.
I-La$_2$O$_2$CO$_3$	427, 315, 670, 721, 867, **1064**	[15]
Ia-La$_2$O$_2$CO3	93, 106, **124**, **137**, **155**, **223**, **298**, **319**, **341**, **441**, **458**, 671, 680, 698, 716, 730, 858, **1050**, **1060**	[15,16]
II-La$_2$O$_2$CO$_3$	**82**, **112**, **125**, **204**, **256**, **363**, **393**, **660**, **675**, **745**, 1066, **1088**	[15,16]
LaCO$_3$(OH)	**149**, **196**, **247**, **377**, **702**, **725**, **725**, **1087**	[17]
Nd$_2$(CO$_3$)$_3$·8H$_2$O	162, **195**, 226, **336**, 684, 730, **761**, **1091**	[18]
NdCO$_3$(OH)	**149**, **198**, **229**, **250**, **371**, **702**, **727**, **1084**	[19]
SrCO$_3$	100, **148**, **180**, 236, **244**, **258**, 510, **710**, **1071**, 1445	[20-22]
FeCO$_3$	**194**, **299**, **731**, **1088**, **1434**, 1738	[22-24]
CoCO$_3$	180, 202, **304**, 725, **1087**, 1430, 1726	[24,25]
NiCO$_3$	**235**, **343**, **736**, **1089**, **1428**, 1731	[24]

3.1.2   Raman/IR vibrational modes of metal oxides

The common method to identify corrosion products is to compare Raman spectra of the corrosion layers with the reference spectra of expected phases [26-31].

Raman signature of iron oxides and other metal oxides are summarized in Table 3.2. Furthermore, because of the lack of reliable literature, Raman study of La$_2$O$_3$-based and CoO.OH compounds will be discussed in the next section. Magnetite (Fe$_3$O$_4$) crystallizes in the spinel structure with space group Fd3m. Iron ions occupy both tetrahedral and octahedral sites. It is an inverse spinel with metal conductivity at room temperature. Owing to the cubic ABCABC dense packing of the oxygen atoms, density reaches 5.18 [32,33]. The crystal structure of maghemite (γ-Fe$_2$O$_3$) is closely related to the crystal structure of magnetite with vacancies (and possible proton insertion). Consequently, the density lowers to 4.87 [33]. The basic structure of γ-Fe$_2$O$_3$ is cubic (space group: P4$_3$32), whereas the ordered distribution of the cation vacancies results in a symmetry reduction (P4$_1$2$_1$2) [34]. The structure of α-Fe$_2$O$_3$

corresponds to the R3c space group with a hexagonal ABAB dense packing of the oxygen atoms [33]. Density is therefore high (~5.23). Structures of goethite (α-FeOOH) and lepidocrocite (γ-FeOOH) are more complex. They can be roughly described as frameworks made of the dense oxygen atom packing presented above. This preserves a layered structure in which many oxygen atoms are missing and some others are replaced by OH⁻ species. The density decreases, and the lowest value is measured for lepidocrocite (d=3). The second order mode at about 1320 cm⁻¹ is generally the stronger one under green laser excitation and can be used for the detection of traces [28,35,36].

Table 3.2: *Raman signature of potential metal oxide compounds*
(Note: the bold character is strong band).

Formula	Raman wavenumber / cm^{-1}	Ref.
A-La_2O_3	**103, 189, 405**	[15,37,38]
C-La_2O_3	116, 270, **312**, 356, 376	[15]
Pr_2O_3	226, **458**, 598, 726	[39,40]
A-Nd_2O_3	**105, 150, 190, 334, 427, 436**	[37,41,42]
SrO_2	**863**	[waal, 1998]
SrO	**520, 540, 560**	
γ-Fe_2O_3	**358, 390, 499, 678, 710**	[28,34,35,43]
α-Fe_2O_3	**226, 247, 292, 406, 495, 600, 700**, 819	[28,35,44]
Fe_3O_4	**297, 319, 523, 666**	[35,43,44]
Co_3O_4	**184, 456, 510, 602, 669**	[45,46]
NiO	210, 406, **541, 723, 901, 1085, 1260**	[47]

3.2 Lanthanum oxides/oxyhydroxide/oxycarbonates

Lanthanum oxide is a well-known compound that highly reacts with water and CO_2, and hydroxide and carbonate compounds are produced [48,49]. This phenomenon also occurs with

Rare earth (RE)-rich compounds such as nickelates ($Ln_2NiO_{4+\delta}$) perovskites. Raman scattering of lanthanum oxide-based materials was studied.

Rare earth (RE) oxides can be formed in hexagonal phase, namely A-type RE oxide, with space group $P\bar{3}m1$. The phonons can be classified according to irreducible representation of the D_{3d} point group: $\left(2A_{1g} + 2E_g\right)$ Raman active and $\left(2A_{2u} + 2E_u\right)$ IR active. Another form, C-type RE sesquioxides, are body center cubic phase with space group Ia-3. This structure is related to fluorite structure with each RE ion located at the centre of the cube from which two of the eight nearest neighbor oxygen of the fluorite structure have been removed. Due to body-centered structure, the unit-cell contains the primitive structure twice. So, only eight unit formulas must be used to theoretically determine the number of vibrations. The irreducible representations for the optical and acoustical of Raman active are 22 modes of $4A_g + 4E_g + 14F_g$ [15,37,50].

La_2O_3, $La_2O_2CO_3$ and $La_2(CO_3)_3.xH_2O$ powders were collected from our collaboration with *SPCTS Laboratory, UMR CNRS 7315, Limoges*. Raman spectra were recorded at elevated temperature (30-800°C) using Labram HR800 Raman micro-spectrometer (Horiba Jobin Yvon SAS, Lonjumeau, France) equipped with Linkam (Linkam Scientific Instruments Ltd., Surrey, United Kingdom) heating stage. The above materials are very hydroscopic. Recording the spectra as a function of the temperature guarantees the collection of convenient spectrum for each phase. The 458 nm line delivered by Ar^+ ion laser was used. The Raman scattering was performed under power of 2 mW throughout an objective of 50x (long working distance). The spectra were collected in the range of 60-4000 cm^{-1}. The spectra results, presented in Figure 3.2, are of 10 accumulations, each lasting 5 seconds.

The Raman scattering of La_2O_3 powder, (Fig. 3.2a), was examined using Linkam device with the heating rate of 10°C.min^{-1}. When La_2O_3 powder sample was kept in the air at room temperature (Fig. 3.2a), it rapidly hydrated Well-defined peaks at 143, 232, 287, 346, and 455 cm^{-1}, as well as a weak broadband at 612 cm^{-1} were observed. An intense signature at ~3606 cm^{-1} was shown due to symmetric stretching mode of O-H. These Raman signatures were rather similar to those in the relevant literature [15], and were attributed to $La(OH)_3$ phase, formed at the powder surface.

a)   b)
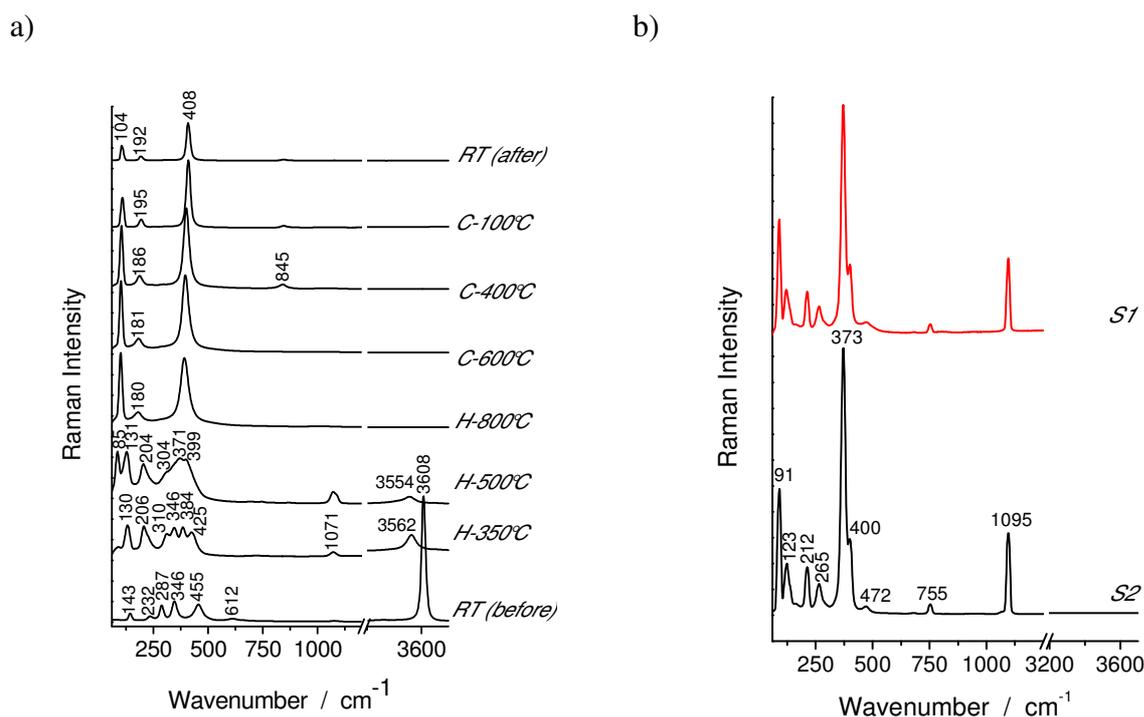
Figure 3.2: *Raman spectra of a) La$_2$O$_3$ based sample at different temperature b) La$_2$O$_2$CO$_3$ at
room temperature.*

Raman spectrum of La$_2$O$_3$-based oxide at 350°C (Fig. 3.2a) presented coexisted phase of
LaOOH and I-La$_2$O$_2$CO$_3$. Raman signatures at 130, 206, 310, 346, 384, and 425 cm^{-1} were
assigned to the LaOOH compound. A weak peak detected at 1071 cm^{-1} is attributed to I-
La$_2$O$_2$CO$_3$. A broad peak at 3562 cm^{-1} of the 350°C Raman spectrum was also observed due
to asymmetric stretching mode of O-H bond. At 500°C, two signatures at ~130 and ~206 cm^{-1}
of LaOOH were remained. However, bands at 300-500 cm^{-1} were modified: i) a broad band at
304 cm^{-1} appeared, and well-defined peaks at 310 and 343 cm^{-1} of spectrum at 350°C
disappeared; ii) peaks at 384 and 425 cm^{-1} moved downshift to 371 and 398 cm^{-1}.
Furthermore, peaks detected at 85 and 1071 cm^{-1} were observed. These could be assigned to
the tetragonal phase of the La$_2$O$_2$CO$_3$ compound.

After heating the sample at 800°C for one hour, the Raman spectrum detected three well-
defined peaks at 104, 181 and 391 cm^{-1}. It showed results similar to those in the literature
available on the subject [15], and assigned to single phase of A-La$_2$O$_3$ type. Consequently, we
recorded Raman spectra during cooling step from 800°C to room temperature. It showed that
the sample remained in the form of A-La$_2$O$_3$ type. However, the Raman spectrum collected

100

after opening the Linkam immediately showed the three peaks (104, 192, and 408 cm^{-1}) with slightly higher wavenumber. In our study, we obtained only a pure A-La$_2$O$_3$ type from the sample of thermally treated La(OH)$_3$ powder. Orera et. al [15] cannot separate between C- and A-La$_2$O$_3$ type by heating LaOOH phase to 400°C in a furnace under vacuum ambient for several hours. The Raman signatures showed at 103, 189, 312, and 404 cm^{-1}.

Figure 3.2b shows well representative Raman spectra of La$_2$O$_2$CO$_3$ powder sample at room temperature. We observed peaks at 91, 123, 212, 265, 373, 400, 472, 755, and 1095 cm^{-1}. These peaks were similar to those in the available literature, which assigned to II-La$_2$O$_2$CO$_3$ type [15]. However, a peak at 122 cm^{-1} was observed to be different from that in the literature - appeared two well-defined peaks at 112 and 125 cm^{-1}.

Table 3.1 indicates the Raman signatures of L$_2$O$_3$-based materials as well as prepared II-La$_2$O$_2$CO$_3$ powder with the litearature data [15].

Table 3.3: *Raman signature (cm^{-1}) of La$_2$O$_3$ based and La$_2$O$_2$CO$_3$ samples.*

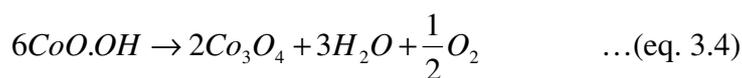| La$_2$O$_3$ based sample								La$_2$O$_2$CO$_3$	II-La$_2$O$_2$CO$_3$
RT	*La(OH)$_3$ [15]*	*350°C*	*LaOOH [15]*	*500°C*	*800°C*	*RT (after)*	*A-La$_2$O$_3$ [15]*	*RT*	*A,Orera [15]*
144	137,8	85		85,8	101,1	105	103,7	91	82,7
233,5	227		116,2w		180,6	193	189,7	122	112,5
287,9	281,7	129	123,2	128,5	391,6	408	405,8	137 b	125,5
346,2	339		135,4		845 w			166 w	
455,7	449		164,7w					212	204,7
613,1 w	605,2 b	205,2	202,4	203,8				265	256,5
	648,8 b, w	226,8 b	216,1	224,8 b				372	363,5
		311,1	312,3	305,5 b				400	393,8
		343,4	344,6	371,6				472	660,3
		382,9	383	398				682 w	675,4
		424,2	424,5	693,1 w				753,5	745
		677 w		747,5 w					1066,5 vw
		714 w		868,6 w				1096	1088
		1069		1071					

Note: vs: very strong, s: strong, m: medium, w: weak, n: narrow, b: broad

3.3 Cobalt oxides/oxyhydroxide

Heterogenite, a cobalt oxyhydroxide has been proposed as an alternative low cost natural material for numerous applications such as battery technology, catalyst, supraconductor and semiconductor sensor [46,51-54]. This material has the formula CoO.OH with a brucite-like structure with layers of edge-sharing Co (III) oxohydroxo octahedral [46,54,55]. Two forms of heterogenite are identified, namely heterogenite-2H and heterogenite-3R. The heterogenite-2H has trigonal symmetry (*R-3m*) while the 3R possesses hexagonal symmetry (*P6$_3$/mmc*). The existence of such forms makes the formation of polytypes possible.

Burlet et al. [46] studied heterogenite (CoO.OH) using Raman spectroscopy (532 nm, 2 mW and x50 LWD). The authors showed four different types of Raman response of natural heterogenite samples; i) heterogenite, ii) dehydroxylated heterogenite, iii) Ni-bearing heterogenite, and iv) bured heterogenite. Show figures from the literature, the spectra of heterogenite exhibits two main peaks; at 495cm^{-1}, 623cm^{-1} and two minor peaks; at 1133 cm^{-1} and 1202 cm^{-1}. The authors also investigated the heterogenite as a function of temperature. Dehydroxylation of heterogenite resulted in the Co-spinel structure (Co$_3$O$_4$). The crystal structure of oxide spinels belongs to the space group O$_h^7$-Fd3m, and a primitive unit cell consists of 2 formula units. The numbers of optically active lattice vibrations under this symmetry, when analyzed by the group theory, yielded 14 irreducible representations of lattice vibrational at Γ point; $A_{1g} + E_g + 3F_{2g}$ (Raman active) + $4F_{1u}$ (IR active) + $F_{1g} + 2A_{2u} + 2E_u + 2F_{2u}$ (inactive). According to Feng Gu et al. [52] and T. Yu et al. [56], they suggested that the Co-spinels Raman signatures at 482, 521, 618, and 690 cm^{-1} were corresponded, respectively, to the E_g, F_{2g}^1, F_{2g}^2, and A_{1g} modes of crystalline Co$_3$O$_4$.

Figure 3.3 shows thermal analysis result of a sample of cobalt oxyhydroxide (CoO.OH). A small flat piece of heterogenite formed in black mining was investigated by thermogravimetry (TG) and thermal expansion (TE). Experimental details are described in appendix D. The thermodynamic behavior, in particular the mass variation with temperature, (Fig. 3.3a), was observed. There were two mass losses at around 350°C and 850°C. This was similar to the study of Deliens [57]. He described the transformation corresponding to the following formula:

$$6CoO.OH \rightarrow 2Co_3O_4 + 3H_2O + \frac{1}{2}O_2 \qquad \text{...(eq. 3.4)}$$

$$Co_3O_4 \rightarrow 3CoO + \frac{1}{2}O_2 \qquad \text{...(eq. 3.5)}$$

The TG curve, Fig. 3.3a, confirms transformation into Co-spinel near 300°C. The theoretical mass loss for the OH⁻ (see eq. 3.4) is 12.6%. In addition, its reversible reduction into cobalt monoxide is at about 900°C, and the theoretical mass loss is about 6.6%.

a) **b)**
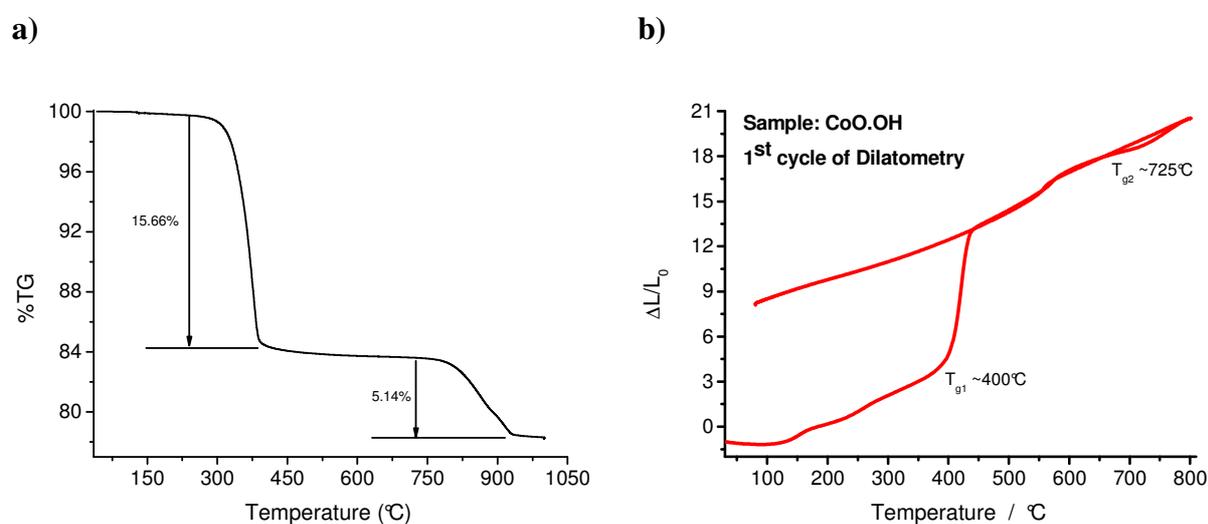
Figure 3.3: *Thermal analysis of CoOOH (black mining) a) TGA curve under He-atmosphere, 10°C.min⁻¹ and b) Therman expansion curve under Ar-atmosphere, 10°C.min⁻¹.*

The thermal expansion curve, (Fig. 3.3b), exhibits a huge expansion jump at 400°C, and a small one at 750°C. The abrupt jump at 400°C is due to dehydroxylation of hetrogenite into Co-spinel. This results in the structural phase transition from hexagonal to cubic phase of Co-spinel.

Figure 3.4 shows Raman spectra of heterogenite and Co-spinel phase. The Raman scattering was performed using 458 nm laser line. The Co-spinel phase was transformed from originated heterogenite material by i) laser-induced heating/transformation ii) thermal treatment at 800°C under argon atmosphere. The Raman spectra presented in Fig. 3.4 show that:

103
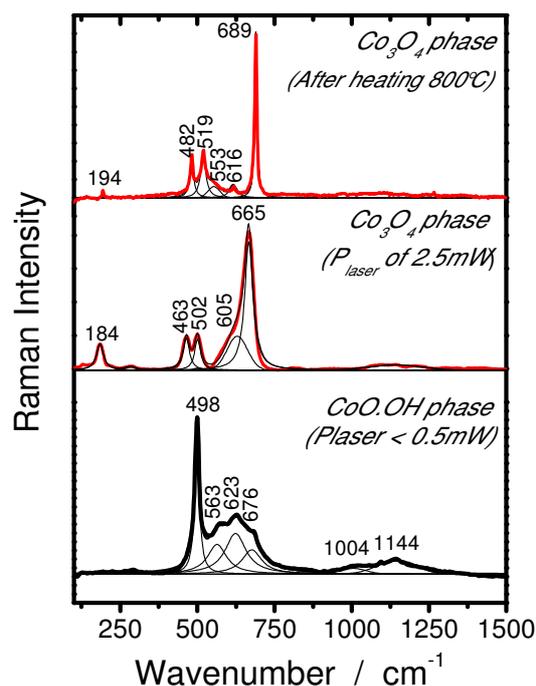
Figure 3.4: *Raman spectra of CoO.OH and Co₃O₄ sample using 458 nm laser line and 50x long working distance objective.*

- Raman spectrum of heterogenite unaffected by laser heating (<0.5 mW) are characterized by a major peak at 498 cm^{-1}, and a broader peak centred at 623cm^{-1}. The broad peak centered at 1144 cm^{-1} are similar to the result of the overlapping of the three minor peaks at 563 cm^{-1}, 623 cm^{-1} and 676 cm^{-1}. These positions are in agreement with those reported by Burlet et. al [46].

- Raman spectrum of laser-induced Co-spinel shows five visible peaks at 184, 463, 502, 605 cm^{-1} (shoulder) and 665 cm^{-1} (major peak). These positions are downshifted (~5-10 cm^{-1}) because of the Raman response to the thermally treated heterogenite sample. This can be attributed to the very small size of the formed spinel crystals (nanometric scale), as has been discussed by Ai and Jiang [58].

- For the Co-spinel structure by artificial heating, the Raman spectrum shows a well-defined peaks at 689 cm^{-1} (main peak) and 616, 519, 482, 194 cm^{-1}. It exhibits a significant upward shift.

References

[1]   H. Matsumoto, Y. Kawasaki, N. Ito, M. Enoki, T. Ishihara, Electrochemical and Solid State Letters 10 (2007) B77.

[2]   M. J. Scholten, J. Schoonman, J. C. van Miltenburg, H. A. J. Oonk, Solid State Ionics 61 (1993) 83.

[3]   S. Gopalan, A. V. Virkar, Journal of the Electrochemical Society 140 (1993) 1060.

[4]   N. Bonanos, K. S. Knight, B. Ellis, Solid State Ionics 79 (1995) 161.

[5]   T. Ishihara, Perovskite Oxide for Solid Oxide Fuel Cells, 2009.

[6]   K. Katahira, Y. Kohchi, T. Shimura, H. Iwahara, Solid State Ionics 138 (2000) 91.

[7]   S. Wienströer, H. D. Wiemhöfer, Solid State Ionics 101–103, Part 2 (1997) 1113.

[8]   K. H. Ryu, S.M. Haile, Solid State Ionics 125 (1999) 355.

[9]   K. Nakamoto, Infrared and Raman Spectra of Inorganic and Coordination Compounds, John Wiley & Sons, Inc., 2008, p. 1.

[10]   K. Nakamoto, Infrared and Raman Spectra of Inorganic and Coordination Compounds, John Wiley & Sons, Inc., 2008, p. 149.

[11]   A. Slodczyk, O. Zaafrani, M.D. Sharp, J.A. Kilner, B. Dabrowski, O. Lacroix, Ph. Colomban, Membranes 3 (2013) 311.

[12]   A. Slodczyk, M. Limage, Ph. Colomban, O. Zaafrani, F. Grasset, J. Loricourt, B. Sala, Journal of Raman Spectroscopy 42 (2011) 2089.

[13]   A. Slodczyk, O. Zaafrani, Ph. Colomban, High water pressure - high temperature autoclave for in situ Raman study of fuel cell/electrolyser materials, Materials Research Society, 2012.

[14]   Ph. Colomban, O. Zaafrani, A. Slodczyk, Membranes 2 (2012) 493.

[15]   A. Orera, G. Larraz, M. Sanjuan, Journal of the European Ceramic Society 33 (2013) 2103.

[16]   I. Atribak, B. Azambre, A. Bueno López, A. García-García, Applied Catalysis B: Environmental 92 (2009) 126.

[17]   RRUFF, Kozoite-(La), $LaCO_3(OH)$. RRUFF Project, Department of Geosciences, University of Arizona, AZ, USA.

[18]   S. M. Morrison, M. B. Andrade, M. D. Wenz, K. J. Domanik, R. T. Downs, Acta Crystallographica Section E: Structure Reports Online 69 (2013) i15.

[19]   RRUFF, Kozoite-(Nd), $NdCO_3(OH)$. RRUFF Project, Department of Geosciences, University of Arizona, AZ, USA.

[20]   RRUFF, Strontianite-$SrCO_3$. RRUFF Project, Department of Geosciences, University of Arizona, AZ, USA.

[21]   W. Kaabar, S. Bott, R. Devonshire, Spectrochimica Acta Part A: Molecular and Biomolecular Spectroscopy 78 (2011) 136.

[22]   A. I. Cuza, Anal Şt Univ   Al I Cuza   Iaşi Geologie 2 (2009) 97.

[23]   D. B. Langille, D. C. O'Shea, Journal of Physics and Chemistry of Solids 38 (1977) 1161.

[24]   H. N. Rutt, J. H. Nicola, Journal of Physics C: Solid State Physics 7 (1974) 4522.

[25]   J. T. Kloprogge, L. V. Duong, M. Weier, W. N. Martens, Applied Spectroscopy 60 (2006) 1293.

[26]   D. Gardiner, C. J. Littleton, K. M. Thomas, K. Strafford, Oxidation of Metals 27 (1987) 57.

[27]   S. C. Tjong, Materials Research Bulletin 18 (1983) 157.

[28]   Ph. Colomban, S. Cherifi, G. Despert, Journal of Raman Spectroscopy 39 (2008) 881.

[29]   D. Neff, S. Reguer, L. Bellot-Gurlet, P. Dillmann, R. Bertholon, Journal of Raman Spectroscopy 35 (2004) 739.

[30]   J. H. Kim, I. S. Hwang, Nuclear Engineering and Design 235 (2005) 1029.

[31]   R. L. Farrow, R. E. Benner, A. S. Nagelberg, P. L. Mattern, Thin Solid Films 73 (1980) 353.

[32]   B. Weckler, H. D. Lutz, European Journal of Solid State and Inorganic Chemistry 35 (1998) 531.

[33]   R. W. G. Wyckoff, Crystal Structures (2nd ed.), Interscience Publishers–John Wiley & Sons: New York, 1964.

[34]   A. N. Shmakov, G. N. Kryukova, S. V. Tsybulya, A. L. Chuvilin, L. P. Solovyeva, Journal of Applied Crystallography 28 (1995) 141.

[35]   F. Froment, A. Tournie, Ph. Colomban, Journal Raman Spectroscopy 39 (2008) 560.

[36]   M. C. Caggiani, Ph. Colomban, Journal of Raman Spectroscopy 42 (2011) 839.

[37]   S. I. Boldish, W. B. White, Spectrochimica Acta Part A: Molecular Spectroscopy 35 (1979) 1235.

[38]   B. M. Faroldi, J. F. Múnera, L. M. Cornaglia, Applied Catalysis B: Environmental 150–151 (2014) 126.

[39]   A. C. Cabral, L. S. Cavalcante, R. C. Deus, E. Longo, A. Z. Simões, F. Moura, Ceramics International 40 (2014) 4445.

[40]   D. Vijayalakshmi, N. Shekar, S. Ramya, P. Sahu, G. Meenakshi, Journal of Alloys and Compounds 505 (2010) 733.

[41]   B. Umesh, B. Eraiah, H. Nagabhushana, B. M. Nagabhushana, G. Nagaraja, C. Shivakumara, R. P. S. Chakradhar, Journal of Alloys and Compounds 509 (2011) 1146.

[42]   B. Umesh, B. Eraiah, H. Nagabhushana, S. C. Sharma, B. M. Nagabhushana, C. Shivakumara, J. L. Rao, R. P. S. Chakradhar, Spectrochimica Acta Part A: Molecular and Biomolecular Spectroscopy 94 (2012) 365.

[43]   M. A. Legodi, D. de Waal, Dyes and Pigments 74 (2007) 161.

[44]   Z. Wang, C. J. Liu, Nano Energy 11 (2015) 277.

[45]   Q. Jiao, M. Fu, C. You, Y. Zhao, H. Li, Inorganic Chemistry 51 (2012) 11513.

[46]   C. Burlet, Y. Vanbrabant, H. Goethals, T. Thys, L. Dupin, Spectrochimica Acta Part A: Molecular and Biomolecular Spectroscopy 80 (2011) 138.

[47]   RRUFF, Bunsenite - NiO. RRUFF Project, Department of Geosciences, University of Arizona, AZ, USA.

[48]   Ph. Colomban, C. Tran, O. Zaafrani, A. Slodczyk, Journal of Raman Spectroscopy 44 (2013) 312.

[49]   Ph. Colomban, Materials Science Forum 251-254 (1997) 833.

[50]   A. Ubaldini, M. M. Carnasciali, Journal of Alloys and Compounds 454 (2008) 374.

[51]   M. A. G. Soler, T. F. O. Melo, S. W. da Silva, E. C. D. Lima, A. C. M. Pimenta, V. K. Garg, A. C. Oliveira, P. C. Morais, Journal of Magnetism and Magnetic Materials 272 (2004) 2357.

[52]   F. Gu, C. Li, Y. Hu, L. Zhang, Journal of Crystal Growth 304 (2007) 369.

[53]   A. L. Soldati, L. Baqué, F. Napolitano, A. Serquis, Journal of Solid State Chemistry 198 (2013) 253.

[54]   C. W. Tang, C. B. Wang, S. H. Chien, Thermochimica Acta 473 (2008) 68.

[55]   J. Yang, H. Liu, W. N. Martens, R. L. Frost, The Journal of Physical Chemistry C 114 (2009) 111.

[56]   T. Yu, Y. W. Zhu, X. J. Xu, Z. X. Shen, P. Chen, C. T. Lim, J. T. L. Thong, C. H. Sow, Advanced Materials 17 (2005) 1595.

[57]   M. Deliens, Les Oxydes hydraté de cobalt du Shaba Méridional, Doctorate Thesis, University of Louvain, Belgium, 1972.

[58]   L. H. Ai, J. Jiang, Powder Technology 195 (2009) 11.

CHAPTER 4

"Combined bulk and surface analysis of the BaCe$_{0.5}$Zr$_{0.3}$Y$_{0.16}$Zn$_{0.04}$O$_{3-\delta}$ (BCZYZ) ceramic proton-conducting electrolyte"

In this chapter, we will report the characterization of BaCe$_{0.5}$Zr$_{0.3}$Y$_{0.16}$Zn$_{0.04}$O$_{3-\delta}$ (BCZYZ) ceramic samples, which were exposed under H$_2$O pressure (60 mbar and 10 bar) at intermediate temperature. The fundamental analysis techniques i.e. IR, Raman spectroscopy, TGA, TE, TEM, and X-ray diffraction are employed.

Combined bulk and surface analysis of the BaCe$_{0.5}$Zr$_{0.3}$Y$_{0.16}$Zn$_{0.04}$O$_{3-\delta}$ (BCZYZ) ceramic proton-conducting electrolyte

Aneta Slodczyk [a,*], Matthew D. Sharp [b], Settakorn Upasen [a], Philippe Colomban [a], John A. Kilner [b]

[a] LADIR UMR7075 CNRS, UPMC, 4 Pl. Jussieu, 75005 Paris, France
[b] Department of Materials, Imperial College London, London SW7 2AZ, UK

ARTICLE INFO

ABSTRACT

BaCe$_{0.5}$Zr$_{0.3}$Y$_{0.16}$Zn$_{0.04}$O$_{3-\delta}$ (BCZYZ) has been advocated as a potential high calibre proton conductor, offering the benefits of both stability and increased proton conductivity. In this work we examine the bulk and surface features of the ceramic in its protonated and unprotonated forms. Following protonation, under H$_2$O pressure as low as 60 mbar, Ba rich surface features are observed at the grain boundary regions, where apparently H$_2$O preferentially attacks. Such surface secondary phases are also noted in the Raman data following a higher pressure treatment of 10 bar, appearing into the sample bulk after 30 h at 500 °C. BCZYZ's stability towards steam is also discussed.

© 2014 Elsevier B.V. All rights reserved.

1. Introduction

Recently, Ln/RE-modified, oxygen deficient perovskite proton-conducting ceramics have been considered as a potential basis of the hydrogen and methanol economy [1–5]. Namely, they can be used as electrolytic membranes (electrolyte and cermet electrodes) of fuel cells, electrolysers and/or CO$_2$/Syngas convertors. In order to meet the standards for industrial application, such membranes should exhibit high proton conductivity in an intermediate temperature range (below 600 °C) and high structural, chemical and mechanical stability under steam and CO$_2$ conditions. Consequently, finding the best proton-conducting perovskite material is a true challenge. Presently, barium cerates are regarded as having amongst the highest proton conductivities reported, though they are unstable in CO$_2$ and steam, in comparison to zirconates which offer reduced proton conductivity but increased stability [6–8]. In combining the BaCe$_{1-x}$Y$_x$O$_{3-\delta}$ and BaZr$_{1-x}$Y$_x$O$_{3-\delta}$ systems, an apparent optimised material could be obtained [9]. The introduction of small amounts of Zn into the structure, e.g. BaCe$_{0.5}$Zr$_{0.3}$Y$_{0.16}$Zn$_{0.04}$O$_{3-\delta}$ (the so called BCZYZ) [9], permits a reduction in high sintering temperatures that is essential in electrolyte-electrode co-firing.

In this work we seek to examine in detail the bulk and surface features of BaCe$_{0.5}$Zr$_{0.3}$Y$_{0.16}$Zn$_{0.04}$O$_{3-\delta}$ ceramic: i) as prepared (non-protonated) ii) protonated under low water vapour pressure (60 mbar, a typical value representative of many laboratory cell tests) and iii) exposed to high water vapour pressure (10 bar, a value required for industrial demonstrators and plants [10,11]), using a variety of techniques: thermogravimetric analysis (TGA), thermal expansion, energy dispersive X-ray spectroscopy (EDX), white light interferometry, infrared spectroscopy (IR), X-ray diffraction and Raman scattering, performed ex situ and in situ using a high temperature-high water pressure autoclave device. The understanding of the surface properties/reactivity and their direct relation with the bulk properties, often neglected in the literature, is necessary to determine the complex behaviour of proton conducting ceramics and to enhance their life time and performance [12,13].

2. Experimental methods

The BCZYZ ceramic was prepared in pellet form (97% of max. theoretical density) using the solid state reaction method based on that described by Tao and Irvine [9] and high temperature sintering (1350 °C). The surfaces of the pellet samples were then ground using SiC paper and subsequently polished with diamond paste down to a 0.25 μm finish prior to all surface studies. Samples were standardised by annealing the as prepared BCZYZ at 950 °C for 12 h in high purity dry ^{16}O (99.9995%) (pO$_2$ = 200 mbar), and this pre-annealing step was performed prior to subsequent protonations.

Low pressure water vapour exposure was performed on the samples by placing them under vacuum before introducing water in the gas phase by heating it in a water bath at a temperature of 45 °C, giving a water pressure of 60 mbar. The sample was then heated to 400 °C for 12 h.

High water vapour pressure treatment was performed using a high temperature/high pressure water vapour (~500 °C, 10 bar, decarbonated water) autoclave which reproduces the operating

* Corresponding author at: Aneta Slodczyk LADIR UMR7075 CNRS, UPMC, 4 Pl. Jussieu, 75005 Paris, France.
E-mail address: slodczyk_aneta@yahoo.com (A. Slodczyk).

Chemical and structural stability of proton conductor perovskite ceramic for fuel cells and electrolyzers

conditions as found in water-steam electrolyser demonstrators [10,11,14,15], for periods of 5 and 30 h. This bespoke autoclave, equipped with a sapphire window and associated with the high sensitivity Raman micro-spectrometer HE 532 (Horiba Jobin Yvon), allowed the observation of the protonation process in situ by Raman scattering [14].

Ex situ Raman scattering was performed using a HR800 spectrometer (Horiba, Jobin Yvon) equipped with a Peltier effect cooled CCD detector. Raman spectra were recorded using 458 and 514 nm wavelengths through the ×50 long distance working Nikon objective. A Linkam heating stage was used to record the Raman spectra of the non-protonated ceramic as a function of temperature. The Raman spectra of the protonated samples were collected on the cross section fracture of freshly broken ceramics immediately after exposure to steam conditions.

TGA was performed between 40 and 1000 °C using a Setaram Setsys Evolution thermobalance. The use of Pt-crucible and He-inert gas atmosphere allowed the significant enhancement of the measurement accuracy.

IR spectra were recorded using the Bruker IR-scope FTIR spectrometer in ATR mode.

X-ray diffraction was carried out on the surfaces of the pellet samples using a Bruker D2 Phaser diffractometer.

EDX and SEM studies were carried out on the as prepared and low pressure protonated sample using a JSM6400 scanning electron microscope fitted with an Oxford Instruments INCA energy dispersive analytical system (EDS), for elemental X-ray analysis.

White light interferometry was performed on the low pressure protonated sample using a Zygo NewView 200 white-light microscope-based interferometer.

3. Results

3.1. Analysis of non-protonated BCZYZ

In order to determine the impact of the proton/protonation on a perovskite ceramic, it is first necessary to have a good understanding of the behaviour of material in a non-protonated state. Consequently we have performed TGA, IR, X-ray and Raman analysis of an as-prepared $BaCe_{0.5}Zr_{0.3}Y_{0.16}Zn_{0.04}O_{3-\delta}$ ceramic. The Raman spectrum characteristic of this compound is presented in Fig. 1a. This spectrum is typical of perovskite-like structure — the low wavenumber region (up to 200 cm^{-1}) reveals the translational vibrations of Ba-cations, whereas the middle (up to 500 cm^{-1}) and high wavenumber ranges are characteristic of bending and stretching vibrations of the BO$_6$ octahedra, respectively. It is noted, in the case of BCZYZ ceramic, that there are potentially 4 different elements in the B-site; consequently we can expect the presence of 4 different polyhedra (CeO$_6$, ZrO$_6$, YO$_6$ octahedron and ZnO$_6$ or ZnO$_4$ octahedron/tetrahedron). The room temperature Raman spectrum is composed of at least 6 rather broad Raman modes similar to those presented by Charrier-Cougoulic et al. [16] and Tu et al. [17] for homologue compounds. The Raman line broadness can be explained by the structural disorder related to the probable presence of nanoregions/nanodomains of different symmetry (for example the ZrO$_6$ with cubic symmetry and orthorhombic CeO$_6$) and of different dimension (shown in the sketch in Fig. 1b). Note that the presence of nanoregions with distinct symmetry is often detected in multicomponent perovskite materials, for example highly disordered relaxor ferroelectrics [18 and refs therein] and even in pure BaZrO$_3$ [19].

It should be stressed that the X-ray diffraction data (Fig. 1d and e) reveals lower symmetry than the cubic with Pm3m space group, which
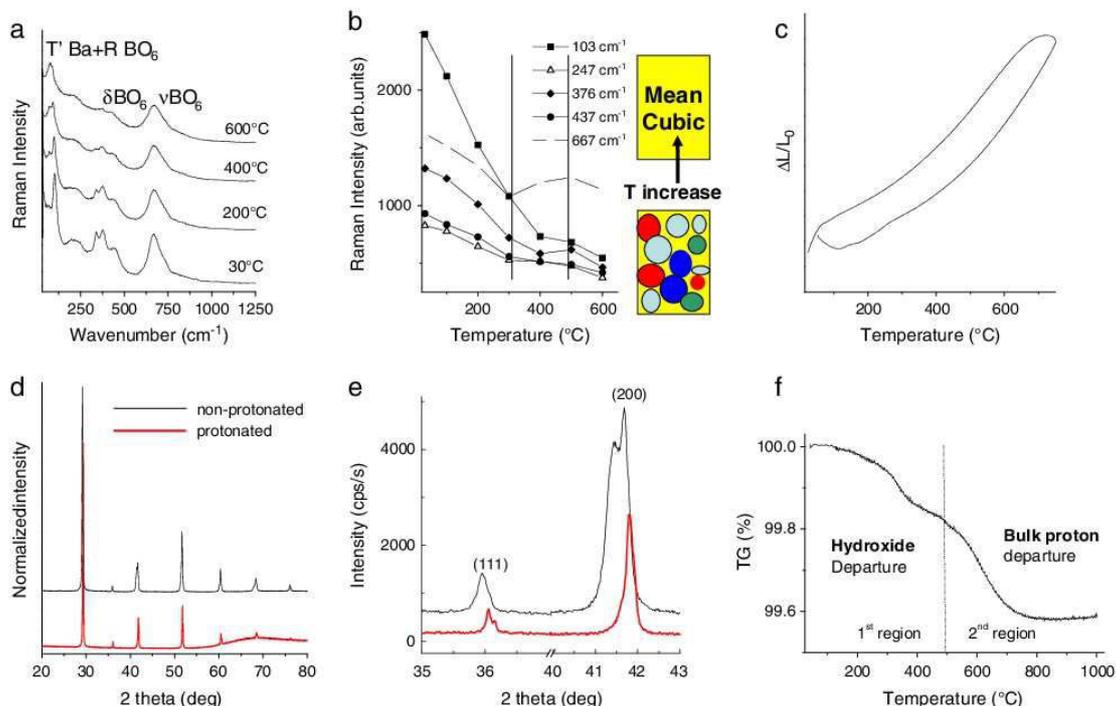
Fig. 1. Characterization of pristine, non-protonated BCZYZ ceramic: a) Raman spectra as a function of temperature. b) Temperature dependences of Raman mode intensities — the lines marked the presence of two structural modifications. Sketch of structural modifications: in room temperature the presence of regions/nanodomains with distinct local symmetry; with the temperature increase system evolves towards mean cubic one. c) Thermal expansion curve. d) Comparison of X-ray diffraction patterns characteristic of non-protonated and low-pressure protonated BCZYZ ceramic. e) Zoom of (111) and (200) Bragg reflections characteristic of non-protonated and low-pressure protonated BCZYZ ceramic. f) TGA curve characteristic of non-protonated BCZYZ ceramic with two unexpected mass losses revealing the presence of hydroxide and bulk protons.

allows the Raman activity, a common feature observed in the case of heavily substituted structures. The exact mean symmetry is however not clear. The characteristic Bragg peaks splitting is not ambiguous: (111) line is not single revealing non-orthogonal system. Literature data [16,17] show that BCZY with Ce-content equal to 0.5 possesses rhombohedral symmetry. However, as shown in Fig. 1c, the (200) Bragg peak is composed of at least 2 components, which reveals a lower symmetry. Note that Tu et al. [17] showed the monoclinic distortions in the case of BCZY with higher Ce-content. The TGA data presented in Fig. 1f may offer another explanation. Namely, two unexpected mass losses are revealed for non-protonated BCZYZ ceramic. According to our previous TG studies [12], the first one detected below 500 °C can be explained by the departure of some secondary phases, most probably hydroxides, while the second one, above 550 °C, is consistent with the departure of bulk protonic species. The TG analysis shows clearly that the non-protonated ceramic already contains some protonic species. The origin of these species is, however, not clear: either formed during the synthesis or during a simple exposure to atmospheric conditions. The first assumption is not consistent with the high sintering temperature. It is noted that the second cycle of TG performed at a temperature lower than the sintering one does not show any further presence of protonic species — the hydroxide secondary phases as well as bulk protons can be easily removed by usual thermal treatment in dry atmosphere above 300 °C and 600 °C, respectively. Taking into account the TGA data, one can suppose that the X-ray pattern can be explained by the coexistence of non-protonated and slightly protonated phases at the surface. The coexistence of similar phases has already been revealed in homologue Ba-based perovskites [20,21]. As shown in Fig. 1e, the X-ray diffraction pattern of the protonated ceramic reveals no splitting of Bragg reflections, consequently a higher symmetry, probably the cubic one. The protonation then leads to the re-symmetrisation of crystal structure as previously demonstrated for Ba and Sr-based, Ln substituted zirconates [22].

Another important point of our study concerns the structural and mechanical stability. Consequently, we have recorded Raman spectra over a wide temperature range (Fig. 1a), covering the operating temperature region. As it can be clearly seen, with temperature increase, some Raman lines become very broad and absolute Raman intensity decreases significantly. Fig. 1b presents the temperature evolution of Raman mode intensities. Such behaviour of intensity is typical of disordered perovskites that achieve true cubic symmetry with heating [19,23]. The true cubic symmetry does not allow Raman activity, the local structural distortions — even of mean cubic symmetry, then gives rise to the Raman spectrum presence. As presented schematically in Fig. 1b, the different nanoregions/nanodomains related to the different octahedral types give rise to important structural distortions detected as high Raman intensity. The higher the deviation from cubic symmetry, the higher the Raman peak number and spectrum intensity [19,23]. With the temperature increase the mean symmetry as well as nanoregions evolve towards the cubic symmetry that is observed as important intensity decrease. The temperature evolution of the Raman mode intensities exhibits 2 minima which points to the presence of two structural modifications. The thermal expansion results (Fig. 1c) show clearly that these modifications exhibit the continuous character. The lack of abrupt changes of the host perovskite structure guarantees the material's mechanical stability.

3.2. Analysis of low-pressure protonated BCZYZ

The EDX, SEM and white light interferometry (Fig. 2) techniques reveal the changes of BCZYZ ceramic following 12 h of treatment at 400 °C under 60 mbar of water vapour pressure.

Fig. 2a shows the presence of surface features, located at the grain boundaries, on the surface of fully dense BCZYZ ceramic, after wet annealing under 60 mbar H$_2$O at 400 °C.
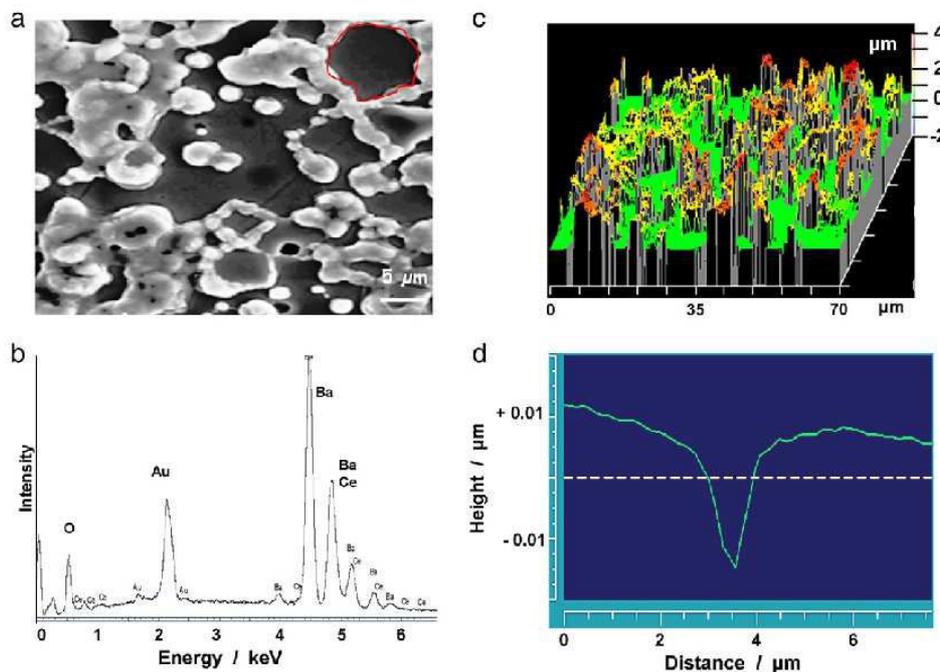

Fig. 2. Polished BCZYZ, annealed in 60 mbar H$_2$O for 12 h at 400 °C SEM micrograph (a) and EDX (b) analysis showing Ba-rich surface features. c) A white light interferometry measurement showing the surface topography. d) The grain, boundary is especially sensitive to the formation of Ba-rich formation.

113

These analyses show the clear formation of secondary phases on the ceramic surface. White light interferometry measurements show that the surface features are uniform and approximately 4 μm above the flat polished regions of the sample (Fig. 2c). However, for this length and temperature of protonation, the surface features are not observed at the entire grain boundary region, and, from the white light interferometry data, it is possible to perform a line measurement across a feature-free grain boundary (Fig. 2d) The EDX results suggest that the surface features are Ba-rich phases such as $BaCO_3$, $Ba(OH)_2,nH_2O$, for example. It is noted that the presence of $Ba(O)$ in the grain boundary is very often observed in the case of perovskite materials [24]. This leads to an unfortunate high reactivity of a ceramic with H_2O and CO_2, and in consequence to the formation of secondary phases.

It should be stressed that the X-ray diffraction pattern, recorded at the pellet surface, (Fig. 1d) shows a changing of symmetry, probably into a cubic one, after low water pressure exposure, but does not reveal the presence of the secondary phases. It is likely that X-ray diffraction is not efficient enough to detect traces of secondary phases. Consequently, the effect of high pressure treatment will be followed by vibrational and TGA methods which are extremely sensitive to detect the secondary phases, even if they are limited to traces, not detectable by diffraction methods.

3.3. Analysis of high-pressure protonated BCZYZ

In order to verify the structural stability under high water vapour pressure (10 bar, 500 °C) we followed the protonation process/operating in situ for periods of 5 and 30 h in a unique autoclave device [14]. The conditions used are typical operating conditions of water-steam electrolysers, and as we have shown in our previous articles [10–14],

they allow the simultaneous successful incorporation of bulk protons without important modifications of host perovskite structure and without the absorption of surface, secondary species, i.e. protonation, in the case of Strontium zirconates. The Raman spectra were systematically recorded through a sapphire window. Note that the in situ Raman scattering is a very powerful technique which allows the successful following of the modifications of the host perovskite structure, the insertion of protons by the presence of intense, broad background as well as the detection of secondary phases superimposed to the background (ABC broad band feature extending from ~3600 to 2000 cm^{-1}) [12,22], even if they are limited to traces not detectable by diffraction methods. Fig. 3a shows the comparison of the room temperature Raman spectra characteristic of non-protonated, 5 h-protonated and 30 h-protonated ceramic. Small differences are detected between the non-protonated and 5 h-protonated ceramic. The main difference is related to the presence of important, intense broad background extending from 500 to 3500 cm^{-1} [22]. The electronic defects due to the insertion of protonic species and the large difference between the diffusion rate of interstitial proton and oxygen atom/vacancy are at origin of such background. This background disappears at room temperature when the structure is subjected to a high pressure (>6 GPa [24]) or after annealing under a water pressure above 500 °C [25,26]. Observation of this background requires the study of the whole 100–4000 cm^{-1} spectral range in a single window, that is rarely performed [27,28].

Moreover, the absolute Raman intensity decrease of the perovskite framework signature (10–800 cm^{-1} range) can be also detected. This can be explained by the symmetrisation of crystal structure after protonation (see Fig. 1d and e for comparison). As we explained above, the lower the distortion, the lower the absolute Raman intensity.
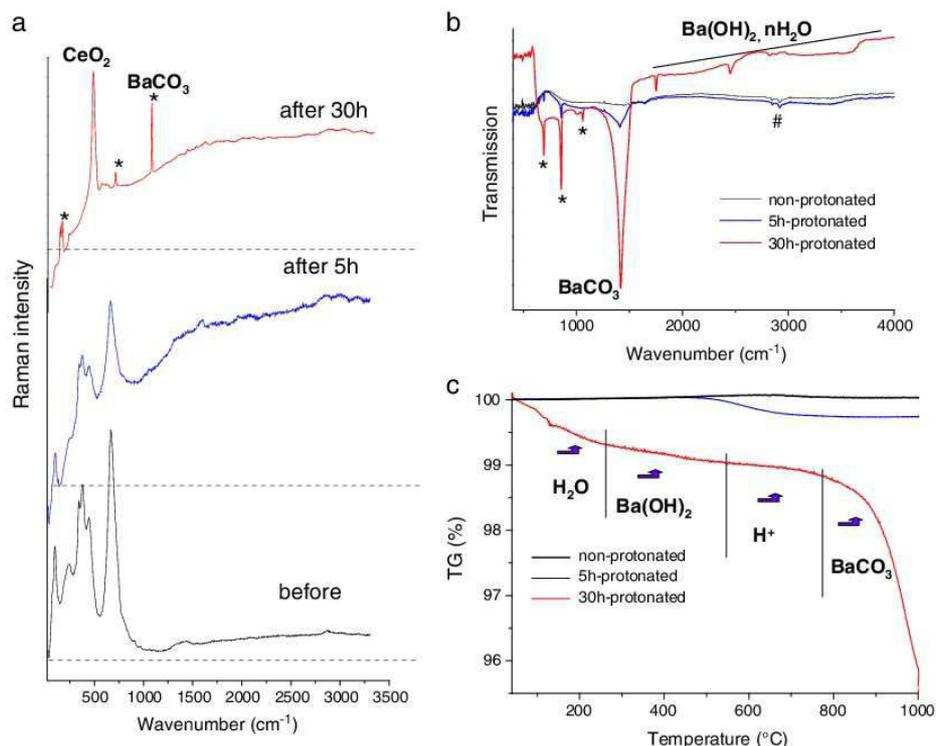

Fig. 3. a) Comparison of Raman (a), IR (b) spectra as well as TGA curves (c) recorded before and after protonation process performed at 500 °C under 10 bars of water vapour pressure during 5 and 30 h. The important modifications are detected after 30 h of protonation. Note, the presence of strong background (standard level background is marked by a line) in the Raman spectra of BCZYZ after protonation. * marks the Raman/IR modes of $BaCO_3$, whereas # the artefacts related to air pollutions. The line highlights the broad bands of hydrated second phases.

On the contrary, the Raman spectrum recorded after 30 h of protonation is totally different. This Raman spectrum is dominated by the strong signature of BaCO$_3$ and CeO$_2$. The Raman intensity is not directly proportional to phase content, the compound built with strong covalent bond having the stronger signature. In the case of BCZYZ, the detected secondary phases are more Raman active than the perovskite structure containing the protons.

In order to better determine/identify the observed secondary phases, we recorded the IR spectra (Fig. 3b) and TGA curves (Fig. 3c). These results are very complementary and show clearly that after 5 h of protonation only very small modifications are detected. These modifications, which consist mainly in the formation of BaCO$_3$, are limited only to the ceramic surface (max 60 μm of depth according to the Raman profilometry). After 30 h of protonation the entire ceramic: surface and bulk show important presence of secondary phases. Raman profilometry (method described in [22]) reveals that the surface (to a depth of 300 μm) contains mostly the BaCO$_3$ whereas bulk is dominated by the CeO$_2$. IR and TGA results reveal also the presence of Ba(OH)$_2$,H$_2$O. The important question is the proportion of BCZYZ perovskite phase and the amount of secondary phases. Further study is necessary to answer this question.

After complex and bulk analysis it is clear that the BCZYZ sample contains different secondary phases and is then partially decomposed. The origin of this instability is not clear. One such explanation to this may be that the sample contains traces of Ba-rich secondary phase at the grain boundary, these traces promoting the densification. Another explanation can be associated with the substitution level − 20%. We had shown before that the BaZrInO$_{3 - d}$ with 75% of In is totally decomposed after protonation in similar conditions [24] whereas BaZrYbO$_{3 - d}$ containing 10% of Yb remains stable for a few months in autoclave [29]. Moreover, since the secondary phases are Ba-rich ones, one can expect that the Ba excess at the A-perovskite site contributes also significantly to the ceramic instability. On the other hand, the Zn ions may come out of the B-site of the perovskite to segregate at grain boundary so that the B-site will be deficient to barium, resulting in instability against water.

4. Conclusions

The BCZYZ ceramic – offering an implied high conductivity and stability as a potential candidate for use as an electrolytic membrane – has been investigated by various experimental techniques well suited to the surface and bulk analysis. The results revealed the presence of traces of secondary phases/protonic species already in the non-protonated ceramic, which are easily removed by one thermal treatment above 300 °C. Operating under steam conditions gives rise to the formation of Ba-rich secondary phases, mostly BaCO$_3$. In the case of treatment under low pressure value (60 mbar/400 °C) for 12 h or high pressure

value (10 bar) during 5 h, these secondary phases appear on the ceramic surface only. Once the operating time under high pressure is increased up to 30 h, the presence of BaCO$_3$ and also CeO$_2$ is detected on the surface and into the bulk pointing to the partial decomposition of the BCZYZ. Consequently, the bulk and surface analysis of BCZYZ ceramic shows clearly that its stability is limited. Complementary investigations (High resolution TEM study of the grain boundary, H-profil by Elastic Recoil Coincidence Spectroscopy, etc.) are needed to establish if the instability is intrinsic to the composition or results from the grain boundary characteristics.

References

[1] M. Ni, M.K.H. Leung, D.Y.C. Leung, Int. J. Hydrogen Energy 32 (2007) 4648.
[2] H. Iwahara, T. Esaka, H. Uchida, N. Maeda, Solid State Ionics 3 (4) (1981) 359.
[3] Ph. Colomban, Proton Conductors Cambridge University Press, Cambridge, 1992.
[4] G.A. Olah, Angew. Chem. Int. Ed. 44 (2005) 2636.
[5] S. Tao, J. Irvine, J.A. Kilner, Adv. Mater. 17 (2005) 1734.
[6] F.L. Chen, O.T. Sorensen, G.Y. Meng, D.K. Peng, J. Mater. Chem. 7 (1997) 481.
[7] S. Bhide, A. Virkar, J. Electrochem. Soc. 146 (1999) 2038.
[8] P. Babilo, T. Uda, S.M. Haile, J. Mater. Res. 22 (2007) 1322.
[9] S. Tao, J. Irvine, Adv. Mater. 18 (2006) 1581.
[10] B. Sala, O. Lacroix, S. Willemin, K. Rhamouni, H. Takenouti, A. Van der Lee, P. Goeuriot, B. Bendjeriou, Ph. Colomban, Patent AREVA − CNRS − ARMINES − SCT FR0755418, 01/06/2007, PCT WO 2008/152317 A2.
[11] B. Sala, F. Grasset, O. Lacroix, A. Sirat, K. Rhamouni, M. Keddam, H. Takenouti, D. Goeuriot, B. Bendjeriou, Ph. Colomban, A. Slodczyk, G. Pourcelly, A. Van der Lee, J.G. Sanchez, Patent AREVA − CNRS − ARMINES − SCT FR 1159221, 12/11/2011.
[12] Ph. Colomban, O. Zaafrani, A. Slodczyk, Membranes 2 (2012) 493.
[13] Ph. Colomban, C. Tran, O. Zaafrani, A. Slodczyk, J. Raman Spectrosc. 44 (2013) 312.
[14] A. Slodczyk, O. Zaafrani, Ph. Colomban, Mater. Res. Soc. Proc. 1385 (2012) 861 (opl.2012).
[15] A. Slodczyk, O. Zaafrani, M.D. Sharp, J.A. Kilner, B. Dabrowski, O. Lacroix, Ph. Colomban, Membranes 3, 2013, 311.
[16] I. Charrier-Cougoulic, T. Pagnier, G. Lucazeau, J. Solid State Chem 142 (1999) 220.
[17] C.S. Tu, R.R. Chien, V.H. Schmidt, S.C. Lee, C.C. Huang, J. Phys. Condens. Matter 24 (2012) 155403.
[18] A. Slodczyk, Ph. Colomban, Materials 3 (2010) 5007.
[19] G. Lucazeau, J. Raman Spectrosc. 34 (2003) 478.
[20] M.C. Verbraeken, H.A.L. Viana, P. Wormald, J.T.S. Irvine, J. Phys. Condens. Matter 23 (2011) 234111.
[21] I. Ahmed, C.S. Knee, M. Kaarlson, S.G. Eriksson, P.F. Henry, A. Matic, D. Engberg, L. Borjesson, J. Alloys Compd. 450 (2008) 103.
[22] A. Slodczyk, Ph. Colomban, S. Willemin, O. Lacroix, B. Sala, J. Raman Spectrosc. 40 (2009) 513.
[23] Ph. Colomban, A. Slodczyk, Opt. Mater. 31 (2009) 1759.
[24] A. Slodczyk, B. Dabrowski, N. Malikova, Ph. Colomban, Mater. Res. Soc. Proc. Vol 1311 (2011)(mrsf10-1311-gg06-25).
[25] A. Slodczyk, M.-H. Limage, O. Zaafrani, Ph. Colomban, F. Grasset, J. Loricourt, B. Sala, J. Raman Spectrosc. 42 (2011) 2089.
[26] O. Zaafrani, Protonation, distorsions structurales et espèces protoniques dans des perovskites lacunaires, PhD Thesis Université Pierre et Marie Curie, Paris, 2010.
[27] S. Okada, A. Mineshige, A. Takasaki, M. Kobune, T. Yazawa, H. Matsumoto, Tetsuo Shimura, H. Iwahara, Z. Ogumi, Solid State Ionics 175 (2004) 593.
[28] F. Giannici, M. Shirpour, A. Longo, A. Martorana, R. Merkle, J. Maier, Chem. Mater. 23 (2011) 2994.
[29] A. Slodczyk, Ph. Colomban, D. Lamago, G. Andre, O. Zaafrani, O. Lacroix, A. Sirat, F. Grasset, B. Sala, J. Mater. Res. 27 (2012) 1939.

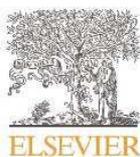# CHAPTER 5

"Structural stability of anhydrous proton conducting SrZr$_{0.9}$Er$_{0.1}$O$_{3-\delta}$ perovskite ceramic vs. protonation/deprotonation cycling: Neutron diffraction and Raman studies"

Here, we will report the structural stability of Er-doped strontium zirconate, SrZr$_{0.9}$Er$_{.16}$O$_{3-\delta}$ (SZ: Er), ceramic samples. The samples were treated under 40 bar water vapor pressure at intermediate temperature. The techniques of neutron diffraction and Raman spectroscopy are mainly employed.

Structural stability of anhydrous proton conducting SrZr$_{0.9}$Er$_{0.1}$O$_{3-\delta}$ perovskite ceramic vs. protonation/deprotonation cycling: Neutron diffraction and Raman studies

Aneta Slodczyk [a,b], Philippe Colomban [a,b,*], Settakorn Upasen [a,b], Frédéric Grasset [c], Gilles André [d]

[a] Sorbonne Universités, UPMC Univ Paris 06, UMR 8233, MONARIS, 75005, Paris, France
[b] CNRS-IP2CT, UMR 8233, MONARIS, F-75005 Paris, France
[c] AREVA NP, Université Montpellier 2, Montpellier 34095, France
[d] Laboratoire Léon Brillouin CNRS-CEA, CEA Saclay, 91191 Gif-sur-Yvette, France

ARTICLE INFO

ABSTRACT

Long-term chemical and structural stability of an ion conducting ceramic is one of the main criteria for its selection as an electrolytic membrane in energy plant devices. Consequently, medium density SrZr$_{0.9}$Er$_{0.1}$O$_{3-\delta}$ (SZE) anhydrous proton conducting ceramic – a potential electrolyte of SOFC/PCFC, was analysed by neutron diffraction between room temperature and 900 °C. After the first heating/cooling cycle, the ceramic pieces were exposed to water vapour pressure in an autoclave (500 °C, 40 bar, 7 days) in order to incorporate protonic species; the protonated compound was then again analysed by neutron diffraction. This procedure was repeated two times. At each step, the sample was also controlled by TGA and Raman spectroscopy. These studies allow the first comprehensive comparison of structural and chemical stability during the protonation/deprotonation cycling. The results reveal good structural stability, although an irreversible small contraction of the unit-cell volume and local structure modifications near Zr/ErO$_5$[] octahedra are detected after the first protonation. After the second protonation easy ceramic crumbling under a stress is observed because of the presence of secondary phases (SrCO$_3$, Sr(OH)$_2$) well detected by Raman scattering and TGA. The role of crystallographic purity, substituting element and residual porosity in the proton conducting perovskite electrolyte stability is discussed.

© 2015 Elsevier Ltd. All rights reserved.

1. Introduction

Proton conducting perovskite ceramics, i.e. A^{2+}(Ba, Sr etc.) B$_x^{4+}$(Zr, Ce, Ti, Nb etc.) B'$_{1-x}^{3+}$(Y, Yb, Er etc.) O$_{3-\delta}$, are widely investigated due to their huge application potential as electrolyte membranes and/or cermet electrodes of new generation clean energy devices such as fuel cells, water electrolyzers and CO$_2$/Syngas converters [1–8]. Comprehension of the relation between crystal structure, proton conduction and chemicals supplied at anode and cathode is a key point to optimize their lifetime and performance. Most of available literature data are focused on a material synthesis, its, mostly room temperature and/or low water pressure, characterization (X-ray, MEB) and conductivity measurements [6–16]. Such studies prove a possibility to obtain

various perovskite materials with a significant proton conduction in an intermediate temperature range (400–600 °C), convenient to avoid the use of expansive catalysers and steels. However they are not sufficient to guarantee successful industrial applications because of the lack of data concerning their lifetime. In order to go further than laboratory cells, complex stability/ageing (chemical, mechanical and structural) tests performed on demonstrators in industrial, operating conditions (typically 10 to 20 bar p(H$_2$O)) [17–19] are the must. The use of high water pressure by industrialists allows an efficiency increase and in consequence to reduce the cost of Hydrogen production/conversion [20–23]. Our previous studies, performed in a strict collaboration with industry partners, showed however that such high water pressure can significantly accelerate a material ageing. Consequently, our protonation procedure performed under very high pressure (40 bar p(H$_2$O)) can be considered as an accelerating stability test which allows very fast to choose the most stable electrolytes and/or electrodes [18, 24, 25].

Chemical and structural stability of proton conductor perovskite ceramic for fuel cells and electrolyzers

It is noteworthy, prior to any stability test, the H-content and the discrimination between surface protonic species (hydroxides, hydroxyoxycarbonates …) and bulk protons – the only species responsible of proton conduction through a dense anhydrous membrane, i.e. the determination of an exact bulk proton nature, should be established [25–30]. The question if the Proton is a Guest or a Host in an anhydrous oxide has been addressed by Y. Baikov [31]. The nature of chemical bonds between the proton and a perovskite framework (hydroxyl ion, free, ionic proton …) remains debated [7, 28, 29, 31–33]. What are the H bulk content and the filling ratio of oxygen vacancies created by the B-cation partial substitution? The proton nature and their content play a crucial role in thermal stability, structural (local or long range order) modifications [25, 29] and in consequence in a conduction mechanism. The apparent lack of such studies performed on ceramics with different densification levels is evident.

Neutron diffraction measurements appear as a very good method to study the chemical and structural stability as a function of proton conduction/proton departure in a wide temperature range [34, 35]. Moreover due to its huge sensibility to hydrogen element, they allowed to measure the proton content [25, 29, 34]. Up to now, this technique has been rarely employed to study proton conducting perovskite materials. Apart from some works performed at low temperature and then not pertinent to understand the proton conduction mechanisms (review in [34]), we can highlight those of Malikova et al. [36] and the group of Irvine [37] dealing with structural modifications in an operating temperature range. For these reasons we have conducted series of neutron diffraction and quasi-elastic neutron scattering campaigns to address these points better [34, 38–41].

We present here neutron diffraction measurements performed in a wide temperature range, RT-900 °C, on medium density (90% of the theoretical density) $SrZr_{0.9}Er_{0.1}O_{3-\delta}$ ($\delta \leq 0.05$) ceramic pieces in non-protonated and two times protonated/deprotonated states. This study was undertaken in order to go further in our general goal, i.e. the characterisation of eventual structural modifications caused by conducting protons during the protonation/deprotonation cycles [25–30, 38–41]. Moreover, the results allowed to complete our previous ones performed on high density $SrZr_{0.9}Yb_{0.1}O_{3-\delta}$ ceramics [41]. Note, our previous neutron diffraction studies showed clearly that a very small content of free bulk protons ($1–5 \ 10^{-3}$ mol/mole), i.e. protons that do not form strong covalent bonds with the perovskite framework and consequently do not show any IR fingerprint [28, 32, 40, 41], induces small, but measurable long range structural modifications. These modifications seem to remain weak enough to guarantee high mechanical and structural stability. It should be stressed that these previous measurements suffer however from few drawbacks [41]: (i) the used, high density SZYb and HSZYb ceramics originated from two different batches which excluded a possibility of their direct comparison; (ii) the obtained neutron beam-time allowed us recording one protonation/deprotonation cycle only. Note, the deprotonation state can be easily obtained by a thermal treatment above 700 °C during a few hours under high dynamic vacuum (10^{-7} Torr). Consequently, for this new neutron measurement campaign (see details in experimental section) the SZE ceramics of lower density (90%) than SZYb (98%) were selected. Such choice allowed us also to study an impact of surface/interface secondary phase(s) on structural/chemical modifications since the surface reaction mechanisms drive an ageing of ceramic membranes. Note, in the case of high density ceramics the presence of surface protonic species in the form of secondary phases can be minimized or even excluded and then one can follow the behaviour of bulk protons only. Hence, the use of medium density ceramics (90%) allows the analysis of both surface (maximized if the sample is made of small grains or is in the form of fine powder) and bulk
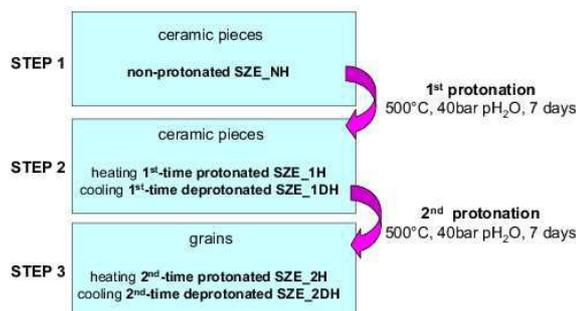

Fig. 1. Sketch presenting the samples used in 3 steps of neutron diffraction campaign.

effects and makes the experimental conditions more comparable with most of literature data performed on not fully dense ceramics [16, 34]. As it can be clearly detected, we changed also a kind of substituting element, namely we replaced the Yb by Er due to its higher stability and monovalency, i.e. Er^{+3}, which hinders internal redox reactions and associated changes of oxygen vacancy number.

Finally it should be stressed that the aim of our neutron diffraction studies (this and the previous ones) was to determine the structural/chemical stability vs. protonation/deprotonation cycling. In order to record many diffraction patterns as a function of temperature in a short time and to avoid the ceramic deprotonation we chose a diffractometer which offers a high neutron flux but a middle resolution. The quality of obtained data does not allow us to determine a complete structure model but is sufficient to compare temperature dependences of the unit-cell parameters of non-protonated and protonated/deprotonated ceramics. Consequently, in order to complete the neutron diffraction data, TGA curves and Raman spectra were systematically recorded before and after each neutron measurement step (Fig. 1). Note, Raman and TGA techniques are more sensitive to the secondary phase detection than diffraction experiments [25–30].

2. Material and methods

2.1. Samples and experimental procedure

Round shaped $SrZr_{0.9}Er_{0.1}O_{3-\delta}$, $\delta \leq 0.05$ [25, 39] (called hereafter **SZE_NH**, NH for non hydrated) medium density (90% of theoretical density) perovskite ceramic pellets (diameter of 20mm) were prepared by the AREVA NP group using the method described elsewhere [17–19, 41, 42]. X-ray, Raman, SEM, elemental analysis, density, TGA and dilatometry measurements were used to verify the ceramic quality and crystallographic purity as previously described [25, 42–45].

Pristine, non protonated ceramics, broken into small pieces with the widths lower than 5 mm (to fill a vanadium cylindrical sample holder) were used in the first step of this neutron diffraction campaign. In order to study structural modifications of this non-protonated, Er-substituted perovskite 20 neutron diffraction patterns were recorded during a heating and a cooling cycle, respectively. As sketched in Fig. 1, after the first step of neutron measurements, the ceramic pieces were placed into a high temperature/high pressure autoclave device [43] and treated at 500 °C, under 40 bar of carbonate-free water vapour pressure during 7 days in order to insert protonic species. According to previous studies, such duration is sufficient to guarantee an homogeneous proton distribution through a ceramic thickness [25,

45]. Such 1st time protonated sample (**SZE_1H**, H for hydrated) was then used during the second step of neutron measurement campaign: a heating cycle allowed to follow the behaviour of protonated (SZE_1H) ceramic whereas a cooling cycle is characteristic of the 1st time deprotonated sample (**SZE_1DH**, DH for dehydrated). The ceramic after the first protonation/deprotonation cycle was then protonated second time in the autoclave following the same procedure. After 7 days of protonation process, a crumbling of ceramic pieces was observed. Consequently the third step of neutron diffraction measurement campaign was performed on millimetric grains: a heating cycle is characteristic of the 2nd time protonated (**SZE_2H**) and a cooling of the 2nd time deprotonated sample (**SZE_2DH**).

2.2. Neutron diffraction

Neutron diffraction measurements were performed in the French neutron facility Orphée research reactor at the CNRS-CEA Léon Brillouin Laboratory (Saclay, France) [46]. The samples (9 g of pristine ceramic pieces and finally 8 g of grains because of fine powder elimination and a sampling for TGA measurements) were placed into a cylindrical vanadium sample holder. Neutron experiments were carried out on a G4.1 Cold Neutron Two-Axis Diffractometer PYRRHIAS equipped with a vertical focusing pyrolytic graphite monochromator and a 800-cells multidetector [46]. The 0.24226 nm wavelength was used. The home-made furnace requiring high vacuum (10^{-7} Torr) allowed collecting neutron diffraction patterns in the 25–900 °C temperature range, both on heating and cooling. Each diffraction pattern was recorded during 1 hour approximately. As explained above, in the case of protonated sample the heating cycle is characteristic of protonated state and the cooling one represents a behaviour of the deprotonated sample. The deprotonation, departure of protons with the temperature increase, is a common feature of proton conducting perovskites. Our previous study showed that a complete deprotonation can be obtained after a thermal treatment above 700 °C during a few hours under high vacuum [25, 38, 39]. Note, the control of a vacuum pressure helps to follow the deprotonation process because of a temporary increase of the pressure value during protonic species departure, the deprotonation being complete when the minimal (10^{-7} Torr) pressure value is again reached. Ex situ TGA measurements confirm the complete deprotonation.

In order to determine the temperature evolution of unit-cell parameters, the FullProf software was used [47]. It should be stressed that the G4.1 limited resolution and 2 theta values (10-95°) do not allowed determining the atom positions. Each diffraction pattern was refined using the Le Bail matching profile procedure [48]. The successful parameters (minimal values of Bragg R factor (R_B), weighted profile R factor (R_{wp}) and χ^2) obtained at a given temperature were used as starting ones at a following temperature value. A few examples of neutron diffraction pattern refinements can be found in Fig. 2 as well as in Fig. S1 and Fig. S3 (S notes Supplementary Materials).

2.3. Raman and thermogravimetric analyses

Before and after each step of the neutron diffraction campaign the samples were carefully controlled by thermogravimetric analysis and Raman scattering. The obtained TG curves and Raman spectra were then compared with our own database containing the TG/Raman signatures of host perovskite structures and all possible secondary phases [25–27, 45].

TG analysis was performed between 40 and 1000 °C using a Setaram Setsys Evolution thermobalance (Caluire, France). The use of Pt-crucible and He-inert gas atmosphere allowed the significant enhancement of a measurement accuracy that is essential in the case of small mass modifications (few % maximally) typical of proton conducting perovskites.

Raman scattering measurements were carried out using a Horiba Jobin Yvon HR800 spectrometer (Lille, France) equipped with a Peltier effect cooled CCD detector. Raman spectra were recorded in a wide spectral range using 458 nm wavelength of an Ar$^+$ ion Coherent Laser ($\sim$10mW at the sample) through a x50 long distance working Nikon objective. Note, the presence of Er element gives rise to strong electronic transitions overlapping the Raman signature of host perovskite structure in a large wavelength range and hence imposes the choice of this blue laser excitation wavelength.

3. Results

3.1. Non protonated SrZr$_{0.9}$Er$_{0.1}$O$_{3-\delta}$ (SZE_NH)

Room temperature neutron diffraction pattern of non-protonated SZE ceramic (Fig. S1, Fig. 2, Fig. 3a) shows an orthorhombic symmetry with the Pnma space group. This is in good agreement with previous structural data characteristic of pure SrZrO$_3$ and SrZr$_{0.9}$Yb$_{0.1}$O$_{2.95}$ [41, 49], and shows clearly that the use of Ln ions (Yb or Er) as a substituting element does not distort the pristine Pnma orthorhombic symmetry. However a higher level of background and a small broadening of Bragg peaks (Fig. 3a and zoom in Fig. S2), well detected in the 2 theta 52-70° range, suggest the presence of secondary phases. Their very low intensity and important width allowed us to assign them to traces of not well symmetrised phases such as SrO. The presence of AO-type traces in the grain boundary is a common problem in the case of perovskite proton conductors [27, 30, 42]. Note, a small alkali earth excess is systematically added in order to optimize a ceramic sintering. If this excess is not totally consumed during the sintering, alkaline earth-based oxide traces react with (carbonated) water and then give rise to the formation of hydroxides and/or carbonates, mostly at the grain boundary surface [27, 30, 43]. It should be stressed that these secondary phases were ignored in our refinement model. This together with the fact that polycrystalline, proton conducting ceramics exhibit a high local disorder related to the presence of oxygen vacancies and protonic species can explain rather high values of reliability factors (Table 1), typical of these compounds [16, 34, 37].

The Raman spectrum (Fig. 4a) confirms well the orthorhombic symmetry of SZE ceramic (characteristic triplet at 116-144-164 cm^{-1}) and simultaneously reveals the traces of SrCO$_3$ (narrow peak at 1071 cm^{-1}), Er$_2$O$_3$ (600 cm^{-1}) and very probably the ZrO$_2$ crystallised within a cubic symmetry. Note, it is impossible to confirm unambiguously the presence of cubic ZrO$_2$ traces by Raman scattering because of the overlapping of its low intense broad Raman signature with that of SZE perovskite. We suppose its presence by the lack of clear splitting of the low wavenumber triplet (116-144-164 cm^{-1}) and an unusual high baseline in the same spectral region (see Raman fitting in Fig. 4b). It should be however stressed that both Raman and neutron diffraction measurements show clearly that the traces of secondary phases are low. The use of such ceramics containing small traces of secondary phases allows following an accelerate ageing.

As presented in Fig. 3b, with the temperature increase some Bragg peaks disappear. This is in agreement with a continuous structural phase transition from the orthorhombic Pnma symmetry to the Imma pseudo-tetragonal one in the vicinity of 700 °C as already reported for non-substituted SrZrO$_3$ [49]. The neutron diffraction patterns characteristics of both distinct symmetries are presented in Fig. 5. The results of Le Bail refinements are presented
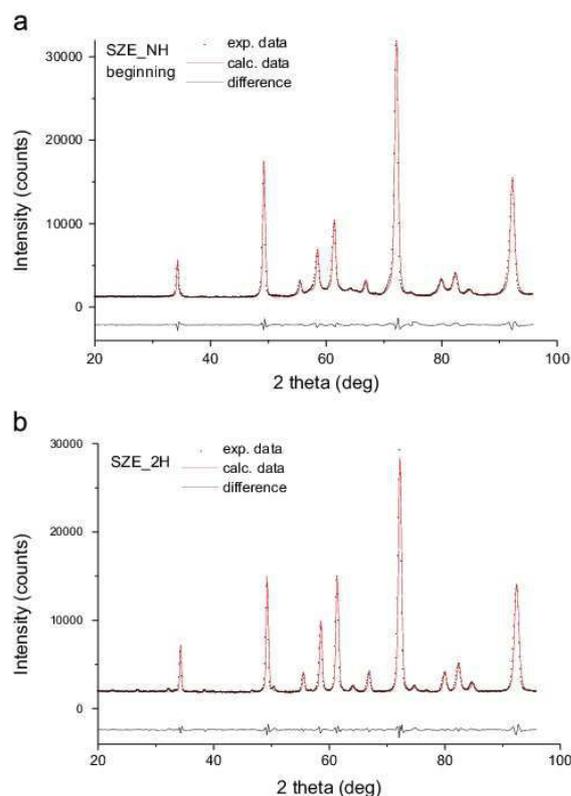
Fig. 2. Examples of neutron diffraction pattern refinement characteristic of (a) non-protonated, pristine (b) 2nd time protonated SZE proton conductor. Other examples can be found in Fig. S1.

in Fig. S3. The orthorhombic-pseudo tetragonal phase transition is well detected by the temperature evolution of unit-cell parameters presented in Fig. 6: above 700 °C a significant deviation from the linear increase is detected in the case of b parameter, simultaneously the a and c parameters reach the same values. The b parameter temperature evolution allows detecting, through a small non-linear deviation, another subtle structural "anomaly" in the vicinity of 300 °C (Fig. 6). Note this modification can be well described within the Pnma space group. Both structural modifications, i.e. the 700 °C phase transition and the small anomaly at 300 °C, seem to be in agreement with our previous neutron diffraction results obtained for highly dense SZYb ceramics [41]. It should be stressed however that in the case of SZYb this additional structural modification was detected near 450 °C. The reason of such temperature difference is not clear. First of all, an important question can be asked: is the ~300 °C anomaly detected in SZE an intrinsic feature of the perovskite Pnma symmetry or is it related to the presence of alkaline earth-based secondary phases and stoichiometry modifications? Note, near 300 °C the decomposition of hydrated SrO is observed. Simultaneously, the SZYb ceramic was almost free from $Sr(OH)_2$ [41]. Further studies performed on higher resolution diffractometer are necessary to clarify this aspect. If this structural modification does not originate from secondary phases, the temperature difference can be explained by the effect of substituting element on the host perovskite structure. It is noteworthy that our previous high pressure Raman study [50] showed clearly that the impact of substituting element on the host structure is much higher than that caused by the presence/

diffusion of protons. This is then probable that the Yb and Er ions can give rise to different content and organization of oxygen vacancies and in consequence to different local structural modifications.

With the temperature decrease, a return to the Pnma orthorhombic symmetry is clearly observed. As shown in Fig. 3a the neutron diffraction patterns and thus symmetries of the SZE ceramic before and after thermal treatment are almost the same. The temperature evolutions of unit-cell volume (Fig. 7a) characteristic of heating and cooling cycles show also the same behaviour. As presented in Table 1, the values of unit-cell parameters before and after thermal treatment are very similar, revealing that the structural modifications as a function of temperature are reversible.

3.2. First time protonated (SZE_1H)/deprotonated (SZE_1DH) $SrZr_{0.9}Er_{0.1}O_{3-\delta}$

Room temperature neutron diffraction pattern (Fig. 3a, Fig. S1) and Raman analysis (Fig. 4) show that SZE ceramic maintains its major orthorhombic symmetry (Pnma) after the first protonation. This symmetry is also observed once the ceramic pieces are deprotonated due to the thermal treatment. However, as it can be clearly seen (Fig. 3a), the neutron diffraction patterns characteristic of the 1st time protonated and deprotonated compound show some differences.

The most significant difference is related to the level of incoherent background intensity, namely, the protonated ceramic shows much higher background level. Since the incoherent background intensity is proportional to the hydrogen content [34, 39, 41], this confirms the presence of protonic species. With the temperature increase the background level decreases according to the deprotonation process. The temperature dependence of background intensity, in very good agreement with the TG analysis, is plotted in Fig. 8a. The TG and neutron data reveal that the protonated ceramic contains surface water (departure at 100 °C), hydroxide ions (departure at 300-400 °C) and a small amount of bulk protons (departure above 550 °C). Consequently, the following formula can be proposed for the 1st time protonated SZE: $SrZr_{0.9}Er_{0.1}O_{3-\delta}(OH)_{0.006}H_{0.004}, 0.015 H_2O$. Such small content of bulk protons has been already observed in our previous studies [25, 28, 29, 34, 39, 41] and seems to be a fingerprint of anhydrous protonated zirconates.

An important content of surface water in room temperature seems to have an impact on the host perovskite structure. Namely, neutron diffraction pattern (Fig. 3a, Fig. 3b, Fig. S1) reveals the presence of additional low intensity Bragg peaks detected at 2 theta: 21.8° (the most intense) and 31.2° (most probably, but it is difficult to distinguish it from a background noise). These additional Bragg peaks may have different origin: secondary phases or a kind of superstructure reflections. These Bragg peaks disappear at 100 °C simultaneously with the departure of surface water. This can suggest that the presence of ordered water layer forms a kind of superstructure and/or structural distortions allow the appearance of Bragg peaks with the hkl not observed within the Pnma space group. Shpanchenko et al. [51] pointed out that the coexistence of perovskite and BaO rock salt type phases allows to incorporate large quantities of water (e.g. Ba_2ZrO_4 can incorporate 2 mol of water). Consequently, such organization can give rise to superstructure Bragg peaks. However in our study the additional peaks are detected only at a low 2 theta range and it is then not possible to determine unambiguously their origin. Further neutron diffraction study performed on a diffractometer offering higher resolution is necessary to determine clearly the type of distortions caused by the hydration.

Careful analysis of room temperature diffraction patterns
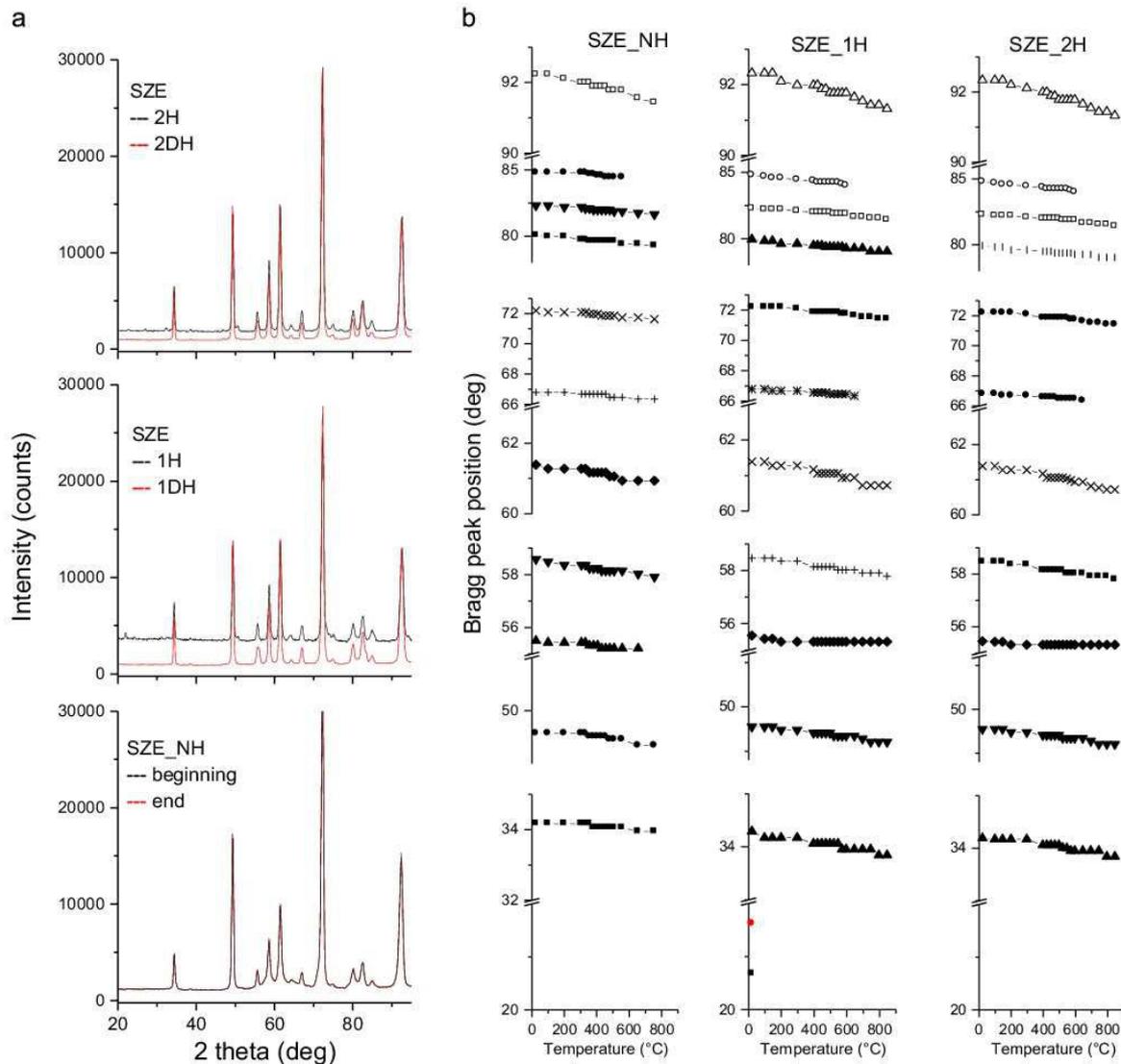
Fig. 3. Neutron diffraction patterns recorded at the beginning and the end of each measurement cycle (a) and temperature dependences of Bragg peak positions (b) characteristic of non-protonated, first time protonated and second time protonated SZE proton conductor. Zoom of neutron diffraction patterns presented in Fig. 3 can be found in Fig. S2.

recorded after the first protonation, and especially deprotonation, reveals the disappearance of the background and broadening near 2 theta=50-70° well observed in the case of non-protonated pristine ceramic (Fig. 3a, Fig. S2). This, together with the fact that Bragg peaks are more symmetrical and show little bit lower FWHM values, suggests higher level of crystallinity/symmetrization. Some differences can be also detected in Raman spectra (Fig. 4). The most important features are the disappearance of some Raman peaks (Er$_2$O$_3$ traces at 600 cm^{-1}) and the increase of those related to the SrCO$_3$ (1071 cm^{-1}). It should be stressed that due to the huge Raman cross section and narrowness, the strontium carbonate phase gives a strong signal even if is limited to traces [25, 26, 45]. Some modifications in the vicinity of Raman peaks centred at 750 cm^{-1} can be also detected (Fig. 4b). Note, as described in our previous articles [44, 50] the Raman modes in this

spectral range are attributed to the vibrations of the ZrO$_6$ octahedron perturbed by substituting elements, oxygen vacancies and protons. Consequently, this reveals that the first protonation modifies the local structure around the Zr/ErO$_5$[] octahedron, according to the filling of some oxygen vacancies and the proton presence.

The structural modifications detected by neutron diffraction and Raman scattering show that two different phenomena can take place during the first protonation process. First of all, it is clear that the high temperature (500 °C), high water vapour pressure (40 bar) treatment has a direct impact on the presence and type of secondary phases: namely the SrO traces were transformed into Sr(OH)$_2$ and SrCO$_3$. The second consequence is a diffusion of the Er ions and O^{2-}/V$_O$ leading to their new distribution. The insertion of water (protons+oxygen ions) modifies also the

Chemical and structural stability of proton conductor perovskite ceramic
for fuel cells and electrolyzers

Table 1

Unit-cell parameters and volume determined by Le Bail profile matching method at the beginning and at the end of each neutron measurement cycle characteristic of non-protonated, 1st time protonated/ deprotonated and 2nd time protonated/deprotonated SZE proton conductor. Reliability factors (R_{wp}, χ^2) are given for better comparison. Values of incoherent background levels (BL) reflecting the H content, are also marked.

	SZE_NH	SZE_1H	SZE_2H
Heating	$T=25C$	$T=20C$	$T=25C$
	$a=5.821$ (7) Å	$a=5.816$ (1) Å	$a=5.818$ (8) Å
	$b=8.239$ (4) Å	$b=8.228$ (1) Å	$b=8.229$ (2) Å
	$c=5.789$ (2) Å	$c=5.784$ (6) Å	$c=5.785$ (1) Å
	$v=277.63$ Å^3	$v=276.79$ Å^3	$v=276.94$ Å^3
	$BL=1020$	$BL=3860$	$BL=2050$
	$R_{wp}=9.5$	$R_{wp}=10.2$	$R_{wp}=9.2$
	$\chi^2=4.3$	$\chi^2=5.6$	$\chi^2=5.1$
Cooling	$T<100C$	$T=32C$	$T=30C$
	$a=5.822$ (3) Å	$a=5.815$ (8) Å	$a=5.817$ (9) Å
	$b=8.240$ (4) Å	$b=8.228$ (4) Å	$b=8.229$ (1) Å
	$c=5.790$ (5) Å	$c=5.784$ (6) Å	$c=5.784$ (8) Å
	$v=277.65$ Å^3	$v=276.74$ Å^3	$v=276.86$ Å^3
	$BL=1020$	$BL=960$	$BL=980$
	$R_{wp}=9.1$	$R_{wp}=8.8$	$R_{wp}=8.6$
	$\chi^2=4.2$	$\chi^2=4.8$	$\chi^2=4.5$

Fig. 5. Neutron diffraction patterns in limited 2 theta range characteristic of non-protonated SZE ceramics recorded at 25 °C and 750 °C. The disappearance of some Bragg peaks reveals the presence of long range order structural phase transition from the Pnma orthorhombic to the Imma pseudo tetragonal symmetry. Results of neutron diffraction refinements at RT, 500 °C and 800 °C can be found in Fig. S3.
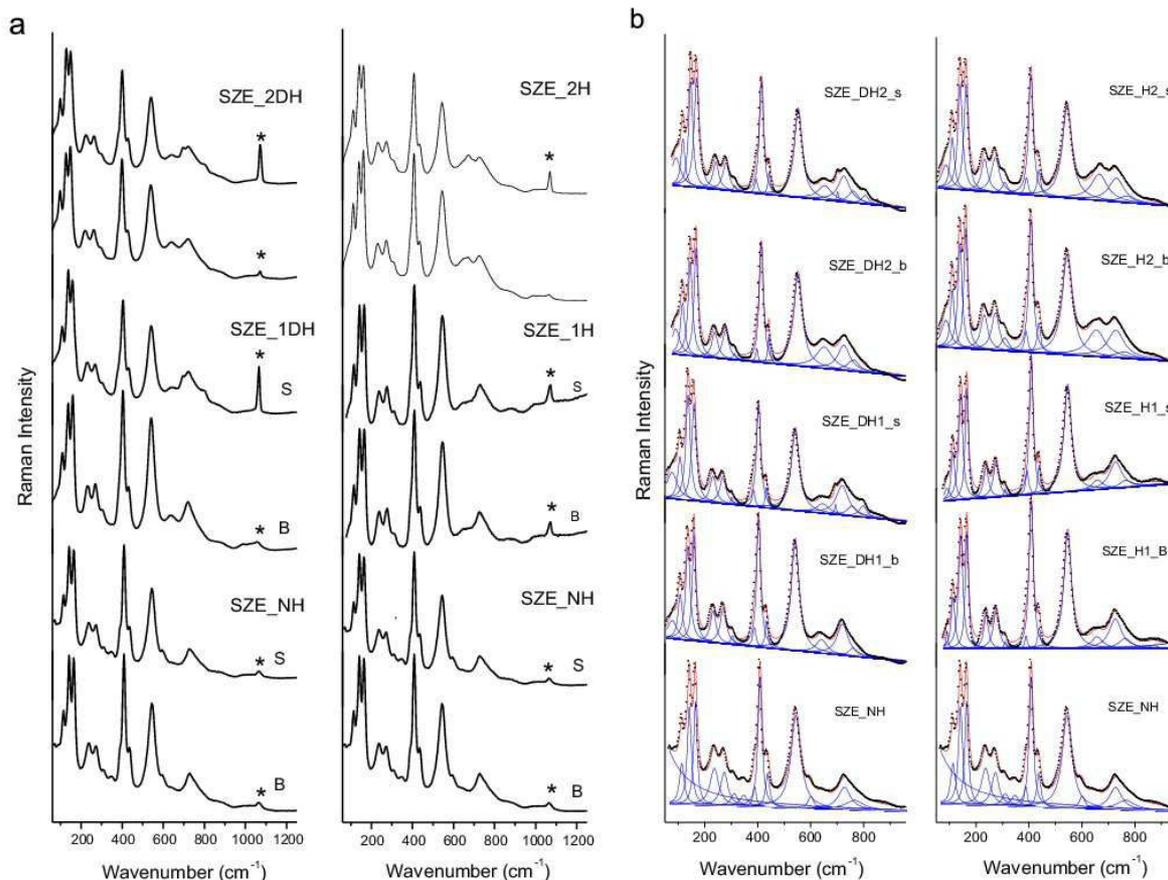
Fig. 4. (a) Raman spectra (S-surface, B-bulk) of non-protonated as well as first and second time protonated/deprotonated SZE proton conductor. The presence of the most characteristic stretching mode of $SrCO_3$ is marked by the asterisks. (b) Fitting of Raman spectra (s-surface, b-bulk) characteristic of non-protonated as well as first and second time protonated/deprotonated SZE proton conductor. The reduced scale allows to distinguish modifications in the ~750 cm^{-1} spectral region related to the oxygen vacancies and protonic species.
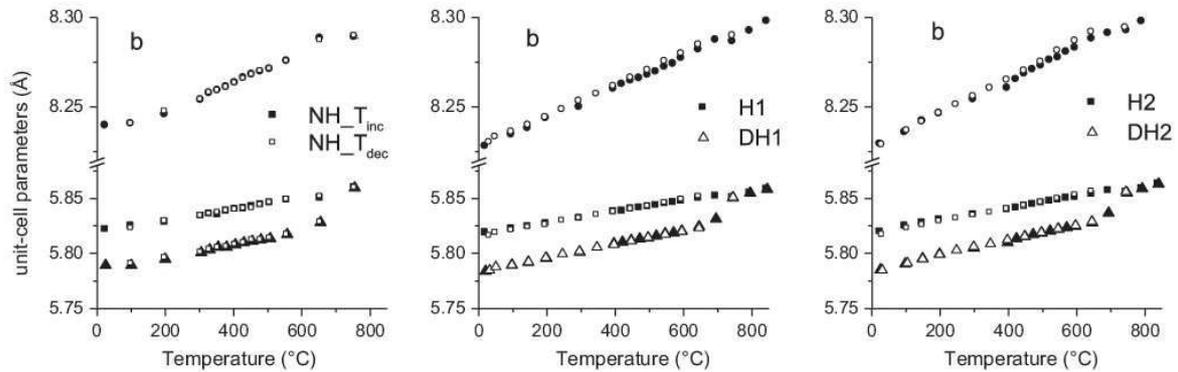
Fig. 6. Temperature dependences of the unit-cell parameters of non-protonated, first and second time protonated SZE proton conducting ceramic.

oxygen vacancy level and distorts/symmetrises the octahedral network, as observed for all studied perovskites (A = Sr, Ba; B = Zr, Ti, Al, Y, Yb) [13, 25, 27, 30, 43–45].

With the temperature increase, the similar orthorhombic – pseudo tetragonal phase transition is observed near 700 °C (Fig. 3b, Fig. 6, Fig. 7a, Fig. S3). As for non-protonated ceramic, the *a* and *c* unit-cell parameters achieve the same value and a small deviation from the linear increase behaviour is detected in the case of *b* one. Analysis of the temperature evolution of *b* parameter behaviour reveals also another very small deviation detected near 300 °C (Fig. 6). This anomaly is smaller that the one detected in the

case of non-protonated ceramic, in agreement with the fact that the presence of protons symmetrises the host perovskite structure [44, 50]. Significant traces of Sr(OH)$_2$ (Fig. 8a) can suggest however that this anomaly is due to the decomposition of Sr(OH)$_2$ observed in the same temperature range. Only additional neutron diffraction experiments performed on a higher resolution diffractometer can clarify this discrepancy.

During the cooling cycle characteristic of structural behaviour of the 1st time deprotonated ceramic, a continuous, reversible structural phase transition from the Imma pseudo-tetragonal symmetry to the Pnma orthorhombic one is clearly detected. The
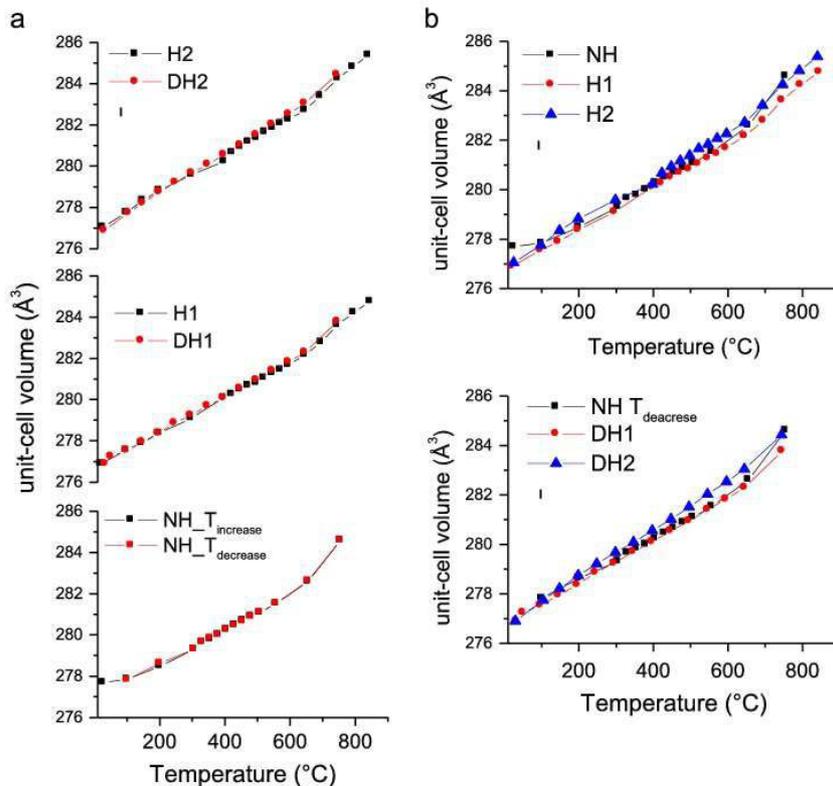
Fig. 7. (a) Temperature dependences of the unit-cell volume of non-protonated, first and second time protonated SZE proton conductor. (b) Comparison of the unit-cell volume vs. temperature between the compound in non-protonated/protonated and non-protonated/deprotonated states. Small vertical lines marked below the sample description give an idea of error values. The b graph with experimental errors can be found in Fig. S4.

Chemical and structural stability of proton conductor perovskite ceramic for fuel cells and electrolyzers
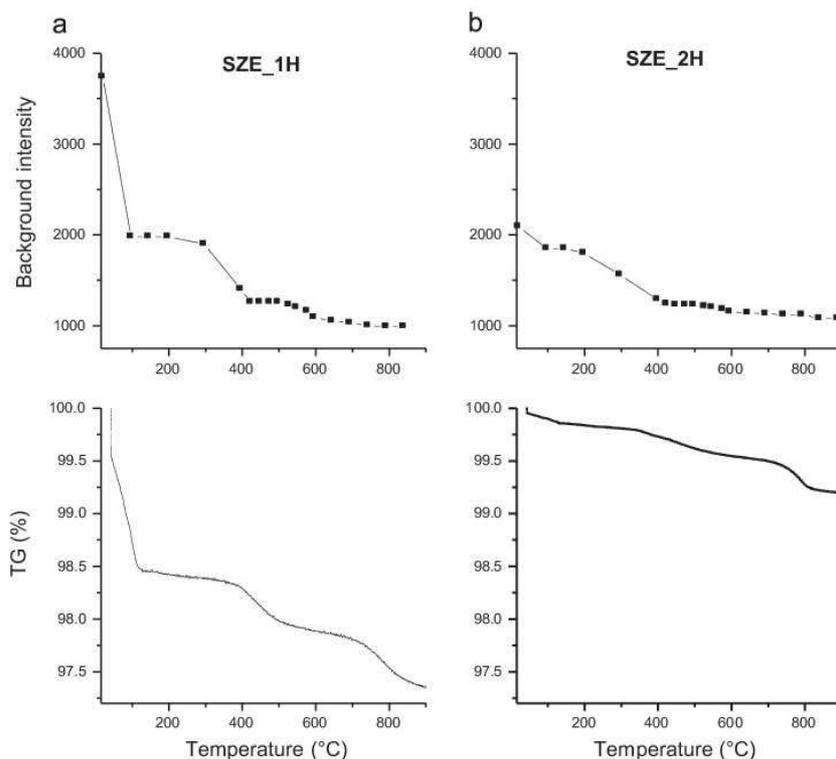
Fig. 8. Comparison of temperature dependences of incoherent background intensity proportional to the content of protonic species and TGA curves characteristic of SZE ceramic protonated first (a) and second (b) time.

temperature evolutions of unit-cell parameters (open symbols in Fig. 6a) show very linear behaviour without any deviation. Their values are very similar to those characteristic of the 1st time protonated compound. Consequently, the room temperature unit-cell parameters (Table 1) are very similar, almost identical if we take into account values of a standard error deviation. It should be stressed that in the case of SZYb measureable differences were detected between the protonated and deprotonated states.

Finally it is important to underline that as during our previous neutron measurements [41] performed on SZYb, the SZE ceramic also exhibits small (0.3%), but measurable contraction of the unit-cell volume (Table 1, Fig. 7b, Fig. S4) after the first protonation. This contraction indicates an irreversible modification of the host perovskite structure.

In conclusion, after the first protonation-deprotonation cycle, the SZE ceramic preserves its mechanical/structural properties and shows even higher level of structural order. We detected also very small chemical modifications, i.e. the SrO trace removing and $SrCO_3$ content increase, as well as the presence of small, irreversible contraction of the unit-cell volume.

3.3. Second time protonated (SZE_2H)/deprotonated (SZE_2DH) $SrZr_{0.9}Er_{0.1}O_{3-\delta}$

After the second protonation, performed in the same conditions, surprisingly a loss of mechanical properties was detected. Namely, applying a small stress (agate pestle), the ceramic pieces crumbled easily into small pieces, smaller than 2mm approximately, and a small part ($\sim$1/8) turned into powder. Note, such submillimetric powder was eliminated and the further measurements were performed on the ceramic grains only. The crumbling

can be explained by a high reactivity of the grain boundary when traces of secondary phases are present [25, 27, 30]. Our previous ageing/protonation studies performed in the autoclave on BZIn, BZYb and SZYb show that the crumbling is observed when traces of secondary phases are detected by Infrared and/or Raman spectrometry [25, 27, 30, 43, 45]. Transmission Electronic Microscopy measurements are necessary to deal better with the grain boundary characterization.

Raman study of the SZE grains (Fig. 4a) shows that the Pnma orthorhombic structure is well preserved. Moreover, a comparable level of $SrCO_3$ was detected before (SZE_1DH) and after the second protonation (SZE_2H). Again, the main difference concerns the Raman peaks in the vicinity of 750 cm^{-1} that reveals the incorporation of protonic species (Fig. 4b). We can thus confirm that the ceramic crumbling has no impact on structural and chemical properties of the SZE bulk material.

Neutron diffraction pattern of the 2nd time protonated SZE (Fig. 2, Fig. 3a, Fig. S1) is in good agreement with the Raman results and confirms the presence of well crystallised orthorhombic symmetry with the Pnma space group. Note, the same symmetry is observed in the case of deprotonated compound (SZE_2DH). The level of incoherent background intensity is higher in the case of protonated sample (Fig. 3a) in agreement with the presence of protonic species. This background level is however smaller that the one detected in the case of 1st time protonated ceramic (Fig. 3a, Fig. 8). The comparison of temperature evolutions of the background intensity and TG analysis (Fig. 8b) reveals the traces of surface water, hydroxides and as usually a small amount of bulk protons. Following formula can be then proposed for the 2nd time protonated SZE: $SrZr_{0.9}Er_{0.1}O_{3-\delta}$ $(OH)_{0.004}$ $H_{0.003}$,0.002 H_2O.

With the temperature increase, the orthorhombic – pseudo

tetragonal phase transition is observed near 700 °C. As for the 1st time protonated compound, a very small deviation from the linear behaviour observed in the case of b parameter vs. temperature, suggests a kind of structural anomaly in the vicinity of 350 °C. The same question can be asked: is it due to the hydroxide departure or is it an intrinsic feature of protonated system?

The 2nd time deprotonated SZE undergoes also the reversible, pseudo-tetragonal-orthorhombic phase transition in the vicinity of 700 °C. With further temperature decrease, a very linear behaviour of the unit-cell parameters is observed revealing the lack of additional structural modifications. As presented in Fig. 7a the temperature evolution of unit-cell volume is very similar for the 2nd time protonated and deprotonated SZE ceramic grains. The room temperature unit-cell parameter values (Table 1) are almost the same. Raman analysis (Fig. 4) confirms also good reversibility of symmetry. The presence of SrCO$_3$ is once again detected. The differences in intensity of the main stretching carbonate peak detected near 1071 cm^{-1}, measured across a ceramic piece fracture, show its heterogeneous distribution, the content is higher on the surface and very small into the bulk.

It is noteworthy that the room temperature unit-cell parameter values after the second protonation are very similar to those determined after the first protonation (Table 1, Fig. 7). This reveals that the second protonation has no important impact on structural modifications and in consequence a high structural reversibility as a function of protonation/deprotonation. However, with the temperature increase, above 200 °C actually, the unit-cell volume values characteristic of the 2nd time protonated SZE are systematically a little bit higher that those of the 1st time protonated ceramic (Fig. 7b). Similar tendency is observed in the case of deprotonated compound.

In conclusion, after the second protonation/deprotonation cycle the SZE compound shows rather good structural stability with the small structural modifications very similar to those detected already after the first protonation/deprotonation. Simultaneously, the traces of secondary phases are still present and a significant ceramic crumbling was easily obtained under hand mortar pestle action.

4. Discussion

Three successive neutron diffraction campaigns performed on the same batch of non-protonated as well as two times protonated/deprotonated SrZr$_{0.9}$Er$_{0.1}$O$_{3-\delta}$ allowed us to go deeper in the study of the structural and chemical stability of anhydrous proton conducting perovskites. These neutron results, supported by Raman and TGA analyses, show that the SZE perovskite exhibits a good structural stability as a function of protonation/deprotonation cycling with a high level of reversibility. The most important structural modification giving rise to the small irreversible unit-cell volume contraction (0.3%) is detected after the first protonation performed at 500 °C under 40 bar of water vapour pressure (Fig. 7b). After the second protonation, similar values of the unit-cell parameters are detected (Fig. 7b, Table 1). Simultaneously, the first protonation plays also a major role (Fig. 4, Fig. 3, Fig. S2) in the presence and type of secondary phases. Namely, during this protonation the SrO/Er$_2$O$_3$ traces are transformed into hydroxides and carbonates (Fig. 4, Fig. 8a). This transformation seems to stabilize the host perovskite symmetry, and even to enhance a crystallization level (Fig. 3, Fig. S2). Consequently, after the first protonation a quite good chemical stability is observed (Fig. 4). However the presence of secondary phases and their important reactivity with water and CO$_2$ lead to an easy ceramic crumbling, detrimental for industrial applications, already after the second protonation. Note, previous studies showed that high density

ceramics ($>$ 95%) retain their pristine mechanical strength after 5 weeks of operating at 500 °C under 50 bar of H$_2$O pressure [43, 45]. This points out that a particular reactivity of the grain boundary can be controlled by the ceramic processing.

These interesting results compared with the previous ones obtained on high density SZYb ceramics [41] allowed us to consider a few important questions/aspects:

i. *The pristine compound density and purity*. The investigated here SZE ceramics exhibit medium density (90%), lower than the ceramics previously used in our studies (95-99%). The results reveal the presence of secondary phase traces: SrO, Er$_2$O$_3$ and SrCO$_3$ (Fig. 4). This is related to the excess of Er and Sr oxides during the synthesis in order to promote a high densification and nominal stoichiometry of a perovskite phase [27, 30, 42, 45]. The presence of secondary phases shows that this excess has not been completely removed during the sintering. The crystallographic/chemical purity of pristine ceramic is the must: our studies (this and previous ones [24, 25, 43]) show clearly that a lifetime of a material containing secondary phases is rather short. The highest structural/chemical stability has been observed in the case of high density SZYb ceramics showing a single perovskite phase only [41, 43, 45].

ii. *The role of secondary phases*. The presence of secondary phases plays a key role in the protonation process. It is clear that the traces of SrO and SrCO$_3$ interact strongly with water vapour leading to the hydroxide formation and to the SrCO$_3$ content increase (Fig. 4, Fig. 8). The Sr(OH)$_2$ content detected after each protonation (Fig. 8) is systematically removed above 300 °C which seems to have a small impact on the temperature evolution of lattice parameters/unit-cell volume (Fig. 6, Fig. 7) as well as on conductivity measurements [16, 52]. The SrCO$_3$ content is limited to traces but seems to increase slightly with the number of protonation/deprotonation cycles (Fig. 4). The results show that secondary phases present once in a pristine material, remain always present in a protonated/deprotonated compound. Moreover, they can easily react with water/CO$_2$ and then transform themselves into more complex forms [26]. In consequence, the presence of secondary phases will always lead to a premature ageing. The SZE crumbling is its first consequence. Further on, more or less important chemical/ structural decomposition of perovskite phase appears as it was already detected in the case of Ba-based homologues [27, 30, 43].

iii. *The type and content of protonic species*. The use of lower density ceramics should, in theory, make the incorporation of protonic species easier due to a higher surface of gas/solid exchange. Indeed, higher content of protonic species was detected in the case of SZE protonated compound (Fig. 8) in comparison with that characteristic of SZYb [41]. However, TGA and incoherent background measurements (Fig. 8) reveal clearly that this increase concerns the surface protonic species (water, Sr(OH)$_2$) only! The content of bulk protons is small, i.e. 2-4 10^{-3} mol/mole, comparable to that previously determined in the case of high density homologues [25, 29, 34]. Important question can be then asked: is it possible to enhance the bulk proton content or does any threshold exist? In order to answer this question, one should consider an effective content of oxygen vacancies, their distribution and how many of them we can fill during the protonation process. These aspects have not been fully resolved yet [33, 45, 53]. Raman study showing important differences in the 700-800 cm^{-1} spectral range (Fig. 4) assigned to the vibrations of octahedra perturbed by the substituting elements, oxygen vacancies and protons (Fig. 4) points that the oxygen vacancy distribution/filling differs between a sample bulk and surface. Further study

should be performed on single crystal to determine the content and the role of oxygen vacancies in the proton species incorporation mechanism as well as in local structure modifications.

Fig. 8 shows also that different contents of surface water are detected. In the case of the first protonation process, the ceramic contains higher water level that modifies the pristine symmetry giving rise to the structure distortions (Fig. 3). Once the SZE ceramic crumbled into small pieces/powder the observed water level is smaller what can suggest that water was present at the total surface (including the pore surface) due to higher porosity and/or in the grain boundary. Simultaneously, the contents of $Sr(OH)_2$ and bulk protons are comparable whatever the dense ceramic or grains.

iv. The role of substituting element. important structural differences were detected between the SZYb and SZE compounds. these differences are related to the presence of additional small structural modifications (450°, 550 °C) as well as the structural irreversibility detected as the unit-cell volume contraction after deprotonation in the case of SZYb ceramic [41]. on the contrary, the Er-based SZ material shows rather High structural reversibility after three thermal heating/cooling and two protonation/deprotonation cycles. Only, very small contraction of the unit-cell volume was detected after the first protonation which suggests that the use of monovalent Er as a substituting ion enhances the reversibility between the protonated and deprotonated states. on the other hand, the Er-substituted compound shows the loss of mechanical strengths related to the presence of secondary phases. since the SZYb and SZE ceramics exhibit different density, the structural/chemical/mechanical differences cannot be explained by the type of substituting element only. in order to go further in the determination of perfect compromise between the composition, especially the substitution level, density and their role in protonation/deprotonation aspects and long term stability, the similar study should be performed but on the ceramics free from secondary phases using a Higher resolution diffractometer.

5. Conclusions

Neutron diffraction, TGA and Raman studies show that $SrZr_{0.9}Er_{0.1}O_{3-\delta}$, a potential candidate for electrolytic membrane of hydrogen economy devices, exhibits rather good structural/chemical stability vs. protonation/deprotonation cycling. Simultaneously, these studies reveal a complex structural behaviour of this anhydrous proton conducting perovskite. The first protonation is crucial, not only because seems to stabilize the major perovskite symmetry and secondary phase level but especially because it changes the local structure, very probably allows the homogenization of substitution element and oxygen vacancy distribution. Further studies, such as environmental XPS, EXAFS, NMR and TEM very sensible to a local ion environment, performed on ceramics and single crystals are necessary to go further in understanding these local modifications. Consequently, the first protonation gives rise to small irreversible structural/chemical modifications which do not change any more through further protonation/deprotonation cycling. The crumbling of SZE ceramic after the second protonation shows clearly that the presence of secondary phases (SrO, $SrCO_3$, $Sr(OH)_2$, …), even limited to traces, at the grain boundary would always lead to a premature ageing. Note, under high pressure enhancing significantly ageing mechanisms, any instability can be detected very fast. This allows us to optimize the structural/chemical stability of a material and in

consequence to propose a good membrane with a very long lifetime (more than 10 000 h) for industrial applications. Further study is however necessary to determine the relations between the structural modifications and proton dynamics vs. operating cycling. The priority should be given to measurements allowing the coupling of diffraction experiment with quasi-elastic ones, performed if possible *in situ* or even *in operando*.

Appendix A. Supplementary material

Supplementary data associated with this article can be found in the online version at http://dx.doi.org/10.1016/j.jpcs.2015.03.025.

References

[1] F. Forrat, G. Dauge, P. Trevoux, G. Danner, M. Christan, Acad. Sci. Paris 259 (1964) 2813.
[2] H. Iwahara, T. Esaka, H. Uchida, N. Maeda, Solid State Ionics 3/4 (1981) 359.
[3] Ph Colomban (Ed.), Proton Conductors Solids, membranes and gel – materials and devices, Cambridge University Press, Cambridge, 1992, 10.1017/CBO9780511524806.
[4] M. Ni, M.K.H. Leung, D.Y.C. Leung, Int. J. Hydrogen Energy 32 (2007) 4648.
[5] H. Matsumoto, S. Okada, S. Hashimoto, K. Sasaki, R. Yamamoto, M. Enoki, T. Ishihara, Ionics 13 (2007) 93.
[6] Ph. Knauth, M.L. Di Vona (Eds.), Solid State Proton Conductors. Properties and Applications in Fuel Cells, John Wiley & Sons, Chichester, 2012.
[7] K.D. Kreuer, Annu. Rev. Mater. Res. 33 (2003) 333.
[8] T. Norby, Solid State Ionics 125 (1999) 1.
[9] T. Kobayashi, K. Abe, Y. Ukyo, H. Matsumoto, Solid State Ionics 138 (2001) 243.
[10] S. Tao, J.T.S. Irvine, J.A. Kilner, Advanced Materials 17 (2005) 1734.
[11] A.S. Nowick, Y. Du, Solid State Ionics 77 (1995) 137.
[12] S. Ricote, N. Bonanos, G. Caboche, Solid State Ionics 180 (2009) 990.
[13] A. Grimaud, J.M. Bassat, F. Mauvy, P. Simon, A. Canizares, B. Rousseau, M. Marrony, J.C. Grenier, Solid State Ionics 191 (2011) 24.
[14] Q. Chen, T.W. Huang, M. Baldini, A. Hushur, A. Pomjakushin, S. Clark, W. Mao, M. Manghnani, A. Braun, T. Graule, J. Phys. Chem. C 115 (2011) 24021.
[15] F. Giannici, M. Shirpour, A. Longo, A. Martorana, M. Merkle, J. Maier, Chem Materials 23 (2011) 2994.
[16] I. Ahmed, C.S. Knee, M. Karlsson, S.G. Eriksson, P.F. Henry, A. Matic, D. Engberg, L. Borjesson, J. Alloys Comp. 450 (2008) 103.
[17] B. Sala, O. Lacroix, S. Willemin, K. Rhamouni, H. Takenouti, A. van der Lee, P. Goeuriot, B. Bendjeriou, Ph.Colomban, Procédé d'optimisation de la conduction ionique d'une membrane conductrice ionique, AREVA, CNRS, ARMINES, SCT, PCT patent WO 2008/152317 A2, 2008 (18-12).
[18] B. Sala, F. Grasset, O. Lacroix, A. Sirat, K. Rhamouni, M. Keddam, H. Takenouti, D. Goeuriot, B. Bendjeriou, Ph Colomban, A. Slodczyk, G. Pourcelly, A. Van der Lee, J.G. Sanchez, Procédé de génération d'hydrogène par électrolyse de vapeur, AREVA, CNRS, ARMINES: French Patent FR (2011) 1159221, 12/11.
[19] O. Lacroix, K. Rahmouni, A. Sirat, H. Takenouti, C. Deslouis, M. Keddam, B. Sala, J. Power Sources 270 (2014) 506.
[20] L.A. Chick, O.A. Marina, C.A. Coyle, E.C. Thomsen, J. Power Source 236 (2013) 341.
[21] L. Magistri, A. Traverso, F. Cerutti, M. Bozzolo, P. Costamagna, A.F. Massardo, Fuel Cells 5 (2005) 80.
[22] W.J. Yang, S.K. Park, T.S. Kim, J.H. Kim, J.L. Sohn, S.T. Ro, J. Power Source 160 (2006) 462.
[23] W. Burbank Jr, D. Witmer, F. Holcomb, J. Power Sources 193 (2009) 656.
[24] S. Upasen, P. Batocchi, F. Mauvy, A. Slodczyk, Ph Colomban, J. Alloys Comp. 622 (2015) 1074.
[25] Ph. Colomban, O. Zaafrani, A. Slodczyk, Membranes 2 (3) (2012) 493.
[26] Colomban, O. Zaafrani, A. Slodczyk, J. Raman Spectrosc. 44 (2013) 312.
[27] A. Slodczyk, B. Dabrowski, N. Malikova, Ph Colomban, MRS Proceedings (2011), http://dx.doi.org/10.1557/opl.2011.107.
[28] A. Slodczyk, Ph. Colomban, O. Zaafrani, O. Lacroix, B. Sala, MRS Proceedings (2011), 10.1557/opl.2011.616.

[29] Ph Colomban, Fuel Cells 13 (2013) 6.

[30] A. Slodczyk, M.D. Sharp, S. Upasen, Ph Colomban, J. Kilner, Solid State Ionics 262 (2014) 870.

[31] Y.M. Baikov, W. Gunther, V.P. Gorelov, Ph Colomban, R. Baddour-Hadjean, Ionics 4 (1998) 347.

[32] Ph. Colomban, J. Tomkinson, Solid State Ionics 97 (1997) 123.

[33] Q. Chen, F. El Gabaly, F.A. Akgul, Z. Liu, B.S. Mun, S. Yamaguchi, A. Braun, Chem. Mater. 25 (2013) 4690.

[34] Ph. Colomban, A. Soldczyk, European Physical J. Special Topics 213 (2012) 171.

[35] M. Karlsson, Dalton Trans,. 42 (2013) 317.

[36] N. Malikova, C.K. Loong, J.M. Zanotti, F. Fernandez-Alonso, J. Phys. Chem. C111 (2007) 6574.

[37] A.K. Azad, A. Kruth, J.T.S. Irvine, Intern. J. Hydrogen Energy 39 (2014) 12804.

[38] A. Slodczyk, Ph Colomban, D. Lamago, M.H. Limage, F. Romain, B. Sala, S. Willemin, Ionics 14 (2008) 215.

[39] A. Slodczyk, Ph Colomban, D. Lamago, G. André, O. Zaafrani, O. Lacroix, A. Sirat, B. Sala, J. Mater. Res. 27 (2012) 1939.

[40] A. Slodczyk, Ph Colomban, O. Zaafrani, N. Malikova, S. Longeville, J.-M. Zanotti, O. Lacroix, B. Sala, Solid State Ionics 252 (2013) 7.

[41] A. Slodczyk, Ph Colomban, G. Andre, O. Zaafrani, F. Grasset, O. Lacroix, B. Sala, Solid State Ionics 225 (2012) 214.

[42] B. Bendjeriou-Sedjerari, J. Loricourt, D. Goeuriot, P. Goeuriot, J. Alloys Compd. 509 (2011) 6175.

[43] A. Slodczyk, O. Zaafrani, M.D. Sharp, J.A. Kilner, B. Dabrowsky, O. Lacroix, Ph. Colomban, Membranes 3 (4) (2013) 311.

[44] A. Slodczyk, Ph Colomban, S. Willemin, O. Lacroix, B. Sala, J. Raman Spectrosc. 40 (2009) 513.

[45] O. Zaafrani, PhD Thesis, UPMC Paris (2010).

[46] ⟨http://www.llb.cea.fr⟩.

[47] J. Rodriguez-Carvajal, FullProf Software, ⟨http://www.ill.fr/⟩.

[48] A. Le Bail, Powder Diffraction 20 (2005) 316.

[49] C.J. Howard, K.S. Knight, B.J. Kennedy, E.H. Kisi, J. Phys. Condens.Matter 12 (2000) L677.

[50] A. Slodczyk, M.H. Limage, O. Zaafrani, Ph Colomban, F. Grasset, J. Loricourt, B. Sala, , J.Raman Spectroscopy 42 (2011) 2089.

[51] R.V. Shpanchenko, E.V. Antipov, L.M. Kovba, Zh. Neorg. Khim 38 (1993) 599.

[52] N. Jalarvo, C. Haavik, C. Kongshaug, P. Norby, T. Norby, Solid State Ionics. 180 (2009) 1151.

[53] M. Karlsson, Phys. Chem. Chem. Phys. (2014), http://dx.doi.org/10.1039/c4cp04112g.

CHAPTER 6

"Protonation and structural/chemical stability of $Ln_2NiO_{4+\delta}$ ceramics vs. H_2O/CO_2: High temperature/water pressure ageing test"

In this chapter, three types of nickelates ceramics formula as $Ln_2NiO_{4+\delta}$ (Ln = La, Pr, Nd), is the first investigated electrode series. We will report on its chemical and structural characterization against medium and high water vapor treatment (20 bar and 40 bar) at intermediate temperature. We will also discuss the ageing of materials against caustic ambient (CO_2 saturated water vapor pressure). The principal analysis techniques i.e. IR, Raman spectroscopy, TGA, TE, and X-ray diffraction are employed.

Protonation and structural/chemical stability of Ln$_2$NiO$_{4+\delta}$ ceramics vs. H$_2$O/CO$_2$: High temperature/water pressure ageing tests

CrossMark

S. Upasen [a,b], P. Batocchi [c], F. Mauvy [c], A. Slodczyk [a,b], Ph. Colomban [a,b,*]

[a] Sorbonne Universités, UPMC Univ Paris 06, UMR 8233, MONARIS, 75005 Paris, France
[b] CNRS-IP2CT, UMR 8233, MONARIS, F-75005 Paris, France
[c] ICMCB, ICMCB-CNRS-IUT-Université de Bordeaux, 33608 Pessac Cedex, France

ABSTRACT

Mixed ionic-electronic conductors (MIEC) such as rare-earth nickelates with a general formula Ln$_2$NiO$_{4+\delta}$ (Ln = La, Pr, Nd) appear as potential for energy production and storage systems: fuel cells, electrolysers and CO$_2$ converters. Since a good electrode material should exhibit important stability in operating conditions, the structural and chemical stability of different nickelate-based, well-densified ceramics have been studied using various techniques: TGA, dilatometry, XRD, Raman scattering and IR spectroscopy. Consequently, La$_2$NiO$_{4+\delta}$ (LNO), Pr$_2$NiO$_{4+\delta}$ (PNO) and Nd$_2$NiO$_{4+\delta}$ (NNO) have been exposed during 5 days to high water vapor pressure (40 bar) at intermediate temperature (550 °C) in an autoclave device, the used water being almost free or saturated with CO$_2$. Such protonation process offers an accelerating stability test and allows the choice of the most pertinent composition for industrial applications requiring a selected material with important life-time. In order to understand any eventual change of crystal structure, the ceramics were investigated in as-prepared, pristine state as well as after protonation and deprotonation (due to thermal treatment till 1000 °C under dry atmosphere). The results show the presence of traces or second phases originating from undesirable hydroxylation and carbonation, detected in the near-surface layers. The proton/water insertion modifies the structure symmetry and the unit-cell volume whatever the low amount (<0.5 wt% equivalent H$_2$O). This result is consistent with long range interaction and in contradiction with the formation of hydroxyl species hypothesis. The reaction mechanisms evidenced after autoclave treatment may be useful to understand the reaction occurring at the electrode surface in SOFC/HTSE systems.

© 2014 Elsevier B.V. All rights reserved.

1. Introduction

During the last decades, perovskite-type oxides have been developed as electrolytes and electrodes for Solid Oxide Fuel Cells (SOFC), including Proton Ceramic Fuel Cells (PCFC), gas separation membranes and High Temperature Steam Electrolysers (HTSE) [1–3]. An efficient electrode material should possess high electronic and ionic conductivity (so called MIEC, mixed ionic-electronic conductor), protonic conductivity for instance in the case of air/hydrogen SOFC/HTSE operating at medium to high temperature. The main goal of these technologies is to reduce the operating temperature in the 500–700 °C range [4–8]. A tolerant behavior vs. CO$_2$ traces is also requested for these compounds. Furthermore, stable materials vs. CO$_2$ are searched for the conversion of CO$_2$ into CH$_4$ or more valuable chemicals by reaction between

carbon dioxide gas and hydrogen produced at the cathode [7]. Recently, perovskite-type ceramics belonging to Ruddlesden–Popper family such as Rare-Earth (RE) nickelates with a general formula Ln$_2$NiO$_{4+\delta}$ (Ln = La, called here after LNO; Pr (PNO) and Nd (NNO)) are proposed as potential FC cathodes [8–12].

The ideal perovskite structure has a cubic symmetry with the $Pm\overline{3}m$ space group [6]. No Raman peaks are expected for such cubic symmetry and thus the Raman spectroscopy is very efficient to detect any structural distortion [13]. The symmetry of Ln$_2$NiO$_{4+\delta}$ is more or less distorted either tetragonal (P42/ncm), or orthorhombic Bmab or Fmmm, depending on the lanthanide elements, the oxygen stoichiometry δ and temperature [14–21]. Phase coexistence is also often reported in polycrystalline materials. As for most of perovskites, the structural phase transitions are observed with the temperature increase, for example in the case of NNO with an oxygen excess, the transition from the orthorhombic symmetry (Fmmm) to the tetragonal (I4/mmm) one is detected between 477/550 °C and 600/627 °C depending on authors [14–21], actually depending on the oxygen partial pressure

* Corresponding author at: Sorbonne Universités, UPMC Univ Paris 06, UMR 8233, MONARIS, 75005 Paris, France.
E-mail address: philippe.colomban@upmc.fr (Ph. Colomban).

Chemical and structural stability of proton conductor perovskite ceramic for fuel cells and electrolyzers

explored during the thermal treatment. This should be stressed, the black color of a material requires special procedure for optical studies in order to avoid any local heating and associated structural changes (oxidation/stoichiometric modification) [22,23].

In this study, the chemical/structural stability of well-densified LNO, PNO and NNO ceramics exposed to high water vapor pressure (40 bar), with or without the CO_2 gas dissolved in the water, at 550 °C during 5 days using the autoclave device have been compared [24]. The high water pressure increases water activity at a ceramic surface and hence enhances reaction (hydroxylation, carbonation, protonation) degrees. Consequently, a significant amount of secondary phases can be formed due to corrosion process. It can be noticed that accelerate and large formation of such undesirable phases makes their detection and characterization easier. Thermogravimetry (TGA), thermal expansion (TE), infrared spectroscopy (IR), Raman spectroscopy (RS) and X-ray diffraction (XRD) were employed in order to identify potential corrosion mechanisms as well as structure modifications involved and/or associated to proton/water reaction/insertion. The combination of the microstructure examination with Raman mapping was used in order to establish the reaction rates. Preliminary conclusions have been reported [25].

Finally we claim to deal also with the complex behavior of proton in the case of anhydrous proton conducting oxides. It should be stressed that the fundamental knowledge on the proton chemical nature (hydroxyl groups or interstitial protons), its exact content, its localization (differentiation between surface defects and bulk species), and the dynamic of protons remain poor and highly debated [26–30]. The unique properties of proton and its low amount (i.e. a doping) in these membranes yield the study difficult. Consequently many authors do not even try to determine the H content in their studied/used materials. The comprehension of the structural modification involved by protonation is required for the understanding of the MIEC electrode ageing.

2. Experimental

2.1. Synthesis and sintering

Commercial powders provided by the Marion Technologies company (Verniolle, France) were isostatically pressed into pellets at 3000 bars for 5 min and then sintered in air at 1350 °C for 4 h. Densities of the as-prepared ceramics measured by the Archimedes method were higher than 95% of the theoretical values.

2.2. Autoclave treatment

Protonation was performed at high temperature/high water vapor pressure using autoclave device (Top Industrie, Vaux le Pénil, France) [14–17]. The ceramics were placed on the gold-foil holder, and then put in the autoclave chamber. Two kinds of water were used: the decarbonated water from ultrapure water system immerged by N_2 gas for 20 min in order to eliminate CO_2 amount (the so-called lean-CO_2 water), and another one, the room temperature CO_2 saturated water (hereafter called rich-CO_2 water). The dwell water pressure is adjusted by controlling the maximal pressure. A ~10% to 20% decrease of the pressure is observed during the dwell duration (550 °C, 5 days), that indicates consumption of water by the ceramic pellets.

2.3. Thermogravimetry analysis

TGA of both as-prepared and protonated ceramic pellets was performed using a Setaram Setsys Evolution (Setaram, Caluire, France) instrument in the 25–1000 °C temperature range (heating rate of 5 °C/min). In order to enhance the accuracy of TG measurements in the studied temperature range, a Pt crucible and Helium atmosphere (99.99%, $H_2O < 3$ ppm vol., $O_2 < 2$ ppm vol., $C_nH_m < 0.5$ ppm vol., Alphagaz-1, Air Liquide, France) were employed. Non-radiative heat transfer is increased in He gas that promotes the instrument sensitivity. Note, the carbon heating resistor guaranties the conservation of low oxygen level.

2.4. Thermal expansion

TE measurements were carried out under argon atmosphere (99.99%, $H_2O < 0.5$ ppm vol., $O_2 < 0.1$ ppm vol., $CO < 0.1$ ppm vol., $CO_2 < 0.1$ ppm vol., $H_2 < 0.1$ ppm vol., $C_nH_m < 0.5$ ppm vol. Alphagaz-2, Air Liquide, France) using a Setaram Setsys 1650 dilatometer instrument equipped with amorphous silica rod and support. Very low thermal expansion of amorphous silica makes a direct comparison of as-measured data possible. Flat pieces of non-protonated and protonated ceramics were measured in 30–500 °C temperature range for three successive heating/cooling cycles with heating rate of 10 °C/min.

2.5. Microstructure

The surface and the fresh fracture sections of each sample, in different states, were analyzed in micro-scale, 50–1000 μm range, using optical Microscope Olympus instrument with the selected, 10×, 50× and 100× objectives. The density of cracks was measured using the cracking-line intercept method (ASTM E112) using 10× objective. The 13 line-bundles were used as intercepting pattern. The distances in between two cracks were measured and the mean value determined.

2.6. Raman microspectrometry

Raman scattering spectra were recorded at room temperature using different exciting laser lines and instruments: (i) the 458 nm line delivered by Kr^+ ion laser; this blue laser line allows avoiding the superimposition of the Raman signature with electronic transitions of 4f ions. Labram HR800 Raman micro-spectrometer (Horiba Jobin Yvon SAS, Longjumeau, France) equipped with a 50× and 10× long working distance Nikon objectives was used; (ii) the 785 nm solid state source line of a Senterra spectrometer (Bruker Optics, Karlsruhe, Germany) equipped with 10× and 50× long work distance objectives; (iii) the 633 nm line of a He–Ne laser using a Labram Infinity spectrometer (Dilor, Lille, France). Different spectra were recorded under different illumination powers per surface unit up to the reaching of a constant wavenumber indicating that the black material is not perturbed by the laser beam.

2.7. Infrared spectroscopy

FT-IR Equinox 55 Irscope microspectrometer (Brucker) was used to record the room temperature infrared spectra between 600 cm^{-1} and 4000 cm^{-1} in an ATR mode using the Diamond ATR (analyzed area ~2 × 2mm^2) or the Germanium micro ATR (noted hereafter μ, analyzed area 20 × 20 μm^2).

2.8. X-ray diffraction

XRD patterns of ground pellets were collected on a PANalitycal X'pert MPD-PRO Bragg–Brentano θ–2θ geometry diffractometer equipped with a germanium primary monochromator over an angular range of $2\theta = 10$–130°. Each acquisition lasted for 64 h. The Cu Kα_1 ($\lambda = 1.54056$ Å) radiation was generated at 45 kV and 40 mA. Unit-cell parameters have been calculated by Le Bail profile matching. The relative quantities of the different phases have been determined according to the ratio of the relative intensities of the major peaks recorded on the XRD patterns.

3. Results and discussion

3.1. Mechanical stability

Compared to other ceramics exposed to high water pressure in similar conditions [24], the investigated LnNO pellets were not crumbled or strongly cracked after 5 days of treatment and retained significant mechanical strength. Optical microscope observations (Fig. 1) do not show cracks at the micron scale but reveal the presence of white scares (using lean-CO_2 water) or significant deposits (CO_2-saturated water). The black color of the ceramics promotes their detection. Large magnification images show two types of surface deposits: rather well-shaped micron-like grains and larger ~50 μm wide flower-like aggregates. On the contrary, after thermal treatment at 1000 °C under dry He atmosphere, the de-protonated PNO and NNO pellets exhibit more or less important crack networks (Fig. 1, mean distance in between cracks is equal to ~200 and 100 μm for PNO and NNO, respectively), not observed in the case of thermally treated non-protonated samples. This should be consistent with a variation of the LnNO unit-cell volume observed after the autoclave treatment (see further). Crack formation after thermal treatment can be assigned to a decrease of the unit-cell volume,
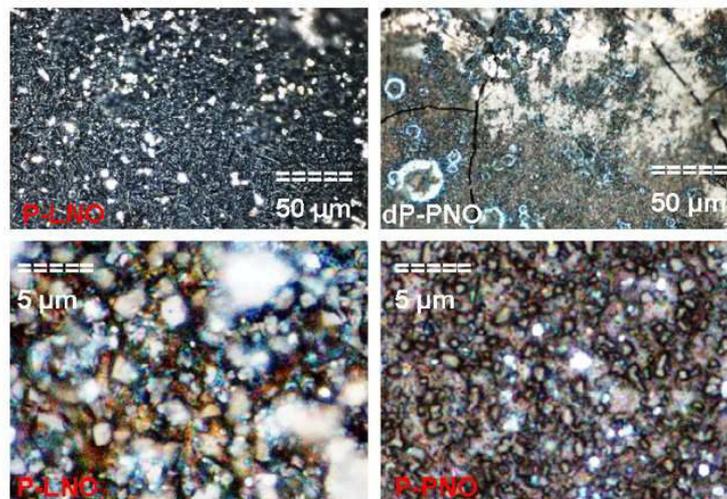
Fig. 1. Optical microphotographs of the surface of protonated LNO (P-LNO) and PNO (P-PNO) ceramics at different magnification. Comparison is given with de-protonated PNO sample (dP-PNO).

due to the departure of volatile species (H_2O) with the temperature increase.

3.2. Chemical and structural modifications

Fig. 2a compares the TGA curves recorded under Helium flux for small pellet pieces of non-protonated and protonated LnNO ceramics. The weight mass loss observed above 500 °C for non-protonated pellets is assigned to the modification of the oxygen stoichiometry, according to the mobility of oxygen ions at intermediate temperature [31]. In order to whip out this contribution, the relative difference in weight loss measured between a pristine ceramic and a protonated one is plotted in Fig. 2b. The subtraction of the thermal behavior of pristine materials heated in the same conditions highlights the contribution due to the autoclave treatment. The mass difference between non- and protonated LnNO pellets is low, but three TG events can be clearly observed for LNO and PNO ceramics: a well-defined down step at ~300 °C, a smaller one at 500–650 °C and a large one at ~900 °C. The NNO behavior does not show any marked TG feature.

The comparison with series of TGA measurements characteristic of materials containing protonic species [21,24,26,32] led us to assign the first well-defined step to hydroxide(s) decomposition (typically occurring at ~300–400 °C), the second one may correspond to the departure of bulk protons and the highest temperature one to the carbonate decomposition (~900 °C). According to the TG data the following formula can be proposed for the whole ceramic pellet with the hypothesis that the ceramic is a single phase and that events below 900 °C can be assigned to water molecule departure due to OH^- and proton loss while CO_2 departure appears above 900 °C: $La_2NiO_{4+\delta}H_{0.77}(OH)_{0.1}(CO_3)_{0.02}$, $Pr_2NiO_{4+\delta}H_{0.53}(OH)_{0.04}(CO_3)_{0.03}$ and $Nd_2NiO_{4+\delta}H_{0.21}$.

Thermal expansion plot (Fig. 2c) shows a contraction jump at ~320 °C during the first heating cycle for both protonated LNO and PNO ceramics (not observed in the literature, see [25]). A very small jump is detected in the NNO expansion curve. The contraction jump may explain the crack network observed at the sample surface after thermal treatment of protonated ceramics (Fig 1). A smaller down jump is also observed at ~200 °C for all samples; it

can be attributed to the contribution of the amorphous silica road that contains some cristobalite and trydimite traces. The very small feature detected at ~450 °C could be the signature of previously reported orthorhombic/tetragonal phase transition [3,12,14–16].

The XRD patterns recorded for LNO, NNO and PNO ground pellets before and after autoclave treatment are reported in Fig. 3. Concerning the initial state, all compounds are well crystallized and show a single phase [12,17]. Corresponding unit-cell parameters and space group symmetry (orthorhombic Fmmm or Bmab) are given in Table 1.

After protonation extra Bragg peaks are clearly visible and can be assigned to the second phases observed at the sample surface by optical microscopy (Fig. 1). Furthermore, a small shift of peaks is observed indicating a change of the unit-cell parameters (see further). For protonated LNO (H-LNO) and NNO (H-NNO) a coexistence of two perovskite phases is evidenced from the Le Bail profile analysis (Table 1).

Analysis of XRD patterns allowed the identification of three types of secondary phases: hydroxides, carbonates and oxides. Their relative ratios in the case of different Lanthanides cations are listed in Table 2. The significant proportion of hydroxides phases detected for PNO can be related to the well-defined 300 °C TG event (Fig. 2a and b) and the presence of large white surface features (Fig. 1). Regarding the LNO compound, the $La(OH)_3$ amount seems to be lower (see Table 2). This could be explained by the reduced mass variation observed in TGA curves. The identification of Ln-oxohydroxide in the case of NNO ceramic is also consistent with the small thermal expansion jump. The high ratio of carbonates observed for LNO sample is in good agreement with the Raman scattering and ATR-FTIR data (see further).

3.3. Characterization of the protonated perovskite

The comparison of the symmetry and the unit-cell parameters determined from XRD powder pattern shows complex structure modifications caused by the autoclave treatment. Notwithstanding the formation of surface secondary compounds, the coexistence of two structural phases can be deduced from Le Bail XRD profile matching analysis. The first phase keeps the pristine orthorhombic

135

Chemical and structural stability of proton conductor perovskite ceramic
for fuel cells and electrolyzers
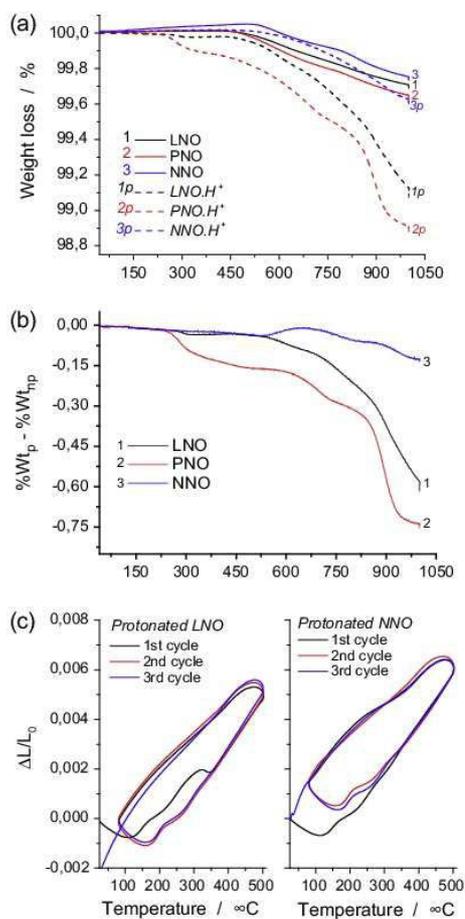
Fig. 2. Representative weight loss of (a) pristine or protonated (p) NNO, LNO and PNO ceramics and corresponding weight loss differences (b); the thermal expansion curves measured on a protonated LNO and NNO ceramics (3 heating–cooling cycles) are given in (c).

symmetry Fmmm (D_{2h} point symmetry) (H-LNO) or Bmab/D_{2h} (H-NNO) and the associated unit-cell variations are very low (Table 1). The second one exhibits the tetragonal I4/mmm/D_{4h} (H-LNO and H-NNO) symmetry and rather significant changes of the unit-cell parameters and volume are observed. The unit-cell volume changes are consistent with the insertion of protonic species into the lattice. Previous studies on the protonation of perovskite pointed out that the proton/water insertion decreases the unit-cell distortions [32,33].

The largest volume variation is measured for LNO whereas the smallest one for PNO. A small volume increase is observed for NNO (+2.5% (Bmab) and +0.2% (I4/mmm). The very low TG weight loss (Fig. 1) indicates that protonation, if occurs, is very low and/or compensated by oxygen stoichiometry variation. On the contrary, a contraction is measured in the case of PNO (2.3%) and LNO (0.2 and 9.3%, for Fmmm and I4/mmm, respectively (Table 1)). It should be noticed that the comparison has been made for different symmetries: thus the I4/mmm unit-cell volume was multiplied by a 2 factor (LNO: $171.86 \times 2 = 343.73$ to be compared with 378.85 Å^3; NNO: $181.98 \times 2 = 363.96$ to be compared with 363.10 Å^3). For both later compounds the TGA curves are consistent with a protonation.
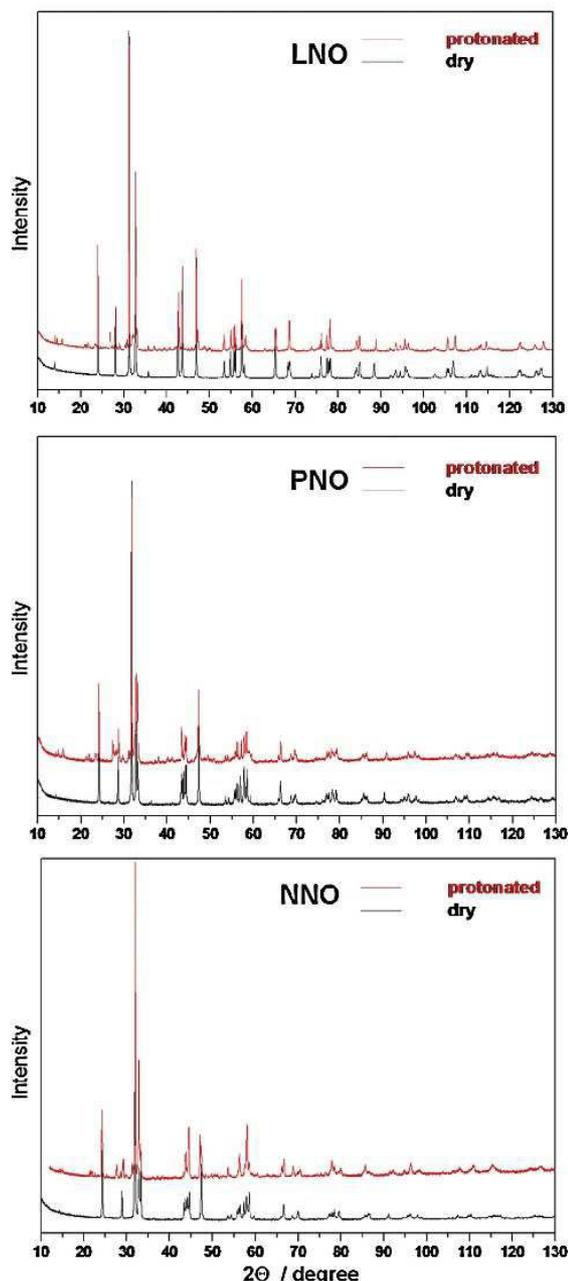
Fig. 3. Comparison of the XRD patterns before and after protonation of LNO, NNO and PNO crushed ceramics. Protonation has been made used lean-CO_2 water.

3.4. Raman signature of pristine nickelates

The collection of Raman spectra of black materials is a difficult task because of the very strong light absorption that induces direct conversion of the photon energy into heat and hence promotes local heating and structural transformations. In consequence, even under low irradiance phase transitions and/or oxidation can be induced by the laser spot [23,23]. Since the degree of light

136

Table 1
Symmetry groups and unit cell parameters of pristine and protonated LnNO ceramics (error in bracket); the pellets have been exposed to lean-CO_2 water.

Phase	Symmetry	Unit-cell parameter			Volume	Δ
		a (Å)	b (Å)	c (Å)	V (Å³)	Δ%
$La_2NiO_{4+\delta}$ LNO	Fmmm orthorhombic	5.4682(2)	5.4590(2)	12.6917(4)	378.85(2)	
H-LNO	Fmmm orthorhombic	5.4744(3)-	5.4680(3)	12.6361(5)	378.25(3)	−0.2
	I4/mmm tetragonal	3.689(1)	3.689(1)	12.630(3)	171.86(8)	−9.3
$Pr_2NiO_{4+\delta}$ PNO	Bmab orthorhombic	5.3841(2)	5.4646(2)	12.4655(3)	366.76(2)	
H-PNO	Bmab orthorhombic	5.398(1)	5.466(1)	12.401(2)	365.9(1)	−2.3
$Nd_2NiO_{4+\delta}$ NNO	Bmab orthorhombic	5.3733(4)	5.4586(4)	12.3797(9)	363.10(4)	
H-NNO	Bmab orthorhombic	5.3864(9)	5.4510(8)	12.398(2)	364.02(9)	+2.5
	I4/mmm tetragonal	3.8544(2)	3.8544(2)	12.249(1)	181,98(2)	+0.2

Table 2
Relative amount in percent of the phases formed at the surface of LnNO ceramics after treatment in autoclave (550 °C, 40 bar, 5 days).

2nd Phase	$La_2NiO_{4+\delta}$ – LNO	$Pr_2NiO_{4+\delta}$ – PNO	$Nd_2NiO_{4+\delta}$ – NNO
$Ln(OH)_3$	3	10	–
LnOOH	–	13	9
LnH_2	–	Traces?	–
Ln_2O_3	4	10	–
$Ln_2O_2CO_3$	2	–	–
$Ln_4Ni_3O_{10}$	6	–	–
$LnNiO_3$	–	Traces	–
NiO	–	Traces	7

absorption strongly varies with the wavelength, the Raman spectra have been recorded with blue (458 nm) and red (785/633 nm) laser excitation lines. Furthermore Rare Earth elements being largely present in the studied compositions, a superimposition of the (huge) 4f electronic transition fluorescence peaks with the Raman signal is currently observed; consequently a comparison of the Raman signal recorded with different wavelengths is necessary to select the most appropriate laser excitation [25]. Under 458 nm and 785 laser excitations broad bands and multiplets due to 4f electronic transition are observed above ~1200 cm^{-1} (i.e. 866.7 nm in absolute scale,) and thus do not overlap with the Raman spectrum. Consequently only spectra recorded under blue excitation are presented in Fig. 4 because of their better quality (see Ref. [25] for spectra recorded under different laser wavelength).

The Raman signature of non-protonated, pristine ceramics will be first discussed. Most of Raman spectra reported in the literature is of poor quality and deals with homologues [34–40]. Ogita et al. [34] analyzed the Raman spectra of Rb_2NiO_4 single crystal with the K_2NiF_4-type structure as well as polycrystalline La_2NiO_4 (514.5 nm, output power of about 300 mW). In the case of tetragonal I4/mmm (D_{4h}^{17}) symmetry 14 optic modes are expected ($2E_g + 2A_{1g} + 5E_u + 4A_{2u} + B_{2u}$), 4 ($2E_g + 2A_{1g}$) being Raman active, and 7 ($4E_u + 3A_{2u}$) infrared active. Nevertheless, it is well established that the symmetry depends on the oxygen stoichiometry which can be modified by sintering and laser heating [37,38]. Ogita et al. assign the Raman peaks detected at 120 cm^{-1} and 358 cm^{-1} to A_{1g} modes associated to the motion of the heavy Rb cations (see Fig. 5). The peak at 188 cm^{-1} was assigned to the E_g mode. Comparing the spectra of polycrystalline La_2NiO_4 with those of Rb_2NiO_4 single crystal, the authors assigned the peaks at 100 and 405–430 cm^{-1} (according to the analyzed spot) to A_{1g} modes. The above reported Raman

signatures can be questioned, in particular the 100–120 cm^{-1} peak because these bands are observed for rare-earth oxides and (oxo)hydroxides (Table 4). Udagawa et al. [35] studied polycrystalline $(La_{1-x}Sr_x)_2NiO_4$ (488 nm, output power of 20 mW). Two Raman modes were observed at 450 cm^{-1} and 240 cm^{-1}, assigned to the Ni–O stretching (A_{1g}) and apical oxygen vibration along the a- or b-axis with E_g symmetry, respectively. Prieto et al. [36] studied the stoichiometric and oxidized Nd_2NiO_4 polycrystalline samples (488 nm, 3 W power). The 440–470 cm^{-1} band is assigned to the Ni–O(2) stretching modes and the features from 750 to 1000 cm^{-1} to the double phonon of the first mentioned modes because of resonance Raman condition [37,38]. The authors observed the Ni–O stretching mode at 670 cm^{-1}. Because, this mode is forbidden in the tetragonal I4/mmm symmetry, some distortion of the unit-cell can be supposed.

The discrepancy between literature data and the black color of the ceramic led us to study the wavenumber shift vs. laser power. Fig. 5 compares the wavenumber shift vs. logarithmic laser power for different samples. Below ~0.3 mW (50× objective) the wavenumber is nearly constant that proves the absence of heating phenomena. As expected [23], a linear wavenumber down shift of the main peaks (Fig. 5) is observed vs. logarithmic laser power for values higher than 0.3 mW, in agreement with the sample heating. In between these two regimes, an up wavenumber jump is observed. This behavior can be assigned to a phase transition/oxidation due to the laser heating in air. Consequently, only Raman data recorded with a low illumination power can be used for comparison with XRD data.

The Raman spectra collected at low illumination power for all pristine LnNO samples (Fig. 4) show triplet located at ~220, 450–470 and 650–675 cm^{-1}; a weak, broad band can also be detected at 590 cm^{-1}. Similar spectra have been recorded at the surface and on fresh section of pristine ceramic pellet. Note, narrow peaks almost disappear under red laser excitation [25] – the spectrum becomes characteristic of low distorted cubic perovskite structure – that could indicate a resonance spectrum under blue laser excitation.

The LNO spectrum is very similar to that of other perovskite compounds, like orthorhombic $LaMnO_{3-\delta}$ [39] and $SrFe_{1-x}Ga_xO_{3-\delta}$ [40]. Note, sometime observed very narrow ca. ~860 cm^{-1} peak is due to CrO_4^{2-} ions pollution arising from the autoclave steel. When the oxygen stoichiometry and the symmetry are modified, a band broadening and an intensity decrease/disappearance of the ~660–700 cm^{-1} peak for LNO and NNO can be observed as for above mentioned homologues perovskite [39,40]. However, the wavenumber up-shift

Chemical and structural stability of proton conductor perovskite ceramic for fuel cells and electrolyzers
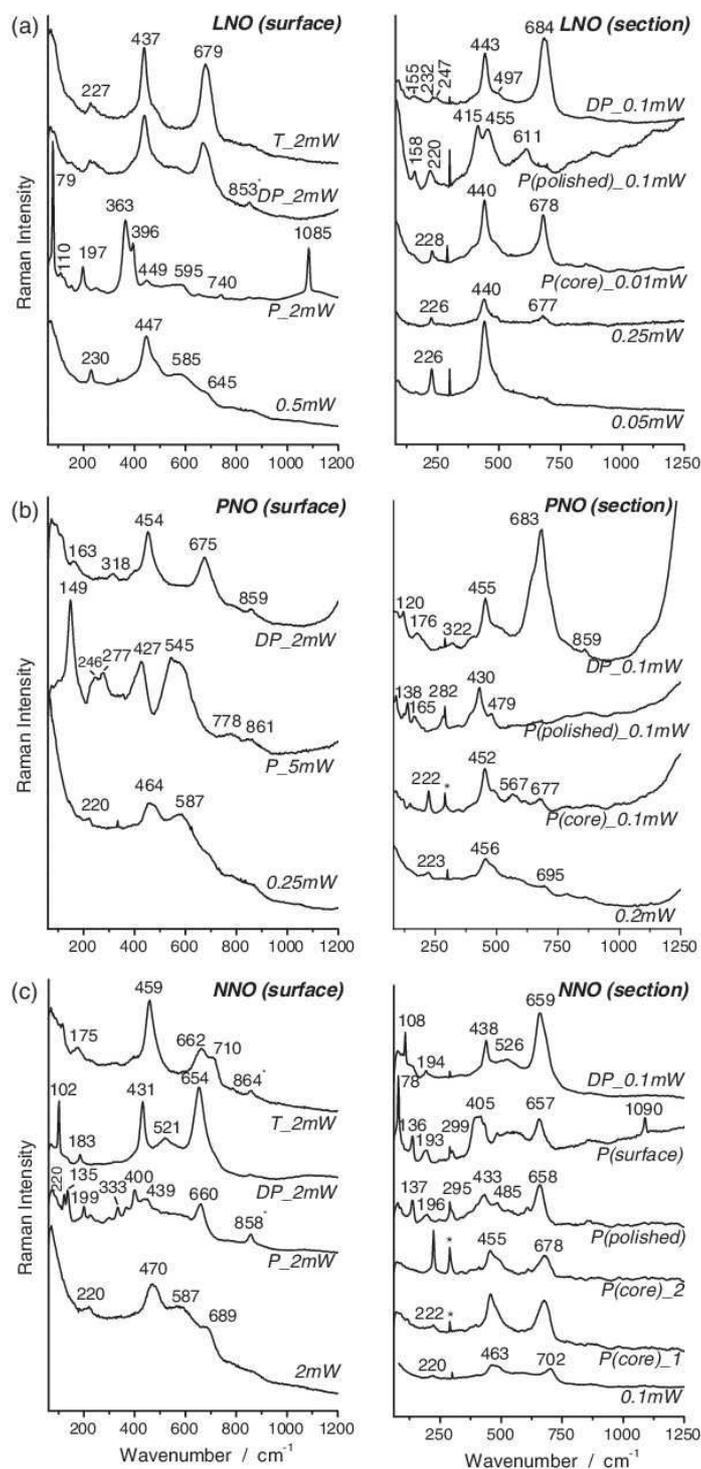
Fig. 4. Representative Raman spectra (a) recorded with blue (458 nm) laser line of pristine, protonated (P: 40 bar, 7 days and 55 bar, 8 days), de-protonated (DP) and thermally treated (T) of LNO (a), PNO (b) and NNO (c). The laser power at sample is given; 50× microscope objective is used. In (b) spectra recorded at low and very low laser power are given. The pellet is polished (P) in order to record representative spectra of the different layers.
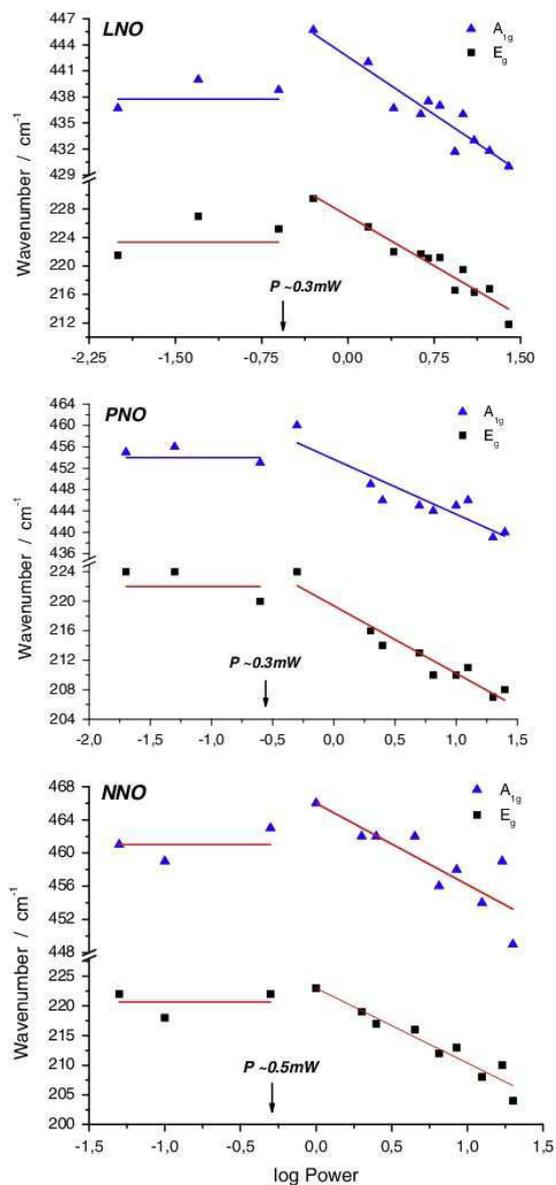
Fig. 5. Semi-logarithmic plot of the wavenumber vs. laser power (0.01 to 30 mW, 488 nm, 50× objective) for LNO, PNO and NNO.

measured for LNO and NNO compounds, cannot be explained by the heating (thermal expansion of the chemical bond led to a down-shift) but indicates a phase transition. The wavenumber and the intensity of the peaks slightly vary from spot to spot and it is not possible to definitely conclude if this small wavenumber shift arises from the local variation of the stoichiometry, grain orientation, stress, etc. At higher laser power irradiance, the wavenumber down-shift can be assigned to thermal lengthening of the M–O bond under the laser spot, as usual. It could be added that in the case of all LnNO thermally treated samples (1000 °C under He atmosphere), the peak at ca. 655 (NNO) to ~680 cm^{-1} (LNO) becomes very significant. This contribution can be assigned to the distortion increase, as previously noted by Prieto et al. for NNO [36], likely to D_{2h}. or even

lower symmetry. Simultaneously a broad feature is observed at ~1350 cm^{-1} that may be the overtone of the mentioned above, 670 cm^{-1} band according to the resonance Raman effect under blue excitation.

The comparison of the spectra (relative band intensity, bandwidth, splitting) clearly demonstrates that the symmetry is slightly different between LNO and the PNO/NNO homologues and changes with temperature. Actually the most important information obtained from the Raman spectrum for perovskite compounds is not only the band number (to be compared with expected number deduced from Group theory analysis), but the Raman intensity that measures the deviation from a cubic mean symmetry [13,23]. The low intensity and important broadness of the PNO and NNO spectra are rather similar to those recorded for rhombohedral Lanthanum Strontium Cobalt Ferrite [25] and rhomboedral perovskite homologues [39,40]. On the contrary, the LNO spectrum is consistent with an orthorhombic symmetry, in agreement with X-ray diffraction (Table 1).

3.5. Reactivity and second phases: hydroxylation and carbonation

Autoclave treatment involves structural changes and corrosion phenomena. Fig. 4 presents typical Raman spectra recorded on the surface and section of the LnNO protonated ceramics. The Raman mapping recorded along a fresh fractured section of autoclave treated ceramics is presented in Fig. 6. An important number of recorded Raman spectra allow detecting the presence of different layers (Fig. 7) and determining their thicknesses. Note, significant FTIR-ATR spectra are shown in Figs 8 and 9. Starting from the surface, 3 characteristic regions can be distinguished: the corroded layer, the 'high' protonated layer and the 'low' or non-protonated core.

A mixture of hydroxide(s), carbonate(s) or hydroxycarbonate(s), can be identified by the presence of narrow peaks, fingerprints of these phases (Table 3, [30,41–46], in agreement with X-ray diffraction, Table 2). Carbonates are well identified due to the C–O narrow Raman stretching mode, centerd at 1086 cm^{-1} for La, and at 1084 cm^{-1} for Nd-based carbonate. Note, the narrow IR bending mode peaking at 853 (LNO, Fig. 8a and a', spectrum noted P_s) and 884 cm^{-1} (PNO, Fig. 8b, spectrum noted P_s1) is characteristic of carbonate [46]. Note, ATR FTIR spectra show unexpected reflection spectra, see further). The carbonate contributions seem to be weaker or disappear for materials treated with the CO_2-lean water (see in Ref. [25]). According to XRD, no carbonates are detected on PNO and NNO surfaces when water with low CO_2 content is used. On the other hand, carbonates are observed for all materials exposed to the CO_2-saturated water vapor pressure.

The Raman spectra of protonated LNO pellet surface (Figs. 4a and 6) show additional peaks at 396, 263, 197 and 79 cm^{-1}. These peaks can be assigned to the hexagonal phase of $La_2O_2CO_3$, in agreement with the XRD data. It can be noticed that the small and constant wavenumber shift by comparison with literature data (Table 3) arises from instrument calibration and different laser power.

The spectrum of protonated PNO (Figs. 4b and 6b) shows a strong peak at 149 cm^{-1} and an additional small one at 277 cm^{-1}; these peaks are very similar to those characteristic of $La(OH)_3$ and LaOOH (Table 3; the spectra of $Pr(OH)_3$ and PrOOH have not been identified in the literature). Careful examination of the protonated LNO Raman spectra also shows a small ~150 cm^{-1} peak attributed to traces of $LaOOH/La(OH)_3$. Most of these phases can also be identified by the IR spectroscopy (see further IR spectra in Fig. 8). The detection of a 122–135 cm^{-1} doublet in Raman spectrum of protonated NNO (Figs. 4c and 6c) and of the 3600 cm^{-1} narrow peak in IR spectrum (not shown) indicates the formation of NdOOH in agreement with XRD data (Table 1). The 335 cm^{-1} peak reveals a formation of

139
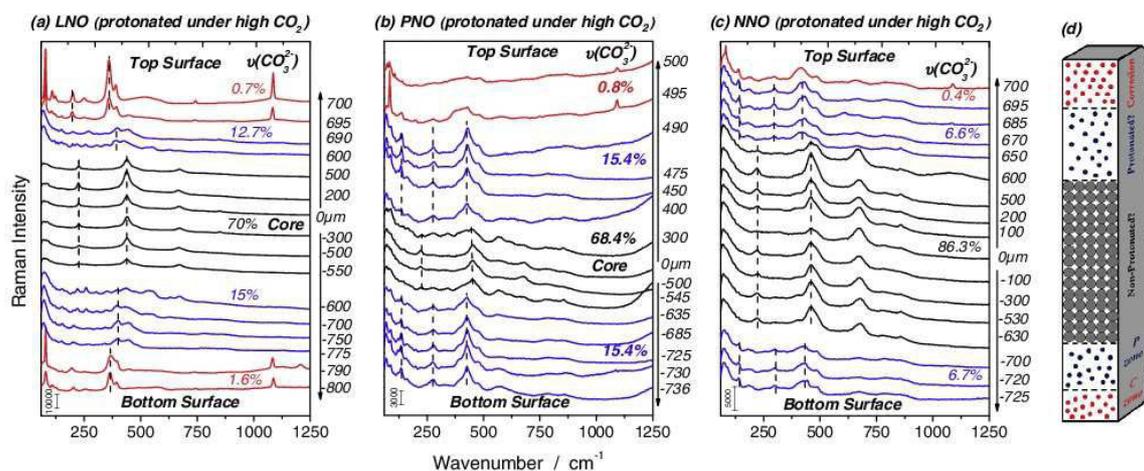
Fig. 6. Raman profilometry along the fresh section fracture of LNO, NNO and PNO ceramic pellets protonated using lean-CO_2 and rich-CO_2 water. The use of low magnification microscope objective (e.g. 10×) lowers the illumination power/surface unit and avoids phase modification under the laser spot. Scheme of different layers detected in LnNO ceramics (d).
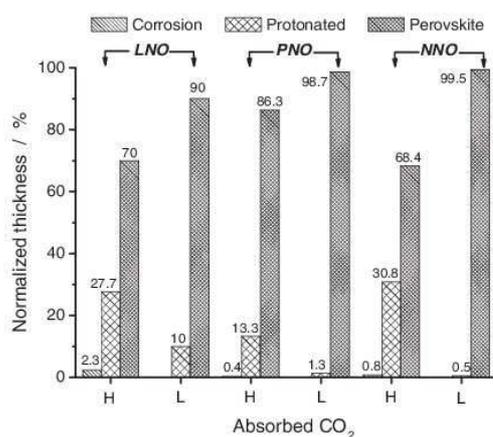
Fig. 7. Comparison of the thickness of the different layers formed after autoclave treatment in CO_2-lean (L) and -rich (H) water for 5 day at °C, 40 bar H_2O.

Table 3
Characteristic peak wavenumber of the LnNO materials in their pristine (LNO, PNO and NNO), protonated (H-LNO, H-PNO and H-NNO) and deprotonated (DP-LNO, DP-PNO and DP-NNO) state. Symmetries deduced from XRD and Raman spectrum are given.

Phase	Symmetry	Main Raman peaks (cm^{-1})			
$La_2NiO_{4+\delta}$ LNO	Fmmm Orthorhombic (D_{2h})		224 m	438 S	
Core-LNO	Fmmm Orthorhombic (D_{2h})	–	228 w	440 S	678 S
H-LNO	I4/mmm Tetragonal (D_{4h})	158 w	220 w	415,455 S	611 m,b
DP-LNO		155 vw	232,247 vw	443 S, 497sh	684 vS
$Pr_2NiO_{4+\delta}$ PNO	Bmab Orthorhombic (D_{2h})		223 vw	454 S	695 vw
Core-PNO	Bmab Orthorhombic (D_{2h})		222 w	452 s	677 w,b
H-PNO		165 vw	252 w	430 S 479 sh?	
DP-LNO		176 vw	320 vw	455 m	683 S
$Nd_2NiO_{4+\delta}$ NNO	Bmab Orthorhombic (D_{2h})		220 w	461 S,b	702 S,b
Core-NNO	Bmab Orthorhombic (D_{2h})		222 w	455 S	678 S
H-NNO	I4/mmm Tetragonal (D_{4h})		195 w	433 S	658 S
DP-NNO			183 w	438 m	659 S
$La_{1-x}Sr_xNiO_4$ [36]			240	450	
Nd_2NiO_4 [38,39]				440–470	670
Rb_2NiO_4 [35]		120/188	(358)	405–430	

Nd_2O_3. There is thus a very good agreement between XRD and vibrational analysis in the identification of formed second phases. Although the resonance character of the NiO Raman spectrum, the broadness of the bands makes its detection difficult. The broad feature centerd at ~1100 cm^{-1} observed in LNO (Fig. 4a) and NNO (Fig. 4c) spectra could be the signature of NiO traces.

ATR-FTIR technique specifically probes the sample surface, typically a few (tenths) micron in-depth penetration: the exact penetration depth varies with the wavenumber depending on the optical index of the crystal probe (diamond or germanium; spectra collected with the small Ge crystal are noted µs, Fig. 8) and the sample [47]. Depending on the band intensity and optical characteristics of the studied solid, the band shape is complex and can be described as a mixture of absorption and reflection signal [47,48]. Measurements made on the non-protonated (T) and de-protonated (DP) samples (Fig. 8) show the absorption spectra characteristic of traces of protonic species adsorbed at the ceramic surface: broad O–H stretching and bending at 3400 and 1650 cm^{-1}. On the other hand, the ATR-FTIR spectra recorded for protonated

ceramics (Fig. 8) exhibit derivative-like signal characteristic of reflection phenomenon: very narrow for low intensity symmetric (at ~745 and 850 cm^{-1}) and broad in the case of intense asymmetric CO_3 bands (~1460 cm^{-1}, Fig. 8a'). Such detection of the strong

Table 4
Main Raman peaks of potential 2nd phase; observed peaks are underlined [44–47].

Compound	Main 2nd phase peaks (cm^{-1})
$La_2NiO_{4+\delta}$ – LNO	La_2O_3: 104, <u>197</u>, <u>404</u>
	$La(OH)_3$: <u>138</u>, 282, 340, <u>450</u>
	LaOOH: <u>123, 135, 199</u>, 312, 344, 383, 424
	I (tetra) $La_2O_2CO_3$: 1064
	Ia (mono) $La_2O_2CO_3$: 1051, 1060
	II (hexa) $La_2O_2CO_3$: <u>82, 204, 364, 394, 1088</u>
	NiO: 546, <u>1092</u>
$Pr_2NiO_{4+\delta}$ – PNO	Pr_2O_3: 104, 187, 406, 840
$Nd_2NiO_{4+\delta}$ – NNO	Nd_2O_3: 106, <u>191</u>, <u>335</u>, <u>428</u>

reflexion spectrum instead of (or superimposed to) the absorption IR spectrum indicates a strong of the optical index of the ceramic, according to the increase of its metallic character, a modification related to the stoichiometry change and/or proton insertion. The intensity increase observed for ceramic treated with CO_2 saturated water is assigned to a larger amount of formed carbonates.

3.6. The 'protonated' nickelates

Raman spectrum of the core of the protonated ceramic pellet (3rd layer) is rather similar to that of the pristine material (Fig. 6). This suggests that the ceramic bulk is not protonated or the protonation level is too small to give significant change. On the contrary, large modifications are observed for the intermediate phase between the ceramic bulk and the corroded layer. (Figs. 4 and 6):

- For LNO: the ca. 440 cm^{-1} mode splits into two peaks (415–455 cm^{-1}). Two new peaks are also detected: $a\sim160\ cm^{-1}$ one appears and a ca. 610 cm^{-1} peak is observed in place of the 678 cm^{-1} one.
- For protonated PNO and NNO the broadening of bands is observed and the splitting is less visible. As for LNO a band downshift and new peaks are observed at $\sim140\ cm^{-1}$.

After thermal treatment (deprotonation), the spectra of all LnNO ceramic become rather similar, with small wavenumber downshift for NNO (Figs. 4 and 8, Table 3). This indicates that the changes induced by the deprotonation are rather similar and the pristine structure is (almost) recovered.

Complementary measurements are necessary to establish if the observation of two different structures arises from the incomplete protonation of the pellet bulk or from the existence of two structures with different H content. The first assumption seems to be more relevant. With the later hypothesis, the small unit-cell variation (Table 1) could be due to modifications of the oxygen stoichiometry during the autoclave treatment.

The differences between pristine and thermally treated ceramics as well as between thermally treated and de-protonated ones, detected by Raman scattering are confirmed by the results of ATR-FTIR: the main IR band of the perovskite structure is well detected in the case of non-protonated samples at ~700–730 cm^{-1}; this band disappears for protonated ceramics (Fig. 8) according to the change caused by the protonation. The ATR-FTIR spectrum is dominated by the reflection spectrum of the corroded layer. Magnification of the Raman high wavenumber range allows detecting the O–H stretching components of hydro- and oxyhy-droxides (Fig. 9b′ and d′). Protonation is however confirmed by comparing the spectra recorded before protonation and after thermal treatment of the protonated ceramic. A significant wave-number shift between pristine and thermally treated (non-proton-ated) material (e.g.; 694–699 cm^{-1} for LNO, 689–717 cm^{-1} for PNO) is observed. This indicates an irreversible modification of the pristine structure after the protonation–deprotonation process.

3.7. Chemical stability

As previously mentioned, the examination of the ceramic cross section from the up -surface to down-one shows more details, in particular when action of CO_2-lean and CO_2-saturated water are compared. Raman spectra recorded according to the so-called profilometry method [33] on previously protonated pellet section fracture are reported in Fig. 6; the measurement steps vary from a few microns close to the surface to 50 μm in the section center. The thickness of the different layers formed by the thermal treat-ment in the autoclave is given in Table 5.

The modification of the upper and lower layers is obvious for LNO (lean- and rich-CO_2 saturated water) and for PNO (rich-CO_2 saturated water only). The use of rich-CO_2 saturated water gives rise to the carbonate formation up to ~10 μm depth after 5 days of treatment at 550 °C/40 bar. The structure of the upper layers in between the modified surface and the ceramic bulk is different.

The detrimental effect of CO_2 is clear (Table 5). The easiest car-bonation of LNO ceramic seems to be obvious. An asymmetry of
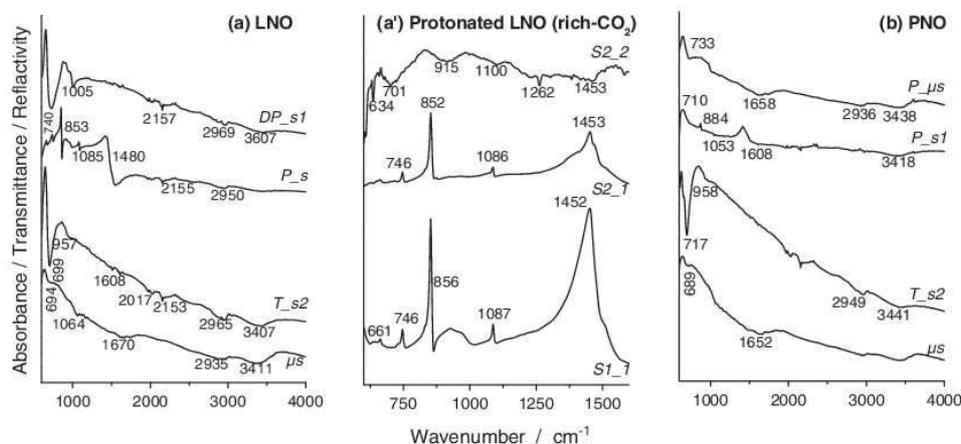
Fig. 8. ATR and microATR-FTIR (μ) spectra recorded at the surface of protonated (P), de-protonated (DP) and thermally treated (T) LNO and PNO ceramics. Comparison is made with protonated LNO ceramic using CO_2 saturated water. The in-depth probed surface layer varies when Germanium (μ ATR FTIR) or Diamond (ATR FTIR) are used.

Chemical and structural stability of proton conductor perovskite ceramic for fuel cells and electrolyzers
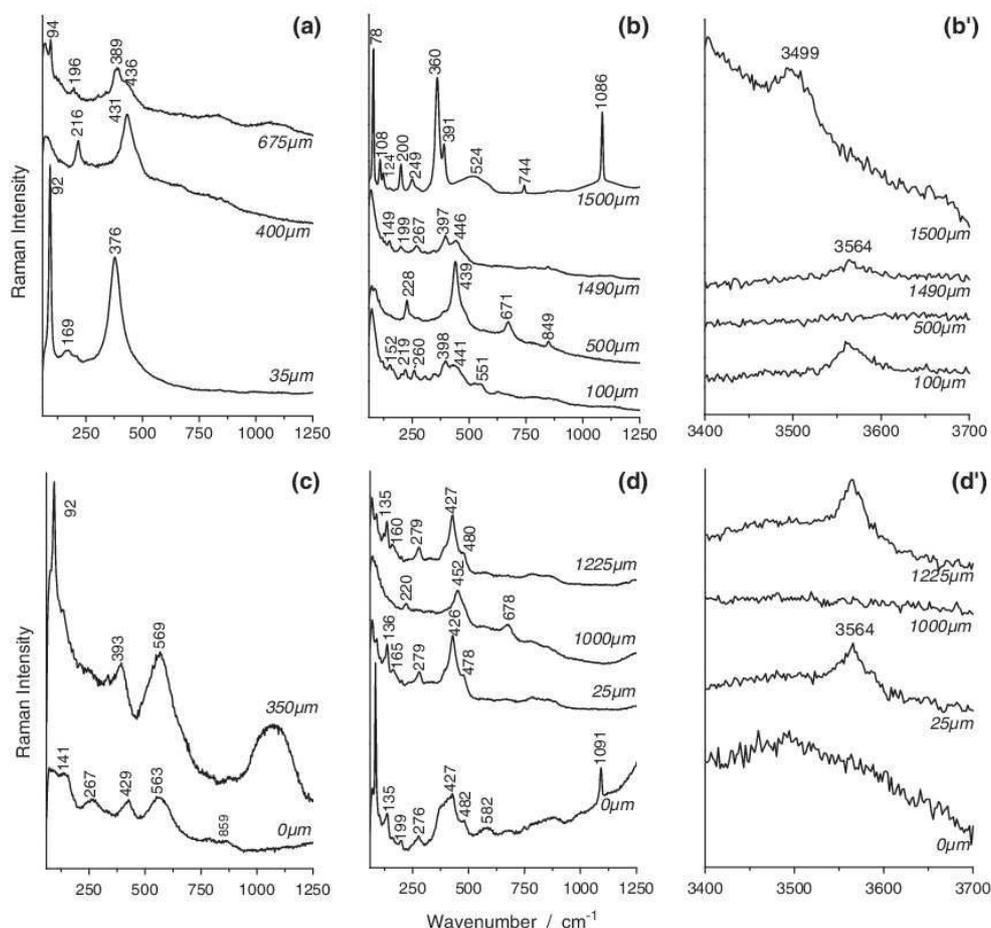
Fig. 9. Detail of the Raman profilometry along the fresh section fracture of LNO (a, b and b') and PNO (c, d and d') ceramic pellets protonated using lean-CO_2 (a and c) and rich-CO_2 (b and b'; d and d') water.

Table 5
Comparison of the in-depth penetration of corrosion and protonation in LnNO dense ceramics.

Normalized in-depth transformation (μm)	$La_2NiO_{4+\delta}$ – LNO		$Pr_2NiO_{4+\delta}$ – PNO	
	Low–High CO_2 water		Low–High CO_2 water	
Top layer	–	0.5	0.5	1
Intermediate layer	6	12	–	7
Core	90	81	99.5	85
Intermediate layer	4	6	–	7
Bottom layer	–	0.5	–	–

the corrosion is observed (Fig. 6). This phenomenon could be related to the sample holder design: one of the surface areas is well exposed to the vapor pressure whereas the other is in direct contact with the gold support.

The number of secondary phase detected by Raman analysis is higher than that observed by XRD. In the Raman technique, the combination of the black color of the pristine material/substrate and of the laser spot can lead to uncontrolled transformations (partial dehydration) under the laser light. The dehydration of

hydrated/hydroxylated Ln derivatives may induce the formation of series of phases that explains the higher number of vibration modes detected by spectroscopy [30]. On the other hand, vibrational spectroscopy is able to reveal the presence of amorphous oxohydroxides not detectable by XRD [22,30].

Considering materials exposed to CO_2-rich water, the Raman spectrum recorded in the bulk of the pellets can be considered as characteristic of the pure pristine perovskite. On the other hand the material located in between the later core and the corroded layer is the protonated phase. The spectrum with strong 93 cm^{-1} narrow peak can be assigned to lanthanum oxide La_2O_3 (Fig. 9a and b). This result reveals that the protonation is not complete and the H content measured by TGA for the whole pellet is lower than the value intrinsically present in the intermediate protonated layer. Taking into account that the volume ratio of the effectively protonated layer retaining the perovskite structure is about 1/3 of the total volume of the LNO and NNO pellets and less than 1/6 of that of PNO ceramic, the following formula could be proposed for the protonated perovskite: $La_2NiO_{4+\delta}H_2$, $Pr_2NiO_{4+\delta}H_4$ and $Nd_2NiO_{4+\delta}H_{0.5}$.

The down shift of the ca. 420–440 cm^{-1} main peak and the unit cell volume variation seem to be consistent with the protonation. These modifications can also be correlated with the lengthening

of Metal–Oxygen bond(s) because of the interaction between some oxygen atoms and interstitial or more or less bounded protons. Actually the nature of the 'inserted' proton is not known, the water insertion equation being

$$H_2O + LNO => LNO[H^+]_x[OH^-]_y$$

Considering the high wavenumber range (Fig. 9b' and d'), at least two different hydroxylated compounds are formed, with characteristic ν_{OH} bands at ~3500 and 3570 cm^{-1}. The narrowness of the later band is consistent with the presence of $Ln(OH)_3$ compound, although no reference data have been found in the literature. The unexpected strong reflexion IR signature of the corrosion film is consistent with a strong modification of the perovskite optical index anticipating an increase of the electronic conduction of H-LNO perovskites.

4. Conclusion

Raman, IR, XRD and TGA studies performed on three LnNO dense ceramics exposed 5 days to high water vapor pressure at 550 °C, i.e. the temperature designed for SOFC and HTSE systems, reveal that these compounds show rather good stability vs. high water pressure until 40 bar. Note, this is a pressure value 2–5 times higher than that required in an industrial use [7]; one can then suppose that the rate of ageing process at lower water pressure should be much lower. Obviously, surface carbonation is increased by using the CO_2 saturated water. $Nd_2NiO_{4+\delta}$ (NNO) ceramic exhibits the highest structural, mechanical and chemical stability. $Pr_2NiO_{4+\delta}$ (PNO) shows the most important content of bulk protons, although it is significant surface hydroxylation. XRD, IR and Raman scattering results allowed to identify the corrosion layer, phases, as (oxo)hydroxides and carbonates. Unit-cell volume contractions are observed in the case of PNO and LNO compounds, the largest one being measured for LNO whereas the smallest is detected for PNO. On the contrary, a small unit-cell volume expansion is observed for NNO but the low TGA mass loss indicates that most of the modifications is rather related to the oxygen stoichiometry change in the used He atmosphere, the protonated layer being rather limited. The local heating under the laser spot induces phase transformation/transition and can lead to data misinterpretations. The use of very low laser power illumination shows similar Raman signature for all protonated perovskite, with a significant downshift of the peak wavenumber, according to modifications of the structure. The peculiar ATR-FTIR spectra recorded on protonated ceramics suggest a modification of the electronic band structure according to the proton insertion, as already detected in the case of Tungsten bronzes [26]. As observed for earth-alkaline proton conducting perovskites [24,30], surface hydroxylation and carbonation competes with water/proton insertion. The reactions taking place in autoclave should also be present at the SOFC/HTSE electrode surface. At the working temperature range hydroxides are good proton conductors [26] and their presence is not detrimental if the formation rate is sufficiently low and if it does not lead to crack formation.

References

[1] T. Ishihara, Perovskite Oxide for Solid Oxide Fuel Cells, Springer, Dordrecht Heidelberg London New York, 2009.
[2] S.J. Skinner, Characterisation of $La_2NiO_{4+\delta}$ using in-situ high temperature neutron powder diffraction, Solid State Sci. 5 (2003) 419–426.
[3] D.J. Buttrey, J.D. Sullivan, G. Shirane, K. Yamada, Influence of oxygen nonstoichiometry on structure and magnetism in $Pr_2NiO_{4+\delta}$, Phys. Rev. B 42 (1990) 3944–3951.
[4] P.M. Geffroy, J. Fouletier, N. Richet, T. Chartier, Rational selection of MIEC materials in energy production processes, Chem. Eng. Sci. 87 (2013) 408–413.
[5] Y. Zheng, W. Zhou, R. Ran, Z.P. Shao, Perovskite as anode materials for solid oxide fuels cells, Progr. Chem. 20 (2008) 413–421.
[6] J. Sunarso, S. Baumann, J.M. Serra, W.A. Meulenberg, S. Liu, Y.S. Lin, J.C.D. da Costa, Mixed ionic-electronic conductivity (MIEC) ceramic-based membranes for oxygen separation, J. Membrane Sci. 320 (2008) 13–41.
[7] B. Sala, F. Grasset, O. Lacroix, A. Sirat, K. Rahmouni, M. Keddam, H. Takenouti, D. Goeuriot, B. Bendjeriou, Ph. Colomban, A. van der Lee, J.G. Sanchez, Procédé de génération d'hydrogène et d'oxygène par électrolyse de vapeur d'eau, WO 2013053858 A1 (18/04/2013).
[8] M. Greenblatt, Ruddlesden–Popper $Ln_{n+1}Ni_nO_{3n+1}$, nickelates: structure and properties, Solid State Mater Sci 2 (1997) 174–183.
[9] G.W. Coors, Protonic ceramic steam-permeable membranes, Solid State Ionics 178 (2007) 481–485, http://dx.doi.org/10.1016/j.ssi.2006.11.004.
[10] T. Sakai, K. Isa, M. Matsuka, T. Kozai, Y. Okuyama, T. Ishihara, H. Matsumoto, Int. J. Hydrogen Energy 38 (2013) 6842–6847.
[11] J. Daily, S. Fourcade, A. Largeteau, F. Mauvy, J.C. Grenier, M. Marrony, Perovskite and A_2MO_4-type oxides as new cathode materials for protonic solid oxide fuel cells, Electrochim. Acta 55 (2010) 5847–5853.
[12] E. Boehm, Doctorate Thesis, Bordeaux University, 2002.
[13] A. Slodczyk, Ph. Colomban, Probing the nanodomain origin and phase transition mechanisms in (un)poled PMN-PT single crystals and textured ceramics, Materials 3 (2010) 5007–5028, http://dx.doi.org/10.3390/ma3125007.
[14] C. Allançon, A. Gonthier-Vassal, J.M. Bascat, J.P. Loup, P. Odier, Influence of oxygen on structural transitions in $Pr_2NiO_{4+\delta}$, Solid State Ionics 74 (1994) 239–248.
[15] M. Zaghrioui, F. Giovannelli, N.PoirotD. Brouri, I. Laffez, Anomalies in magnetic susceptibility of nonstoichiometric $Nd_2NiO_{4+\delta}$ ($\delta = 0.049, 0.065, 0.077, 0.234$), J. Solid State Chem. 177 (2004) 3351–3358.
[16] K. Shikawa, K. Metoki, H. Miyamoto, Orthorhombic–orthorhombic phase transition in $Nd_2NiO_{4+\delta}$ ($0.067 < \delta < 0.224$), J. Solid State Chem. 182 (2009) 2096–2103.
[17] E. Boehm, J.-M. Bassat, P. Dordor, F. Mauvy, J.-C. Grenier, Ph. Stevens, Oxygen diffusion and transport properties in non-stoichiometric $Ln_{2-x}NiO_{4+\delta}$ oxides, Solid State Ionics 176 (2005) 2717–2725.
[18] T. Nakamura, K. Yashiro, K. Sato, J. Mizusaki, Oxygen nonstoichiometry and defect equilibrium in $La_{2-x}Sr_xNiO_{4+\delta}$, Solid State Ionics 180 (2009) 368–376.
[19] T. Nakamura, K. Yashiro, K. Sato, J. Mizusaki, Thermally-induced and chemically-induced structural changes in layered perovskite-type oxides $Nd_{2-x}Sr_xNiO_{4+\delta}$ ($x = 0, 0.2, 0.4$), Solid State Ionics 181 (2010) 402–411.
[20] A.L. Soldati, L. Baqué, F. Napolitano, A. Serquis, Cobalt–iron Red–ox behavior in Nanostructured $La_{0.4}Sr_{0.6}Co_{0.8}Fe_{0.2}O_{3-\delta}$ Cathodes, J. Solid State Chem. 198 (2013) 253–261.
[21] Ph. Colomban, O. Zaafrani, A. Slodczyk, Proton content and nature in perovskite ceramic membranes for medium temperature fuel cells and electrolysers, Membranes 2 (2012) 493–509.
[22] M.C. Caggiani, Ph. Colomban, Raman identification of strongly absorbing phases: the ceramic black pigments, J. Raman Spectrosc. 42 (2011) 839–843.
[23] G. Gouadec, Ph. Colomban, N.P. Bansal, Raman study of Hi-Nicalon-fiber-reinforced Celsian composites: II, Residual stress in Fibers, J. Am. Ceram. Soc. 84 (2001) 1136–1142.
[24] A. Slodczyk, O. Zaafrani, M.D. Sharp, J.A. Kilner, B. Dabrowski, O. Lacroix, Ph. Colomban, Testing the chemical/structural stability of proton conducting perovskite ceramic membranes by in situ/ex situ autoclave Raman microscopy, Membranes 3 (2013) 311–330, http://dx.doi.org/10.3390/membranes3040311.
[25] S. Upasen, P. Batocchi, A. Slodczyk, Ph. Colomban, F. Mauvy, Structural stability of $Ln_2NiO_{4+\delta}$ ceramics under high temperature and high water pressure operating conditions, in: Proc. IDHEA 2014 International Discussion on Hydrogen Energy and Applications, Nantes, 12–15 Mai 2014.
[26] Ph. Colomban, Proton Conductors-Solids-Membranes and Gels-Materials and Devices, Chemistry of Solid State Materials (N°2), third ed., Cambridge University Press, Cambridge, 2011. http://dx.doi.org/10.2277/052138317X.
[27] Ph. Colomban, J. Tomkinson, Novel forms of Hydrogen in solids: the 'ionic' proton and the 'quasi-free proton', Solid State Ionics 97 (1997) 123–134.
[28] K.D. Kreuer, Proton-conducting oxides, Ann. Rev. Mater. Res 33 (2003) 333–359.
[29] Ph. Colomban, Latest developments in proton conductors, Ann. Chim. Sci. Mat. 24 (1999) 1–18.
[30] Ph. Colomban, C. Tran, O. Zaafrani, A. Slodczyk, Aqua oxyhydroxycarbonate second phases at the surface of Ba/Sr-based proton conducting perovskites: a source of confusion in the understanding of proton conduction, J. Raman Spectrosc. 44 (2013) 312–320.
[31] E. Boehm, J.M. Bassat, M.C. Steil, P. Dordor, F. Mauvy, J.C. Grenier, Oxygen transport properties of $La_2Ni_{1-x}Cu_xO_{4+delta}$ mixed conducting oxides, Solid State Sci. 5 (2003) 973–981.
[32] A. Slodczyk, Ph. Colomban, G. André, O. Zaafrani, F. Grasset, O. Lacroix, B. Sala, Structural modifications induced by free proton in proton conducting perovskite ceramic membrane, Solid State Ionics 225 (2012) 214–218.
[33] A. Slodczyk, Ph. Colomban, S. Willemin, O. Lacroix, B. Sala, Indirect Raman identification of the proton insertion in the high temperature [Ba/Sr][Zr/Ti]O_3 modified perovskite protonic conductors, J. Raman Spectrosc. 40 (2009) 513–521.
[34] N. Ogita, M. Udagawa, K. Kojima, K. Ohbayashi, Infrared and Raman study of $(La_{1-x}Sr_x)_2NiO_4$ and $La_2(Ni_{1-x}Cu_x)O_4$, J. Phys. Soc. Jpn. 57 (1988) 3932–3940.
[35] M. Udagawa, T. Yamaguchi, N. Ogita, K. Ohbayashi, M. Kato, Y. Maeno, T. Fujita, Raman scattering study of $(La_{1-x}Sr_x)_2NiO_4$, Physica C 185–189 (1991) 1039–1040.

[36] C. Prieto, A. de Andrés, M. Medarde, J.L. Martinez, M.T. Fernandez-Diaz, J. Rodriguez-Carvajal, R. Saez-Puche, F. Fernandez, EXAFS and Raman study of stoichiometric and oxidize Nd_2NiO_{4+}, J. Solid State Comm. 80 (1991) 975–980.

[37] W. Wang, Y. Liu, C. Xu, C. Zheng, G. Wang, Synthesis of NiO nanorods by a novel simple precursor thermal decomposition approach, Chem. Phys. Lett. 362 (2002) 119–122.

[38] R.E. Dietz, G.I. Parisot, A.E. Meixner, Infrared absorption and Raman scattering by two-magnon processes in NiO, Phys. Rev. B 4 (1971) 2302–2310.

[39] R. Laiho, K.G. Lisunov, E. Lahderanta, V.S. Stamov, V.S. Zakhvalinskii, Ph. Colomban, P.A. Petrenko, Yu.P. Stepanov, Lattice distortions, magnetoresistance and hopping conductivity in $LaMnO_{3+\delta}$, J. Phys.: Condens. Matter 17 (2005) 105–118.

[40] I.A. Leonidov, M.V. Patrakaeev, J.A. Bahteeva, E.B. Mitberg, V.L. Kozhevnikov, Ph. Colomban, K.R. Pöppelmeier, High-temperature phase equilibria in the oxide systems $SrFe_{1-x}Ga_xO_{2.5}$ – $SrFe_{1-x}Ga_xO_3$ ($x = 0$, 0.1, 0.2), J. Solid State Chem. 179 (2006) 1093–1099.

[41] A. Ubaldini, M.M. Carnasciali, Raman characterisation of powder RE_2O_3 (RE = Nd, Gd, Tm, and Lu), Sc_2O_3 and Y_2O_3, J. Alloys Comp. 454 (2008) 373–378.

[42] D. Vijayalakshmi, N.V.C. Sekar, S. Ramya, P.C. Sahu, G. Meenakshi, Investigation of diphasic region in the $Pr_2O_3 + Sm_2O_3$ mixed oxide system at various temperatures, J. Alloys Comp. 505 (2010) 733–738.

[43] A. Orera, G. Larraz, M.L. Sanjuan, Spectroscopic study of the competition between dehydration and carbonation effects in La_2O_3-based materials, J. Euro. Cer. Soc. 33 (2013) 2103–2110.

[44] B.M. Faroldi, J.F. Múnera, L.M. Cornaglia, In situ characterization of phase transformation and reactivity of high surface area lanthanum-based Ru catalysts for the combined reforming of methane, Appl. Catal. B 150–150 (2014) 126–137.

[45] J. Gouteron, D. Michel, A.M. Lejus, J. Zarembowitch, Raman spectra of lanthanide sesquioxide single crystals: correlation between A and B-type structures, J. Solid State Chem. 38 (1981) 288–296.

[46] S. Gunasekaran, G. Anbalgan, S. Pandi, Raman and Infrared spectra of carbonates of calcite structure, J. Raman Spectrosc. 37 (2006) 892–899.

[47] K. Ohta, R. Iwamoto, Experimental proof of the relation between thickness of the probed surface layer and absorbance in FT-IR/ATR spectroscopy, Appl. Spectrosc. 39 (1985) 418–425.

[48] Bruker Application Note, <http://www.bruker.com/fileadmin/user_upload/8-PDF-Docs/OpticalSpectrospcopy/FT-IR/ALPHA/AN/AN79_ATR-Basics_EN.pdf> June 2014.

144

CHAPTER 7

"Chemical and structural stability of $La_{0.6}Sr_{0.4}Co_{0.2}Fe_{0.8}O_{3-\delta}$ ceramic vs. medium/high water vapor pressure"

In this chapter, we will present the chemical and structural characterization of $La_{0.6}Sr_{0.4}Co_{0.2}Fe_{0.8}O_{3-\delta}$ (LSCF6428) ceramic samples, as our second investigated electrode series. The protonation treatments were under medium and high H_2O pressure (20 bar and 40 bar) at intermediate temperature. The result will also be demonstrated ageing of the material against CO_2-saturated water vapor pressure. The principal analysis techniques i.e. IR, Raman spectroscopy, TGA, TE, and X-ray diffraction are employed.

Chemical and structural stability of La$_{0.6}$Sr$_{0.4}$Co$_{0.2}$Fe$_{0.8}$O$_{3-\delta}$ ceramic vs. medium/high water vapor pressure

Settakorn Upasen[a,b], Pierre Batocchi[c], Fabrice Mauvy[c], Aneta Slodczyk[a,b], Philippe Colomban[a,b,*]

[a]*Sorbonne Universités, UPMC Univ Paris 06, UMR 8233, MONARIS, 75005 Paris, France*
[b]*CNRS, UMR 8233, MONARIS, F-75005 Paris, France*
[c]*CNRS, Université de Bordeaux, ICMCB, 87 Av. du Dr Schweitzer, F-33608 Pessac Cedex, France*

Abstract

During the last decades, perovskite-type oxides have received large attention as potential electrolytes and electrodes for Solid Oxide Fuel Cells (SOFC), including Proton Ceramic Fuel Cells (PCFC), gas separation membranes and High Temperature Steam Electrolysers (HTSE). A thermal treatment in an autoclave, at a temperature close to an operating temperature, was used to measure the chemical stability of La$_{0.6}$Sr$_{0.4}$Co$_{0.2}$Fe$_{0.8}$O$_{3-\delta}$ (LSCF6428) ceramic under medium and high water pressure ($\sim$20 and 40 bar). This mixed ionic$-$electronic conductor (MIEC) exhibits interesting properties as cathode of fuel cell materials. The reactivity rate of the investigated LSCF6428 sample under the protonation process conditions (several weeks at 550 °C using CO$_2$-free and CO$_2$-saturated water) was studied in order to evaluate a potential use of this compound. Bulk and surface structural/chemical changes were characterized by optical microscopy, TGA, dilatometry, Raman and ATR-FTIR spectroscopy. The results revealed only minor surface modifications in the case of ceramic treated under medium vapor pressure (20 bar) using CO$_2$-free water. On the contrary, under higher pressure (40 bar) and CO$_2$-saturated water several second phases were detected, namely strontianite, cobalt oxides and hematite. The chemical/structural stability of LSCF6428 is compared with previously investigated Rare-Earth nickelate ceramics: La$_2$NiO$_{4+\delta}$ / Pr$_2$NiO$_{4+\delta}$ / Nd$_2$NiO$_{4+\delta}$.
© 2015 Elsevier Ltd and Techna Group S.r.l. All rights reserved.

Keywords: B. Spectroscopy; B. Surface; C. Corrosion; D. Perovskite; E. Fuel cell; Lifetime

1. Introduction

Solid Oxide Fuel Cells (SOFC) received considerable attention because of their high efficiency and low pollution emissions [1]. The oxygen ion conducting SOFCs based on zirconia/ceria electrolyte operate at high temperature, typically above 800 °C. Such a high working temperature reduces the material's lifetime and increases significantly operating costs. To overcome these drawbacks, recent studies have paid attention to proton conducting electrode/electrolyte materials able to operate at lower temperatures (500–700 °C) [2–5]. Such lower operating temperatures allow the use of less

expensive steels and keeping of low-cost catalyzers. Reversibly, the electrochemical cells can be adapted to be used in High Temperature Steam Electrolyzer (HTSE). One great advantage of proton conductors for HTSE is the production of dry pure hydrogen in the cathode side. Electrode materials should exhibit important mixed ionic and electronic conductivity (MIEC) as well as show high efficiency and high stability vs. protons and/or oxygen/hydrogen. Furthermore, they should be also stable vs. other gas components such as CO$_2$, NO$_x$ which could reduce the stability and the efficiency of the MIEC-materials as well as accelerate its ageing through chemical/structural transitions [6–8].

Different perovskite-related oxides exhibiting a large range of properties regarding to the variety of structure and chemical compositions have been tested as electrodes successfully [9]. Among various electrodes, La$_{0.6}$Sr$_{0.4}$Co$_{0.2}$Fe$_{0.8}$O$_{3-\delta}$ (LSCF6428) exhibits excellent ionic–electronic conducting properties over a

*Corresponding author at: Sorbonne Universités, UPMC Univ Paris 06, UMR 8233, MONARIS, 75005 Paris, France.
Tel.: +33 144272785; fax: +33 144273021.
E-mail address: philippe.colomban@upmc.fr (P. Colomban).

wide temperature range [10]: for example at 900 °C the electronic conductivity can reach 230 S cm^{-1} whereas oxygen conductivity is close to 0.2 S cm^{-1} [11,12]. Proton conductivity is expected but not yet demonstrated. Only few results are reported in the literature concerning electrochemical characterizations of similar MIEC-materials as a function of $p(H_2O)$ [3,13,14]. At room temperature, LSCF shows almost cubic structure, with a small orthorhombic or rhombohedral distortion in the case of low Co and Sr contents. At high temperatures and/or high Sr content, a cubic phase is observed [15–17]. Structural stability of LSCF7382 was analyzed under H_2 atmosphere in a wide temperature range; reversible transition from the perovskite $ABO_{3-\delta}$ phase to the brownmillerite $A_2B_2O_{5+\delta}$ was detected at 250–300 °C. Moreover, decomposition of the structure into Co, La_2O_3, SrO and $LaSrFeO_4$ was observed above 750 °C [18,19].

In our previous studies, we demonstrated the potential of the high pressure/middle temperature autoclave to study the chemical stability of various perovskite-type electrolytes and electrodes vs. high pressurized water [20,21]. Such treatment (550–600 °C, 10–40 bar $p(H_2O)$) that allows also incorporation of protonic species into a host material structure is called "Protonation". Note, the use of medium pressure allows also to optimize the economic efficiency of Fuel Cells and Electrolysers. Operating conditions (typically 10–20 bar $p(H_2O)$) are the must. The use of high water pressure by industrialists allows an increased efficiency and in consequence decreasing of hydrogen production/conversion cost [22–27]. Our previous studies, performed in a strict collaboration with Industrial partner, showed however that high water pressure can significantly accelerate a material ageing [20]. Consequently, our protonation procedure performed under high pressure (40 bar $p(H_2O)$) can be considered as an accelerated stability test which allows very fast to choose the most stable material [22,23].

The protonation process leads to subtle modifications of a material structure whatever the small amount of incorporated protons [28–35]. The quantity of CO_2 dissolved in the water used is one of the stringent parameters. With high water pressure, the water activity at the ceramic surface increases, and enhances many reactions (hydroxylation, carbonation, or protonation). Consequently, a significant amount of secondary phases can be formed in relatively small experimental time (days to weeks). Careful analysis of the secondary phases with usual analytical techniques permits the study of the corrosion mechanism. Following the procedure of the previous studies, the LSCF6428 ceramic sample was treated under medium/high water vapor pressure ($\sim$20 and $\sim$40 bar) at 550 °C for several days using a home-designed autoclave device [20,28–32]. Two kinds of water were used: i) CO_2-free water and ii) CO_2-saturated water. Thermogravimetry (TGA), thermal expansion (TE), X-ray diffraction (XRD), Attenuated Transmitted Reflected Fourier Transform-infrared spectroscopy (ATR FT-IR), Raman spectroscopy (RS) were employed in order to identify corrosion films as well as eventual structural changes associated to the proton/water insertion. The aim of this study is the comprehension of the reaction mechanisms in operating proton conductor-based device conditions. Structural/chemical modifications allowing to estimate ageing of LSCF6428

ceramic were compared with other alternative cathode materials, namely Ln-nickelates [21].

2. Materials and methods

2.1. Sample preparation

A ceramic of $La_{0.6}Sr_{0.4}Co_{0.2}Fe_{0.8}O_{3-\delta}$ (LSCF6428) composition, called hereafter 'as-prepared' sample, was prepared in pellet form ($\varnothing = \sim$16 mm, thickness = 1.48 mm, theoretical density of 95% max.). The preparation method was described by Mauvy et al. [3]. Commercial powders provided by Marion Technologies (Verniolle, France) were isostatically pressed into pellets at 3000 bar for 5 min and then sintered in air at 1350 °C for 4 h. The thermal treatment of as-prepared sample was carried out from 40 °C to 1000 °C using a TG balance (heating rate = 10 °C/min, 3 cycles) under He atmosphere. (99.99%, $H_2O < 3$ ppm vol., $O_2 < 2$ ppm vol., $C_nH_m < 0.5$ ppm vol., Alphagaz-1, Air Liquide, France).

2.2. Autoclave treatment

The as-prepared ceramic was treated under high/medium water vapor pressure (20/40 bar, 550 °C, CO_2-free and CO_2-saturated water) for period of 8–47 days using the home designed autoclave device [20,28–32]. This device is equipped with a temperature and pressure controller, which allows us to follow the protonation process/incorporation of water/protonic species from the pressure drop. Note, Fig. S1 (Supplementary material) illustrates temperature and pressure curves recorded during the protonation process. The curves consist of two regions – start-up and protonation. The pressure drop in the protonation region was adjusted to 30 bar by the mean of a small leak valve. The further pressure decreases with time is related to the absorption of water by the ceramic. The sample weight was systematically analyzed by non-destructive techniques after each run of autoclave treatment in order to observe the kinetic of protonation/reactions.

2.3. Optical microscope analysis

Micro-structures were analyzed on the surface as well as on a fresh fracture section of protonated samples using an Optical Microscope Olympus BX51 instrument. The 50 × and 100 × objectives were selected in order to observe microstructure modifications in the 5–1000 μm range. Grains and pores sizes were measured using a line-intercept method (ASTM E112) with high magnification (10 μm) of the micro-feature. Image contrast was optimized using the Microsoft Office Picture software.

2.4. Thermal analysis

TGA was performed between 40 °C and 1000 °C using a Setaram Setsys Evolution thermobalance. The use of Pt-crucible and He-atmosphere (99.99%, $H_2O < 3$ ppm vol., $O_2 < 2$ ppm vol., $C_nH_m < 0.5$ ppm vol., Alphagaz-1, Air Liquide, France) allows the significant enhancement of the measurement accuracy.
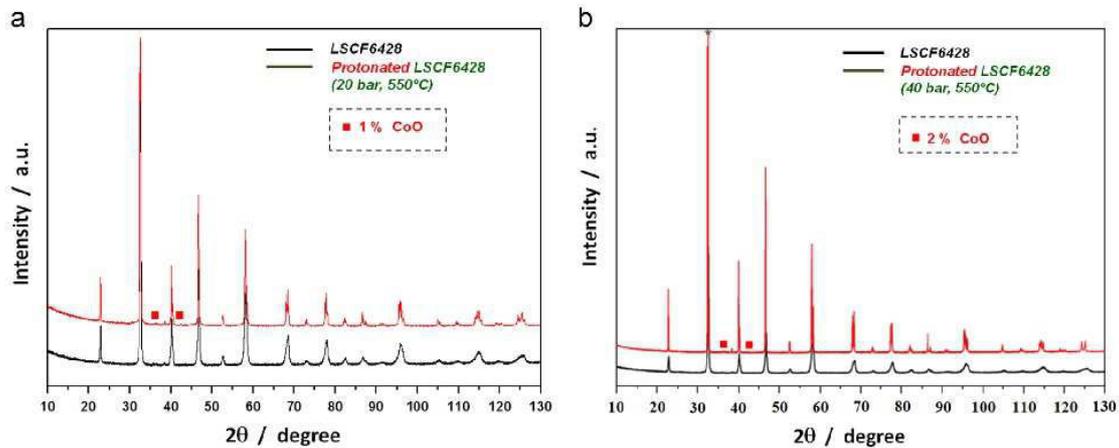
Fig. 1. Comparison of X-ray patterns (a) as-prepared vs. protonated LSCF6428 under 20 bar CO$_2$-free water; (b) as-prepared vs. protonated LSCF6428 under 40 bar CO$_2$-free water.

Thermal expansion (TE) measurements were carried out between 40 °C and 600 °C under Ar-atmosphere (99.99%, H$_2$O < 0.5 ppm vol., O$_2$ < 0.1 ppm vol., CO < 0.1 ppm vol., CO$_2$ < 0.1 ppm vol., H$_2$ < 0.1 ppm vol., C$_n$H$_m$ < 0.5 ppm vol. Alphagaz-2, Air Liquide, France) using a Setaram Setsys 1650 dilatometer instrument equipped with amorphous silica rod and support.

2.5. Vibrational spectroscopy analysis

Raman spectra were recorded at room temperature under 458 nm and 514 nm wavelengths using a HR800 spectrometer (Horiba, John Yvon) equipped with a Peltier effect cooled CCD detector. The measurements under 785 nm wavelength were also performed using the solid state source line of a Senterra spectrometer (Bruker Optics, Karlsruhe, Germany). Raman spectra were recorded between 50 cm^{-1} and 4000 cm^{-1} through the 50× long working distance objectives (N.A.=0.50). It was previously pointed out that moderate power of illumination may significantly heat the black ceramic samples [21,36]. Consequently, in order to select the convenient laser power and to avoid phase transformation, preliminarily power tests were performed by varying the output power from 0.1 to 20 mW. Correct signal/noise ratios were obtained with relatively high counting duration of 100–500 s. The spectra were fitted using Origin Software. The Raman mapping, furthermore, was performed on fresh fracture section of the protonated samples. The spectra were recorded from fresh surface deep to the sample's core with interval line of a few microns (5–50 μm).

ATR FT-IR spectra were recorded between 600 cm^{-1} and 4000 cm^{-1} at room temperature using the Bruker IR-scope FTIR spectrometer in ATR modes: a Diamond ATR (2 × 2 mm^2) and a Germanium micro ATR (20 × 20 μm^2) crystal.

2.6. X-ray diffraction

XRD patterns of ground pellets were collected on a PANalitycal X'pert MPD-PRO Bragg-Brentano of θ–2θ
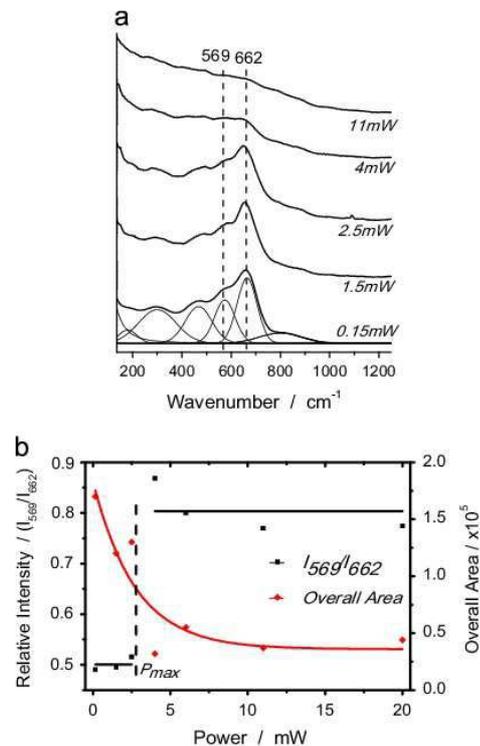
Fig. 2. (a) Raman spectra (458 nm) of as-prepared LSCF6428 ceramic as a function of laser power. (b) Oxidation relative intensity peak (I_{569}/I_{662}) versus laser power.

geometry diffractometer equipped with a germanium primary monochromator over an angular range of 2θ=10–130°. Each acquisition lasted for 64 h. The Cu-Kα$_1$ (λ=1.54056 Å) radiation was generated at 45 kV and 40 mA. Unit-cell parameters were calculated by Le Bail profile matching. The phase

identification was carried out using the ICCD database and PANatycal X'pert highscore software. The relative quantities of the different phases were estimated according to the ratio of the relative intensities of the major peaks recorded in the XRD patterns.

3. Results and discussion

3.1. Characterization of the pristine LSCF ceramic

3.1.1. Mean symmetry

The XRD results presented in Fig. 1 show that LSCF6428 exhibits a single rhombohedral phase with R-3c space group. The pristine symmetry of the material investigated here is then similar to the previous literature studies [3,37,38]. Structural modifications involved by the autoclave treatment will be discussed in Section 3.3.

3.1.2. Raman scattering

Because of the black color of the as-prepared LSCF6428 sample that leads to high conversion of the laser beam to heat at the examined spot, Raman spectra shown in Fig. 2a were recorded as a function of laser power (0.1–20 mW, 458 nm, 135–1250 cm^{-1}). At the lowest power ($\sim$0.15 mW), the spectrum reveals the presence of typical LSCF perovskite phase consisting of a main peak at 662 cm^{-1} and three broad bands at 569, 470, and 292 cm^{-1}. A small broad band at 180 cm^{-1} is also detected. The first two bands at 662 and 569 cm^{-1} are similar to those observed in the literature [18,39–42]. It should be noted that according to its complex composition, LSCF6428 can be considered as a solid solution between $La_{1-x}Sr_xCoO_{3-\delta}$ (LSC) and $La_{1-x}Sr_xFeO_{3-\delta}$ (LSF). The large bandwidth is related to the Co/Fe and La/Sr partial substitutions. The group theory analysis in the case of rhombohedral symmetry with the R-3c space groups predicts 18 optical phonons of irreducible representations [40]. Fives modes ($A_{1g}+4E_g$) are Raman actives, and eight modes ($3A_{2u}+5E_u$) are IR actives, while the remaining modes ($2A_{1u}+3A_{2g}$) are inactive. According to the literature [39], the Raman bands at 650 and 590 cm^{-1}, typical of the LSCF material, correspond to E_g modes.

With increase of the laser power, the temperature at the sample surface increases, which can lead to oxidation reaction. Simultaneously a wavenumber downshift is expected and observed under 2.5 mW laser beam. According to the study of Siebert et al. [18], the Raman spectrum of fully oxidized LSCF7382 exhibits an overlapping of two broad bands centered at 560 and 630 cm^{-1}. Our spectra showing bands at 569 and 662 cm^{-1}, Fig. 2a, are consistent with a low oxygen deficiency. Overall area of spectrum and relative intensity between the bands at 569 and 662 cm^{-1}, plotted as a function of the output laser power, are shown in Fig. 2b. The result shows a decrease of the sum of peak area with the increase of the laser power. This vanishing of Raman signature is consistent with the progressive transition toward the cubic structure [20,43]. Moreover, a jump of the relative intensity (I_{569}/I_{662}) at 2.5 mW of laser power was clearly observed and

indicates a phase transition due to local heating under the laser beam. Consequently, only the Raman spectra recorded below this limit power of 2.5 mW, can be considered as showing the "true" signature of the pristine LSCF6428 ceramic at room temperature, as analyzed by XRD (Fig. 1).

Raman spectra, Fig. 3, were recorded under different laser lines: 458 nm, 514 nm and 785 nm with 50$\times$ objectives in several surface spots. The 458 nm spectrum under 0.15 mW laser power shows the signatures of a pure LSCF perovskite phase as discussed earlier. A rather similar spectrum is obtained under 3 mW with 785 nm exciting line indicating a lower light absorption – and heating – in near IR range. Additional narrow Raman peaks at about 685, 518, and 480 cm^{-1} were observed. These peaks can be assigned to the contribution of Co_3O_4 second phase. A reference spectrum given in Fig. 3 has been obtained by heating of CoOOH heterogenite [44]. The small wavenumber shift and relative intensity change arise from the (pre)resonance Raman effect [45]. No "well-defined" spectrum of CoO phase seems to be available in the literature. Very low intense spectrum with
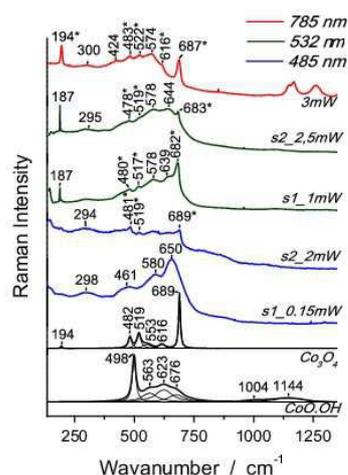
Fig. 3. Raman signatures of as-prepared LSCF6428 ceramic at different surface area/laser power/wavelengths and of Co_3O_4 obtained by thermal treatment of CoOOH [44]. (*corresponds to Co_3O_4 traces).
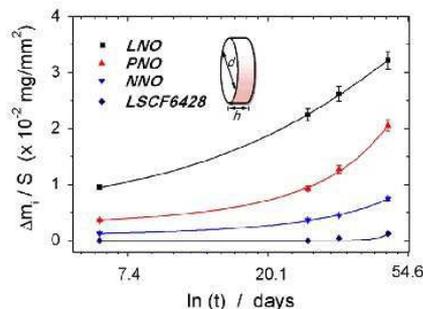
Fig. 4. Mass uptake evolution of LSCF6428 ceramic pellet during 47 days of protonation treatment (20 bar of CO_2-free water and 550 °C).

broad bands at 465 and 675 cm^{-1} is given by Tang et al. [46]. According to Tang et al. assignment, the CoO contribution in the Raman spectrum is detected by the broadening of the 461 cm^{-1} peak. Alternatively, the Raman spectrum of CoOOH (Fig. 3) shows a narrow peak at 498 cm^{-1} and a broad feature at ~620 cm^{-1} that may explain the rather high intensity of the ~480 cm^{-1} peak. Anyway, the intense light absorption of the black material promotes the transformation of (hydroxylated) CoO into Co$_3$O$_4$ under the laser beam. The observation of a band at ~1140 cm^{-1} is also consistent with hydroxylated CoO [44]. Traces of metal transition oxides are commonly observed in similar compounds [46].

3.2. Protonation treatment under medium/high pressure

3.2.1. Reactivity vs. water

The investigated LSCF6428 ceramic was treated, similarly to our previously investigated nickelate-based samples [21,36], using an autoclave device under ~20 bar of CO$_2$-free water pressure at 550 °C. The mass variation between pristine and protonated ceramics was recorded versus time. Consequently, the mass difference per sample surface area (mg/mm^2) exposed to water pressure was calculated using Eq. (1). The graph of the calculated mass change vs. protonation time is plotted in semi-logarithmic scale as shown in Fig. 4.

$$\text{Mass uptake}\left(\text{mg/mm}^2\right) = \frac{m_i - m_0}{S} \qquad i = 1, \ 2, \ 3, \ \dots \ \dots$$

$$(1)$$

where m_0 is the as-prepared sample weight (mg), m_i is the sample weight of $i=1, 2, 3\dots$ protonation runs up to the complete studied time range and S is sample surface area, $2\pi r^2 + h(2\pi r)$.

The exponential fitting curves, Fig. 4, reveal very low corrosion of the LSCF6428 ceramic in comparison with our previously investigated nickelates [21,36]. The reactivity rate of the LSCF6428 sample is about 1:42, 1:22 and 1:8 of the reactivity rate in the case of LNO, PNO and NNO sample,

respectively. Hence, the LSCF6428 ceramic exhibits the highest stability under 20 bar of CO$_2$-free water pressure at 550 °C.

3.2.2. Microstructures

The samples were categorized in different states; as-prepared/pristine (a), as-prepared sample thermally treated at 1000 °C (a'), protonated (b, c, d), and deprotonated by thermal treatment at 1000 °C (b', c', d'). Fig. 5 illustrates the surface microstructure features of each sample states. The surface of as-prepared sample (Fig. 5a) as well as that of the thermally treated sample (Fig. 5a') show grains of ~1–2 μm with pores of ~2–10 μm. A white contour is observed at the grain periphery and assigned to 2nd phase traces already identified by XRD and Raman analysis. In the case of the ceramic protonated under 40 bar of CO$_2$-free water for a short period of 8 days (Fig. 5b), the observed surface habits are similar to those detected for the as-prepared sample. However, we observe an increase of the number of grains affected by the white contour. This may indicate an increase of the secondary phase content. In the case of thermally treated protonated LSCF6428 using CO$_2$-free water (Fig. 5b' and c'), the surface habit remains rather similar to that of the as-prepared and thermally treated as-prepared samples, in agreement with good stability of the ceramic.

In the case of the ceramic protonated under CO$_2$-saturated water, the surface features were more affected – small aggregates (~4 μm) were covered by another phase. After deprotonation performed at 1000 °C (Fig. 5c'), the microstructure remains rather stable. By comparison with previously analyzed protonated nickelate homologs [21,36], no crack was observed neither for the protonated nor the deprotonated LSCF6428 ceramics, treated either under CO$_2$-free or CO$_2$ saturated water.

3.3. Chemical and structural modifications

3.3.1. Thermogravimetry and thermal expansion

Fig. 6a compares the TGA curves of non-protonated and protonated LSCF6428 ceramic. According to the oxygen
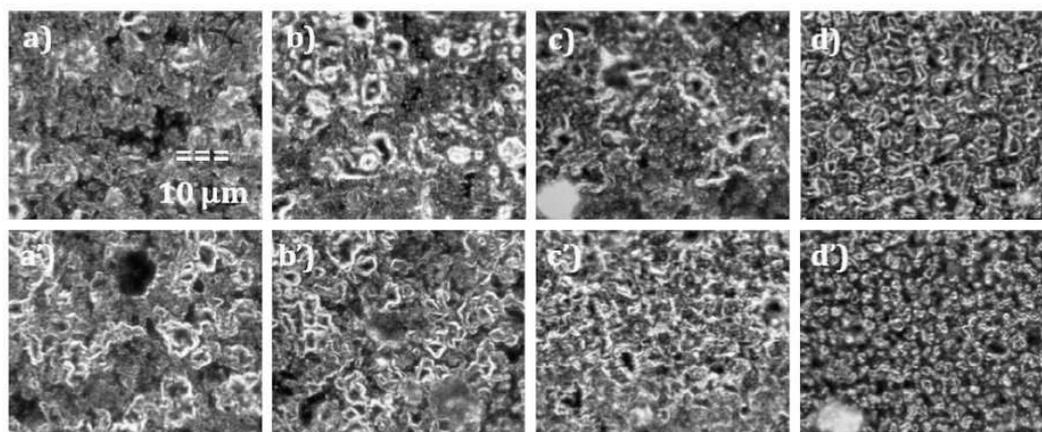
Fig. 5. Micro-features (10 μm) of LSCF6428's surface sample in different states (a) as-prepare sample (b) 40 bar of CO$_2$-free water pressure for 8 days (c) 20 bar of CO$_2$-free water pressure for 47 days (d) 40 bar of CO$_2$-saturated water pressure for 8 days.
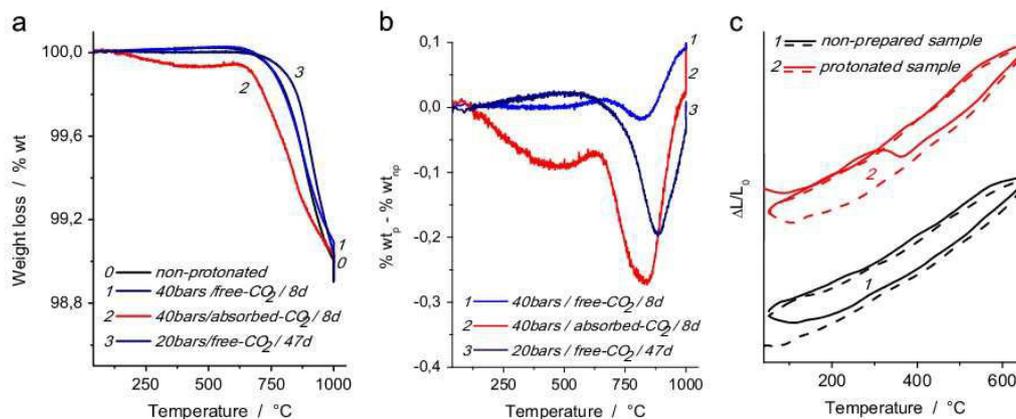
Fig. 6. (a) Thermal analysis of as-prepared and protonated LSCF6428 (b) corresponding TG weight loss difference, %wt$_p$ − %wt$_{np}$. (c) Two consecutive thermal expansion (length variation/initial length) curves of as-prepared and protonated LSCF6428 under free-CO$_2$ water pressure.

mobility [11,15,16], the weight loss observed above 600 °C (He atmosphere) in the case of non-protonated pellets can be related to the equilibration of the oxygen stoichiometry with the new environment, different from the sintering atmosphere [47]. The variation is very weak according to previous measurement of the oxygen stoichiometry [2]. Furthermore the low delta value limits the number of vacancies. In order to highlight the contribution solely due to the autoclave treatment, the oxygen stoichiometry variation was suppressed by subtracting the measure made on the non-protonated, as-prepared sample: the relative mass-loss difference between non-protonated and protonated samples is plotted in Fig. 6b. The difference curve clearly shows the presence of one weak peak at ~400 °C in the case of medium-pressure (~20 bar) protonated samples. For the high-pressure (40 bar) protonation, a second stronger peak is observed at ~800 °C. According to previous studies [20,28,29], the phenomenon at 300–400 °C can be assigned to the decomposition of hydroxide(s), and that at ~800–900 °C to the carbonate decomposition.

According to the above TG data, the hypothesis that the ceramic exhibits a single phase and that the initial δ oxygen stoichiometry is not modified at 550 °C in the autoclave, the following formula can be proposed for protonated LSCF6428 ceramic under 40 bar of CO$_2$-absorbed water pressure: La$_{0.4}$Sr$_{0.6}$Fe$_{0.2}$Co$_{0.8}$O$_{3-\delta}$(OH)$_{0.01}$(CO$_3$)$_{0.04}$. In the case of ceramics treated under free-CO$_2$ water pressure in both medium and high pressures, the content of hydroxides moieties was much lower (< 0.001 mol/mol pH$_2$O).

Comparison of thermal expansion (TE) curves characteristic of non-protonated and protonated LSCF6428 samples is presented in Fig. 6c. The area located in-between heating and cooling curves of pristine, non-protonated sample is rather small, revealing stability of the material (measured temperature range is far below the sintering temperature of the ceramic pellet). Only the first heating TE curve of protonated pellet (~40 bar of CO$_2$-free vapor pressure) shows clearly a contraction jump at ~350 °C. A similar phenomenon was observed in our previous works devoted to stability studies of nickelate-based oxides

[21,36]. Furthermore, a study on phase transition of LSCF7382 under H$_2$ atmosphere by Siebert et al. [18], points out the transformation from rhombohedral perovskite structure to orthorhombic A$_2$B$_2$O$_5$ brownmillerite phase at 350 °C. Formation of a hydroxide film at the ceramic surface could also explain the presence of such a jump since dehydration of hydroxides is observed in this temperature range. The lack of cracks in the ceramic pellet is more consistent with the assignment of this jump modification to the presence of 2nd phase surface film than to the effect of the phase transition involving a contraction of the unit-cell in the bulk.

3.3.2. Unit-cell symmetry

Fig. 1a and b compares XRD patterns of as-prepared and 20 bar protonated/40 bar protonated using CO$_2$-free water LSCF6428, respectively. Extra Bragg's peaks observed after protonation treatment confirm the presence of cobalt oxide(s), namely CoO. According to the refinement of XRD patterns and relative ratio analysis, the amount of cobalt oxide(s) traces can be estimated to 1–2% depending on the protonation pressure – the higher pressure value, the higher percentage of CoO. The detection of Co$_3$O$_4$ by Raman spectroscopy could be due to the presence of both CoO and Co$_3$O$_4$. Note, the higher Raman intensity of Co$_3$O$_4$ hinders the observation of CoO signature and/or the oxidation of CoO can appear under the laser beam heating. Taking into account the unit-cell parameters and space group given in Table 1, it is clear that the protonated LSCF6428 keeps the rhombohedral symmetry, no matter the protonation pressure value is. The protonation treatment under medium and high pressure causes a small expansion of unit-cell volume: 0.57% for 20 bar protonation and 1.10% for 40 bar protonation. This volume expansion could be consistent with the contraction shown in Fig. 6c, because of the departure of protons inserted in the perovskite structure.

3.3.3. Vibrational spectroscopy analysis

Raman spectra recorded at the surface of protonated LSCF6428 samples, Fig. 7a, clearly reveal the presence of

Table 1
XRD analyses of as-prepared and protonated LSCF6428 samples.

Sample	Phase symmetry of perovskite structure	Space group	Unit-cell parameters			V (Å³)	ΔV (%)
			a (Å)	b (Å)	c (Å)		
LSCF6428	Rhombohedral	R-3c	5.4878 (5)	5.4878 (5)	13.374 (4)	348.8 (1)	–
LSCF6428.H$^+$ (20 bar CO$_2$-free water)	Rhombohedral+CoO	R-3c	5.4936 (8)	5.4936 (8)	13.423 (8)	350.8 (2)	+0.57
LSCF6428.H$^+$ (40 bar CO$_2$-free water)	Rhombohedral+CoO	R-3c	5.5107(1)	5.5107(1)	13.4088(3)	352.64(1)	+1.10

Fig. 7. Raman spectra of LSCF6428 ceramic in different states, protonated and deprotonated, recorded (a) on surface (b) in bulk. (Note: the used symbols are described in Table 2 and sample labels are indicated in the text).

Table 2
Raman wavenumbers of the different second phases found on the bulk and surface of protonated LSCF6428 ceramics.

Phase	Symbol*	Wavenumber (cm^{-1})$^+$	References
SrO	ϕ	560, 540, 520	[51]
SrO$_2$	Δ	863	
Co$_3$O$_4$	σ	686, 614, 520, 479, 191	[44,52–54]
γ-Fe$_2$O$_3$	γ	700, 600, 495, 406, 292, 247, 226	[48]
LaO.OH	μ	424, 383, 345, 312, 216, 202, 165, 135, 123, 116	[49]
SrCO$_3$	•	1446, 1071, 710, 511, 258, 245, 237, 180, 148, 100	[50,55]
I-La$_2$O$_2$CO$_3$	**	1064, 868, 721, 670, 315	[49]

*Symbols used in Fig. 7.
$^+$ Underline Raman wavenumbers are observed in this study.

secondary phases, i.e. oxide(s), hydroxide(s) and carbonate(s) depending on protonated/thermal treatment conditions (Table 2).

i) In the case of protonation performed under 20 bar using CO$_2$ free-water (20 bar, P20), Raman signatures at 688, 611, 493, 407, 289, and 221 cm^{-1} were observed. These Raman peaks are assigned to hematite, α-Fe$_2$O$_3$ [48].

ii) For higher pressure of CO$_2$ free-water (40 bar, P40), the Raman spectrum shows traces of lanthanum oxycarbonate (La$_2$O$_2$CO$_3$). Our reference spectra of LaOOH(CO$_3$) and La

(OH)$_3$ obtained by in-situ thermal treatment of hydroscopic La$_2$O$_3$ powder are given in Fig. S2 (Supplementary material). The Raman signature detected at 1066 cm^{-1} is assigned to internal stretching mode (A_{1g}) of C–O bonds [49].

iii) For the ceramic treated under 40 bar of CO$_2$-saturated water pressure (40 bar, P40/CO$_2$), Raman spectra recorded at the surface show carbonate signature: the peaks at 1073, 702, 247, 182, and 150 cm^{-1} were assigned to strontium carbonate, SrCO$_3$, with its characteristic 1073 cm^{-1} symmetric stretching mode (ν_1) of C–O bond [50]. A peak at ∼865 cm^{-1} and a weak band at ∼567 cm^{-1} can be

assigned to a strontium oxide/peroxide. This result is similar to that presented in the study of Waal [51], where a peak at 863 cm^{-1} is attributed to the O–O stretching mode of SrO_2 composition, and three very weak bands at 563, 537, and 522 cm^{-1} are assigned to translation modes of Sr–O vibrational unit. The presence of Sr-based oxides could be related to the thermal decomposition of the Sr-carbonate under the laser spot because of a black matrice.

Fig. 7b shows representative Raman spectra recorded in the bulk of LSFC6428 ceramic treated under different protonation conditions. Measurements are made on the fresh fracture of the ceramic pellet, from surface to the bulk centre.

i) Raman spectra characteristic of the sample treated under 20 bar/CO_2-free (at 510 µm bulk) and 40 bar/CO_2-saturateded water (at 50 µm bulk), reveal the presence of traces of Cobalt spinel (Co_3O_4: 689, 618, 523, 485, and 195 cm^{-1}). However, some slight peak downshifts are detected between pure Co_3O_4 and that present in protonated LSCF6428.

ii) Raman spectrum recorded on bulk, 50 µm depth (protonated under 20 bar, Fig. 7b), shows the bands at 606, 501, 404, 288 and 221 cm^{-1} which are characteristic of hematite (α-Fe_2O_3) [56].

ATR-FTIR technique specially probes the surface, typically a few (tenths) micron in-depth penetration: the exact penetration depth varies with the wavenumber depending on the optical index of the crystal probe (diamond or germanium, Fig. 8). Depending on the band intensity and optical characteristic of the investigated solid (the higher optical index, the higher reflection), the band shape is complex and can be described as a mixture of absorption and reflection signal [57,58]. Thus, it is not possible to discuss the crystallinity of the second phases. The ATR-FTIR tests were performed on the as-prepared (a and b), protonated in different conditions (c–e) and thermally treated as-prepared (f) samples. A sharp peak observed at ~3604 cm^{-1} can be assigned to the stretching mode of OH^- in $Sr(OH)_2$. This contribution confirms the presence of protonic species absorbed on the ceramic surface. The absorption bands at 600–1500 cm^{-1} detected in the case of protonated samples correspond to traces of $SrCO_3$ [30]. The strong absorption peak centered at 1422 cm^{-1} and the band at 701 cm^{-1} are assigned to the asymmetric stretching (v_3) and bending (v_4) vibrations of C–O bonds, respectively. A strong narrow peak at ~859 cm^{-1} can be assigned to the out-of-the-plane bending (v_2) mode, and that observed at ~1071 cm^{-1} to the fully symmetric stretching (v_1) mode of CO_3^{2-} ions. The absorption bands characteristic of Sr $(OH)_2$, and $SrCO_3$ observed here are similar to those presented in the literature [59,60].

3.4. LSCF6428 chemical stability

A Raman mapping was performed on the cross-section of a fresh fractured sample – from the top surface (directly exposed

to the vapor pressure) down to the bottom one (in contact with the autoclave chamber) in step of few micron to 50 µm. This procedure is the so-called Raman profilometry method discussed in details in our previous studies [20,21,35,36]. Fig. 9 compares the Raman mapping spectra recorded for ceramics protonated using three distinct conditions: 20 bar of free-CO_2 water pressure (47 days), 40 bar of free-CO_2 water pressure (8 days) and 40 bar of CO_2-saturated water pressure (8 days). The relative volume section of phase modification is summarized in Table 3.

Due to the possibility of focusing at the microscale on a sample surface, the Raman technique has higher ability than the usual XRD technique to detect even small structural changes as well as secondary phases. However, the combination of the black color of the matrix/substrate and the laser spot can lead to uncontrolled heating and then structural/chemical transformations (partial dehydration/oxidation) under the laser light as discussed in Section 3.1.2. The dehydration of those hydrated/hydroxylated substrate derivatives may induce phase transitions/transformations and hence a higher number of phases that explains the higher number of phases detected by vibrational spectroscopy. Furthermore, the vibrational spectroscopy techniques are able to reveal the presence of amorphous oxyhydroxides, not detectable by XRD [20,30]. Since the Raman intensity depends on the chemical bond polarizability, minor phases may have a stronger signature than the major matrix.

No transformation on the top layer of protonated LSCF6428 is observed after protonation under 20 bar. Traces of hematite (α-Fe_2O_3) and cobalt oxide are observed in some spots in the bulk due to defects formed in the powder processing and/or sintering. On the contrary, the Raman spectra characteristic of the ceramics protonated under 40 bar of both CO_2-free and -saturated water, show the presence of carbonate compounds (nearly surface, < 1 µm) as well as other hydroxide(s)/oxide(s) phases. The carbonate phases are identified as strontianite ($SrCO_3$) and lanthanum oxycarbonate (I-$La_2O_2CO_3$). Hydroxide(s)/oxide(s)   phase   are   identified   as   lanthanide
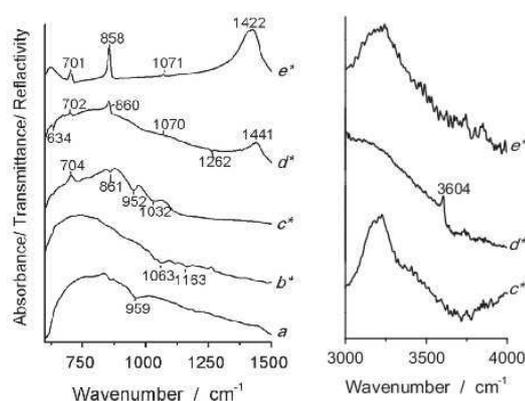
Fig. 8. ATR and micro ATR-FTIR spectra recorded at the surface of as-prepared (a, b), protonated under 20 bar free-CO_2 (c), under 40 bar free-CO_2 (d), 40 bar absorbed-CO_2 (e) and thermal treatment (f). (Note:*indicates the spectra collected with the µ-ATR Ge crystal).
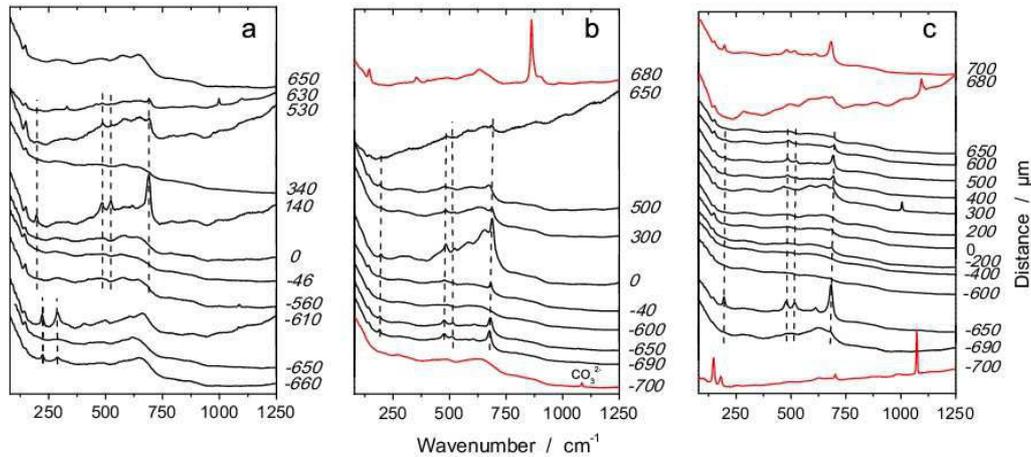
Fig. 9. Raman mapping along the fresh cross-section fracture of LSCF6428 ceramic pellets protonated under (a) 20 bar of CO_2-free water, (b) 40 bar of CO_2-free water, and (c) 40 bar of CO_2 saturated water.

Table 3
Comparison of corrosion in LSCF6428 dense ceramic.

Section (%)	Protonation conditions		
	20 bar/47 days free-CO_2 water	40 bar/8 days free-CO_2 water	40 bar/8 days saturated-CO_2 water
Top layer	< 0.1	~0.4	~0.7
Core	99.9	99.2	98.9
Bottom layer	< 0.1	~0.4	~0.4
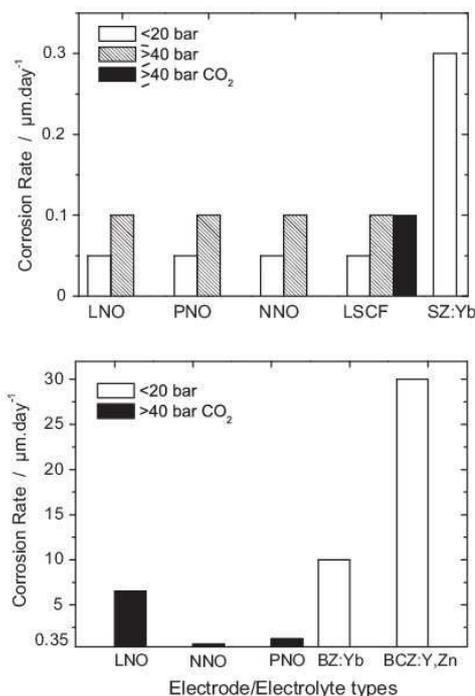
Fig. 10. Comparison of corrosion rate (μm/day) of various electrolytes [20] and electrodes treated in an autoclave under different conditions (see text for label).

oxyhydroxide (LaOOH) and cobalt oxides (Co_3O_4). Note, comparison of 2nd phase volumes between medium and high vapor pressure protonation treatments indicates that they are not significantly different.

4. Conclusions

According to the protonation treatment ($\sim$20 and $\sim$40 bar of CO_2-free or CO_2-saturated water, 550 °C) and several advanced analysis techniques, we can summarize that the LSCF6428 ceramic exhibits very good stability under medium and high water pressure, 5–30 times better than nickelates homologs (Table S1). XRD results show that the structure of protonated pellets remains rhombohedral (R-3c) with a small unit-cell expansion related to proton incorporation. Only traces of secondary phases were detected in the ceramic bulk. XRD reveals the formation of CoO. Fe_2O_3 traces are also observed within the bulk as processing defects. Raman spectroscopy shows the presence of oxyhydroxide(s). According to TG results, the content of OH^- (< 0.01 mol/mol H_2O) is very low. Raman mapping allows an identification of surface corrosion products: the hematite (α-Fe_2O_3), cobalt oxides (CoO/Co_3O_4), tetragonal lanthanum oxycarbonate (I-$La_2O_2CO_3$), and strontianite ($SrCO_3$). The type and content of these secondary phases depend on the protonation conditions (i.e. CO_2 contents, pressure, and duration times). As expected, the highest content of carbonates is found after the treatment using CO_2-saturated water.

Fig. 10 compares the rate of the formation of the corrosion film thickness formed at the surface of 'dense' ceramic pellets used as electrolytes (BCZ:YZ, $BaCe_{0.5}Zr_{0.3}Y_{0.16}Zn_{0.04}O_{3-\delta}$; BZ:Yb, $BaZr_{0.9}Yb_{0.1}O_{3-\delta}$; SZ:Yb, $SrZr_{0.9}Yb_{0.1}O_{3-\delta}$) [20] and electrodes ($Ln_2NiO_{4+\delta}$,Ln=La, LANO, Ln=Pr, PRNO and Ln=Nd, NdNO; LSCF6428) [21]. Under medium water pressure the stability of electrode materials and of strontium zirconate electrolyte is good. Under high water pressure barium-base perovskite electrolytes are no more stable and if the water has been saturated with CO_2 the superior stability of LSCF compound is demonstrated whatever the lower carbonation of Pr and Nd-based compounds vs. La, Ba or even Sr homologs.

Appendix A. Supporting information

Supplementary data associated with this article can be found in the online version at http://dx.doi.org/10.1016/j.ceramint. 2015.07.035.

References

[1] A.B. Stambouli, E. Traversa, Solid oxide fuel cells (SOFCs): a review of an environmentally clean and efficient source of energy, Renew. Sustain. Energy Rev. 6 (2002) 433–455.

[2] A. Grimaud, F. Mauvy, J.M. Bassat, S. Fourcade, L. Rocheron, M. Marrony, J.C. Grenier, Hydration properties and rate determining steps of the oxygen reduction reaction of perovskite-related oxides as H^+-SOFC cathodes, J. Electrochem. Soc. 159 (2012) B683–B694.

[3] B. Philippeau, F. Mauvy, C. Mazataud, S. Fourcade, J.-C. Grenier, Comparative study of electrochemical properties of mixed conducting Ln_2NiO_{4+d} (Ln=La, Pr, Nd) and $La_{0.6}Sr_{0.4}Co_{0.2}Fe_{0.8}O_3-d$ as SOFC cathodes associated to $Ce_{0.9}Gd_{0.1}O_2-d$, $La_{0.8}Sr_{0.2}Ga_{0.8}Mg_{0.2}O_3-d$ and $La_9Sr_1Si_6O2_{6.5}$ electrolytes, Solid State Ion. 249–250 (2013) 17–25.

[4] M.-B. Choi, B. Singh, E.D. Wachsman, S.-J. Song, Performance of $La_{0.1}Sr_{0.9}Co_{0.8}Fe_{0.2}O_3-\delta$ and $La_{0.1}Sr_{0.9}Co_{0.8}Fe_{0.2}O_3-\delta-Ce_{0.9}Gd_{0.1}O_2$ oxygen electrodes with $Ce_{0.9}Gd_{0.1}O_2$ barrier layer in reversible solid oxide fuel cells, J. Power Sources 239 (2013) 361–373.

[5] M. Žunić, G. Branković, F. Basoli, M. Cilense, E. Longo, J.A. Varela, Stability, characterization and functionality of proton conducting NiO– $BaCe_{0.85-x}Nb_xY_{0.15}O_3-\delta$ cermet anodes for IT-SOFC application, J. Alloy. Compd. 609 (2014) 7–13.

[6] S. Engels, T. Markus, M. Modigell, L. Singheiser, Oxygen permeation and stability investigations on MIEC membrane materials under operating conditions for power plant process, J. Membr. Sci. 370 (2011) 58–69.

[7] J. Yi, T.E. Weirich, M. Schroeder, CO_2 corrosion and recovery of perovskite-type $BaCo_{1-x-y}Fe_xNbyO_{3-\delta}$ membranes, J. Membr. Sci. 437 (2013) 49–56.

[8] X. Tan, N. Liu, B. Meng, J. Sunarso, K. Zhang, S. Liu, Oxygen permeation behavior of $La_{0.6}Sr_{0.4}Co_{0.8}Fe_{0.2}O_3$ hollow fibre membranes with highly concentrated CO_2 exposure, J. Membr. Sci. 389 (2012) 216–222.

[9] T. Ishihara, Perovskite Oxide for Solid Oxide Fuel Cells, Springer, New-York, 2009.

[10] L. Qiu, T. Ichikawa, A. Hirano, N. Imanishi, Y. Takeda, $Ln_{1-x}Sr_xCo_{1-y}Fe_yO_{3-\delta}$ (Ln=Pr, Nd, Gd; x=0.2, 0.3) for the electrodes of solid oxide fuel cells, Solid State Ion. 158 (2003) 55–65.

[11] G.C. Kostogloudis, C. Ftikos, Properties of A-site-deficient $La_{0.6}Sr_{0.4}Co_{0.2}Fe_{0.8}O_3-\delta$-based perovskite oxides, Solid State Ion. 126 (1999) 143–151.

[12] S. Carter, A. Selcuk, R.J. Chater, J. Kajda, J.A. Kilner, B.C.H. Steele, Oxygen transport in selected nonstoichiometric perovskite-struture oxides, Solid State Ion. 53–56 (Part 1) (1992) 597–605.

[13] P. Batocchi, F. Mauvy, S. Fourcade, M. Parco, Electrical and electrochemical properties of architectured electrodes based on perovskite and A_2MO_4-type oxides for protonic ceramic fuel cell, Electrochim. Acta 145 (2014) 1–10.

[14] J. Dailly, S. Fourcade, A. Largeteau, F. Mauvy, J.C. Grenier, M. Marrony, Perovskite and A_2MO_4-type oxides as new cathode materials for protonic solid oxide fuel cells, Electrochim. Acta 55 (2010) 5847–5853.

[15] H.L. Lein, K. Wiik, T. Grande, Thermal and chemical expansion of mixed conducting $La_{0.5}Sr_{0.5}Fe_{1-x}Co_xO_{3-\delta}$ materials, Solid State Ion. 177 (2006) 1795–1798.

[16] S.-i. Hashimoto, Y. Fukuda, M. Kuhn, K. Sato, K. Yashiro, J. Mizusaki, Oxygen nonstoichiometry and thermo-chemical stability of $La_{0.6}Sr_{0.4}Co_{1-y}Fe_yO_{3-\delta}$ (y=0.2, 0.4, 0.6, 0.8), Solid State Ion. 181 (2010) 1713–1719.

[17] F. Prado, N. Grunbaum, A. Caneiro, A. Manthiram, Effect of La^{3+} doping on the perovskite-to-brownmillerite transformation in $Sr_{1-x}La_xCo_{0.8}Fe_{0.2}O_3-\delta$ (0 ≤ x ≤ 0.4), Solid State Ion. 167 (2004) 147–154.

[18] E. Siebert, A. Boréave, F. Gaillard, T. Pagnier, Electrochemical and Raman study of $La_{0.7}Sr_{0.3}Co_{0.8}Fe_{0.2}O_3-\delta$ reduction, Solid State Ion. 247–248 (2013) 30–40.

[19] N. Grunbaum, L. Dessemond, J. Fouletier, F. Prado, A. Caneiro, Electrode reaction of $Sr_{1-x}La_xCo_{0.8}Fe_{0.2}O_3-\delta$ with x=00.1 and 0.6 on $Ce_{0.9}Gd_{0.1}O_{1.95}$ at 600 ≤ T ≤ 800 °C, Solid State Ion. 177 (2006) 907–913.

[20] A. Slodczyk, O. Zaafrani, M.D. Sharp, J.A. Kilner, B. Dabrowski, O. Lacroix, Ph. Colomban, Testing the chemical/structural stability of proton conducting perovskite ceramic membranes by in situ/ex situ autoclave Raman microscopy, Membranes 3 (2013) 311–330.

[21] S. Upasen, P. Batocchi, F. Mauvy, A. Slodczyk, Ph. Colomban, Protonation and structural/chemical stability of $Ln_2NiO_{4+\delta}$ ceramics vs. H_2O/ CO_2: high temperature/water pressure ageing tests, J. Alloy. Compd. 622 (2015) 1074–1085.

[22] B. Sala, F. Grasset, O. Lacroix, A. Sirat, K. Rahmouni, M. Keddam, H. Takenouti, D. Goeuriot, B. Bendjeriou, Ph. Colomban, Method for the Optimization of the Conductivity of a Ion Conducting Membrane, AREVA, CNRS, ARMINES, SCT; Patent WO 2008/152317 A2, December, 18, 2008.

[23] B. Sala, F. Grasset, O. Lacroix, A. Sirat, K Rhamouni, M. Keddam, H. Takenouti, D. Goeuriot, B. Bendjeriou, Ph. Colomban, A. Slodczyk, G. Pourcelly, A. Van der Lee, J.G. Sanchez, AREVA, CNRS, ARMINES, Patent EP 12773302.0-1360, October, 11, 2012.

[24] L.A. Chick, O.A. Marina, C.A. Coyle, E.C. Thomsen, Effects of temperature and pressure on the performance of a solid oxide fuel cell running on steam reformate of kerosene, J. Power Sources 236 (2013) 341–349.

[25] L. Magistri, A. Traverso, F. Cerutti, M. Bozzolo, P. Costamagna, A.F. Massardo, Modelling of pressurised hybrid systems based on integrated planar solid oxide fuel cell (IP-SOFC) technology, Fuel Cells 5 (2005) 80–96.

[26] W.J. Yang, S.K. Park, T.S. Kim, J.H. Kim, J.L. Sohn, S.T. Ro, Design performance analysis of pressurized solid oxide fuel cell/gas turbine hybrid systems considering temperature constraints, J. Power Sources 160 (2006) 462–473.

[27] W. Burbank Jr, D.D. Witmer, F. Holcomb, Model of a novel pressurized solid oxide fuel cell gas turbine hybrid engine, J. Power Sources 193 (2009) 656–664.

[28] Ph. Colomban, Aneta Slodczyk, Oumaya Zaafrani, Olivier Lacroix, Johan Loricourt, Frederic Grasset, Beatrice Sala, What is the true nature of conducting proton in perovskite ceramic membrane: hydroxyl ion or interstitial proton?, MRS Proc (2011) http://dx.doi.org/10.1557/ opl.2011.616 /mrsf10-1309-ee03-21.

[29] Ph Colomban, A. Slodczyk, D. Lamago, G. Andre, O. Zaafrani, O. Lacroix, S. Willemin, B. Sala, Proton dynamics and structural

modifications in the protonic conductor perovskites, J. Phys. Soc. Jpn. 79 (Suppl.A) (2010) S1–S6.

[30] Ph Colomban, C. Tran, O. Zaafrani, A. Slodczyk, Aqua oxyhydroxycarbonate second phases at the surface of Ba/Sr-based proton conducting perovskites: a source of confusion in the understanding of proton conduction, J. Raman Spectrosc. 44 (2013) 312–320.

[31] A. Slodczyk, Ph. Colomban, S. Willemin, O. Lacroix, B. Sala, Indirect Raman identification of the proton insertion in the high-temperature [Ba/Sr][Zr/Ti]O$_3$-modified perovskite protonic conductors, J. Raman Spectrosc. 40 (2009) 513–521.

[32] A. Slodczyk, M. Limage, Ph. Colomban, O. Zaafrani, F. Grasset, J. Loricourt, B. Sala, Substitution and proton doping effect on SrZrO$_3$ behaviour: high-pressure Raman study, J. Raman Spectrosc. 42 (2011) 2089–2099.

[33] A. Slodczyk, Ph. Colomban, D. Lamago, G. Andre, O. Zaafrani, O. Lacroix, A. Sirat, F. Grasset, B. Sala, Optimum temperature range for the proton dynamics in H-doped BaZrO$_3$:Yb dense ceramics-a neutron scattering study, J. Mater. Res. 27 (2012) 1939–1949.

[34] A. Slodczyk, Ph. Colomban, G. Andre, O. Zaafrani, F. Grasset, O. Lacroix, B. Sala, Structural modifications induced by free protons in proton conducting perovskite zirconate membrane, Solid State Ion. 225 (2012) 214–218.

[35] A. Slodczyk, Ph. Colomban, N. Malikova, O. Zaafrani, S. Longeville, J.-M. Zanotti, O. Lacroix, B. Sala, Bulk protons in anhydrous perovskites —neutron scattering studies, Solid State Ion. 252 (2013) 7–11.

[36] S. Upasen, P. Batocchi, A. Slodczyk, Ph. Colomban, F. Mauvy, Structural stability of Ln$_2$NiO$_{4+d}$ under high temperature and high water pressure operating conditions, in: Proceedings of International Discussion on Hydrogen Energy and Applications, Nantes, France, 2014.

[37] L.W. Tai, M.M. Nasrallah, H.U. Anderson, D.M. Sparlin, S.R. Sehlin, Structure and electrical properties of La$_{1-x}$Sr$_x$Co$_{1-y}$FeyO$_3$. Part 2. The system La$_{1-x}$Sr$_x$Co$_{0.2}$Fe$_{0.8}$O$_3$, Solid State Ion. 76 (1995) 273–283.

[38] C.C. Wang, T. Becker, K. Chen, L. Zhao, B. Wei, S.P. Jiang, Effect of temperature on the chromium deposition and poisoning of La$_{0.6}$Sr$_{0.4}$Co$_{0.2}$Fe$_{0.8}$O$_{3-\delta}$ cathodes of solid oxide fuel cells, Electrochim. Acta 139 (2014) 173–179.

[39] M. Liu, D. Ding, K. Blinn, X. Li, L. Nie, M. Liu, Enhanced performance of LSCF cathode through surface modification, Int. J. Hydrog. Energy 37 (2012) 8613–8620.

[40] S. Rousseau, S. Loridant, P. Delichere, A. Boreave, J.P. Deloume, P. Vernoux, La$_{1-x}$Sr$_x$Co$_{1-y}$FeyO$_3$ perovskites prepared by sol-gel method: characterization and relationships with catalytic properties for total oxidation of toluene, Appl. Catal. B: Environ. 88 (2009) 438–447.

[41] W. Araki, T. Yamaguchi, Y. Arai, J. Malzbender, Strontium surface segregation in La$_{0.58}$Sr$_{0.4}$Co$_{0.2}$Fe$_{0.8}$O$_{3-\delta}$ annealed under compression, Solid State Ion. 268 (Part A) (2014) 1–6.

[42] J.-W. Lee, Z. Liu, L. Yang, H. Abernathy, S.-H. Choi, H.-E. Kim, M. Liu, Preparation of dense and uniform La$_{0.6}$Sr$_{0.4}$Co$_{0.2}$Fe$_{0.8}$O$_{3-\delta}$ (LSCF) films for fundamental studies of SOFC cathodes, J. Power Sources 190 (2009) 307–310.

[43] A. Slodczyk, M.D. Sharp, S. Upasen, Ph. Colomban, J.A. Kilner, Combined bulk and surface analysis of the BaCe$_{0.5}$Zr$_{0.3}$Y$_{0.16}$Zn$_{0.04}$O$_{3-\delta}$ (BCZYZ) ceramic proton-conducting electrolyte, Solid State Ion. 262 (2014) 870–874.

[44] C. Burlet, Y. Vanbrabant, H. Goethals, T. Thys, L. Dupin, Raman spectroscopy as a tool to characterize heterogenite (CoO·OH) (Katanga Province, Democratic Republic of Congo), Spectrochim. Acta Part A: Mol. Biomol. Spectrosc. 80 (2011) 138–147.

[45] G. Gouadec, Ph. Colomban, Raman spectroscopy of nanomaterials: how spectra relate to disorder, particle size and mechanical properties, Progr. Cryst. Growth Charact. Mater. 53 (2007) 1–56.

[46] C.-W. Tang, C.-B. Wang, S.-H. Chien, Characterization of cobalt oxides studied by FT-IR, Raman, TPR and TG-MS, Thermochim. Acta 473 (2008) 68–73.

[47] E. Boehm, J.M. Bassat, M.C. Steil, P. Dordor, F. Mauvy, J.C. Grenier, Oxygen transport properties of La$_2$Ni$_{1-x}$Cu$_x$O$_{4+\delta}$ mixed conducting oxides, Solid State Sci. 5 (2003) 973–981.

[48] M.A. Legodi, D. de Waal, The preparation of magnetite, goethite, hematite and maghemite of pigment quality from mill scale iron waste, Dyes Pigments 74 (2007) 161–168.

[49] A. Orera, G. Larraz, M. Sanjuan, Spectroscopic study of the competition between dehydration and carbonation effects in La$_2$O$_3$-based materials, J. Eur. Cer. Soc 33 (2013) 2103–2110.

[50] W. Kaabar, S. Bott, R. Devonshire, Raman spectroscopic study of mixed carbonate materials, Spectrochim. Acta Part A: Mol. Biomol. Spectrosc. 78 (2011) 136–141.

[51] D. De Waal, K.J. Range, M. Konigstein, W. Kiefer, Raman spectra of the barium oxide peroxide and strontium oxide peroxide series, J. Raman Spectrosc. 29 (1998) 109–113.

[52] H. Samata, D. Kimura, S. Mizusaki, Y. Nagata, T.C. Ozawa, A. Sato, Syntesis and characterization of neodymium oxyhydroxide crystals, J. Alloy. Compd. 468 (2009) 566–570.

[53] Q. Jiao, M. Fu, C. You, Y. Zhao, H. Li, Preparation of hollow Co$_3$O$_4$ microspheres and their ethanol sensing properties, Inorg. Chem. 51 (2012) 11513–11520.

[54] J. Yang, H. Cheng, R.L. Frost, Synthesis and characterisation of cobalt hydroxy carbonate Co$_2$CO$_3$(OH)$_2$ nanomaterials, Spectrochim. Acta Part A: Mol. Biomol. Spectrosc. 78 (2011) 420–428.

[55] A.I. Cuza, The Raman Study of Certain Carbonates, Anal Şt Univ Al I Cuza Iaşi Geologie, 2, 2009, pp. 97–112.

[56] F. Froment, A. Tournie, Ph. Colomban, Raman identification of natural red to yellow pigments: ochre and iron-containing ores, J. Raman Spectrosc. 39 (2008) 560–568.

[57] Application Note AN79: Attenuated Total Reflection (ATR) – a versatile tool for FT-IR spectroscopy. Bruker Optics Inc., 2011 [cited 3 January 2015]. Available from: ⟨http://www.bruker.com/fileadmin/user_upload/8-PDF-Docs/OpticalSpectrospcopy/FT-IR/ALPHA/AN/AN79_ATR-Basics_EN.pdf⟩.

[58] K. Ohta, R. Iwamoto, Experimental proof of the relation between thickness of the probed surface layer and absorbance in FT-IR/ATR spectroscopy, Appl. Spectrosc. 39 (1985) 418–425.

[59] M.A. Alavi, A. Morsali, Syntheses and characterization of Sr(OH)$_2$ and SrCO$_3$ nanostructures by ultrasonic method, Ultrason. Sonochem. 17 (2010) 132–138.

[60] P. Ptáček, E. Bartoníčková, J. Švec, T. Opravil, F. Šoukal, F. Frajkorová, The kinetics and mechanism of thermal decomposition of SrCO$_3$ polymorphs, Ceram. Int. 41 (2015) 115–126.

Appendix A

Protonation Treatment: autoclaves and procedures

The steam under medium and high pressure at moderate temperature is extremely reactive and dangerous. The design and implementation construction autoclaves route are required special procedures.

In previous study [1], the principal of Autoclave's use has been was established. Table C.1 lists the principal characteristic of used Autoclave devices. Controlling the protonation of the ceramic (water vapor pressure treatment according to the temperature) led to install different autoclaves programmable temperature. The pressure can be limited to a value lower than the saturation pressure by manually opening a safety valve to allow water vapor to escape. Figure A.1 gives the saturation pressure of water vapor depending on the temperature. The curves consist of two regions - start-up and protonation. The pressure drop in the protonation region was adjusted to 30 bar by the mean of a small leak valve. The further pressure decreases with a time is related to the absorption of water by the ceramic. The sample weight was systematically analyzed by non-destructive techniques after each run of autoclave treatment in order to observe the kinetic of protonation/reactions as a function of time.

Table A.1: *Principal characteristic of Autoclaves.*

Name	Volume (Littre)	Thermodynamic parameters			Safety (bar)	Sealing	Closing Force (Nm)
		Water volume (ml)	T_{max} (°C)	P_{max} (bar)			
HTP *(600°C/100Bars)*	0.125	1-5	600	100	120±10%	metal	50
Autoclave *(Hublot sapphire Optic)*	0.05	1	360/600	50	60±10%	metal	50

---

[1] O. Zaafrani, Dotoral thesis "Protonation, distorsions structurales et espèces protoniques dans des pérovskites lacunaires", Université Pierre et Marie Curie, Paris, France, 2010.
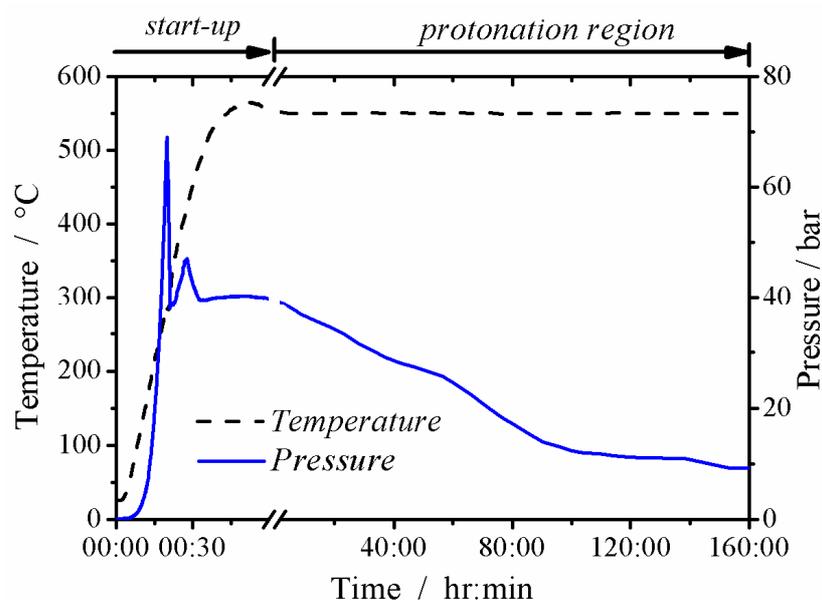
Figure A.1: *Example of a plot presenting pressure drop and temperature evolution v.s. protonation time.*

In this research, the as-prepared $Ln_2NiO_{4+\delta}$ and LSCF6428 ceramics were treated in different conditions as shown in Table A.2. The treatment under high vapor pressure (~40 bar) is to accelerate the material's ageing while the one under medium vapour pressure (~20 bar) is a working condition.

Table A.2: *Protonation treatment conditions.*

	Temperature °C	Time days	Pressure bar	CO_2-absorbed water	Note
Run I	550	8	40	No	
					Accelerated ageing
Run II	550	8	40	Yes	
Run III	550	47	20	No	Working condition

A.1 Preperation of wter use

According to the aim of study, we performed the protonation treatment using two kinds of water:

i) CO_2-free water or decarbonated water - we use of distilled water, and then deionized them by ion exchange resins "Milli-Q plus". Furthermore, a quantity of this deionized water was purged by nitrogen gas (N_2) for several hours in order to ensure of free CO_2 absorbed water.

ii) CO_2-absorbed water or carbonated water– we use a commercial sparkling water "Perrier". The quantity of bicarbonate (HCO_3) is 390 mg/l.

A.2 Procedure of "*ex-situ*" Autoclave treatment

The ex-situ autoclave treatment was performed using HTP (600°C/100bars) autoclave device, as shown in Figure A.2. The status of the seals has been importantly verified by our previous study [1]. The seal is an oval ring having a conical surface alloy Nimonic A80 with very high chromium content. The billet alloy Nimonic A80 has been widely investigated, and found in the USA. The "ring" tests were carried out by AREVA NP to specify the fracture strength and enable the sizing TOP Industry.

The procedure of protonation treatment is summarized in four steps:

i) *Preparing the sample and autoclave* – placing the sample into the "goal-foil" holder in order to avoid direct contact between samples and autoclave chamber that may produce the contamination, then, put gently the samples into the autoclave chamber. Introducing the prepared water for 5 ml into the autoclave chamber, and immediately close the autoclave device using 50 Nm force of ratchet. (Note: carefully close for 2-3 times in order to ensure that the device is tightly closed. Set the autoclave chamber with the conventional heater and controller, and carefully connect the right electric wire between the heater and controller to avoid any electrical circuit short.

---

[1] O. Zaafrani, Dotoral thesis "Protonation, distorsions structurales et espèces protoniques dans des pérovskites lacunaires", Université Pierre et Marie Curie, Paris, France, 2010.
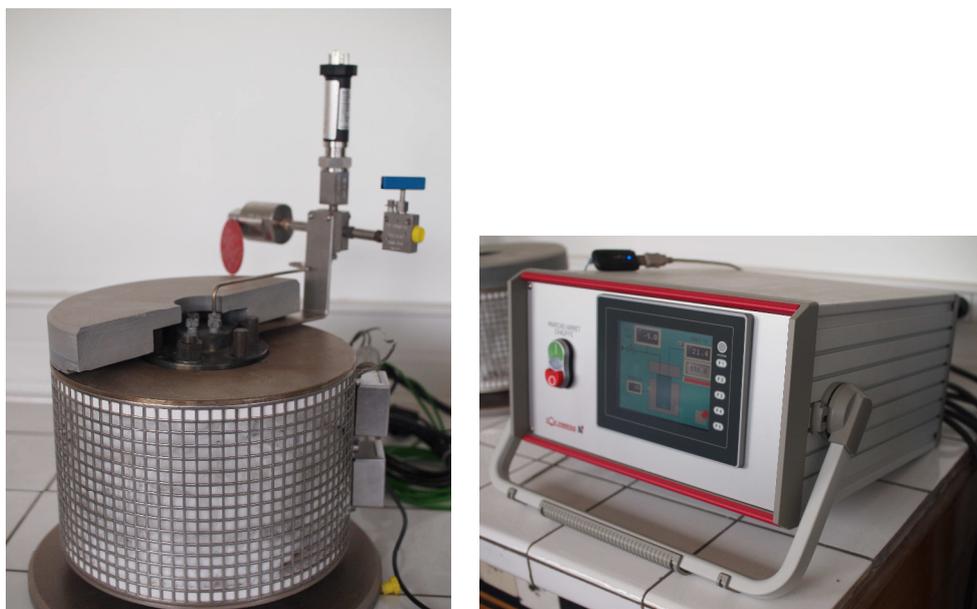
Figure A.2: *HTP (600°C/100bars) autoclave device; heater and autoclave chamber (left), pressure and temperature controller (right).*

ii) *Start-up procedure* – after setting up the autoclave in good condition, we then start the machine. First, set the target temperature as 75-100°C, and press the "green" button to start the machine. When the actual temperature is close to the target temperature, we increase the target temperature to 150°C, ... , 550°C. Note: increasing systematically the target temperature (interval step of 50-100°C) and observing carefully the pressure increase. The pressure can be limited below the limit of the saturation pressure by controlling the amount of water introduced. In case that the actual pressure is higher than target pressure, we can manually opening a safety valve (yellow) allowing the water vapor escapes, and adjust to the set pressure at investigated temperature (Table A.2).

iii)*Treatment observation* – after the machine is stable at working conditions, we should observe at least 30-45 minutes. By then, the observation as well as data transfer should be regularly done every 1-2 days until the end of the treatment.

iv)*Shutdown and opening* – to shut down the treatment system, we first stop the machine by the "red button" and leave it cool down for several hours until the temperature of

the autoclave equilibrium to ambient temperature. Note: it is necessary not to open the hot autoclave in order to avoid a damaging of screw and ring connectors.

A.3 Procedure of "*in-situ*" Autoclave treatment

The implementation of the "*in-situ*" Raman experiment is an online simulation of steam electrolyzer at working conditions, which required the original design and principal knowledge of an optical autoclave cell with a sapphire window. The autoclave, Figure A.3, is formed of enclosures, which can heat up to 360°C, and up to 50 bars. An additional sample holder oven can heat up to 600°C. The autoclave is equipped with a micro-Raman spectrometer of high sensitivity HE532 Horiba Jobin Yvon (Fig. A.3). The Raman spectra are recorded as a function of temperature under controlled water pressure. The preliminary testing condition was done by our previous study [1]. The tests showed that the optical device of the spectrometer including the x50 objective Nikon (long working distance) and optical head Horiba Jobin Yvon SuperHeads containing Edge filters is heated. Therefore, the design of a more complex with double-cooled compressed air and liquid nitrogen vapor variable rate was necessary to relieve this heating problem. The most difficulty, however, is to avoid condensation of water on sapphire (cold wall of the autoclave) and to record the proper Raman spectra. To do so, a perforated metal screen was employed.
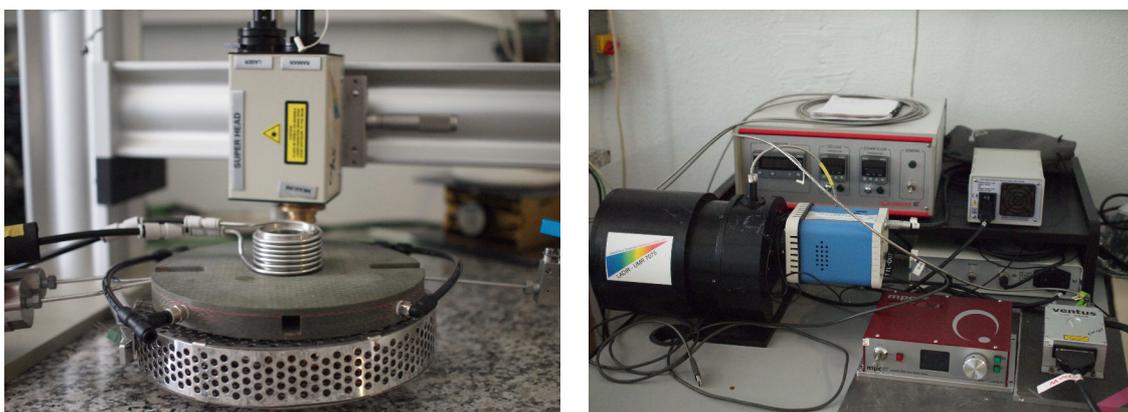
Figure A.3: Hublot sapphire Optic autoclave *(left)* equipped with HE532 Horiba Jobin Yvon source *(right)*.

---

[1] O. Zaafrani, Dotoral thesis "Protonation, distorsions structurales et espèces protoniques dans des pérovskites lacunaires", Université Pierre et Marie Curie, Paris, France, 2010.

The procedure of "*in-situ*" autoclave treatment is summarized in four steps:

i) *Preparing the sample and autoclave* – following the first step of "ex-situ" autoclave treatment, however, the sample is placed directly into the autoclave chamber (without the goal-foil holder) and the quantity of prepared water is only 0.5-1 ml. Ensure the connection of the optical cell to the thermal control unit; Connect the thermocouples, the heater for heating the cell, and the pressure sensor to the temperature regulation device. Verify that the heat regulation unit is at ambient temperature and pressure.

ii) *Positioning of the optical head Horiba Jobin Yvon SuperHeads* – to obtain a good Raman spectra while the sample is protonated, we first measure the distance between the optical head and sample surface. We noted the number of distance by the measuring tools. Note: this number of distance is fixed during the experiment.

iii) *Cooling procedure* - Open the valve of the compressed air at a maximum and turn on the suction pump for circulating liquid nitrogen coupled a Variac autotransformer to its maximum level. Adjust the autotransformer that is coupled to 80 volts and which enables it to adjust flow of liquid nitrogen to flow to 0-270 volts.

iv) *Start-up and Raman measuring procedure* - after setting up the autoclave in good condition, we then start the machine. First, we switch on the machine, and then set the target temperature i.e. 100°C. When the actual temperature reaches to the target temperature, we could examine the Raman scattering at the fixed position that we have set up in the step 2. Note: the step of target temperature should be designed before starting the experiment. While running the Raman scattering, we should observe and note carefully the actual temperature and pressure. In case that the actual pressure is higher than safety pressure, we can manually opening a safety valve (yellow) allowing the water vapor escapes.

v) *Shutdown and opening* – to shut down the treatment system, we first switch down the machine by the same button, and leave the autoclave are cooled for several hours until the temperature of the autoclave equilibrium to ambient temperature. Note: it is necessary not to open the hot autoclave in order to avoid a damaging of screw and ring connectors.

Appendix B

Optical Microscopy: grains and pores size measurement

Microscopes are instruments designed to produce magnified visual or photographic images of small objects. The microscope must accomplish three tasks: produce a magnified image of the specimen, separate the details in the image, and render the details visible to the human eye or camera. This group of instruments includes not only multiple-lens designs with objectives and condensers, but also very simple single lens devices that are often hand-held, such as a magnifying glass.

B.1 Olympus BX51 Instrument

The optical components contained within modern microscopes are mounted on a stable, ergonomically designed base that allows rapid exchange, precision centering, and careful alignment between those assemblies that are optically interdependent. Together, the optical and mechanical components of the microscope, including the mounted specimen on a glass micro slide and coverslip, form an **optical train** with a central axis that traverses the microscope stand and body.

The microscope optical train (BX51) typically consists of an illuminator (including the light source and collector lens), a substage condenser, specimen, objective, eyepiece, and detector, which is either some form of camera or the observer's eye. Research-level microscopes also contain one of several light-conditioning devices that are often positioned between the illuminator and condenser, and a complementary detector or filtering device that is inserted between the objective and the eyepiece or camera. The conditioning device(s) and detector work together to modify image contrast as a function of spatial frequency, phase, polarization, absorption, fluorescence, off-axis illumination, and/or other properties of the specimen and illumination technique. Even without the addition of specific devices to condition illumination and filter image-forming waves, some degree of natural filtering occurs with even the most basic microscope configuration.

Figure B.1: *Olympus optical microscope (BX51) equipment.*

B.2 Cracking-line-intercept measurement (ASTM E112)

To determine the intercept distance between crack-network on the surface samples, the microscope with x20 objective (focalization of 100 µm), OLYMPUS was employed.

The intercept method derives a "G number" by superimposing a pattern over the image and counting how many times that pattern "intercepts" with a crack line. The cracking line-intercept analysis is simply described in 4 steps:

i.   Draw a single dot at middle-left edge of the investigated micro-scale image.

ii. Draw testing lines from the dot to another edge (top, right and bottom) in fixed angle ($\theta \sim 25°$).

iii. Measure the crack distance which the testing line drawn cross over, given d_{Ni} where i is testing-line number and n = measuring distant number.

iv. Statistical calculation for an average distance of each testing line:

$$\bar{d}_i = \frac{\left(\sum_{n=1}^{N} d_{Ni}\right)}{N} \qquad \text{… (eq. B.1)}$$

Figure B.2 shows an example result of cracking line-intercept measurement for deprotonated PrNO and NdNO ceramics.

a) PrNO
n = 45, i = 11
Average distance = 212.17µm
Min = 72.83µm, Max =449.06µm
S.D = ±87.54µm

b) NdNO
n = 94, i = 11
Average distance = 92.41µm
Min = 24.22µm, Max =325.96µm
S.D = ±17.25µm

Figure B.2: *Cracking line-intercept result of a) de-protonated PrNO and b) de-protonated NNO ceramics.*

B.3 Measurement of pore and grain size

In order to measure the size of grains and pore, a suitable magnification of image should be considered. In this test, we employed an objective x100, which provides magnification of 20 µm. The measurement procedure was following the four steps of line intercept analysis as discussed earlier.

Figure B.3 shows a result of protonated LSCF6428 sample. The grains/pores size is the approximately diameter which the testing-line drawn across. To precise and accurate the test, we examined for several surface areas of each investigated sample, consequently the standardize deviation (±µm) are given.
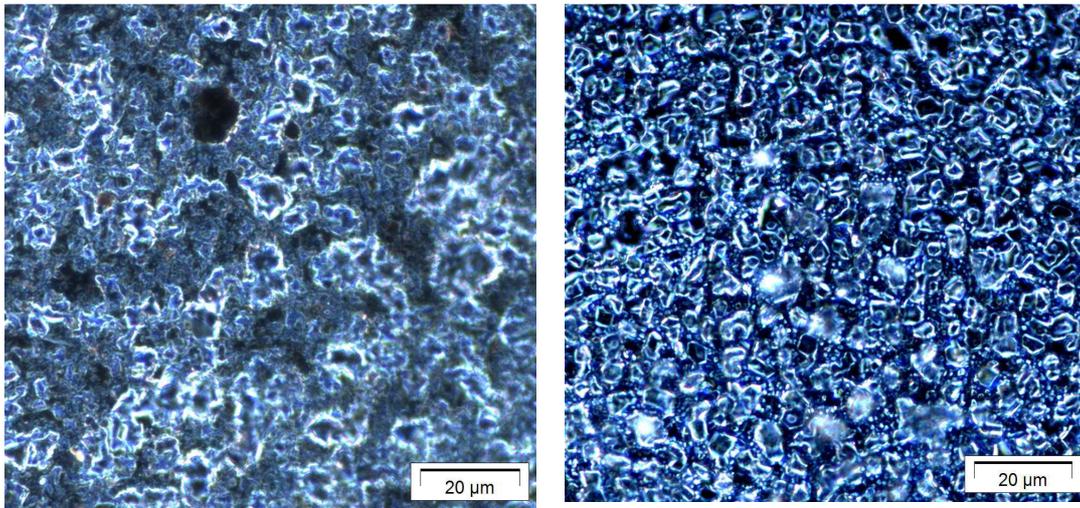
a) **LSCF6428**

n = 13, i = 4

Average grains size =6.87 µm

Min = 4.04 µm, Max =10.92 µm

S.D = ±5.17 µm

b) LSCF6428.H$^+$

n = 33, i = 5

Average grains size =4.27 µm

Min = 2.20 µm, Max = 9.86 µm

S.D = ±3.10 µm

Figure B.3: *Micro-features of a) pristine LSCF6428 and b) protonated LSCF6428 using CO$_2$-saturated water.*

Appendix C

Thermal Analysis

Thermal analysis is a series technique where physical properties i.e. mass, dimension enthalpy, of a material are measured as a function of time, while the material is subjected to a temperature program. The physical properties are thus measured as a function of temperature. This method plays an important role in the characterization of ceramics and inorganic electronic materials because the synthesis and applications of these materials generally involve such a wide range of temperature. Hence, the evaluation of their composition, properties, reactivity as a function of temperature and time is of vital importance.

To observe such characteristic of perovskite-oxide ceramics as a function of temperature, this research employed Thermogravimetry (TGA) and Thermal Expantion (TE).

C.1 Thermogravimetry (TG)

Thermogravimetric analysis (TGA) is an analytical technique used to determine a material's thermal stability and its fraction of volatile components by monitoring the weight change that occurs as a specimen is heated. The measurement is normally carried out in air or in an inert atmosphere, such as Helium or Argon, and the weight is recorded as a function of increasing temperature. Sometimes, the measurement is performed in a lean oxygen atmosphere (1 to 5% O2 in N2 or He) to slow down oxidation. In addition to weight changes, some instruments also record the temperature difference between the specimen and one or more reference pans (differential thermal analysis, or DTA) or the heat flow into the specimen pan compared to that of the reference pan (differential scanning calorimetry, or DSC). The latter can be used to monitor the energy released or absorbed via chemical reactions during the heating process. In particular case perovskite or perovskite-like materials, although the investigated materials are formed in nonstoichiometry, this measurement is viable and convenient method to follow the changes quantitative of materials.

During the TGA testing process, a sample of analyzed material is placed into an alumina cup, which supported on and analytical balance located outside the furnace chamber.

The sample cup is heated according to a predetermined thermal cycle and the balance sends the weight signal to the computer storage, along with the sample temperature and elapsed time. The TGA curve plots the TGA signal, converted to percent weight change on the y-axis against the reference material temperature on the x-axis. Therefore, the results of the test is a graph of the TGA signal, that is, weight loss or gain converted to percent weight loss on y-axis plotted versus the sample temperature in degree Celsius on x-axis, as presented in Figure C.1.
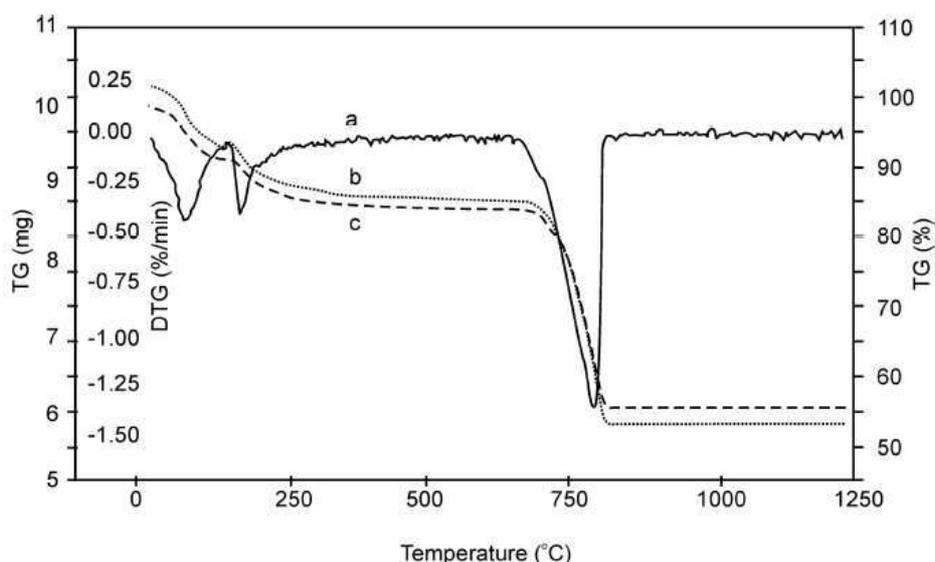
Figure C.1: *TGA and DTG curve of CaCO3 at heating rates of (b) 10°C.min^{-1} (c) 3 °C.min^{-1}.*

The TG curve presented as weight loss or weight gain processes are possibly assigned as water desorption, structural water release, structural decomposition, carbonate decomposition, gas evolution, sulfur oxidation rehydration, and other transformation. For example, pure $CaCO_3$, the TG curve in Fig. D.1 indicates the decomposition of $CaCO_3$ in a single step between 800 °C and 950°C to form stable CaO and the gas carbon dioxide. This can explained the chemistry of $CaCO_3$ when it is heated:

$$CaCO_3(s) \rightarrow CaO(s) + CO_2(g) \qquad \ldots(eq.\ C.1)$$

MW: 100.1   56.1   44

208
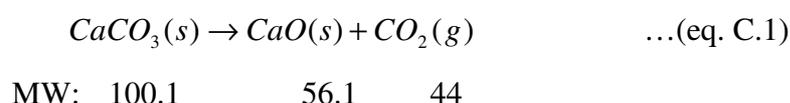
Now again consider the Fig. D.1, it indicates the mass lost percentage by the sample is 44 (100.1-56.1) between 800 and 950°C. This exactly corresponds to the mass changes calculations based on stoichiometry of the decomposition of CaCO3 expressed by the chemical Eq. D.1. As in this case, percentage weight loss of CaCO3 will be

$$m\,(\%) = \frac{MW\left(CO_2\right)}{MW\left(CaCO_3\right)} \times 100 \qquad \ldots\text{(eq. C.2)}$$

In the case of complex mixture compound, for example, a mixture of calcium, strontium and barium oxalates, their thermogram presented in Figure C.2 noticed that in between 100 and 250°C the water of hydration is evolved from all metal oxalates. After the loss if the water, the curve exhibited a horizontal weight level from 250-360°C, which corresponds to the composition for anhydrous metal level from oxalates. Then all the three oxalates decomposed simultaneously to the carbonates and the process completed at 500°C. From 500°C to 620°C, the anhydrous carbonates were stable. On further heating, the CaCO3 decomposed in the temperature range 620°C-860°C to oxide followed by the decomposition of SrCO3 from 860°C to 1100°C at which BaCO3 began to decompose.
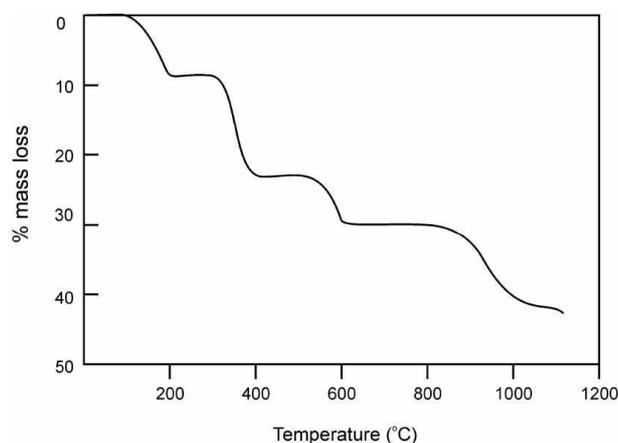
Figure C.2: *TGA curve of the mixture of calcium, strontium and barium oxalate.*

TGA instrument:

In this study, perovskite-related ceramic samples were thermally investigated using Setaram Setsys Evolution (Setaram, France) instrument as shown in Figure C.3. The investigated temperature range was in between 25°C (or room temperature) and 1000°C. The

heating rate of 10°C/min was used. In order to enhance the accuracy of the TG measurement at temperature below 700°C, a Pt crucible was employed.
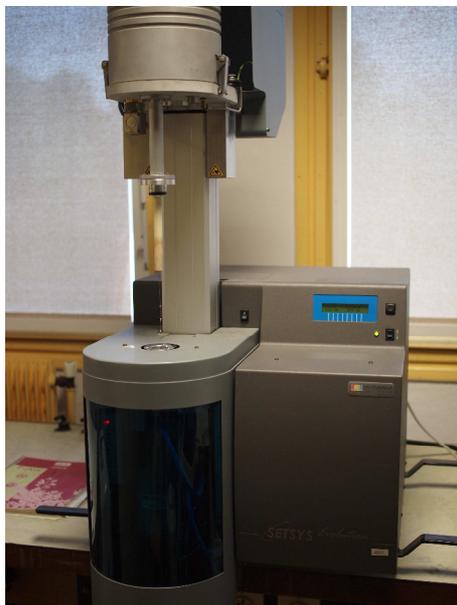
Figure C.3: *Thermogravimetry (TG) Setaram Setsys Evolution (Setaram, France) instrument.*

In every thermogravimatric tests, a minimum 50 mg of investigated ceramic piece was performed under He atmosphere. The specification of such He gas is high purity of 99.99%, Alphagaz-1 grade (H_2O < 3 ppm vol., O_2 < 2 ppm vol., C_nH_m < 0.5 ppm vol.) provided by Air Liquide company, France.

D.2 Thermal Expansion (TE)

Nearly all materials expand on heating due to increased atomic vibrations. For ceramics, the magnitude of this expansion is related to the phases present and the pore-size distribution of the ceramic. Thermal expansion is typically measured using a thermo dilatometer. The thermal expansion of refractory ceramics is related to the potential thermal-shock resistance. For structural ceramics, thermal expansion is a critical design parameter for the design of expansion joints. Thermal expansion is commonly reported as the coefficient of linear thermal expansion (α) which is the slope of the thermal expansion curve. The linear coefficient of thermal expansion is calculated as:

$$\alpha = \frac{L_2 - L_1}{L_0(T_2 - T_1)} = \frac{\Delta L}{L_0 \Delta T} \qquad \text{...(eq. C.3)}$$

where L_0 is the original length, L_2 is the length at temperature T_2 and L_1 is the length at temperature T_1. The units of α are thus K^{-1} or $°C^{-1}$. Conversion factors are:

To convert	to	Multiply by
$10^{-6}/K$	$10^{-6}/F$	0.55556
$10^{-6}/°F$	$10^{-6}/K$	1.8
ppm/°C	$10^{-6}/K$	1
$10^{-6}/°C$	$10^{-6}/K$	1
$(\mu m/m)/°F$	$10^{-6}/K$	1.8
$(\mu m/m)/°C$	$10^{-6}/K$	1
$10^{-6}/R$	$10^{-6}/K$	1.8

The coefficient of thermal expansion is also often defined as the fractional increase in length per unit rise in temperature. The exact definition varies, depending on whether it is specified at a precise temperature (true coefficient of thermal expansion or $\overline{\alpha}$ or over a temperature range (mean coefficient of thermal expansion or α). The true coefficient is related to the slope of the tangent of the length versus temperature plot, while the mean coefficient is governed by the slope of the chord between two points on the curve. Variation in CTE values can occur according to the definition used. When α is constant over the temperature range then $\alpha = \overline{\alpha}$. Finite-element analysis (FEA) software such as (MSC software) requires that α be input, not $\overline{\alpha}$.

Heating or cooling affects all the dimensions of a body of material, with a resultant change in volume. Volume changes may be determined:

$$\frac{\Delta V}{\Delta V_0} = \alpha_V \Delta T \qquad \text{...(eq. C.4)}$$

Where ΔV and V_0 are the volume change and original volume, respectively, and α_V represents the volume coefficient of thermal expansion. In many materials, the value of α_V is anisotropic; that is, it depends on the crystallographic direction along which it is measured. For materials in which the thermal expansion is isotropic, α_V is approximately $3\alpha_1$.

To determine the thermal expansion coefficient, two physical quantities (displacement and temperature) must be measured on a sample that is undergoing a thermal cycle. Three of the main techniques used for CTE measurement are dilatometry, interferometry, and thermomechanical analysis.

In this study, the mechanical dilatrometry technique was employed. With this technique, a specimen is heated in a furnace, and the displacement of the ends of the specimen is transmitted to a sensor by means of push rods. The precision of the test is lower than that of interferometry, and the test is generally applicable to materials with CTE above 5×10^{-6}/K (2.8×10^{-6}/°F) over the temperature range of –180 to 900 °C (–290 to 1650 °F). Push rods may be of the vitreous silica type, the high-purity alumina type, or the isotropic graphite type. Alumina systems can extend the temperature range up to 1600 °C (2900 °F) and graphite systems up to 2500 °C (4500 °F). ASTM Test Method E 228 coves the determination of linear thermal expansion of rigid solid materials using vitreous silica push rod or tube dilatometers.

TE (Dilatrometry) instrument:

The TE measurements, in this study, were performed using a Setaram Setsys 1650 dilatometer instrument equipped with amorphous silica rod and support, as shown in Figure C.4. The very low thermal expansion of amorphous silica makes a direct comparison of as-measured data possible. Flat pieces of the investigated perovskite-related oxides ceramics are measured in 30-700°C temperature range in both heating and cooling for three successive cycles with heating rate of 10°C.

A ceramic piece with ~10 mm. was placed into the dilatometry instrument, and pressed by the am amorphous silica rod with the charge approximately 150 N. The measurement were then run under argon atmosphere. The argon gas is Alphagaz-2 grade (99.99% purity: H_2O < 0.5 ppm vol., O_2 < 0.1 ppm vol., CO < 0.1 ppm vol., CO_2 < 0.1 ppm vol., H_2 < 0.1 ppm vol., C_nH_m < 0.5 ppm vol.) provided by Air Liquide company, France.

Figure C.4: *The thermal expansion (TE) Setaram Setsys 1650 dilatometer instrument equipped with amorphous silica rod and support.*

Appendix D

IR and Raman spectroscopy

Molecules consist of atoms which have a certain mass and which are connected by elastic bonds. As a result, they can perform periodic motions, they have *"vibrational degrees of freedom"*: all motions of the atoms in a molecules relative to each other are a superposition of so-called *"normal vibrations"*, in which all atoms are vibrating with the same phase and *"normal frequency"*. Their amplitudes are described by a *"normal coordinate"*. Polyatomic molecules with n atoms possess 3n-6 normal vibrations (c.a. linear molecules have 3n-5 normal vibration), which define their *"vibrational spectra"*. The spectra depend on the masses of the atoms, their geometrical arrangement, and the strength of their chemical bonds.

D.1 Theoretical of Molecular vibrations

The easiest way of modeling molecular vibrations is to imagine the atoms in a molecule as balls, and the chemical bonds connecting them as massless spring. Such a ball-and spring model for a diatomic molecule is illustrated in Figure D.1. Let us assume that the masses of the two atoms are m_1 and m_2 respectively, and that the restoring force (F) of the spring is proportional to the displacement x of the atoms from their equilibrium position.
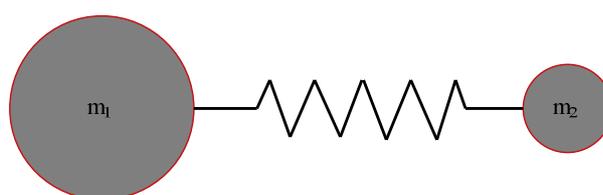
Figure D.1: *The ball and spring model for a diatomic molecule.*

$$F = -kx \qquad \text{… (eq. D.1)}$$

where k is the force constant of the spring, in N. m^{-1}, which is a measure of the strength of the bond between the two atoms. Equation D.1 is Hooke's law, and the resulting motion is simple harmonic. Based on these assumptions the ball-and-spring model is a harmonic oscillator. The

vibrational frequency, ν_0, in Hz, of the harmonic oscillator in terms of classical mechanics is given by

$$\nu_0 = \frac{1}{2\pi}\sqrt{\frac{k}{m}} \qquad \text{… (eq. D.2)}$$

where m is the reduced mass in kg

$$m = \frac{m_1 m_2}{m_1 + m_2} \qquad \text{… (eq. D.3)}$$

In vibrational spectroscopy, it is common to use the wavenumber unit $\tilde{\nu}$, which is expressed in cm^{-1}. This is the number of waves in a length of the centimeter, the reciprocal wavelength, and is given by the following relationship:

$$\tilde{\nu} = \frac{1}{\lambda} = \frac{\nu}{c} \qquad \text{… (eq. D.4)}$$

where λ is the wavelength and c is the velocity of the light in vacuum $(2.9979 \times 10^8 \ ms^{-1})$. The wavenumber unit has the advantage of being linear with energy.

D.3 The symmetry of molecules and molecular vibrations

Most crystals exhibit macroscopically visible symmetry axes and planes. In order to utilize the symmetry of molecules and crystals for vibrational spectroscopy, the symmetry properties have to be defined conveniently.

For treating symmetry properties of molecules, symmetry operators are defines, which when applied to a molecule, bring it into coincidence with itself. For molecules there are five types of symmetry operators:

E   *Identity operator*, a trivial but necessary operator

i   *Inversion operator*, representing reflection at a center of symmetry

σ   *Refrection operator*, representing reflection on a plane

C_n^k n-fold rotation operator, defining k successive rotations by an angle of $2\pi/n$ about and n-flod rotation axis (proper axis), n is the order of the axis

S_n^k n-fold rotation-reflection operator, defining k successive rotation-reflections about an n-fold rotation-reflection axis (improper axis): rotation by an angle of $2\pi/n$, followed by reflection on a plane perpendicular to the axis

Further, symmetry elements are defined, these are the geometrical loci of all points which remain invariant when a symmetry operation is carried out. The names of the symmetry elements introduced by *Schoenfies* (1891) are given below, followed by the international notaion, introduced by *Hermann* (1928) and *Mauguin* (1931):

Notation by:	*Schoenfies*	*Hermann/ Mauguin*
Identity	E	1
Center of symmetry	i	$\bar{1}$
Symmetry plane	σ	m
Proper axis	C_n	2, 3, 4, …
Improper axis	S_n	$\bar{2}, \bar{3}, \bar{4}$, …

Several symmetry operators may be applied to the same molecule, these constitue a point group. A group is a well defined concept in mathematics. The name point group indicates that at least one point (center of mass) remains unmoved, when the symmetry operations are carried out. There is a limited number of point groups of molecules. Crystallographs count 32 point groups, since only operators related to 1-, 2-, 3-, 4-, and 6-fold symmetry axes may be applied to parallelepipeds filling the space of crystals. In molecular spectroscopy, 5-, 7-, 8-fold symmetry axes also exist, which increases the number of point groups in this field.

Point groups are usually characterized by symbols, introduced by *Schoenfies* (1981). Indeed, IUPAC recommended the use of such *Schoenfies* notation. The *Schoenfies* symbols representing the point groups of molecules are defined as follows:

C_1 no other symmetry element

C_n an n-fold proper axis

D_n an n-fold proper main axis C_n and n 2-fold axes C_2 perpendicular to the main axis

D_{nh} an n-fold proper main axis C_n , n 2-fold axes C_2 perpendicular to the main axis and a 'horizontal' mirror plane perpendicular to the main axis

C_{nh} a C_n main axis and a 'horizontal' mirror plane perpendicular to the main axis

C_{nv} a C_n main axis and n 'vertical' symmetry planes σ_v ; if n is an even number, there are n/2 planes σ_v and n/2 planes σ_d bisecting the angles between σ_v

D_{nd} an n-fold proper main axis C_n , n 2-fold axes C_2 perpendicular to the main axis, and n 'vertical' planes σ_d bisecting the angles between all neighboring C_2 axes

S_n an n-fold improper main axis S_n

T   all axes of a regular tetrahedron

T_d all axes and planes of a regular tetrahedron

O   all axes of a cube

O_h all symmetry elements of a cube

I_h all symmetry elements of an icosahedrons

$C_{\infty v}$ a C_∞ axis and an infinite number of 'vertical' planes σ_v

$D_{\infty v}$ a D_∞ axis and an infinite number of 'vertical' planes σ_v and a 'horizontal' plane σ_h

D.4 The infrared spectrum

Infrared spectroscopy is based on the interaction of electromagnetic radiation with a molecular system, in most cases in the form of absorption of energy from the incident beam. The frequencies of the absorption bands ν_s are proportional to the energy difference between the vibrational ground and exited stated, Figure D.2.
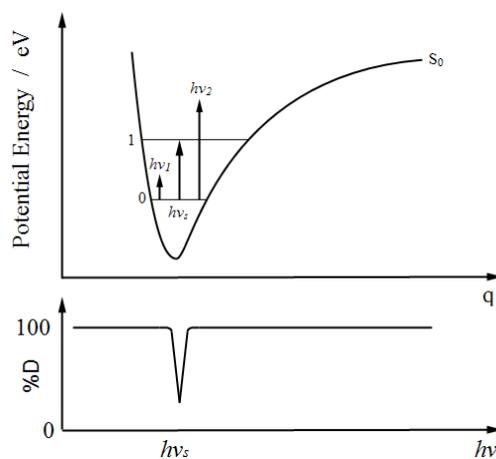
Figure D.2: *Principal of infrared absorption and its spectrum.*

The quanta of the energy, i.e. $h\nu_l$, $h\nu_s$, and $h\nu_2$ hit a molecule, and only $h\nu_s$ is absorbed, and give the infrared absorption spectrum. A quantum mechanical treatment of the vibrations of a crystal as a harmonic oscillator shows that phonon energies are quantized, with

$$E_i = \left(n_i + \frac{1}{2}\right) h\nu_i \qquad \dots \text{(eq. D.5)}$$

where n_i is the quantum number and ν_i is the normal frequency associated with the normal coordinate Q_i.

A crystal is capable of directly absorbing a photon that corresponds to an energy of vibration, given in Eq. D.5. Because the photons are polarized, the electric field of the photon must be capable of interesting with the vibration. An electric field will then create a force on charged particles, such as the positive and negative ions consisting the crystal. As the electric field points in one direction, the electric dipole may be stretched along an axis of the crystal. However, when the electric field points in the opposite direction, the electric dipole becomes compressed. This results in a vibration of the system. The photon-dipole interaction leads to the selection rule for infrared absorption – vibrations are infrared-active if there is a change in the dipole moment during the vibration, further if the dipole is not changed during the vibration, an incident photon will not be capable of exciting the vibration.

The absorption bands due to the vibrational transitions are found in the wavelength of 2.5 … 1000 µm, which is equivalent to a wavenumber range of $\tilde{\nu}$ = 4000 … 10 cm^{-1}. One of the most distinct and easily recognizable peaks in an IR spectrum is the broad O-H absorption of alcohols and phenols. The broad O-H peak is placed by a sharp signal around ~3600 cm^{-1}.

D.5 the Raman spectrum

The Raman effect, named for the Nobel prize work by Chandrasekhra Venkata Raman in 1928, is an inelastic light scattering effect resulting from the excitation or de-excitation of vibrational modes. In the simple case of a single molecule, Figure D.3, an incident photon can either scatter elastically, known as Rayleigh scattering, or scatter inelastically and excite or absorb a vibrational mode of the molecule. In a crystal lattice, the photon may scatter from a lattice phonon that will change the energy of the phonon. The energy loss or gain of the inelastically scattered photon corresponds to the energy of a vibrational level, or phonon level,

of the system. If a phonon is created at a higher energy state, then the scattered photon will have less energy than the incident photon. Alternatively, a phonon can be annihilated, resulting in a scattered photon having greater energy than the incident photon.

Raman scattering is a phenomenon with a low probability of occurrence. Only one in 106 of incident photons is inelastically scattered. Because the majority of incident light is Rayleigh scattered, Raman detector systems must remove this elastically scattered light from the collected light, or else the Rayleigh scattered light can overwhelm the weaker Raman signal. Raman scattering is typically performed non-resonantly, meaning that the energy of the incident photons does not equal any energy difference between any phonon levels of the lattice. In the most common conceptual description, the photon excites the system to a virtual state before decaying to the ground state (Rayleigh) or an excited vibrational state (Raman). This can be seen in Figure D.3a.
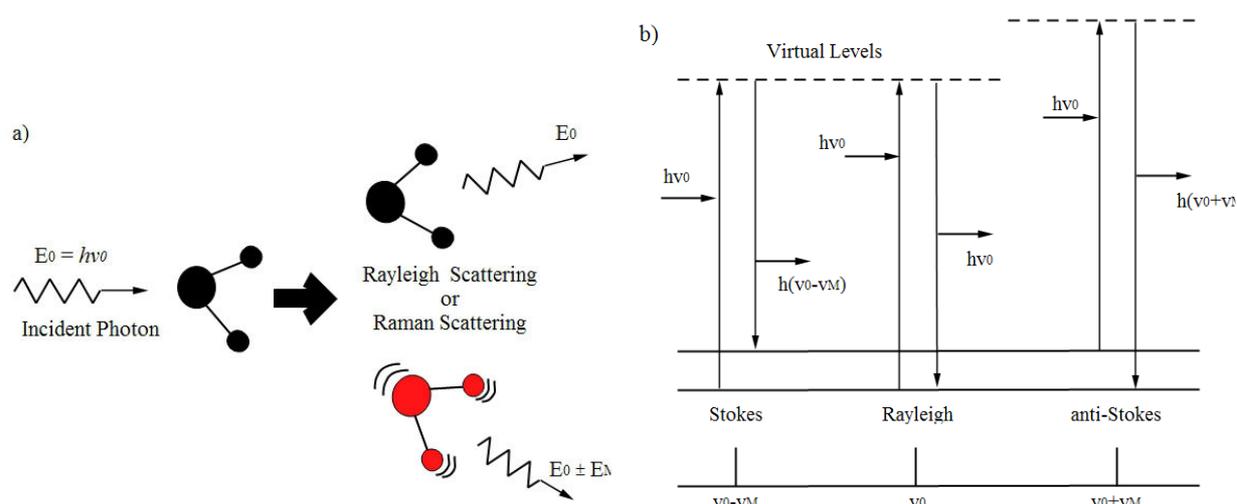
Figure D.3: *a) Schematic Rayleigh and Raman scattering processes (an incident photon can either scatter elastically or inelastically from a molecule) and b) Stokes scattering and anti-Stokes scattering.*

Stokes scattering and anti-Stokes scattering, Fig. D.3b, are the terms applied to whether a phonon is created or annihilated, respectively. Anti-Stokes scattering is a much weaker effect than Stokes scattering. All Raman data collected in this study, used for purposes of determining peak positions, are Stokes signals, corresponding to scattered photons of lower energy than the incident photons.

In a classical approach, the oscillating electric field E of the incident light with frequency ν_0 and amplitude E_0 can be written as

$$E = E_0 \cos 2\pi \nu_0 t \qquad \text{...(eq. D.6)}$$

This electric field interacts with and distorts the electron cloud of the lattice, inducing an electric dipole P given by

$$P = \alpha E \qquad \text{...(eq. D.7)}$$

where α is the polarizability of the lattice. If the lattice is vibrating with frequency ν_m and amplitude q_0, then the nuclear displacement can be written as:

$$q = q_0 \cos 2\pi \nu_m t \qquad \text{...(eq. D.8)}$$

For small amplitudes, α is a linear function of q, and can be expanded as

$$\alpha = \alpha_0 + \left(\frac{\partial \alpha}{\partial q}\right)_0 q + ..., \qquad \text{...(eq. D.9)}$$

where the partial derivative is evaluated at the equilibrium nuclear position. Combining equation D.6 – D.9, gives:

$$P = \alpha_0 E_0 \cos 2\pi \nu_0 t + \frac{1}{2}\left(\frac{\partial \alpha}{\partial q}\right)_0 q_0 E_0 \left[\cos\{2\pi(\nu_0 + \nu_m)t\} + \cos\{2\pi(\nu_0 - \nu_m)t\}\right] \text{ ...(eq. D.10)}$$

where the first term n the right side of the equality in Eq. D.9 is the Rayleigh scattering term, which has a frequency equal to the incident frequency, ν_0. The stoke and anti-Stokes terms, having frequencies shifted from the incident frequency, are $\nu_0 - \nu_M$ and $\nu_0 + \nu_M$, respectively. The partial derivatives of the polarizability act as coefficients for the Stokes and anti-Stokes terms, thus indicating that these Raman terms are non-zero only if there is a change in the polarizability ($\partial \alpha / \partial q \neq 0$) when the molecule vibrates. If the polarizability does not change during a vibration, this coefficient is zero, and the vibration is not Raman-active.

D.2 Vibrational spectroscopy (IR and R) instruments

In this study, ATR FT-IR spectra were recorded between 600 cm^{-1} and 4000 cm^{-1} at room temperature. The Bruker IR-scope FTIR spectrometer (Fig. D.4 left) in ATR modes with a Diamond ATR and a Germanium micro ATR crystal were employed. The different of the use of a semispherical germanium prism and diamond prism gives different local scale area: 2x2 mm^2 for Diamond and 20x20 µm^2 for Germanium.

Raman spectroscopy a LabRam HR800 (Horiba Jobin Yvon, Fig. D.4 right) was employed. This equipment is provided with a 458 and 514.5 nm emission of Ar+ laser (coherent I-90C-6), a focal length of 80 mm and Paltier cooled CCD detector. A300 lines/mm grating is used, allowing the recording the completely spectral range of our interest in one acquisition and the spectral resolution of the equipment is around 1.5 cm^{-2}. Reyleigh filtering is achieved using BragGrate Notch Filter. For measurements under 785 nm wavelength, we performed using the solid state source line of a Senterra spectrometer (Bruker Optics, Karlsruhe, Germany). The Olympus microscope coupled to the spectrometer and an automatically motorized XY stage were used with 50x long working distance objective. With this objective, the analyzed diameter area is about 3 µm. In order to avoid the decompositions and/or structural changes effected by laser heating, the laser power is varied using the density filters.

Figure D.4: *The Bruker IR-scope FTIR spectrometer (left) and a Raman spectroscopy LabRam HR800 (Horiba Jobin Yvon) (right).*

Appendix E

X-ray diffraction (XRD)

X-ray diffraction is a common and powerful tool for determining the crystal structure of a material. However, sample preparation is crucial, and the technique cannot examine all varieties of samples. The sample must be a single crystal, a uniform surface, or powder, all of which require a long-range order for coherent x-ray diffraction.

E.1 Theoretical

Atoms within a crystal lattice are formed regular planes with spacing *d* between each plane. Coherent x-rays incident upon these regular planes can reflect off these planes and constructively interfere if the path length difference is a multiple of the wave-length of the light. Knowing the angle at which the light scatters from these planes allows determination of the distance between each plane. Many different planes may exist in a regular crystal lattice, defined by coplanar atoms in the various crystal sites throughout the lattice. The incident x-rays will, therefore, be capable of scattering off all these planes that lead to constructive interference at many different angles. Information about the crystal structure can be determined from this diffraction pattern.

The spacing between atomic planes, d, is determined using Bragg's law,

$$2d \sin \theta = m\lambda \qquad \qquad \text{…(eq. E.1)}$$

Where θ is the angle between the incident light and the lattice planes, m is an integer describing the order, and λ is the wavelength of the incident light. X-rays are used because, to achieve measurable diffraction, the wavelength must be on the order of d. Because the x-ray diffraction (XRD) spectrum and structure of spinel are well known, the lattice parameter can be calculated by knowing the Miller indices of each spinel diffraction peak.

Figure E.1 illustrated a visualization of the Bregg equation. A set of crystallographic lattice planes with distances d_{hkl} is irradiated by plane wave x-rays impinging on the lattice planes at an angle θ. The relative phase shift of the wave depends on the configuration of

atoms as is seen for the two darker atoms in the top plane and one plane beneath. The phase shift comprises of two shares, Δ_1 and Δ_2, the sum of which equals $2d\sin\theta$ for any arbitrary angle θ. Constructive interference for the reflected wave, however, can only be achieved when the phase shift $2d\sin\theta$ is a multiple of the wavelength.

$$\Delta_1 + \Delta_2 = 2d\cos(90° - \theta) = 2d\sin\theta$$
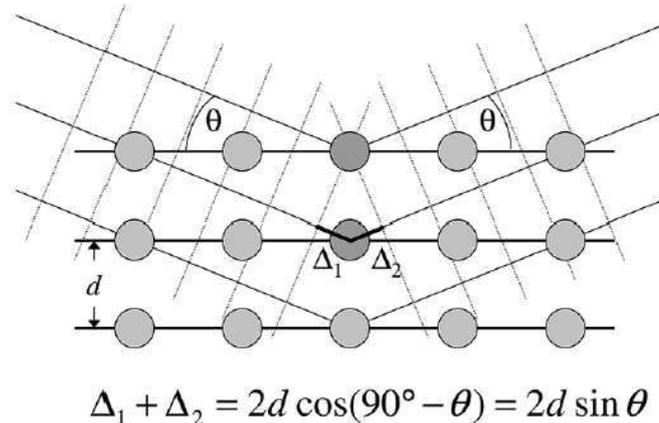
Figure E.1: *Visualization of the Bregg equation. Maximum scattered intensity is only observed when the phase shifts add to a multiple of the incident wavelength λ.*

Miller indices are reciprocal fractions along each dimension that define a plane within the lattice and are commonly denoted as three numbers, hkl, which represent the fraction of each dimension of the lattice. For the cubic system, the dimensions are the standard Cartesian coordinates x; y; z. For example, the (100) represents a plane in the yz plane. The (200) surface would be a yz plane halfway along the x dimension of the crystal.

For a cubic lattice, the diffraction spacing, d, can be related to the lattice parameter, *a* and the Miller indices, (hkl), by

$$d = \frac{a}{\sqrt{h^2 + k^2 + l^2}} \qquad \text{…(eq. E.2)}$$

Intensities of the X-ray diffraction peaks are affected by many variables such as the electron distribution around any atom or ion and the structure of the crystal. Scattering of the x-rays occur from the electron cloud surrounding the atom or ion, and, therefore, the intensities are a sum of all scattering from the electron cloud. Because the spacing within the electron cloud is smaller than the wavelength of the incident X-ray, partially destructive

224

interference occurs from the sum. Moreover, an atomic scattering factor, f_0, can be calculated for atoms and ions. The structure factor, F_{hkl}, describes how the atomic arrangement of the crystal affects the x-ray diffraction peaks. The Rietveld refinement method, named for Le Bail Rietveld who developed the method, incorporates all of the variables that affect diffraction peaks, and involves the least squares fit to refine structural information of the sample.

It should be emphasized that the Bragg equation (Eq. E.1) is valid for any lattice structure, not only the simple cubic one. The generalization is easily performed by just inserting the interplanar spacing *dhkl* of the crystal lattice under investigation. Table 1.1 gives the relation of *dhkl* and the unit cell parameters for different crystal classes.

Table E.1: *Interplanar spacing dhkl for different crystal systems and their dependency on Millar indices hkl. Parameters a, b abd c give the lengths of the crystallographic unit cell, while α, β and γ specify the angles between them.*

Crystal system	Constraints	$\dfrac{1}{d_{hkl}^2} =$
Cubic	$a = b = c$ $\alpha = \beta = \gamma = 90°$	$\dfrac{h^2 + k^2 + l^2}{a^2}$
Tetragonal	$a = b \neq c$ $\alpha = \beta = \gamma = 90°$	$\dfrac{h^2 + k^2}{a^2} + \dfrac{l^2}{c^2}$
Orthorhombic	$a \neq b \neq c$ $\alpha = \beta = \gamma = 90°$	$\dfrac{h^2}{a^2} + \dfrac{k^2}{b^2} + \dfrac{l^2}{c^2}$
Hexagonal	$a = b \neq c$ $\alpha = \beta = 90°$ $\gamma = 120°$	$\dfrac{4}{3}\dfrac{h^2 + hk + k^2}{a^2} + \dfrac{l^2}{c^2}$
Trigonal/ Rhombohedral	$a = b = c$ $\alpha = \beta = \gamma$	$\dfrac{\left(h^2 + k^2 + l^2\right)\sin^2\alpha + 2(hk + hl + kl)\left(\cos^2\alpha - \cos\alpha\right)}{a^2\left(1 - 3\cos^2\alpha + 2\cos^3\alpha\right)}$
Monoclinic	$\alpha = \gamma = 90°$	$\dfrac{h^2}{a^2\sin^2\beta} + \dfrac{k^2}{b^2} + \dfrac{l^2}{c^2\sin^2\beta} - \dfrac{2hl\cos\beta}{ac\sin^2\beta}$

The study of powder diffraction patterns allows implementing other methods such as the refinement of cell parameters to go to the structure refinement.

E.2 Instrument and measurement conditions

In this study, XRD patterns of ground pellets were performed by Batocchi's group at ICMCB, Université de Bordeaux, France. The investigations were collected using a PANalytical X'pert MPD-PRO Bragg-Brentano.

The operating range is θ-2θ geometry diffractometer equipped with a germanium primary monochromator over an angular range of $2\theta = 10$-$130°$. Each acquisition lasted for 64 hours. The Cu-Kα_1 ($\lambda = 1.54056$ Å) radiation was generated at 45 kV and 40 mA. Unit-cell parameters were calculated by Le Bail profile matching. The phase identification was carried out using the ICCD database and PANatycal X'pert high score software. The relative quantities of the different phases were estimated according to the ratio of the relative intensities of the major peaks recorded in the XRD patterns.

Appendix F

Neutron Diffraction

Among most other methods, neutron is a powerful and direct method allows a detailed understanding of the static and dynamic properties on an atomic scale of materials that occur in our environment. Combined with x-ray scattering a very large range of momentum and energy transfer can be covered thanks to the high complementary of both techniques. The most relevant, unique character of neutrons that cannot be matched by any other techniques, can be summarized follows [1] :

- The neutron interacts with the atomic nucleus and not with the electrons as x-rays do. This has important consequences: i) the response of neutrons from light atoms like hydrogen or oxygen is much higher than for x-rays, ii) neutron can easily distinguish atoms of comparable atomic number, iii) neutrons distinguish isotopes: for example, deuteration of macromolecules allows to focus on specific aspects of their atomic arrangement or their motion.

- For the same wavelength as hard X-ray, the neutron energy is much lower and comparable to the energy of elementary excitations in matter. Therefore, neutrons do not only allow the determination of the 'static average' chemical structure, but also the investigation of the dynamic properties of the atomic arrangements that are directly related to the physical properties of materials.

- By virtue of its neutrality, the neutron is rather weakly interacting with matter, which means that there is almost no reaction damage to living objects under study. Also, the rather weak interaction with matter results in a large penetration depth and therefore the bulk properties of matter can be studied. This is also important for the investigation of materials under extreme conditions such as very low and high temperature, high pressure, high magnetic and electric fields, etc.

---

[1] A. Furrer, Neutron Scattering in Novel Materials, World Scientific Publishing, Singapore, 2000.

- The neutron carries a magnetic moment that makes it an excellent probe for the determination of magnetic structures and magnetic excitations.

F.1 Properties of Neutron

The neutron is a nuclear particle with a mass rather close to that of the proton:

$$m_n = 1.675 \times 10^{-27} kg \qquad\qquad \dots \text{(Eq. F.1)}$$

The neutron does not exist naturally in free form, but decays into a proton, an electron, and and anti-neutrino. The neutron lifetime, τ = 886 s, is much longer than the time of a neutron within a scattering experiment, where each neutron spends merely a fraction of a second.

Neutrons for scattering experiments are usually extracted from a moderator, which shows down neutrons produced in a spallation source or reactor. The thermalized neutron are extracted from the source through beam ports, which are either evacuated or helium filled tubes looking into moderator. If the moderator is designed correctly, the probability $P(\upsilon)$ of neutrons having a velocity between υ and $\upsilon+d\upsilon$ follows a Maxwell-Boltzmann distribution:

$$P(\upsilon) \cdot d\upsilon = 4\pi \cdot \left(\frac{m}{2\pi \cdot k_B T} \right) \cdot \upsilon^2 \cdot e^{-\frac{m\upsilon^2}{2} \cdot \frac{1}{k_B T}} d\upsilon \qquad\qquad \dots \text{(Eq. F.2)}$$

where m is the neutron mass, k_B is the Boltzmann constant (1.381x10^{-23} J.K^{-1}.mol^{-1}) and T is the temperature of the moderator material. The maximum of P(υ) is reached for the neutron velocity $\upsilon = \sqrt{2k_B T/m}$. This relation shows the reason of using the popular terms hot, thermal and cold neutrons. The maximum neutrons fluxes measured by Laboratoire Léon Brillouin (LLB) is 17.5x10^9 neutrons.cm^{-2}.s^{-1} for the cold source, 7.52x10^9 neutrons.cm^{-2}.s^{-1} for the hot source, and 3.93x10^9 neutrons.cm^{-2}.s^{-1} for the thermal one [1].

---

[1] Experimental Facilities, Laboratoire Leon Brillouin, CEA Saclay, France, 2003.

F.2 Interaction of Neutrons with condensed matter

The neutron interaction with matter is weak. In the following distinguish between three different cases as shown in the Fig. F.1:

- *Absorption:* the neutron beam intensity is reduced when crossing the sample, but the propagation direction stays unchanged.

- Refraction: the incident beam changes its direction, but is not weakened. The deflection angle (α) is small (a few degrees).

- Scattering: the incident neutron plane wave is scattered by the nuclei and yield an outgoing spherical wave of reduced intensity at the scattering angle 2θ.

a) absorption   b) refraction   c) scattering
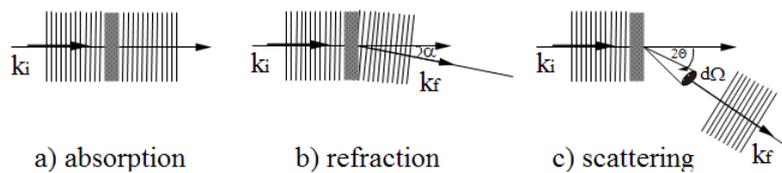
Figure F.1: *Schematic view of the three different types of neutron interaction with matter.*

F.2.1 Absorption

In this process, some neutrons lost by being absorbed in the nuclei, which then emit radiation or undergo fission. The intensity of the transmitted neutron beam is given by

$$I(d) = I_0 e^{-N_0 \sigma_a d} = I_0 e^{-\mu d} \qquad \text{… (Eq. F.3)}$$

Where I_0 is the intensity of the incoming neutrons, N_0 the density of the nuclei, σ_a the corresponding absorption cross section and d the thickness of the sample.

The values σ_a have been determined experimentally; they are generally small with a few well-known exceptions. It is conventional to tabulate σ_a for a neutron $\upsilon = 2200$ m/s (corresponding to $\lambda=1.8$ Å). For most elements, the energy of thermal neutrons is far off from any absorption resonance; in this case, σ_a is inversely proportional to the neutron velocity.

An important application of absorption is the detection of neutrons using materials with large σ_a (e.g. ^{3}He). Neutron detectors are based on exothermic reactions. The energy released in these processes is orders of magnitudes higher than the kinetic energy of the thermal neutrons being detected. The pulse height generated by the ion pairs is therefore almost independent of the energy of the detected neutrons, unfortunately it hence cannot be used for energy analysis.

F.2.2 Refraction

For neutron technique, a refraction index defined by scattering densities may be defined instead. Assuming that an incoming neutron wave is scattered from a thin plate, Fig. F.2, the refractive index n_r can be derived by integrating the overlap of the non-scattered incoming wave with the scattered one over the radius element L of the plate with thickness Δ yielding Fresnel integrals. If L is large compared to the neutron wavelength λ, the integral can be solved.
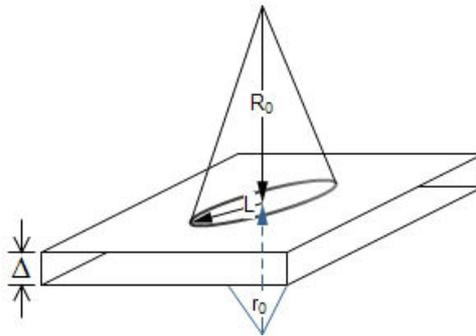
Figure F.2: *Refraction from a thin plate with thickness, Δ.*

The refraction index is then given by:

$$n_r = 1 - \frac{1}{2\pi} \rho \bar{b} \lambda^2 \qquad\qquad \dots \text{(Eq. F.4)}$$

where ρ is the number of nuclei per unit volume and $\bar{b}$ is the mean value of the scattering length of the nuclei. Total refraction can be reached for glancing angles

$$\gamma_c \leq \cos^{-1} n_r \qquad\qquad \dots \text{(Eq. F.5)}$$

where the glancing angle for neutrons with wavelength $\lambda=1$ Å is e.g. as small as 6' for natural nickel.

F.2.3   Scattering

The principal of the scattering of particles by a sample is the same for most kinds of radiation. The geometry of a scattering experiment is shown in Fig. F.3. Incident particles (neutrons, photons, etc.) having a wavevector k_i and a flux F (particles per cm^2 and s) are acattered by the sample into the element of solid angle $d\Omega = \sin \Theta d\Theta d\Phi$. then the number of particles scattered per second into $d\Omega$ with wavevector k_f is given by

$$I = F\left(\frac{d\sigma}{d\Omega}\right)d\Omega \qquad\qquad \dots \text{(Eq. F.6)}$$

where $d\sigma/d\Omega$ is the differential cross-section with the dimension of an area.
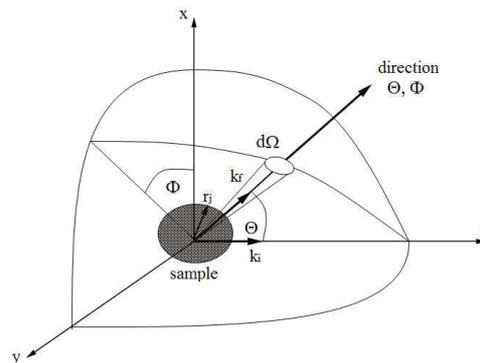
Figure F.3: *Geometry for a scattering experiment. A plane wave of neutron that propagates along the z-direction is scattered by the sample into a solid angle dΩ.*

In a general sample, the neutron scattering length varies from nucleus to nucleus. This can be due to the variation of the nuclear spin direction, or to variation between isotopes of the same element – or between different elements. The latter is a static disorder that for a macroscopic sample can be treated in the same way as a time-dependent disorder, since we can assume the sample is large enough to essentially represent an ensemble average.

F.3 Instrumental aspects

In this research, the neutron diffraction measurements were performed in the French neutron facility Orphée research at the CNRS-CEA Léon Brillouin Laboratory (Saclay, France).

A cylindrical vanadium sample holder is employed. Neutron experiments were carried out on a G4.1 cold Neutron Two-Axis Diffractometer PYRRHIAS equipped with a vertical focusing pyrolytic graphite monocrometer and a 800-cells multi-detector. The wavelength of 0.24226 nm was used. The collecting neutron diffraction patterns were home-made furnace requiring high vacumm (10^{-7} Torr).

LIST OF TABLE

LIST OF FIGURE

Abstract:

The chemical and structural stability of well-densified ceramics potentially used as H_2/air fuel cell/electrolyzer (and perhaps in CO2/Hydrocabons Converter) electrolyte or electrodes vs. CO_2-free/saturated pressurized water has been studied. The pressurization maximizes the efficiency of the energy conversion systems. Four types of pervoskite-related oxide ceramics were concerned: $BaCe_{0.4}Zr_{0.5}Y_{0.1}Zn_{0.04}O_{3-\delta}$ (BCZYZ), $SrZr_{0.9}Er_{0.1}O_{3-\delta}$ (SZE), $Ln_2NiO_{4+\delta}$ (LNO, Ln = La, Pr, Nd), and $La_{0.6}Sr_{0.4}Co_{0.2}Fe_{0.8}O_{3-\delta}$ (LSCF6428). Dense ceramic samples were exposed at 550°C to water vapor pressure in an autoclave for days to weeks. The protonation treatments were performed in two different conditions: operating condition (≤20 bar of CO_2-free water pressure, 550°C) and accelerated aging conditions (≥40 bar of CO_2-free/CO_2-saturated water pressure, 550°C). The pristine and 'protonated' samples were characterized using various analysis techniques: Optical Microscopy, Thermogravimetry, Thermal Expansion, (micro/macro) ATR FTIR, Raman micro-spectroscopy, X-ray and Neutron Scattering. The study reveals that under the operating condition (≤20 bar), the stability of LNO/LSCF6428 electrode materials and of SZE electrolyte appears good, while the BCZYZ electrolyte exhibit significant corrosion. The superior stability of LSFC6428 exposed in extreme CO_2-water vapor atmosphere was demonstrated about 5 to 30 times better than LNO and SZE homologues. The surface secondary phases form at the grain boundary. The protonation modifies more or less the structure symmetry, the unit-cell volume/parameter and the phase transition sequence in relation with the modification of the oxygen vacancy distribution. The proton doping level for different samples is also discussed.

Keywords: proton conductor, perovskite, hydrogen, autoclave, protonation, structure, stability, TGA, thermal expansion, Raman spectroscopy, ATR FTIR, X-ray diffraction, neutron diffraction, electrolyte, electrode, PC-SOFC, PC-SOEC

Résumé:

La stabilité structurale et chimique de céramiques bien densifiées candidates pour leur utilisation comme électrolyte ou matériau d'électrode de piles à combustible, électrolyseur H_2/air ou même de convertisseur CO_2/Hydrocarbures a été étudiée vis-à-vis de l'eau sous pression (autoclave, eau pauvre ou saturée en CO_2). La pressurisation maximise l'efficacité des dispositifs. Quatre familles de pérovskites ont été considérées: $BaCe_{0.4}Zr_{0.5}Y_{0.1}Zn_{0.04}O_{3-\delta}$ (BCZYZ), $SrZr_{0.9}Er_{0.1}O_{3-\delta}$ (SZE), $Ln_2NiO_{4+\delta}$ (LNO, Ln = La, Pr, Nd), and $La_{0.6}Sr_{0.4}Co_{0.2}Fe_{0.8}O_{3-\delta}$ (LSCF6428). Les céramiques denses sont traitées à 550°C en autoclave plusieurs jours à plusieurs semaines, soit dans des conditions de fonctionnement (≤20 bar, eau sans CO_2, 550°C), soit en vieillissement accéléré (≥40 bar eau sans ou saturée de CO_2, 550°C). Les céramiques ont été analysées avant et après 'protonation' par Microscopie Optique, Thermogravimétrie, Expansion Thermique, (micro/macro) ATR FTIR, Raman micro-Spectroscopie, diffraction des rayons X et des neutrons. En condition de fonctionnement (≤20 bar), la stabilité des matériaux d'électrodes LNO/LSCF6428 et de l'électrolyte SZE est bonne, alors que la céramique BCZYZ se corrode. La céramique LSFC6428 soumis à des conditions sévères (eau saturée en CO_2, 40 bar) est 5 à 30 fois moins corrodée que les composés LNO and SZE. La corrosion s'initie en surface, aux joints de grains. La protonation modifie plus ou moins la symétrie, le volume et les paramètres de la maille unitaire ainsi que les transitions de phase en relation avec la modification de la distribution/organisation des lacunes d'oxygène. Le niveau de dopage en proton des différents matériaux est aussi discuté.

Mots clés : conducteur protonique, pérovskite, hydrogène, autoclave, protonation, structure, stabilité, ATG, dilatation thermique, ATR FTIR, spectroscopie Raman, diffraction des rayons X, diffraction des neutrons, électrolyte, électrode, PC-SOFC, PC-SOEC